U.S. ARMY

FY24

PROCEEEDINGS OF THE U.S. ARMY COMBAT CAPABILITIES DEVELOPMENT COMMAND CHEMICAL BIOLOGICAL CENTER

IN-HOUSE LABORATORY INDEPENDENT RESEARCH AND CHEMICAL BIOLOGICAL ADVANCED MATERIALS MANUFACTURING SCIENCES PROGRAMS


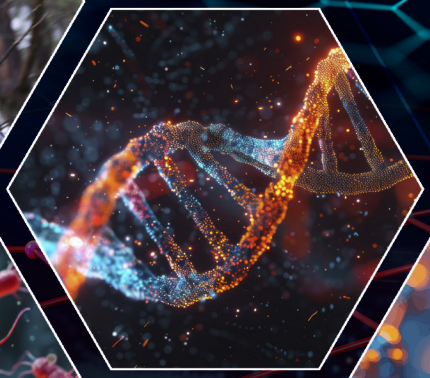

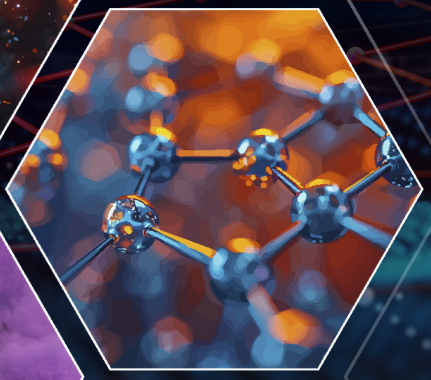


DEVCOM CHEMICAL BIOLOGICAL CENTER

Message from the In-house Laboratory Independent Research Program Director

I am pleased to present the sixteenth annual edition of the Proceedings of the U.S. Army Combat Capabilities Development Command Chemical Biological Center's (DEVCOM CBC) In-house Laboratory Independent Research (ILIR) and Chemical Biological Advanced Materials Manufacturing Science (CBAMMS). As the Senior Research Scientist (ST) for Chemistry and Director of the ILIR and CBAMMS programs, I am proud to lead the Center's Army-funded basic research and innovation programs. These programs offer DEVCOM CBC one of the most significant f unding s ources t o conduct in house research towards the needs of the Center.

Together, the ILIR and CBAMMS programs continue to leverage congressional funding to advance fundamental basic research and produce new data and capabilities, scientific p ublications, t echnical r eports, p atentable knowledge, and develop partnerships with external collaborators. To help guide these efforts, Center leadership continues to evaluate research thrust areas and use feedback from the workforce and program evaluators to critically evaluate research programs and individual projects. The focus of the basic science research programs continues to align to and support the Army Modernization Strategy, conducting research aligned to Chemical and Biological Sensing, Rational Molecular Synthesis and Nano-system Design, Synthetic Biology, Materials, and Obscuration sciences.

The FY24 ILIR and CBAMMS programs concluded with another successful Technical Advisory Board (TAB) Review, featuring reviewers from the United States Military Academy, DEVCOM Army Research Laboratory, and DEVCOM ARL Army Research Office. In FY24, a panel of experts from DEVCOM CBC produced and presented a holistic review of the past, current, and future efforts focused on Synthetic Biology and Biomanufacturing, two areas of recent focus by the Center. A summary of the information presented by these leaders is included in this report. The TAB Review also featured a ceremony honoring COL F. John Burpo and his dedication to basic science research at DEVCOM CBC. COL Burpo's long-term engagement with the program.

This report concludes with a technical manuscript from each of the FY24 ILIR and CBAMMS projects that details the advances made during the period of performance. If you have questions regarding the ILIR Program or this report, please contact the DEVCOM CBC Public Affairs Office at usarmy.apg.devcom-cbc.mbx.communications-office@army.mil

Sincerely,
Patricia (Trish) McDaniel, Ph.D.
Senior Research Scientist (ST) for Chemistry

Strategic Mission and Vision

The U.S. Army Combat Capabilities Development Command Chemical Biological Center (DEVCOM CBC) is the Nation's principal research and development resource for non-medical chemical-biological (CB) defense. DEVCOM CBC has the unique ability to advance the mission of the Joint Warfighter and other stakeholders, while leveraging historical expertise, advanced equipment, and state-of-the-art facilities. The Center takes pride in its legacy of solutions born from more than a century of innovation.

Mission

DEVCOM CBC's mission is to provide innovative chemical, biological, radiological, nuclear, and explosive (CBRNE) defense capabilities to enable the Joint Warfighters' dominance on the battlefield and interagency defense of the homeland. This mission recognizes that the Center's range of influence, while rooted in CB warfare defense, can be applied to all types of challenges in chemistry or biology. The Center's advanced capabilities in synthetic biology and materials science leverage existing core capabilities in biotechnology and decontamination sciences to develop next-generation capabilities that ensure our warfighters are always prepared to operate on the modern and future battlefield.

Vision

DEVCOM CBC's vision is to be the Army's premier research and engineering center generating CBRNE solutions for the Army, DoD, the Nation, and our Allies. For more than 100 years, the Center has been a distinct asset, providing innovative and economical CB defense technology solutions through scientific and engineering expertise, coupled with our unique facilities and collaboration with partners.

FIGURE 1 COL F. John Burpo and LTC Victor Jaffett, Techincal Advisory Board Reviewers, along with Dr. Patricia McDaniel, ILIR and CBAMMS Program Director, listen to scientific presentations and provide feedback to PIs and their teams.

DEVCOM CBC Basic Research Project Selection and Evaluation Process

ILIR and CBAMMS Program Overview

The DoD defines basic research as a "systematic study directed toward greater knowledge or understanding of the fundamental aspects of phenomena and of observable facts without specific applications toward processes or products in mind."[1] To foster and sustain basic research, the DoD created and supports an In-house Independent Research (ILIR) program in each DEVCOM center. The Army's Core 6.1 program, which adheres to the guidelines outlined in DoD Instruction 3201.04, dictates that "each DoD component that operates an R&D laboratory or center shall support an ILIR program" and that these laboratories "shall be given wide latitude in the use of ILIR funds…to enable performance of innovative, timely, and promising work without requiring formal and prior approval."[2] Therefore, the purpose of the ILIR program is to identify and fund innovative basic research projects that are high-risk but have high potential payoff for fulfilling future Army capability needs.

The Department of the Army has also established a separate, directed basic research effort for DEVCOM Centers to fund basic research related to their missions and align to the challenges outlined in the Army Modernization Strategy. As such, DEVCOM CBC's Chemical Biological Advanced Manufacturing Material Science (CBAMMS) program funds projects that focus on the fundamental science related to novel material science and signal management through smoke and obscuration.

The ILIR and CBAMMS programs help to foster increased innovation within the Center. They are viewed as a critical part of the Center's efforts to ensure a high level of quality in basic science; to foster innovation in the areas of chemistry and biology; mentor junior investigators in the art and practice of laboratory science; and to explore new technological innovations and phenomenology at the boundaries of chemistry, biology, mathematics, or physics. These projects must also focus on expanding the state-of-the-possible in support of CBRNE defense missions. ILIR and CBAMMS projects receive funding for up to three years and are expected to result in peer-reviewed publications, technical reports, patents, and/or present their findings at local and national scientific gatherings.

ILIR and CBAMMS Project Selection

Each year, the ILIR and CBAMMS programs solicit the Center's researchers for innovative proposals that correspond to topics highlighted in the DEVCOM CBC Research and Operations (R&O) Directorate's Strategic Roadmap. A panel of external reviewers evaluate and score each proposal on its scientific objective, methodology, investigator qualifications, and the proposed budget. Of these four categories, the scientific objectives and methods are given more weight in the overall score for each project. The panel and program director rank proposals according to merit and written feedback for each project is shared with each PI and guides the Center's ongoing mentoring of researchers. Only proposals deemed basic research by the reviewer panel are considered eligible for funding.

In FY24, the ILIR call for proposals requested proposals focused on Aerosol Sciences, Chemical and Biological Sensing, Computational Design and Development, Future Threats, Panomics and Molecular Toxicology, Rational Molecular Synthesis and Nano-system Design, and Synthetic Biology while the CBAMMS program focused on Materials, Signal Management (Obscuration), and other topics related to surfaces, interfacial dynamics, thin film materials, catalysis, and opto-electronic/sensory technologies. In FY24, sixteen ILIR and CBAMMS proposals were submitted, reviewed, and critiqued by a reviewer panel comprised of scientists from the United States Military Academy, DEVCOM Army Research Laboratory – Army Research Office, and DEVCOM Chemical Biological Center. Of the submitted proposals, two new ILIR projects and three new CBAMMS projects were funded. These projects, along with four ILIR and seven CBAMMS continuations, made up the basic science portfolios totaling $3.6M of funding in FY24.

1 *DoD Financial Management Regulation, DoD 7000.14-R, Vol. 2B, Ch. 5*

2 *In-House Laboratory Independent Research Program, DoDI 3201.04, October 15, 2018*

ILIR and CBAMMS Project Evaluation

Projects selected for funding are reviewed quarterly; these reviews of project performance provide guidance to the program's participants to ensure projects meet significant milestones, that substantive new knowledge is being produced, ensure knowledge is transferred to DEVCOM CBC and the broader scientific community, and to help course correct when projects experience complications. Each quarterly review features a different focus. Quarter one includes discussions on the project objectives and proposed methods. Quarter two focuses on initial data, project's risks and mitigation strategies, and any necessary course corrections. Quarter three focuses on the technical advancements made by each project.

In quarter four, DEVCOM CBC holds an external review, known as the Technical Advisory Board (TAB) Review, to assess year-to-date performance of the funded ILIR and CBAMMS projects. Comments and feedback from this review are used to justify continued funding, to course correct individual projects facing substantial roadblocks, and to pause or terminate funding for individual ILIR or CBAMMS projects. The comments and insights provided by the expert panel are used to improve the quality and content of individual research projects, the scientific focus of the ILIR and CBAMMS portfolios, and to guide the overall mission of the programs into the future.

PROPOSAL SCORING CRITERIA

Exceptional 4 Comprehensive and complete in all areas; meets all significant objectives; offers a comprehensive project that exceeds the ILIR vision and is supportable by the proposed approach; has few weaknesses which are easily correctable.

Acceptable 3 Meets most of the significant objectives and is responsive to the ILIR vision; offers a feasible technical solution; weaknesses are readily correctable; proposal is complete to the extent that an award could be made in present terms.

Marginal 2 Minimally meets ILIR vision and objectives (i.e., offers a project vision that is marginally supported by the proposed approach, and/or claims are not documented or substantiated); significant deficiencies exist.

Unacceptable 1 Fails to meet significant characteristics of the ILIR vision and/or objectives stated in the Solicitation; has weaknesses and/or deficiencies that are significant and of such magnitude that they cannot be corrected without extensive discussion/major revision of the proposal.

	REVIEWERS							
	1	2	3	4	5	6	7	AVG
Scientific Objective	4	3	4	3	3	3	1	3.0
Methods and Approach	4	2	3	2	3	2	2	2.6
PI Qualifications	3	3	4	3	3	3	3	3.1
Budget	3	3	3	1	3	3	3	2.7
Overall Evaluation	3.7	2.7	3.5	2.3	3.0	2.7	2.0	**2.8**

FOUR REVIEWERS FROM DIFFERENT FEDERAL DEFENSE ORGANIZATIONS SERVED ON THE FY24 TAB PANEL, INCLUDING:

- **COL F. John Burpo, Ph.D.**
  Department Head and Professor
  Department of Chemistry and Life Science
  United States Military Academy
- **LTC Victor Jaffett, Ph.D.**
  Director - Chemistry Program and Assistant Professor
  Department of Chemistry and Life Science
  United States Military Academy
- **Dawanne Poree, Ph.D.**
  Scientific Integration Officer
  United States Army Combat Capabilities Development Command Army Research Laboratory - Army Research Office
- **Katherine Akingbade, Ph.D.**
  Deputy Program Manager and Civilian Microbiologist/Biochemist
  United States Army Combat Capabilities Development Command Army Research Laboratory

In FY24, the TAB panel was tasked by the program director with producing an unbiased assessment of the content, quality, innovation, accomplishments, and relevance of the R&O basic science programs. Each project was evaluated based on seven areas: (1) scientific objectives, opportunity, and significance, (2) research methodology, (3) connections to the broader community, (4) overall capabilities and metrics, (5) use of PowerPoint, (6) use of time, and (7) overall presentation, with criteria 1–4 weighted as the most important. In FY24, the panel recommended all eligible projects but one receive continued funding and provided critical feedback to enhance the impact of several of the ongoing projects. Individual scores, portfolio reviews, and the key points from the TAB discussion were all used to generate a report for both project PIs and DEVCOM CBC leadership.

In FY24, the panel felt the funds invested in the portfolios resulted in excellent productivity and that the projects spanned a diverse set of topics important to the Army Modernization Strategy. The panel remarked that each PI successfully articulated how their work supported DEVCOM CBC-aligned mission spaces and incorporated many different skills, state-of-the-art tools, and cutting-edge experimental methods.

While the two portfolios had many strengths, reviewers provided several recommendations and actions to improve both programs. Many projects did a good job of ensuring their work was basic science in nature but reviewers urged the PIs to keep an eye toward their potential Army application and conduct experiments in environments applicable to the warfighter. Similarly, program participants should be encouraged to collaborate across disciplines and look for opportunities to combine capabilities and create synergized technologies that benefit the defense community. Reviewers also focused on the ability of PIs to transition their projects from 6.1 funding to stakeholders or transition partners, suggesting PIs identify collaborators prior to receiving funding, utilize the first year to solidify those relationships, refine the nature of collaboration and make progress on potential avenues for transition during the second year, and finalize the transition during the third year. To increase the likelihood of a project continuing after its ILIR or CBAMMS period of performance, PIs should use the TAB Review as an opportunity to practice selling their research for future pitches, including only the information and data relevant to the potential collaborator or stakeholder interested in their technology.

Seedling Program Overview

The Seedling program funds smaller, quick-turn (less than one year), “outside-the-box” exploratory basic research projects using funds obtained under the authority of 10 U.S.C. § 4123 Funding Laboratory Enhancements Across (X)-4 Categories (FLEX-4). Under FLEX-4, directors of DoD laboratories are directed to use funds to foster innovative basic and applied research, transition technologies into next-gen capabilities for warfighters, increase workforce development, and revitalize and recapitalize laboratory infrastructure and equipment. Seedling projects showing promise have the potential to transition to larger ILIR or CBAMMS projects or to external funding sources. Seedling projects also undergo a similar proposal review, selection, and evaluation process as ILIR and CBAMMS projects; however, the Seedling review process is conducted internally at DEVCOM CBC and is more streamlined to fit the lower funding threshold. In FY24, 15 proposals were received, and 11 projects received funding that focused on Rational Molecular Synthesis and Nano system Design, Chemical and Biological Sensing, Computational Design and Development, Emerging Threats, and Synthetic Biology. These projects received their funding at the end of FY24 and will be fully reported on in the FY25 edition of the Annual Proceedings Report.

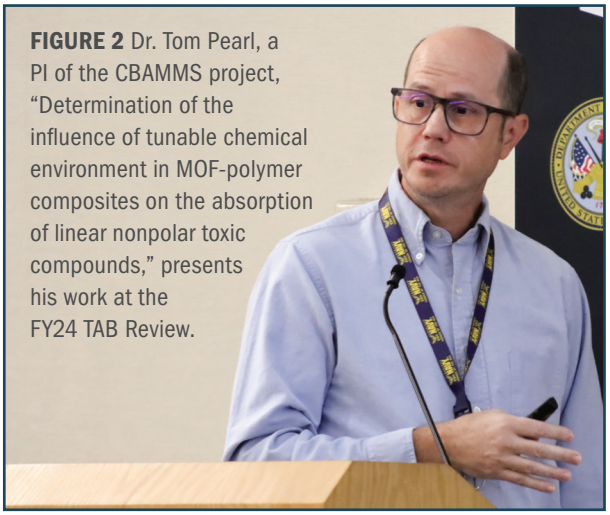

FIGURE 2 Dr. Tom Pearl, a PI of the CBAMMS project, “Determination of the influence of tunable chemical environment in MOF-polymer composites on the absorption of linear nonpolar toxic compounds,” presents his work at the FY24 TAB Review.

In addition to reviewing the ILIR and CBAMMS programs, the TAB Review provided senior leaders and the external reviewers an opportunity to review topics of importance to the Center and look for future opportunities to expand capabilities, strengthen ongoing relationships with partners, and fill voids within the scientific or defense communities. In FY24, synthetic biology and biomanufacturing leaders and subject matter experts examined their programmatic history, current capabilities, and future goals for the Center and presented their thoughts on the Center’s progress to the TAB Reviewers.

DEVCOM CBC Synthetic Biology and Biomanufacturing Center Review

Synthetic biology, the design and construction of novel biological systems of organisms to produce novel products, became a focus for DEVCOM CBC in the early 1990's. Early success led the Center to make further investments in related areas, namely production of novel biomaterials by synthetically modified microbes using fermentation. A recent capability assessment conducted by the Department of Defense identified shortcomings and weaknesses in the nation's supply chain and ability to produce critical chemicals domestically. This assessment spurred an investment of over $50 million from across the Defense Community to establish the necessary infrastructure and personnel to support a robust synthetic biology and biomanufacturing community within the Center. This funding enabled DEVCOM CBC to renovate existing facilities, modernize large-scale fermentation, solid-liquid purification, supporting analytical equipment, and establish new spaces for a bioprocess optimization lab and large-scale downstream processing lab. The Center hired and developed an experienced team of researchers with backgrounds in chemical engineering, mechanical engineering, biology, and chemistry to stand up and run the facilities. Today, there are approximately a dozen scientists and personnel that staff the U.S. Army Biomanufacturing Facility and contribute to its mission to support military-relevant applications through securing sufficient supply of synthetic biology and biomanufacturing-synthesized materials to effectively investigate target advanced material applications in field-relevant contexts. The Facility uses a three part approach to Secure, Strengthen, and Scale its biomanufacturing capabilities in support of these prototyping efforts:

- **SECURE:** Enhancement of existing cold-storage equipment established in accordance with industry best practices has created a strain repository capable of handling approximately 500,000 biological samples in a secure, "behind-the-fence" laboratory with 24/7 power and temperature monitoring. This repository includes redundant back-up systems in case of long-term power loss and features an information management system for organization and sample tracking.

- **STRENGTHEN:** The bioprocess optimization and bench-scale downstream processing laboratories allow for optimization and analysis of process efficiency at high throughput and small-scale levels. These labs generate data directly applicable toward scale up processes and improve the speed of scale-up while substantially decreasing overall costs.

- **SCALE:** The facility's pilot-scale fermentation lab and downstream processing lab allow for large-scale production, isolation, and purification of biomanufactured materials and chemicals. These materials can then be used in advanced material prototype testing or undergo further modifications and development in industrial-scale manufacturing of material.

Despite the biomanufacturing facility's infancy, several success stories with collaborative external partnerships have already been realized (see insert). In the future, the Center will continue to investigate important areas of research including next-gen energetics and propulsion materials, lightweight composite materials fabrication, vehicle protection system improvement, and miniaturized air supplies and water-less decontamination systems.

Material	Collaborators	Funding Agency
Biocarbonized Nanofibers (BioCNF) Increase fitness for decontamination and protection	DARPA MIT DEVCOM Armament Center	• Defense Advanced Research Projects Agency • Office of the Under Secretary of Defense for Research and Engineering (OUSD(R&E)) Tri-Service Biotechnology for a Resilient Supply Chain
Biocement Fabricate concrete for new applications and repair of old structures	Air Force Research Lab	• Air Force Research Laboratory • OUSD(R&E) Tri-Service Biotechnology for a Resilient Supply Chain
Cellulose Refine production of assets including batteries, supercapacitors, fibers, and filters	Army Research Lab DEVCOM Soldier Center	• OUSD(R&E) Seedling • OUSD(R&E) Tri-Service Biotechnology for a Resilient Supply Chain • DOD Manufacturing Science and Technology Program ManTech
Melanin UV protection and energy storage applications	Naval Research Lab	• OUSD(R&E) Biotech Optimized for Operational Solutions and Tactics • OUSD(R&E) Tri-Service Biotechnology for a Resilient Supply Chain

The ILIR and CBAMMS programs began prioritizing Synthetic Biology as a research thrust area in 2013, seeking to fill a strategic void at the Center where innovative research ideas could be crowdsourced from the workforce. These ideas were required to have the potential to add new capabilities to the Center, provide an opportunity for researchers to connect with external collaborators and transition partners, gain access to state-of-the art laboratories and equipment, and help keep the Center up to date with trends across scientific disciplines. In FY24, six synthetic biology and biomanufacturing based projects were funded to explore novel approaches to safeguard bioproduction strains, cell-free protein synthesis, and biology-based decontamination strategies. These basic research projects will help to lay the groundwork for future applied work and translational research at the Biomanufacturing Center to support the warfighter and defense community.

FIGURE 3 By investing in the necessary infrastructure and workforce, DEVCOM CBC is poised to lead in the Biomanufacturing and Synthetic Biology spaces for years to come. Here, Drs. Nathan McDonald and Jessica Tague work in laboratory space associated with the Biomanufacturing Center and together help guide DEVCOM CBC's efforts in these emerging areas.

FY24 Basic Research Program Highlights

In April FY24, Ms. Priscilla Lee was awarded the Rising Star Award from the Northeastern Maryland Technology Council. This award recognizes individuals who demonstrate the potential to be excellent, long-term contributors to building the Science, Technology, Engineering, and Mathematics workforce or advancing innovation and technology.

In May 2024, Dr. Jennifer Lee was presented with an On-the-Spot Special Act Award from the Defense Threat Reduction Agency for her work in biomedical engineering and basic science research. These awards are meant to recognize employees for leading or going above and beyond on a project that advances the mission of the agency.

FY24 BASIC RESEARCH PROGRAM PRODUCTIVITY

8	14	1	2
Publications	Presentations or Proceedings	Patent Filed	Projects Transitioned

8 Publications

- Aviles-Rosa, E.; Schultz, J.; Maughan, M.N.; Gadberry, J.D.; DiPasquale, D.M.; Farr, B.; Henderson, A.; Best, E.; Discepolo, D.R.; Buckley, P.; Perry, E.B.; Zoran, D.L.; Hall, N.J. A canine model to evaluate the effect of exercise intensity and duration on olfactory detection limits: the running nose. *Front Allergy.* **2024**, *5*, p 1367669.
- Lee, M.S.; Lee, J.A.; Biondo, J.R.; Lux, J.E.; Raig, R.M.; Berger, P.N.; Bernhards, C.B.; Kuhn, D.L.; Gupta, M.K.; Lux, M.W. Cell-Free Protein Expression in Polymer Materials. *ACS Synth. Biol.* **2024**, *13* (4), pp 1152–1164.
- Languirand, E.; Parrilla, E.; Smith, N.; Collins, M.; Unruh, A.; Lefkowitz, L.; Phung, C.; Sen, A. Exploring MOF-based Micromotors as SERS Sensors. *Smart Biomedical and Physiological Sensor Technology XXI,* **2024**; Vol. 13059.
- Maughan, M.N.; Gadberry, J.D.; Sharpes, C.E.; Buckley, P.E.; Miklos, A.E.; Furton, K.G.; DeGreeff, L.E.; Hall, N.J.; Greubel, R.R.; Sloan, K.B. Calibrating canines-a universal detector calibrant for detection dogs. *Front. Allergy.* **2024**, *5*, p 1366596.
- McDonald, N.D.; Antoshak, E.E. Towards a Yersinia pestis lipid A recreated in an Escherichia Coli scaffold genome. *Access Microbiol.* **2024**, *6* (7).
- Polk, A.L.; Dean, S.W.; Flickinger, M.R.; Chintersingh, K.L.A.; Scott, D.G.; Valdes, E.R.; Fisher, K.R.; Weihs, T.P. Identifying a combination of intermetallic and thermite reactions that result in a non-expanding compact. *Combust. Flame*. **2024**, *262*, p 113343
- Van de Voorde, K.M.; Kozawa, S.K.; Mack, J.A.; Thompson, C.B. Influence of Cross Linker Functionality and Photoinitiator Loading on Network Connectivity and Actuation in 3D Printed Model Thermosets. *ACS Appl. Polym. Mater.* **2024**, *6* (7), pp 3918–3929.
- Varady, M.J.; Schenning, C.S.; Thompson, C.B.; Mantooth, B.A.; Peterson, G.W.; Pearl, T.P. Solvent Selection Guided by Self-Consistent Field Theory for Improved Dispersion of Metal-Organic Frameworks in Polymers. *ACS Appl. Polym. Mater.* **2024**, *6* (1), pp 888–895.

14 Presentations and Proceedings

- McDonald, N.D, Walters, E., Rhea, K. Designing Membrane-Bound Proteins as Sensors for use in Cell Free Protein Systems. *Cell Free Systems Conference*. Austin, TX, **17 November 2023**.
- Lee, M. Cell-free synthetic biology for sensing, biosynthesis, and smart materials. *Presented at ACS Spring 2024*. New Orleans, LA, **17 March 2024**.
- Kozawa, S. Stabilizing CFPS materials using solution blow spun polymer nanofiber mats: Influence of polymer properties and processing on activity and water transport. *Presented at ACS Spring 2024.* New Orleans, LA, **17 March 2024**.
- Pearl, T.P., Varady, M.J.; Thompson, C.B.; Mantooth, B.A.; Peterson, G. W. Control of multi-way chemical interactions for solids dispersal in polymer thin films and impact on composite materials properties. *Presented at ACS Spring 2024*. New Orleans, LA, **17 March 2024**.
- Buckley, P.E. Project IronDog. *Presented at the Hold the Line K9 Conference*, Myrtle Beach, SC, **9–11 April 2024**.
- Love, C.E. and Crumbley, A. Sporulated Phage: Towards the Goal of "Ready and Waiting" Phage Decon. *Presented at United States Military Academy at West Point Faculty Seminar*, West Point, NY, **15 April 2024**.
- Buckley, P.E. Project IronDog. *Presented at the Canadian Police Canine Association, Calgary*, Canada, **15–18 April 2024**.
- Buckley, P.E. Project IronDog. *Presented at the Military Working Dog Symposium*, Alpena, MI, **10–15 May 2024**.
- Kulisiewicz, A.; Tovar, T.; Garibay, S.; Harland, J.; Browe, M.; Navin, J.; Controlling the heterogeneous catalysis of zirconium clusters bound to modified SBA-15. *Presented at ACS Mid-Atlantic Regional Meeting*, State College, PA, **5–7 June 2024**.
- Lee, J. Solution blow spinning of cell-free functionalized polymer fibers. *Presented at 2024 Synthetic Biology: Engineering, Evolution & Design (SEED).* Atlanta, GA, **26 June 2024**.
- Kozawa, S. Understanding Polyelectrolytes to Mimic Biological Structures. *Presented at Polymer Physics Gordon Research Symposiu*m. Mount Holyoke, MA, **20 July 2024**.
- Kulisiewicz, A.; Tovar, T.; Garibay, S.; Harland, J.; Browe, M.; Navin, J.; Controlling the heterogeneous catalysis of zirconium clusters bound to modified SBA-15. *Presented at ACS National Meeting*, Denver, CO, **18–22 August 2024**.
- Kuhn, D. Exploration into enhanced attenuation of aerosolized fibers. *Presented at the American Chemical Society Fall National Meeting*. Denver, CO, **22–25 August 2024**.
- Pearl, T.P. Basic Research Thrusts for CB Protection and Hazard Mitigation: Understanding Interactions of Toxic Compounds with Polymers, Composites, and Multifunctional Materials. *Presented at visits to DEVCOM Solder Center and Boston University,* Natick, MA and Boston, MA, **28–29 August 2024**.

1 Patent Filed

- Jennifer Lee†, Susan Kozawa, John Biondo, Kristian Van de Voorde†, Anne Walker, Matthew Lux, Marilyn Lee. Functionalization of polymer fibers and particles via incorporation of cell-free expression. Application number 63/595,852. Filed 11/03/2023.

2 Projects Transitioned to Customer Funding

- The ILIR project, "Fundamental exploration into advanced plasmonic ceramic nitrides as multispectral obscurants" led by Dr. Danielle Kuhn will continue as part of the core S&T 6.2 "Development of Obscurants" funding line through FY31, though a specific funding amount has not yet bet determined.
- The CBAMMS project, "Developing design rules for CBRN-relevant additive manufacturing systems by probing network structure" transitioned to the Defense Threat Reduction Effort CB11220 that will focus, in part, on developing swatches suitable for the next generation of respirator systems. This effort will run from FY25–30 and will provide $180–250k each year.

Meet our FY24 Principal Investigators

The FY24 Principal Investigators (PIs) encompass a diverse group of scientists across the Research and Operations Directorate and all four divisions. Here, biographies of each PI that participated in the FY24 ILIR, CBAMMS, or Seedling programs are alphabetically listed along with their branch and division information.

Casey Bernhards, Ph.D.
Research Biologist, Applied Synthetic Biology and Olfaction Branch, Sensor Technologies and Biomaterials
ILIR Program

Dr. Casey Bernhards earned her Ph.D. in Biological Sciences in 2014 from Virginia Polytechnic Institute and State University. After graduating, she joined DEVCOM CBC as a National Research Council Postdoctoral Fellow sponsored by the Defense Threat Reduction Agency. She then continued to support DEVCOM CBC as a Senior Scientist with Excet, Inc. before converting to a civilian Research Biologist in 2021. Dr. Bernhards leads projects related to synthetic biology and microbial genetics. Her research focuses on genetically engineering bacteria for beneficial purposes; studying genome engineering tools, such as clustered regularly interspaced short palindromic repeats gene editing, as emerging threats; and developing cell-free biosensors using engineered genetic circuits.

Mr. Matthew Browe received a B.S. in Chemical Engineering from Pennsylvania State University and an M.S. in Chemical Engineering from the University of Delaware in 2011 and 2022, respectively. Mr. Browe began working at DEVCOM CBC as a Chemical Engineer in 2011, focusing on permeation, micro breakthrough testing, and evaluation of sorbent and barrier materials. His efforts include extensive analysis and data compilation of novel sorbents and metal organic framework (MOF) polymer hybrid films, identifying trends in performance with justification from theory, and materials characterization. Recently, Mr. Browe's research has focused on machine learning and the utilization of Python to develop a regression model that can predict MOF reactivity against toxic chemicals of interest as a function of the physical and chemical properties of a MOF.

Matthew Browe
Chemical Engineer, Protective Materials Development Branch, Protection Division
CBAMMS and Seedling Programs

Patricia Buckley, Ph.D.
Supervisory Biologist, Deputy Division Chief, Sensor Technologies and Biomaterials Division
CBAMMS Program

Dr. Patricia Buckley earned a B.S. in Biology from James Madison University before studying Biotechnology at Johns Hopkins University, receiving a M.S. in 2000. Dr. Buckley continued her education at the University of Maryland where she earned a Ph.D. in Environmental Pathology in 2013. Currently, Dr. Buckley works as a Supervisory Biologist at DEVCOM CBC where she leads a team that focuses on a variety of topics including the use of cell-free lysates in fieldable sensors and the utilization of Military Working Dogs' olfactory senses in field detection.

Anna Crumbley, Ph.D.
Research Chemical Engineer
Biomanufacturing Branch, Sensor Technologies and Biomaterials
Seedling Program

Dr. Anna M. (Annie) Crumbley is a Research Chemical Engineer with the U.S. Army DEVCOM Chemical Biological Center Biomanufacturing Branch. She is a Principal Investigator responsible for the Biomanufacturing pilot-scale operations at DEVCOM CBC. She received a Bachelor of Science in Chemical Engineering from the University of Alabama, in Tuscaloosa, Alabama in 2015 and a Ph.D. in Chemical and Biological Engineering from Rice University in Houston, Texas, in 2020. After completing her doctorate, Dr. Crumbley was awarded a postdoctoral fellowship through the National Research Council Research Associateship Program, which she completed with DEVCOM CBC in 2021.

Mr. Davies received his bachelor's degree in Physics from the University of Delaware. He specializes in applied Design of Experiments for research and engineering. He is actively promoting the use of Design of Experiments across the U.S. Army DEVCOM Chemical Biological Center at Aberdeen Proving Grounds, MD.

Jay Davies
Research Physicist, Decontamination Sciences Branch, Protection Division
Seedling Program

Shaun Debow
Chemical Chemical Engineer, Obscuration & Nonlethal Engineering Branch, Protection Division
Seedling Program

Mr. Shaun Debow attended the University of Iowa, completing B.S. degrees in Computer Science and Chemistry and an M.S. in Chemical and Biological Engineering. Mr. Debow then joined DEVCOM CBC as a General Engineer, where he completed comprehensive courses and training on rocket and warhead design, eventually transitioning to his current role as a Chemical Engineer in 2010. In this capacity, Mr. Debow has served as the DEVCOM CBC chief rocket scientist and liaison to the Tactical Aviation and Ground Munitions Project Office with the Program Executive Office Missiles and Space. Mr. Debow has published many articles and submitted patent applications on materials and decontamination sciences.

Dr. Erik Emmons is a Research Physicist specializing in optical spectroscopy techniques, particularly molecular vibrational spectroscopy. He received a Ph.D. in Physics from the University of Nevada, Reno, in 2007. At DEVCOM CBC, Dr. Emmon's focuses his research on the use of spectroscopic methods such as Raman spectroscopy for detection of explosives, narcotics, and chemical warfare agents.

Erik Emmons, Ph.D.
Research Physicist, Spectroscopy Branch, Sensor Technologies and Biomaterials
Seedling Program

Danielle Kuhn, Ph.D.
Research Chemist, Smoke & Target Defeat Branch, Protection Division
ILIR Program

Dr. Danielle Kuhn attended the State University of New York at Cortland and Binghamton University, studying Chemistry at both institutions, earning a B.S. and Ph.D., respectively. Following her doctoral degree, Dr. Kuhn joined the DEVCOM CBC Smoke and Target Defeat Branch as a National Research Council Postdoctoral Fellow in 2016 and became a civilian Research Chemist in 2018. Dr. Kuhn's research has focused on the synthesis of novel materials and evaluating their obscuration ability. Dr. Kuhn's research has led to the publications of several papers and presentations at multiple national conferences and most recently contributed to the discovery of the highest performing obscurant material to date.

After earning an M.S. in Inorganic Chemistry from the University of Delaware, Ms. Ann Kulisiewicz began working as a Chemist for Leidos in the CBR Filtration Branch in 2015. Three years later, she transitioned to her current role as a DEVCOM CBC Research Chemist, still within the CBR Filtration Branch. Ms. Kulisiewicz's work focuses on the synthesis, characterization, and testing of MOFs for filtration applications which has led to multiple peer reviewed journal articles and presentations at the American Chemical Society National Meeting & Exposition.

Ann Kulisiewicz
Research Chemist, Protective Materials Development Branch, Protection Division
CBAMMS Program

Jennifer Lee, Ph.D.
CBiomedical Engineer, BioChemistry Branch, CBRNE Assessment Division
CBAMMS and Seedling Programs

Dr. Jennifer Lee, a Biomedical Engineer at DEVCOM CBC, first studied Biomedical Engineering at the University of North Carolina at Chapel Hill, earning a B.S. in 2008. Dr. Lee continued her education at the University of Florida where she earned a Ph.D. in Biomedical Engineering in 2013. Following her doctoral work, Dr. Lee worked as a Postdoctoral Fellow at both the University of Florida and at the National Cancer Institute. In 2021, Dr. Lee joined DEVCOM CBC as a DTRA matrix employee where she researches cell-free protein synthesis and its incorporation into polymer matrices.

Ms. Priscilla Lee attended the University of Maryland, College Park where she earned a B.S. and M.Eng. in Bioengineering. As an undergraduate student, Ms. Lee served as an undergraduate research assistant as an A Scholar's Program for Industry-Oriented Research in Engineering Research Fellow (more commonly referred to as the ASPIRE Program) and conducted research as a B.S./M.S. student. In 2023, Ms. Lee began a doctoral program at Johns Hopkins University with a focus on Biomedical Engineering. Ms. Lee was a recipient of the SMART Scholarship as a recruitment scholar before she began her current position as a Biologist at DEVCOM CBC in 2021.

Priscilla Lee
Biologist, Molecular Toxicology Branch, Threat Agent Sciences Division
ILIR and Seedling Program

Courtney Love
Biologist, BioTechnology Branch, CBRNE Assessment Division
ILIR Program

Ms. Courtney Love studied chemistry at both Wayne State University and the University of Maryland at College Park, earning a B.S. and M.S., respectively. Following her M.S. degree, Ms. Love joined Joint Research and Development, Inc. and worked as a contractor for DEVCOM CBC. As a contractor, Ms. Love engaged with the Defense Threat Reduction Agency regarding chemical warfare agent response promoters and MAGPIX immunoassay development. In the summer of 2021, Ms. Love joined DEVCOM CBC as a Biologist where she has engaged in bacteriophage basic and translational research.

Nam-Phuong Nguyen holds a M.S. in Biotechnology - Biosecurity and Biodefense and a B.S. in Chemistry and works as a Senior Chemist within Chemical Biological Application and Risk Reduction Business Unit. Ms. Nguyen has over eighteen years of experience conducting chemical analyses of chemical warfare agents and unknown materials using various state-of-the-art, high technology, and complex instrumentation. Ms. Nguyen is also responsible for planning, coordinating, and conducting laboratory field operations involved in the recovery and demilitarization of chemical warfare materials. She has extensive experiences in the development and validation of analytical methods for environmental applications in support of various agencies including the U.S. Army Corps of Engineers, U.S. Department of Agriculture, the Defense Threat Reduction Agency, Food Emergency Response Network, and the U.S. Secret Service.

Nam-Phuong Nguyen
Chemist, Environmental Monitoring Laboratory Branch, Chemical Biological Application and Risk Reduction Business Unit
Seedling Program

Monica McEntee, Ph.D.
Research Chemist, Protective Materials Development Branch, Protection Division
Seedling Program

Dr. Monica McEntee is a Research Chemist in the Protective Materials Development Branch under the Research & Operations Division. She obtained her Ph.D. in Chemistry at the University of Virginia and obtained her dual B.S. degrees in Mathematics and Chemistry at Virginia Tech. Presently, her work at DEVCOM CBC focuses on the development of materials that can bind and neutralize chemical warfare agents. These materials are investigated using ultra-high vacuum analytical techniques including x-ray photoelectron spectroscopy, mass spectrometry, and infrared spectroscopy.

Dr. Thomas Pearl is a Research Chemist within the Decontamination Sciences Branch at DEVCOM CBC. As a Research Chemist, Dr. Pearl specializes in elucidating contaminant and decontaminant chemical interactions with military-relevant materials that drive mass transport behavior and reactivity. Dr. Pearl studied Physics at Carleton College and Chemistry at the University of Chicago where he earned a B.A. in 1994 and a Ph.D. in 2000, respectively. His areas of expertise include nanoscale and solid-state physics and chemistry with a focus on the properties and behavior of surfaces, interfaces, and thin films. Dr. Pearl has published 20 DEVCOM CBC technical reports and 40 peer reviewed publications.

Thomas P. Pearl, Ph.D
Research Chemist, Decontamination Sciences Branch, Protection Division
CBAMMS Program

Amee Polk, Ph.D.
Research Chemical Engineer, Obscuration & Nonlethal Engineering Branch, Protection Division
CBAMMS Program

Dr. Amee Polk earned a B.Ch.E. in Chemical Engineering from the University of Delaware followed by a M.S. in Biotechnology and a D. Eng. in Material Science Engineering, both from Johns Hopkins University. Dr. Polk's training includes ten years of experimental design and development in pyrotechnics and explosives, most of which occurred within the Pyrotechnics and Explosives Branch at DEVCOM CBC. Prior to joining DEVCOM CBC, she worked as the lead test engineer for the Large-Scale Chemical Warfare Agent Test Facility. In 2018, Dr. Polk was awarded the Bernard E. Douda Young Scientist Award from the International Pyrotechnics Society and has been granted several patents in the field of pyrotechnics and explosives. She and her research accomplishments were featured in the Johns Hopkins University Material Science in Extreme Environments 2022 annual newsletter and is a member of the International Pyrotechnics Society.

Prior to joining DEVCOM CBC, Ms. Katherine Rhea began her scientific career at the University of Maryland, College Park where she earned a B.S. in Biological Sciences. After graduation in 2011, Ms. Rhea worked as an Environmental Technician/Project Manager with Martel Laboratories JDS, Inc. Ms. Rhea then joined Battelle Eastern Science Technology Center as a Senior Technician where she worked until 2014. Following her time at Battelle, she joined DEVCOM CBC where she predominately worked in basic and translational research in cell free protein synthesis and gene editing technologies. In 2023, Ms. Rhea earned her M.S. in Biotechnology from Johns Hopkins University.

Katherine Rhea
Biologist, BioChemistry Branch, CBRNE Assessment Division
ILIR Program

Emily Stricklin
Biologist, Agent Fate Branch, Threat Agent Sciences Division
Seedling Program

Ms. Emily Stricklin studied Biology Ecological Science at Northwestern college in Orange City, Iowa, earning a B.A.in 2016. For the following five years, Ms. Stricklin served as lab manager at the University of Nebraska-Lincoln in the Entomology Department working on Agricultural Pest Management. Ms. Stricklin joined Excet, Inc. as a contractor supporting Molecular Toxicology Branch's Per- and polyfluoroalkyl substances biomagnification research and studies assessing the toxicity of aqueous fire-fighting foams. Ms. Stricklin joined DEVCOM CBC as a Biologist in 2024 where she leads research efforts in plant and invertebrate toxicology and conducts lab management.

Dr. Kristian Van de Voorde graduated from the University of Southern Mississippi in 2016 with a B.S. in Polymer Science and from the University of Delaware in 2021 with a Ph.D. in Materials Science and Engineering. His research focused on the development of tissue engineered scaffold for regenerative medicine. Dr. Van de Voorde has also focused on structure-property relationships from a molecular and processing perspective to readily tune bulk properties to suite specific applications. He joined the Respiratory Protection Branch at DEVCOM Chemical Biological Center after graduate school where he explores structure-property relationships in additive manufacturing and enabling the development of next generation of protective equipment.

Kristian Van de Voorde, Ph.D.
Chemical Engineer, Respiratory Protection Branch, Protection Division
CBAMMS and Seedling Programs

Max Wamsley, Ph.D.
Chemist, Intelligent Sensing for Detection Branch, Sensor Technologies and Biomaterials Division
Seedling Program

Dr. Max Wamsley earned his Ph.D. in Chemistry from Mississippi State University in December 2024 as a SMART Scholar. He also holds a Bachelor of Science in Biochemistry with a minor in Computer Science from Centenary College of Louisiana. Max's doctoral research focused on advancing spectroscopic technologies through the development of new methodologies and instrumentation. His dissertation showcased an innovative approach to optical spectroscopy. During his doctoral studies, Dr. Wamsley published eight peer-reviewed articles, four of which featured his supplementary cover art that he designed and submitted three patent applications.

Table of Contents

Each year, the ILIR and CBAMMS projects are presented to and scored by academic and government scientists at the FY24 Technical Advisory Board Review. Scores and comments from the reviewers are used to rank projects within each program and improve the execution of the science being conducted. The ILIR and CBAMMS projects, along with a brief abstract describing their goals and achievements, are separated by program and ranked according to their scores while the Seedling projects are listed alphabetically by the principal investigator's last name.

In-house Laboratory Independent Research (ILIR) Projects

Chemical Biological Advanced Materials Manufacturing Science (CBAMMS) Projects

69 Developing design rules for CBRN-relevant additive manufacturing systems by probing network structure and system free volume

*Chase B. Thompson, Jordan A. Mack, Kristian M. Van de Voorde**

Photopolymerization additive manufacturing has gained traction as a method to produce materials for multiple applications in tissue engineering and soft robotics among others but how resin formulations can impact crosslinked 3D printed parts remains undefined. In this study, model resins were printed with precise control over crosslinker functionality and photoinitiator concentration to influence the structure of the crosslinked network which revealed a strong relationship between the connectivity and heterogeneity as initiator content is increased. The reported findings highlight the need for a deep understanding of the polymerization pathways utilized in resin 3D printing as it is the foundation towards predicting functional properties of 3D printed crosslinked systems.

79 Structure-property relationships dictating pressure drop and particle capture in emulsion-templated polymer foams

*Chase B. Thompson, Gregory W. Peterson**

Emulsion-templated foams are a versatile, scalable platform that show promise for tunable particle capture and pressure drop properties, but there have been no widespread studies that correlate air flow through these materials to their chemistry and morphology. This project seeks to establish structure-property relationships in a series of high internal phase emulsion polymer foams in relation to how these materials capture and retain particulate matter. Knowledge gained from this project will aid in future technologies to enable particle capture and further protect the warfighter in adversarial environments.

83 Molecular modeling of toxic industrial chemicals on metal-organic frameworks for next-generation filtration applications

Matthew A. Browe, Adam R. Hinkle, Ivan O. Iordanov, Wesley O. Gordon, John Landers, Shivam Parashar, Alex Neimark*

Military personnel are at risk of toxic chemical exposure but can be better protected by incorporating metal-organic frameworks in filtration applications. This work discusses the molecular modeling studies that were performed to determine the ability of a wide variety of zirconium-based metal-organic frameworks to act as filtration media against specific toxic chemicals of interest using Monte Carlo methods and molecular dynamics methods. Specifically, reactive molecular dynamics studies were performed to understand the atomic-level details of the HCl activation synthesis of MOF-808, where formate modulator groups are removed from the node and ultimately substituted with hydroxyl species. The effect of temperature and HCl concentration on the mechanistic data was explored and will be used to inform additional metal-organic framework and decontamination studies.

93 MOF straws: Optimizing transport phenomena through the development of design rules for metal-organic framework hollow fibers

Trenton Tovar, Matt Browe, Mark Harrison, John Mahle*

Using a customizable injection molding process developed and patented in-house, we can control the hollow fiber dimensions (inner diameter, fiber wall, metal-organic framework loading) by tuning a combination of parameters at both the macroscopic and nano scales. With the ability to fine tune fiber dimensions and properties, the transport phenomena (vapor, liquid) through the fibers, and subsequently through fiber arrays can be controlled. The development of these MOF hollow fibers has broad implications beyond chemical and biological filtration and may serve as a lightweight alternative to conventional filtration media employed across the defense, space, and healthcare industries.

Seedling Projects

Full details of the FY24 Seedling projects and their results will be included in the FY25 edition of this report.

Eukaryotic cell-free expression of complex proteins

Jennifer Lee, Stephanie Cole, Thomas Biel, Steven Blum*

Unlike *E. coli*-based cell-free expression (CFE) systems, eukaryotic CFE systems can produce proteins with the native post translational modifications required for functionality. This effort will assess commercially available eukaryotic CFE kits for their ability to produce an acetylcholinesterase-Fc antibody fusion protein studied by our collaborators to probe the feasibility of eukaryotic CFE kits to produce complex proteins and determine how future efforts should be directed to build a robust eukaryotic CFE platform in-house.

Functionalized fumed silica for chemical threat neutralization

Monica McEntee

This project is focused on developing functionalized fumed silica (FFS), silica decorated with functional groups, as a novel material for neutralizing chemical warfare agent threats. The reactivity and binding of chemical warfare agent simulants on synthesized FFS will be investigated using both dose-extraction and infrared spectroscopic techniques. If successful, this research would direct the development of FFS capable of binding and neutralizing specific chemical threats relevant not only to DEVCOM CBC, but the scientific community at large.

Development of reactive elastic resins for vat polymerization 3D printing to enable in situ MOF growth for Advanced CBRN protective equipment

Kristian Van de Voorde, Chase Thompson, Ann Kulisiewicz, Sergio Garibay*

This project addresses the challenges faced in incorporating metal-organic frameworks (MOFs) into polymer matrices for advanced protective equipment. Previous efforts encountered issues with MOF accessibility to gases or vapors and the potential for MOFs to shed when only physically mixed into the matrix. This effort pioneers a novel approach that combines a 3D printable elastomeric resin with a post-processing step to covalently bind MOFs to the material's surface. This approach ensures MOFs remain accessible to gases and vapors while preventing MOF shedding, enhancing performance and durability of the final product. Here, we seek to leverage established surface science techniques and DEVCOM CBC's expertise in 3D printing formulations to enable limitless geometries to enhance the safety and capabilities of military personnel in challenging environments.

"Spray tans" for CBRNE protection - melanin coating formulation for heat and radiation protection

Anna Crumbley

Melanin is a pigment widely found in nature known to have heat, radiation, and signature management properties. A collaboration between DEVCOM CBC and the Naval Research Lab developed a highly scalable melanin production process using Vibrio natriegens, a fast-growing microorganism but focused on efficiently producing raw powder. This project focuses on understanding the solubility properties of melanin powder and evaluating its performance in coating formulations to enable applications-based development in heat protection, radiation, and signature management applications using melanin.

Illumination techniques to improve biological sampling on complex surfaces

Max Wamsley

This project will develop illumination techniques to improve sample detection on complex surfaces during Raman analysis. This research will use broadband and ultraviolet light to enhance sample visibility, evaluate illumination parameters using a CHROLIS-C1 LED system, assess surface illumination challenges, and mitigate relevant interferences to optimize filters and setups for sample isolation. This work seeks to further the development of an illumination chamber for the Portable Microscopy Chemical Detection System, adding biological sample triage capabilities and will lead to AI/ML-driven automated biological sample identification in portable Raman microscopy, with future funding sought to further develop Portable Microscopy Chemical Detection System.

Rapid analysis for navigating experimental research (RANGER)

Jay Davies

This project develops a user-friendly JMP® software application to assist DEVCOM CBC researchers and engineers in designing and analyzing robust, reproducible experiments focused on two-group comparisons. By leveraging JMP® software capabilities to automate critical decisions in experimental design/analysis, this tool has the potential to enhance the accuracy and reliability of research outcomes, thereby advancing scientific discovery and innovation at the CBC.

Computationally-guided electrochemical design of metal-organic framework-polymer interfaces

Matthew Browe, Brandon Blount*

Designing interfaces in metal-organic framework (MOF)-polymer composite membranes remains a challenge in development of protective barrier materials. Electrodeposition methods are advantageous for generating quality MOF-polymer interfaces through the precise control of properties such as particle size, layer thickness, and degree of polymerization of the monomer unit by adjusting parameters such as deposition potential and time. Using a potentiostat and a benchmark conductive polyaniline system, this effort examines electrodeposition of precursors of UiO-66 and derivatives with polyaniline to determine effect of physical and chemical properties of the MOF and parameters of the electrodeposition process on the interface quality, using quantum chemical calculations to interpret results.

Establishing a toxicity assessment of filter adsorbents

Priscilla Lee, Desiree Harris, Fiona Sheridan, Hannah LaPadula, Kathleen Au*

Recently, there have been issues with carbon granules and other particles leaking out of individual protection filters on gas air purifying mask. This effort will work to establish a workflow to assess the toxicological effects of these leaked materials on the human body by characterizing particle size of the filter adsorbents and developing sterilization techniques for in vitro cytotoxicity assessment. The results from cytotoxicity assays will provide baseline information to establishing standards in filter specifications.

Quantum imaging and spectroscopy for chemical detection

Eric Emmons

Quantum imaging and spectroscopy with entangled photons is a potentially valuable technique for sensitive and selective detection of chemical threats, but it is necessary to quantitatively determine its capabilities. In this project, we will develop and characterize an entangled photon source for use in quantum imaging and spectroscopy. This work will have the benefit of developing for DEVCOM CBC expertise in these techniques and an assessment of their advantages compared to conventional techniques.

A standard method for analysis of per- and polyfluoralkyl substances in environmental samples by liquid chromatography with tandem mass spectrometry

Nam-Phuong Nguyen

Per- and polyfluoroalkyl substances (PFAS) are organic compounds that pose environmental and human health concerns. PFAS analysis using liquid chromatography mass spectrometry is the choice technique as it can detect and quantify PFAS compounds in various environmental matrices. This study aims to develop a method to detect PFAS in samples that can determine method detection limit, percent analyte recovery, detection limit, and limit of quantification. The goal of this project is to enable samples that need to be screened for PFAS but are potentially contaminated with chemical warfare agents to be analyzed in the same lab. This capability may foster additional collaborations among DEVCOM CBC, DOD, and research groups on the detection of PFAS.

Soil temperature effects on chemical exposure risk assessment using earthworm reproduction test

Emily Stricklin

Current risk assessments of exposure to chemicals are based on toxicity data established in standardized tests conducted at “room” temperature. The relevance of such data may be diminished for geographic regions with greater average temperatures. The proposed research will test the hypothesis that increasing soil temperature by 5 °C will affect reproduction toxicity for the model test species *Eisenia andrei.* This research could lead to modifications of international standardized test protocols to more accurately represent the exposure conditions in the field and provide more realistic toxicity assessments.


ILIR
PROJECTS

Designing membrane-bound proteins as sensors for use in cell-free protein systems

Nathan D. McDonald[a], Ethan N. Walters[b], Frank J. Kragl III[a], Katherine A. Rhea[a]*
[a]U.S. Army Combat Capabilities Development Command Chemical Biological Center, Research & Operations Directorate, 8198 Blackhawk Rd, Aberdeen Proving Ground, MD 21010
[b]Oak Ridge Institute for Science and Education, 1299 Bethel Valley Rd, Oak Ridge, TN 37830

ABSTRACT

Cell-free expression systems are a mechanism for research and development of transcription and translation without needing a whole cell organism. The use of tunable synthetic structures comprised of artificial membranes within a cell-free expression system could improve the study and control membrane-based biosensors systems. For the initial approach of a membrane-based sensor in cell-free expression, we chose a well-characterized two-component system, a signal transduction pathway that enables bacteria to sense and respond to stimuli. QseBC, a well-characterized, relevant two-component system and virulence factor regulator found in *Escherichia coli* that is activated by quorum sensing autoinducers, epinephrine and norepinephrine suited for transition into cell-free expression was chosen for this study. Here we describe our efforts to implement the QseBC biosensor into a cell-free expression system by measuring fluorescent output in the presence of epinephrine using a plasmid encoding superfolder green fluorescent protein controlled by the qseBC promoter. We evaluated the functionality of the sensor in cell-free expression plate based liquid reactions and lyophilized plate and ticket reactions and observed superfolder green fluorescent protein production in the presence of epinephrine within 15 minutes of rehydration. We verified an alternative nickel sensing two-component system was functional within the cell-free expression system. Overall, cell-free expression systems are a viable platform for development of membrane-based sensors.

Keywords: Cell-free expression, bacterial two component system

1. INTRODUCTION

The recent development and commercialization of cell-free expression (CFE) systems have enabled major advancements in the field of synthetic biology. Cell free lysates are not a novel concept and have been widely used in basic research since the 1960s when translation machinery was first extracted from cells. Since then, lysates have been a standard mechanism for studying transcription and translation without the biological hindrance of whole organisms or membrane structures. Mass-produced and ready to use kits like myTXTL and PureXpress have provided high throughput and standardized mechanisms for targeted research and assay development. These *Escherichia coli*-based CFE systems have been used in a variety of applications including but not limited to prototyping, biosensors, viral synthesis, large scale bio manufacturing, production of synthetic substrates, and integration into the Design-Build-Test-Learn workflow. Despite the widespread use of these systems across a multitude of research applications, a major gap still exists in membrane-based biosensors. The CFE systems offer a unique platform to introduce complex, synthetically derived custom membranes comprised of targeted membrane sensor proteins that are traditionally difficult to study in whole cell organisms.[1,2]

CFE researchers have largely avoided the use of membranes within CFE reactions as one of the main purposes of using these systems is to remove the physical barriers that membranes create and introducing phospholipids/membrane structures back into these systems may seem counterintuitive. However, controlled introduction of specific membranes and associated proteins in a "tunable" fashion in what has been deemed TXTL synthetic cells could improve the ability to study and control membrane-based sensor systems. The only published example of this work included the introduction of external lipids containing membrane channels to a cell-free synthesis reaction. The system was given necessary building blocks of transcription and translation externally and green fluorescent protein was produced internally. The experiment determined that membranes and membrane proteins can function in a typical cell-free reaction and the artificial membranes or synthetic cells can be adjusted to contain varying amounts of membrane

proteins that effect the internal production of protein.[3] This system, although not as complex as a membrane-based sensor, appropriately lays the foundation for larger more elaborate membrane associations.

The initial approach for a membrane-based sensor should involve a well-characterized and thoroughly understood system. The logical first step would be that of bacterial two-component systems (TCS) which are signal transduction pathways that enable organisms to sense and respond to stimuli both inside and outside of the cell. These TCSs are widely used in the field of synthetic biology and have been engineered to induce an immune response, release drugs into a system, activate enzymes or the biological stress response and even trigger artificial biochemical pathways to improve genetically engineered systems. These pathways can be manipulated and modified into custom biosensors that can detect any manner of biological or chemical stimuli. These systems, as a tool, enable researchers to increase detection capabilities and help to generate a better understanding of complex biological systems.

The prototypical TCS consists of an RNA molecule or protein that binds to a ligand and responds by altering gene expression. Most TCS sensors consist of sensor histidine kinase (SHK), a response regulator (RR), and an output promotor (Figure 1). The SHK consists of a transmembrane portion with an N-terminal sensor domain and a C-terminal transmitter domain. A trigger ligand binds to the sensor domain, typically located outside of the cell, and initiates a conformational change within the SHK that relays to the transmitter domain that kinase activity needs to increase. The transmitter domain, now in the activated state, modifies the RR, via phosphorylation, at its N-terminal receiver domain. This initiates a conformation change within the RR that communicates to the C-terminal DNA binding-domain that transcription should begin. When a triggering ligand is no longer present, the SHK transmitter domain will also dephosphorylate the RR, which halts transcription and closes the response loop.[4]

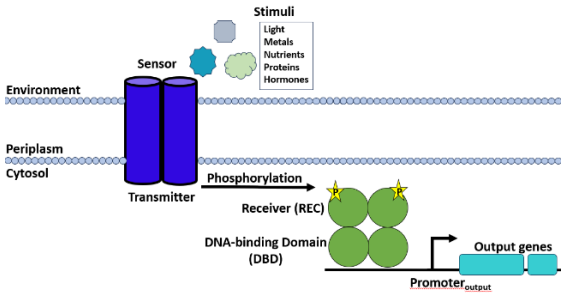

Figure 1. Representative schematic of a bacterial two component system (TCS).

A specific, well-characterized and relevant TCS with the potential to transition into cell-free protein systems is that of QseBC, a quorum sensing, and virulence regulator found in *Enterobacteria* and *Pasteurella.* QseC is the SHK located on the cytoplasmic membrane with the sensor domain located within the periplasmic space and the transmitter domain resting inside of the cytoplasm. QseB is the RR that is modified by QseC, it consists of a receiver domain and a helix-turn-helix DNA binding-domain. In *Escherichia coli*, the model system of choice, the QseC responds to autoinducer-3 and epinephrine/norepinephrine (Figure 2). QseC functions as an adrenergic receptor and binding of epinephrine/norepinephrine can be inhibited by adrenergic antagonists, which offers another built in mechanism of control within the system. The QseBC TCS activates transcription of the qseBC promotor as well as the flhDC promotor of the flagella regulon. The qseBC promotor controls the expression of ygiW, a protein which enables increased resistance to stressors through modification of the lipopolysaccharides while the *flhDC* promotor controls the expression of proteins that increase motility thus enhancing virulence and survival capabilities.[5–8]

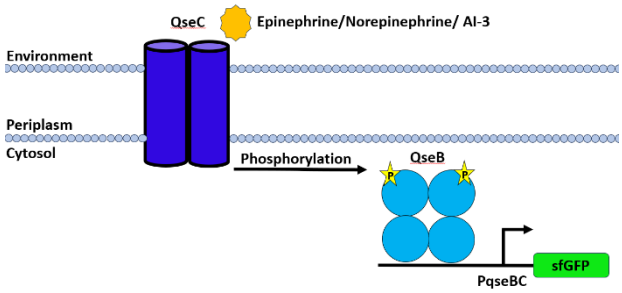

Figure 2. The QseBC TCS is activated by epinephrine/norepinephrine/AI-3 and turns on qseBC promotors.

Together the CFE systems and bacterial TCS have the potential to make a novel sensing mechanism. The further development and exploration of membrane-based systems within a cell-free protein system has the potential to enhance our understanding of CFE and TCSs as well as push the boundaries within the field of synthetic biology. *E. coli* proves to be the best model to use for both CFE and TCSs since it is the most well characterized and historically the most productive and functional of the CFE systems that have been published. This should translate to the highest probability of success when attempting to implement an *E. coli* based TCS into an *E. coli* based CFE. Here, we show that a bacterial TCS (QseBC) can be incorporated into artificial membranes and can be used as a membrane-based sensor in an *E. coli* CFE to sense epinephrine. This work highlights the ability of CFE systems to produce membrane-based biosensors entirely within the CFE system and suggests that future work using alternative TCS based biosensors of relevance could serve as alternative approaches to enhance detection and potential medical countermeasures in a safe and efficient manner.

2. MATERIALS AND METHODS

2.1 Extract Preparation

In general, cell free lysates were produced following the work previously described by the Jewett lab.[9] When necessary, the protocol was modified as follows to accommodate the scale of the preparation:

Note: Day 13 must be performed in sequential order, but Day 4 may begin up to two weeks after Day 3 ends.

Day 1: Inoculate 4 fresh plates of 2XYTP agar from a glycerol stock of DeltaLacZ KO *E. coli* and incubate at 37 °C for 16–18 hours.

Day 2: Using a large loop, scrape all material from two starter plates and transfer it into 750 mL of 2XYTP broth in a 2.8 L Erlenmeyer flask. Repeat this for the additional two starter plates, for a total of 1.5 L of inoculated media. The cultures should be inoculated 16 hours before the start of the final culture and incubated at 37 °C with a shaking speed of 200 rotations per minute (rpm). For 100 L fermentation, the media was prepared in the IF 150 L (New Brunswick Scientific) fermenter by adding 3.1 kg of 2XYT media powder, 700 g of Potassium Phosphate dibasic (Sigma Cat, P3786), 300 g of Potassium phosphate monobasic (Sigma, P5655) and 5 mL of antifoam 204 (Sigma, A8311) to 100 L of deionized (DI) water. The media was allowed to aerate overnight with a rotor speed of 100 rpm, airflow of 20 standard liters per minute and the temperature set to 37 °C.

Day 3: The overnight cultures were combined and OD_{600} measured using a spectrophotometer (Genesys 20, Fisher Scientific) and the inoculation amount calculated. The 100 L culture is seeded at a starting density of approximately 0.05 OD_{600} using a 2 L pre-sterilized transfer bottle to inject the media with the appropriate amount of overnight culture based on starting optical density. The fermenter settings were adjusted to 300 rpm, 50 standard liters per minute air flow and the dissolved oxygen meter was calibrated to 100 %. The OD_{600} was measured every hour until 0.6–1.0 at which point the culture was induced with 100 mL of 1M Isopropyl B-D-1-thiogalatopyranoside (GoldBio, I2481C) for a final concentration of 1mM. The fermentation continued and when dissolved oxygen levels fell below 50 % the rotation speed was increased to 500 rpm (this usually occurs around OD_{600} 2–2.5). Upon reaching OD 3.5, the culture was cooled to 4 °C and the centrifugation process initiated. The material was centrifuged using a pre-chilled (4 °C) powerfuge pilot, 1.1 L bowl, system (CARR Biosystems) in ~8 hours. When the entire 100 L culture has been processed the centrifuge is deconstructed and the bowl scraped of all pelleted bacteria. The pellet was flattened into Ziploc bags, ~300 g per bag, and placed at -80 °C.

Day 4: Pellet material is removed from the freezer and allowed to thaw on ice. The material was resuspended using 1 mL of S30B buffer per gram of cell mass. The material was passed through a microfluidizer at 15,000 psi, and the lysate was collected in its entirety. The resulting lysate material was clarified by centrifugation at 12,000 x g for 10 minutes. Runoff reactions were performed on the clarified lysate material by heating to 37 °C , with shaking at 200 rpm in a standard shaking incubator (New Brunswick). After heating, the material was clarified further by centrifugation at 12,000 x g for 10 minutes and the resultant supernatant was placed in 250 mL dialysis flasks (Fisher, 87762) inside of 5-gallon buckets (Home Depot) filled with S30B buffer, 2 flasks per bucket, and allowed to dialyze overnight (24 h).

Day 5: After the material has sufficiently dialyzed it is further clarified by centrifugation at 12,000 x g for 10 minutes and the resulting supernatant is aliquoted and flash frozen using liquid nitrogen.

2.2 Cell-free reactions

All regents were prepared as previously described and combined into a single energy buffer mix and aliquoted and flash frozen for use.[10] When preparing reactions, 100 µL (1 mg) of 1-Palmitoyl-2-oleoyl-sn-glycero-3-phosphocholine (POPC), 100 µL of 1palmitoyl-2-oleoyl-sn-glycero-3-phospho-L-serine (POPS) lipids or 50 µL of POPC and 50 µL of POPS lipids placed in a 5 mL glass test tube and nitrogen gas was used to evaporate any excess chloroform. The lipids were kept on an ice rack until mixed with the cell free extract and energy buffer. Each reaction consisted of 55 µL of extract, 54 µL of Energy buffer, 1 µL of 10 mg/mL Epinephrine (Sigma, E4375) in water and various amounts of DNA and recombinant protein as noted for each experiment. All volumes were normalized, and water was used to compensate in the negative controls. Each reaction was sonicated in a water bath (Cole Parmer, Unit #) at 37 °C for 30 minutes to 24 hours. After sonication reactions were pipetted into a 96 well U bottom plate for reading on a Biotek H1 plate reader at F:488, 525 from the bottom. Paper ticket-based reactions were read on an LiCor Odyssey XF Imager at the 700 nm wavelength, with the shape tool used to highlight and quantify the cell free spots. Optical settings were adjusted for background for each ticket assay.

2.3 Strains and plasmids

E. coli strain NEB 10-beta (New England Biolabs, C3019) was used for all DNA expression of cell-free plasmids. All cell-free constructs were cloned in the pY71 vector that was cut from pY71-sfGFP (Addgene, 102634) or pY71 vector cut from pY71-LacZ.

3. RESULTS

3.1 Determining optimal lipid composition

To determine if performance could be enhanced by altering lipid composition, three separate lipid solutions were prepped for analysis. A solution with 1 mg of POPC, a solution with 1 mg of POPS and a combination of 500 µg of each lipid. The cell free components other than the lipid solutions were prepared as a mastermix and distributed between the reactions to maintain consistency. As shown in Figure 3, the POPC lipid solution outperforms the POPS and combination solutions suggestion that POPS has a negative or detrimental effect on the overall reaction productivity.

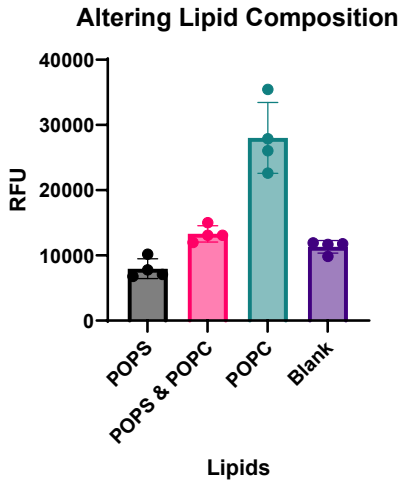

Figure 3. Plate reader data from identical reaction conditions except for altering of lipid composition. POPC lipids are the most ideal lipids for use in these CFE systems.

3.2 Initial comparison of liquid versus lyophilized reactions

The optimal concentration of Epinephrine for comparison of liquid reactions to lyophilized reactions was determined by performing a titration series of epinephrine in a standard plate-based cell free reaction series that varied only the

concentration of epinephrine (Figure 4). The highest concentration of epinephrine 15 µg inhibited the reaction and the lowest concentration of the reaction 0.24 µg has a significantly decreased signal. The remaining concentrations from 0.47 µg to 7.5 µg clustered around each other suggesting any of these concentrations could be used to determine productivity and success of the cell free reaction and TCS system.

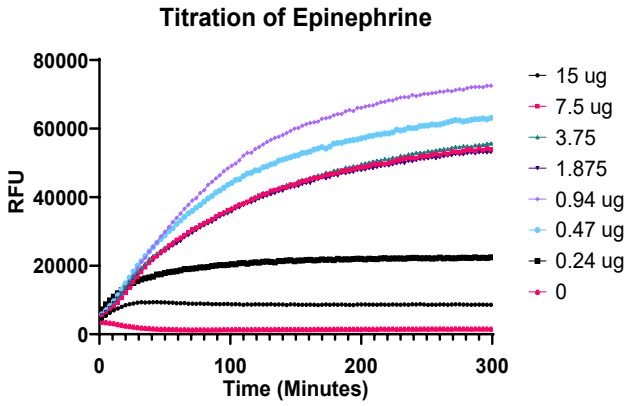

Figure 4. Titration of epinephrine in CFE system to determine optimal concentration for future reactions and comparisons.

A cell free reaction mix containing POPC lipids and 10 nM of plasmid DNA concentrations was prepared and split in half. Half of the reaction mix was run on a plate reader as a liquid reaction (Figure 5, blue bars) and the other half was lyophilized overnight in the same volume as the liquid reactions. The following day this CFE mix (Figure 5, red bars) was rehydrated with the same concentration of epinephrine, 7.5 µg, and ran on the plate reader immediately. The lyophilized reactions performed almost as well as the liquid reactions even after lyophilization.

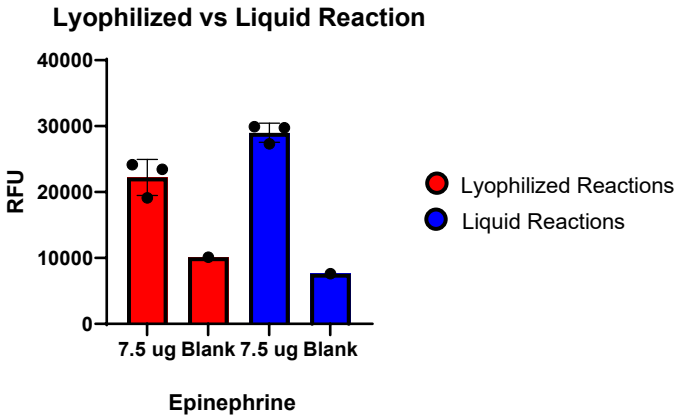

Figure 5. Comparison of fresh liquid reactions to lyophilized reactions in the presence of the same amount of Epinephrine.

3.3 Assessing speed of the QseBC sensor in the CFE system

To assess the reaction speed of this system after lyophilization we ran both plate and ticket reactions without any modifications to the original assay components. We determined that the ticket reactions were much slower than the plate-based reactions despite being developed from the same batch of CFE material. Lyophilized plate reactions (Figure 6) generate a positive response within 10–15 minutes of addition of epinephrine whereas the ticket reactions (Figure 7) required about 30–40 minutes to see a positive response. The difference between the assay times required indicated a need for further optimization of the paper-based ticket reactions.

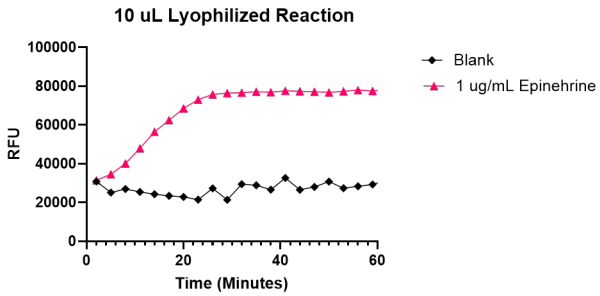

Figure 6. Three separate CFE reactions were prepared and spiked with 1 ug/mL of epinephrine. The average of these reactions was plotted to assess reaction speed. A positive signal is noted at halfway point in the rise of the curve around 10-15 minutes.

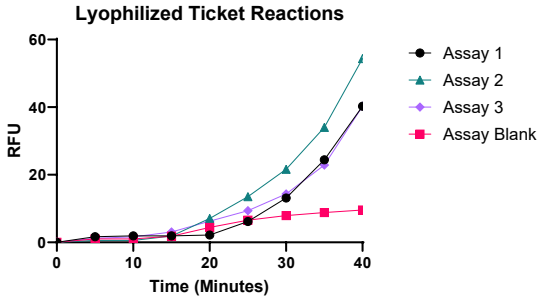

Figure 7. Three separate CFE reactions were prepared and spiked with 1 ug/mL of epinephrine. The separate reactions were plotted to assess reaction speed. A positive signal is noted at halfway point in the rise of the curve around 30–35 minutes.

3.4 Assessing the stability of the QseBC sensor in the CFE system

Ticket assays that had been stored at -80 °C for three and a half months were removed and rehydrated with 2 µL of 1 ug/mL epinephrine. Reaction time of the assay was identical to the ticket assays when they were first made, and we saw a positive result at 33 minutes (Figure 8). These results are encouraging and despite other CFE mixes showing a significant decline in productivity after only a month of storage the TCS system appears to be more stable. Further modifications will need to be implemented to achieve room temperature or longer storage.

3.5 Increasing the reaction speed of the QseBC sensor in the CFE system

To increase the reaction speed of this system after lyophilization we determined that decreasing the rehydration volume of the ticket assay allows the CFE reaction to remain more concentrated and allows the necessary response to carry out at a more rapid speed. When decreasing the volume from 2 µL to 0.5 µL, while maintaining the same epinephrine concentration, we saw an increase in response time from 30–40 minutes to 20–25 minutes. With the addition of 30 mg/mL of maltodextrin, a known cytoprotectant as well as potential energy source for the CFE reaction, we saw an additional increase in positive response time from 20–25 minutes to 10–15 minutes which matched the previous lyophilized plate reaction speed we sought to achieve.

Figure 8. The stored ticket assay shown at 33 minutes with quantified fluorescence.

3.6 Assessing the functionality of an alternative bacterial nickel sensing TCS

To determine performance of an alternate bacterial TCS, reaction conditions established using the QseBC TCS were applied to a Nickel sensing TCS system. These reactions were spiked with 10nM of each DNA plasmid, py71-rppA, py71-rppB, and nickelresponse-sfGFP, 1 mg of POPC lipids and allowed to run overnight. The reaction was then exposed to 400 µg/mL Nickel (II) Sulfate and run in liquid form in a standard plate reader. Four separate reactions were prepared, and each reaction displayed a significant increase in florescent response over the blank indicating that the CFE system was capable of successfully functioning with an alternative TCS (Figure 9).

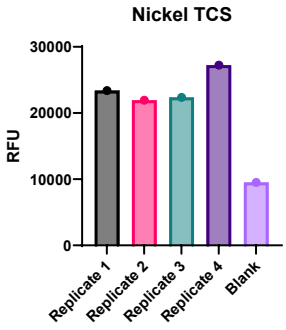

Figure 9. Nickel sensing TCS shows a positive result in four separate CFE reactions.

4. DISCUSSION

Bacterial TCSs have been broadly studied and have been found to sense a variety of different stimuli ranging from temperature, light, heavy metals, antimicrobials, and many other small molecules and metabolites. Furthermore, previous work has shown that TCS can be evolved in vitro to alter the ligand binding specificity opening the door for the development of novel proteins capable of sensing molecules of Department of Defense (DOD) interest.[11] We plan to take the application and workflow developed for QseBC as well as the Nickel TCS and apply the same techniques to an alternative TCS with more impact to continue assessing if it is a broadly applicable process across multiple TCSs in CFE. Cell-free systems designed at sensing external stimuli offer several advantages over whole-cell biosensors or alternative sensing systems. One of the primary utilities of cell-free systems is that they can be freeze-dried for storage with the necessary components for function. In the field, these freeze-dried sensors can be rehydrated with the sample of interest and the cell-free reaction will run as expected. The goal of this work is to continue to progress to the point of a field deployable DOD relevant biosensor that generates a response within 20 minutes at ambient temperatures for a high impact DOD target. Further research is required to optimize the sensor itself, determine the appropriate reagents for stability in a ruggedized system, and transition this sensor to a format that is readily visual to the naked eye.

The immediate next steps to achieve this goal are to implement an alternative TCS system that senses the explosive TnT and many of its derivatives. This sensor previously mentioned in the synthetic biology literature and designed in the early 2000s is a retargeted ribose binding protein that was engineered to detect TNT.[12] If these methods prove successful the likelihood of implementing this workflow effectively for this bacterial TCS becomes more probable and could provide a high impact in a field where colorimetric, field stable, and sensitive assays are in high demand.

ACKNOWLEDGMENTS

We would like to thank Dr. Daniel Phillips for assistance in everything lipid and liposome and the Combat Capabilities Development Command Chemical Biological Center In-house Laboratory Independent Research Program for thoughtful discussion and programmatic support. Funding was provided by the U.S. Army via the In-house Laboratory Independent Research Program (PE 0601101A Project 91A) at the Combat Capabilities Development Command Chemical Biological Center.

REFERENCES

[1] Garenne, D.; Haines, M.C.; Romantseva, E.F.; Freemont, P.; Strychalski, E.A.; Noireaux, V. Cell-free gene expression. *Nat. Rev. Methods Primers*. **2021,** *1* (49).
[2] Cole, S.D.; Miklos, A.E.; Chiao, A.C.; Sun, Z.Z.; Lux, M.W. Methodologies for preparation of prokaryotic extracts for cell-free expression systems. *Synth. Syst. Biotechnol*. **2020**, *5* (4), pp 252–267.
[3] Garenne, D.; Thompson, S.; Brisson, A.; Khakimzhan, A.; Noireaux, V. The all-E. coliTXTL toolbox 3.0: new capabilities of a cell-free synthetic biology platform. *Synth. Biol*. **2021**, *6* (1), ysab017.
[4] Lazar, J.T.; Tabor, J.J. Bacterial two-component systems as sensors for synthetic biology applications. *Curr. Opin. Syst. Biol.* **2021**, *28*, p 100398.
[5] Weigel, W.A.; Demuth, D.R. QseBC, a two-component bacterial adrenergic receptor and global regulator of virulence in Enterobacteriaceae and Pasteurellaceae. *Mol. Oral Microbiol*. **2016**, *31* (5), pp 379–97.
[6] Moreira, C.G.; Sperandio, V. The Epinephrine/Norepinephrine/Autoinducer-3 Interkingdom Signaling System in Escherichia coli O157:H7. *Adv. Exp. Med. Biol.* **2016**, *874*, pp 247–61.
[7] Clarke, M.B.; Sperandio, V. Transcriptional autoregulation by quorum sensing Escherichia coli regulators B and C (QseBC) in enterohaemorrhagic E. coli (EHEC). *Mol. Microbiol*. **2005**, *58* (2), pp 441–55.
[8] Sperandio, V.; Torres, A.G.; Kaper, J.B. Quorum sensing Escherichia coli regulators B and C (QseBC): a novel two-component regulatory system involved in the regulation of flagella and motility by quorum sensing in E. coli. *Mol. Microbiol*. **2002**, *43* (3), pp 809–21.
[9] Levine, M.Z.; Gregorio, N.E.; Jewett, M.C.; Watts, K.R.; Oza, J.P. Escherichia coli-Based Cell-Free Protein Synthesis: Protocols for a robust, flexible, and accessible platform technology. *J. Vis. Exp*. **2019**, *25* (144).
[10] Silverman, A.D.; Kelley-Loughnane, N. Lucks, J.B.; Jewett, M.C. Deconstructing Cell-Free Extract Preparation for in Vitro Activation of Transcriptional Genetic Circuitry. *ACS Synth. Biol*. **2019**, *8* (2), pp 403– 414.
[11] Kohanski, M.A.; Collins, J.J. Rewiring bacteria, two components at a time. *Cell*. **2008**, *133* (6), pp 947–948.

Fundamental exploration into advanced multispectral obscurants

Danielle L. Kuhn*, Jill B. Harland
U.S. Army Combat Capabilities Development Command Chemical Biological Center, Research & Operations Directorate, 8198 Blackhawk Rd, Aberdeen Proving Ground, MD 21010

ABSTRACT

Obscuration plays an integral role in protecting the warfighter. These obscurant materials absorb, scatter, or emit radiation in the visible, infrared, and millimeter wavelengths of the electromagnetic spectrum to interrupt the line of sight between an objective and observer. However, current fielded obscuration technologies (i.e., broadband obscurants such as brass and graphite and carbon fiber) for millimeter are limited in obscuring modern devices due to low obscuring performance, incompatibilities with explosive dissemination, and poor de-agglomeration of the materials upon dissemination in atmospheric conditions. This project seeks to systematically explore the factors that generate a material with high performance capabilities, by exploring a variety of metal coated carbon fibers, which were characterized by scanning electron microscopy, electron paramagnetic resonance, and millimeter wavelength measurements (in collaboration with the University of Delaware). By tuning a material's geometry, composition, aspect ratio, and conductivity, obscurant materials were fabricated with higher obscuration performance and; therefore, better able to protect the warfighter.

Keywords: Obscuration, millimeter wave, radar, fibers

1. INTRODUCTION

The electromagnetic spectrum is one of the most important domains in military operation. Electromagnetic warfare encompasses military communications and sensors. Obscurants are materials that will absorb, scatter, or emit radiation in the electromagnetic spectrum, decreasing the electromagnetic energy available for sensors to detect important assets. Obscurants and smokes are critical components in the defense of weapons, vehicles, and personnel. Obscurants work by interrupting the line of sight between an objective and observer. Current obscuration materials have many limitations, including agglomeration, not being adapted to modern "smart weapons," toxicity, limitations in dissemination techniques, and the logistical load on the warfighter. This study focuses on the millimeter wave (MMW) region of the electromagnetic spectrum. Radar and missile seeking radar operate in the MMW area of the electromagnetic spectrum. Radar has several different bands that operate at different frequencies. Obscurants can affect radar systems performance by attenuating the returning signal, which will affect the range that the target is being detected or mask the target signal by creating background noise from scattering. The current U.S. Army standard material in use is carbon fiber. Carbon fiber is widely used due to its low density and high conductivity.[1,2] In general, a high performing millimeter wave material will have a high aspect ratio and high conductivity. Fibers act as an antenna, where the electrons oscillate along the fiber causing attenuation.[3] The theory behind how conductive fibers can absorb or scatter in the electromagnetic spectrum has been established.[4–15] Radar consists of multiple bands at different frequencies, with the most sensors operating in the X-band (8–12 GHz) and K_a band (27–40 GHz).[16] The frequency at which the fiber attenuates can be controlled by the length of the fiber. The length of the fiber or dipole is half the wavelength of the radar frequency signal.[3] The following equation can be used to calculate expected frequencies attenuated based on length of the fiber, where the length of the dipole is equal to the constant 143 MHz/meter is divided by frequency in MHz:

$$\text{Length} = 143/\text{frequency} \quad (1)$$

Metal and metal alloys inherently have a high conductivity, but pure metal fibers are dense and heavy and would have a hard time staying aloft compared to carbon fiber, a key aspect of creating a good obscurant cloud. On the other hand, metal coated carbon fibers have the potential to increase conductivity compared to carbon fiber due to the skin effect[17] and have a decreased weight by unit volume compared to pure metal fibers, so a high performing cloud could potentially be generated. Carbon fiber was chosen as the core fiber instead of fiber materials like glass fibers, not only because it is the current field material, but also because based on Schelkunoff electromagnetic shielding theory, the co-effect of reflection and absorption mechanism are enhanced due to the high permeability in carbon fiber.[1] The core

of carbon fiber was also chosen due to the effects of skin depth. The skin effect is the fiber diameter of translucency. Above this diameter the performance decreases with increasing diameter (aka thicker metal coatings) and below this diameter it becomes transparent and adsorption of the electromagnetic energy occurs. For the samples presented below, the fiber diameter is near the level of transparency, so the core fiber material will have an impact on performance. In this work, we explore different electroplated metal carbon fibers with a variety of different metal coatings, bound copper salts to carbon fiber, and brass coated carbon fiber. These fiber samples were characterized by a Scanning Electron Microscope (SEM) equipped with Energy Dispersive X-ray Spectroscopy (EDX) for elemental mapping and Electron Paramagnetic Resonance (EPR) spectroscopy. Performance measurements of the material in the millimeter wave spectrum was evaluated and factors that most influenced performance measurements were investigated, such as metal type, coating thickness, coating uniformity, or oxidation state of the metal.

2. EXPERIMENTAL

2.1 Materials and synthesis procedures

2.1.1 Electroplated metal coated carbon fibers

Electroless and electrolytic plated carbon fiber was coated with copper, nickel, or an alloy of copper and nickel. The amount of metal was varied from 16–52 %. These samples were acquired from James Cropper Advanced Materials.

2.1.2 Iron coated carbon fibers

Iron coated carbon fibers were obtained several years ago and had been stored in a warehouse for over 5 years. Originally, the fibers were prepared in two different methods, where the iron was peroxided before application and the other where the iron was reduced before application. Due to long storage, the fibers were both oxidized and the integrity of the coating was diminished.

2.1.3 Synthesis of copper salt bound carbon fibers

AS4 carbon fiber is surface modified with carboxylic acid groups. To bind copper salts, the carbon fiber was treated with base. A 10 M NaOH solution was prepared and the carbon fiber was stirred in the base solution overnight. The carbon fiber was then rinsed with deionized water. A 10 M solution of copper acetate and copper bromide were prepared in deionized water. The rinsed base treated carbon fiber was then stirred in the copper salt solution overnight. The fibers were rinsed in deionized water to remove unbound excess salt. The fibers were air dried in the hood for several days, before analysis.

2.1.4 Brass coated carbon fibers

A 1 M suspension of 6000 rich brass was prepared in isopropanol. AS4 carbon fiber was dipped in the brass solution using tweezers and left to air dry overnight. An airbrush method was also used to coat the fibers. An airbrush was loaded with the brass suspension and the carbon fiber was hung to a white cardboard by tape and airbrushed with the brass. Better coverage was achieved with the solution dip method and the amount of brass could be controlled by changing the concentration of the brass solution.

2.1.5 Sample preparation for analysis and millimeter wave measurements

Fiber samples were obtained in tows and then cut to length. The fibers for this study were cut in house using a pressure cutter. Sharp blades on a roll were placed at exact distances to cut the fibers to length (4 mm or 10 mm). The fibers were then cast in either polyurethane foam or epoxy for performance measurements.

2.2 Characterization

2.2.1 Scanning electron microscope with energy dispersive s-ray analysis

A JEOL JSM-6360LV SEM equipped with a IXRF Systems Model 550i EDX system was used. Samples were prepared on SEM stubs using carbon tape. No charging was seen so the samples were not gold coated. A 10 mm working distance, 20 mV, and 35 spot size was used for EDX analysis.

2.2.2 Electron paramagnetic resonance spectroscopy

EPR spectra were obtained on a Bruker X-band EMX spectrometer, equipped with an Oxford Instruments liquid-nitrogen cryostat. Spectra were taken at 115 K, with 20 mW microwave power and 1 G modulation amplitude. The sample was prepared by filling an EPR tube with pure copper coated carbon fiber to just over an inch in the tube.

2.2.3 MMW measurements

In collaboration with the Prof. Mark Mirotznik Lab at the University of Delaware a focused beam measurement system was used where a gaussian beam is used to measure the materials response from 4–40 GHz. The samples were cast in either polyurethane foam or epoxy resin (Beast Bond brand). For the epoxy samples about 5 mg of fiber sample was used and the fibers were randomly distributed during the mixing process with the plastic spatula. The epoxy was allowed to set over the course of 24 hours. The polyurethane samples used either 100 mg or 25 mg and were cast at the University of Delaware using a homemade wooden frame and fast forming polyurethane foam.

3. RESULTS AND DISCUSSION

3.1 Characterization of metal coated carbon fibers

Several metal coated carbon fibers were investigated to find a fiber that would outperform the currently fielded material of carbon fiber. The fiber samples that were investigated were electroplated copper coated carbon fiber (CuCF) with different oxidation states of copper and different percentages of copper loading, electroplated nickel coated carbon fiver (NiCF), an alloy of copper and nickel coated carbon fiber (Ni/CuCF), iron coated carbon fiber (FeCF), synthesized copper carbon fiber, and brass coated carbon fiber. SEM images were taken of the fiber samples to determine how well coated the fiber samples were, how uniform the coatings were, and any debris from over plating present on the fibers (Figure 1). Figure 1 also shows the uncoated carbon fiber.

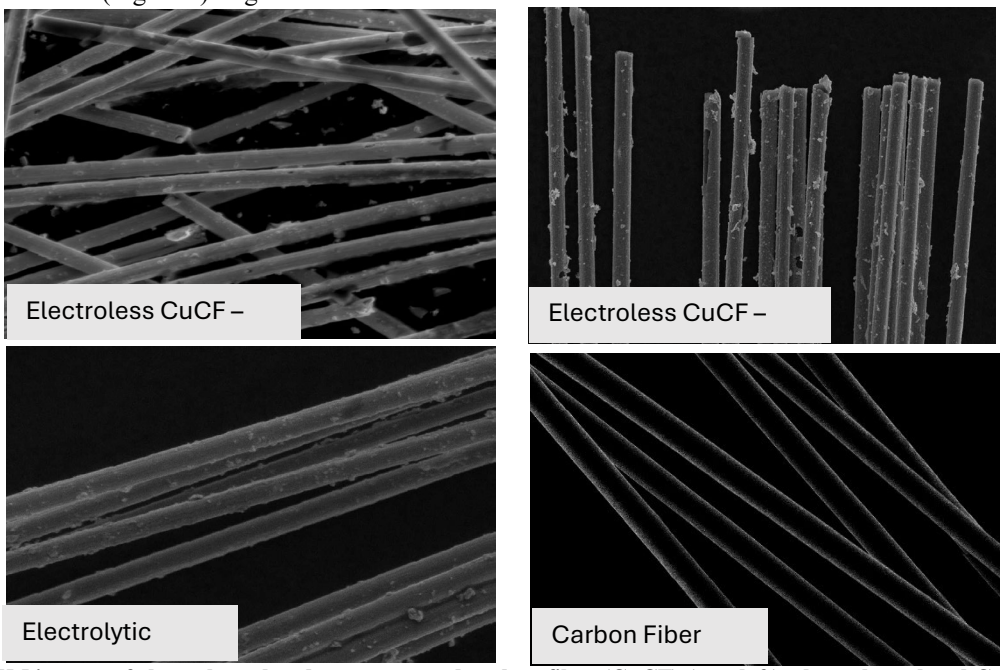

Figure 1. SEM images of electroless plated copper coated carbon fiber (CuCF) (top, left), electroless plated CuCF that has oxidized (top, right), electrolytically coated CuCF (bottom, left), and uncoated carbon fiber (bottom, right).

Overall, by visually inspecting the SEM images the samples appear very well plated. Some of the underlying carbon fiber can be seen in some of the fiber samples and there are some particulates on the surface, but overall, the carbon fiber is well coated by the copper coating. The uniformity of the sample should play a role, because a uniform coating of the metal is needed to conduct electrons across the surface and conductivity affects the obscuration performance of the material. The synthesized CuCF samples tested this theory. Surface modified carbon fiber (AS4 CF) has carboxylic functional groups on the surface. The CF was base treated to deprotonate the surface functional groups so that those sites would be available to bind copper salts, either $Cu(OAc)_2$ or $Cu(Br)_2$. The amount of copper bound to the surface

was investigated using SEM/EDX elemental mapping of copper on the surface (Figure 2). Most likely the iron oxidized overtime and the coating

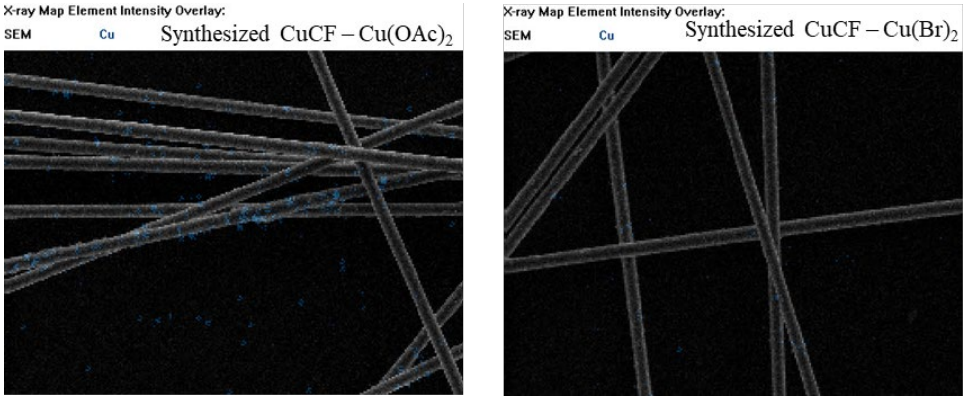

Figure 2. SEM images with EDX elemental map overlay of copper in blue of copper acetate salt bound to a base treated surface modified carbon fiber (left) and copper bromide salt bound to a base treated surface modified carbon fiber (right).

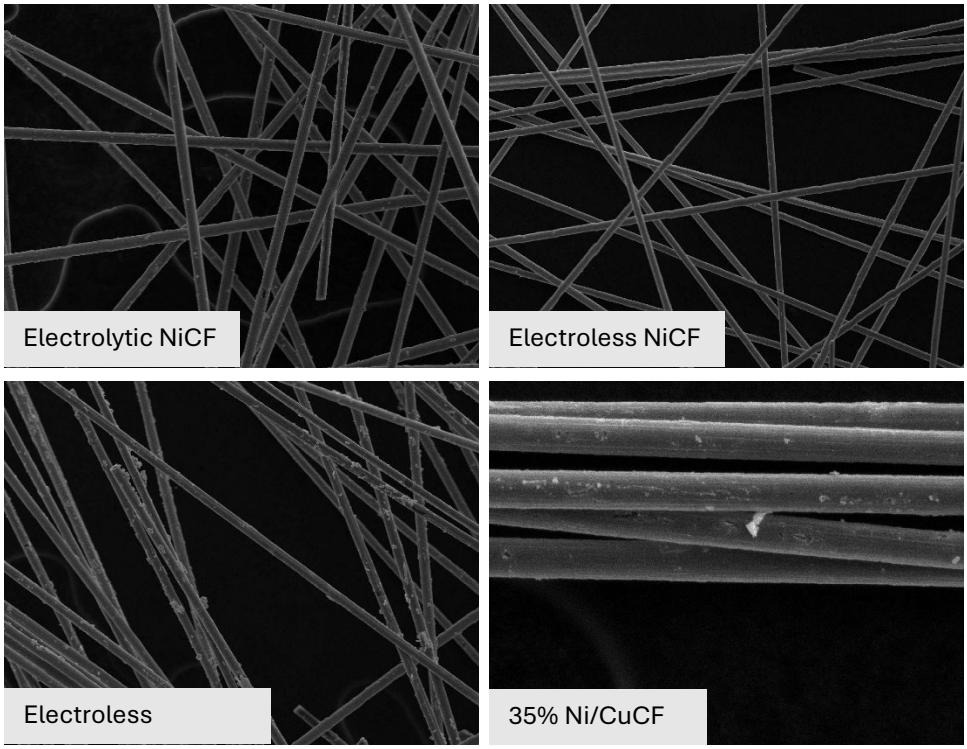

Figure 3. SEM images of electrolytically plated nickel coated carbon fiber (NiCF) (top, left), electroless plated NiCF (top, right), electroless plated alloy Ni/CuCF (bottom, left), and 35 % Ni/CuCF (bottom, right).

In the case of either salt, there was not a large amount of copper bound to the surface. The next metal coated carbon fiber investigated was NiCF and Ni/CuCF. The SEM images of these samples showed uniform coatings, with very little flaking or particulates seen on the surface (Figure 3). FeCF was the worst coated sample. The SEM image in Figure 4, reveal mostly bare carbon fibers. Most likely, the iron oxidized overtime and the coating disintegrated off the carbon fiber. The final material investigated was the brass coated carbon fiber. Brass is the standard infrared obscurant material and carbon fiber is the standard millimeter wave (MMW) material (Figure 4).

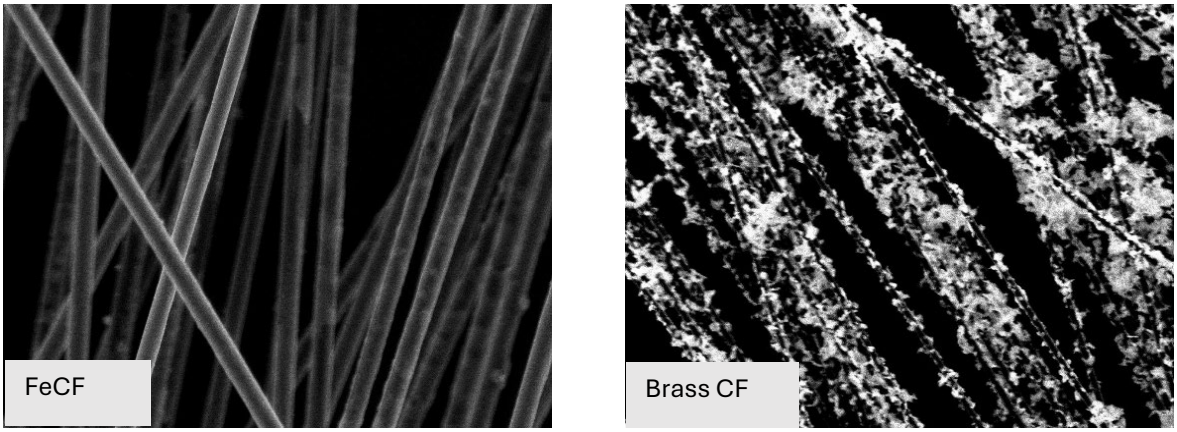

Figure 4. SEM images of iron coated carbon fiber (FeCF) (left), and brass coated surface modified carbon fiber (right).

Another factor that was explored was oxidation state of the copper metal. In theory, the oxidized copper should have a lower conductivity and thus be a worse performer. SEM/EDX (Figure 5, right) showed the clear presence of oxygen. EPR spectroscopy was utilized to identify the exact oxidation state of the copper. The peak at a g-value of 2.02 indicates a Cu^{2+} species is present (Figure 5, left).

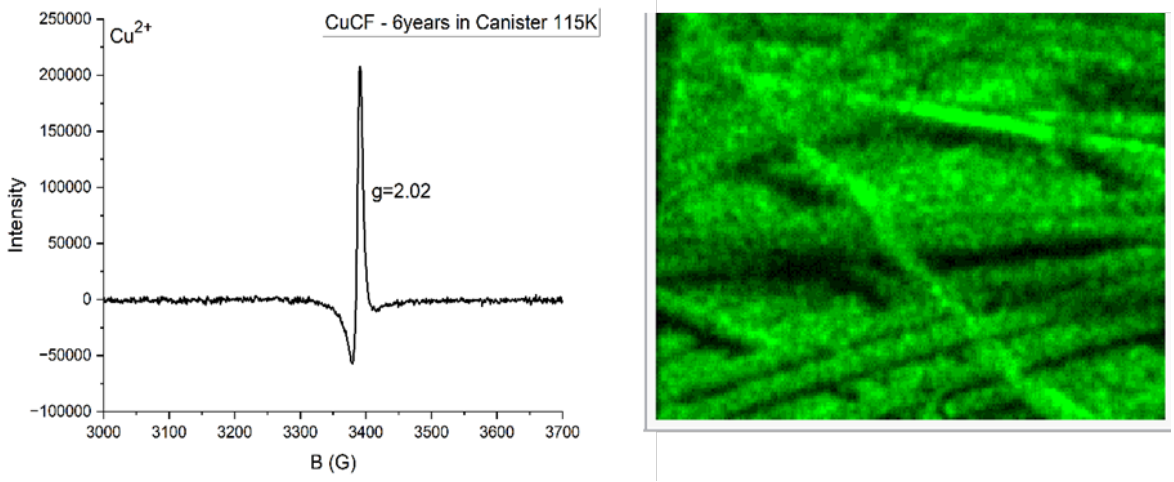

Figure 5. EPR spectrum of electroless coated carbon fiber (CuCF) at 115K with a g-value at 2.02 (left), and EDX elemental spectrum of oxygen in green overlayed on a SEM image of electroless coated CuCF (right).

3.2 Millimeter wave performance measurements

The obscuration performance of the material is determined by the mass extinction coefficient (MEC). The MEC is measured by taking a set concentration of cut fiber and casting the material in foam or epoxy and measured using the focused beam MMW measurement system. The raw data intensity is in dB and can be converted to MEC by the Beer-Lambert Law.

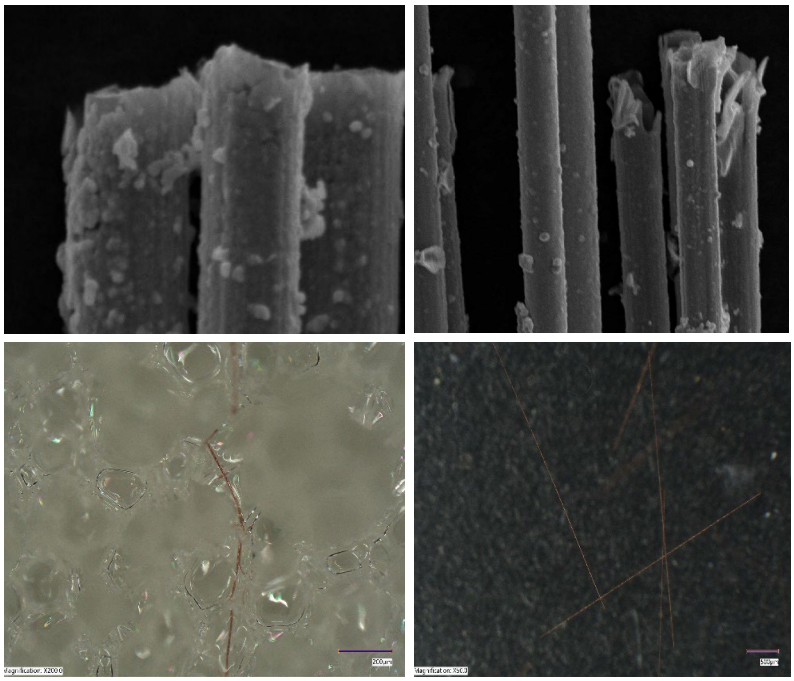

Figure 6. SEM image of CuCF cut with a pressure cutter (top, left), SEM image of CuCF cut with scissors (top, right), digital microscope images of CuCF cast in polyurethane foam (bottom, left), and digital microscope image of CuCF cast in epoxy (bottom, right).

The length of the fiber determines at what frequency a response is seen. The way in which the fiber is cut can affect the coating and therefore the performance. (Figure 6). When the fibers are cut to length using scissors the ends of the metal coatings become frayed and broken, whereas if a pressure cutter is used the coating at the fiber ends are intact.

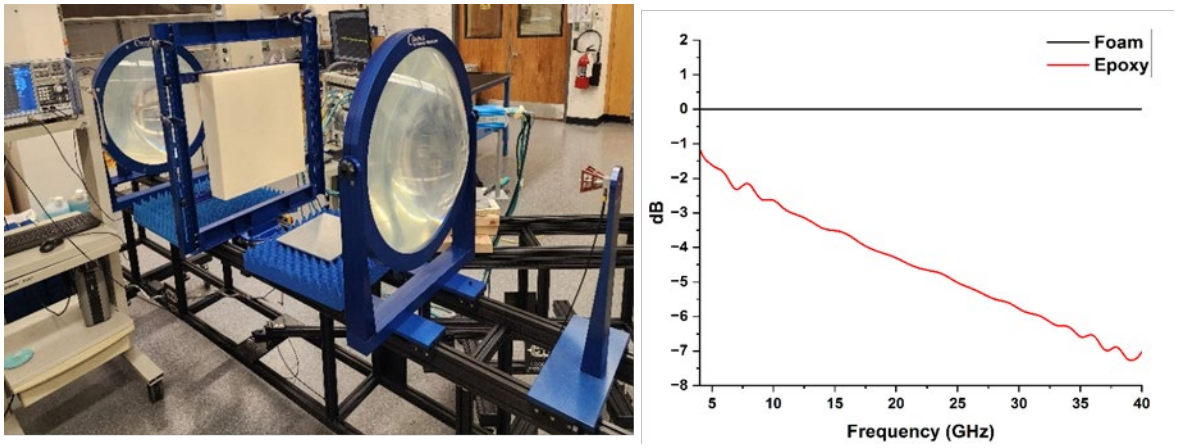

Figure 7. Millimeter wave measurement setup (left) and raw spectrum of foam vs epoxy dB response in the frequency range of 4–40 GHz (right).

All samples measured were cut via the pressure cutter method. Originally, the samples were cast in polyurethane foam, because it is silent in the MMW measurements (Figure 7), but in the process of the foam setting it forms bubbles that bend and break the fibers (Figure 6). Since the length of the fibers needs to be maintained, epoxy was utilized. Epoxy has a large background signal, but this was corrected for in data workup by background subtraction. The advantage of the epoxy is the arrangement of the fibers can be visually assessed to ensure random orientations to mimic what would be seen in the cloud, and the epoxy cures without bubble formation, so the fibers remain undisturbed. Once the fibers are cast in the epoxy, they are measured in the MMW measurement system (Figure 7). Samples are measured from 4–40 GHz and the epoxy is rotated four times and the data is averaged to correct for any orientational bias of the fiber dispersion.

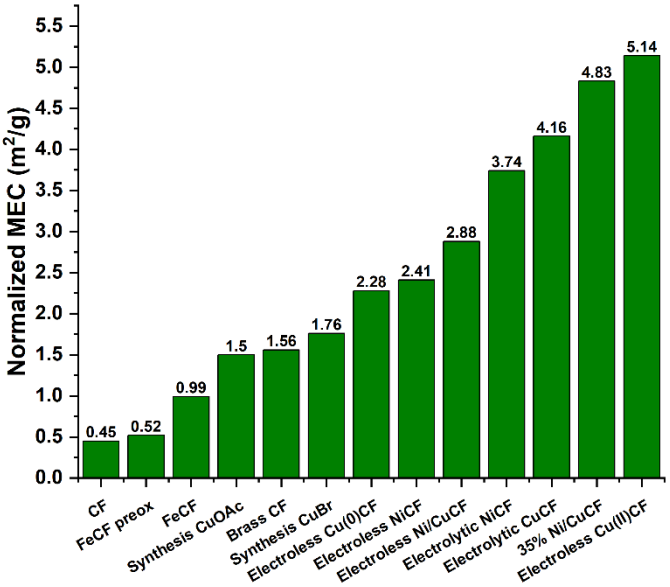

Figure 8. Normalized MEC values of fiber samples.

Normalized MEC values for the fiber samples are shown in Figure 8. The lowest performing material is the army standard carbon fiber. The best performer was the electroless plated CuCF. The FeCF had a normalized MEC value of less than 1 m^2/g. The low performance of FeCF, is most likely due to very little iron coating being present on the fibers. The brass coated carbon fiber had a normalized MEC value of 1.56 m^2/g. Not only did the brass enhance performance, but this material has the potential capability of obscuring a larger range of the electromagnetic spectrum, given brass material has known obscuration ability in the infrared wavelengths. The synthesized CuCF did not perform as well as the electroplated samples. This result shows that having a uniform metal coating is a key factor in performance. The presence of copper on the surface did increase the MEC value compared to carbon fiber, so some enhancement was seen, but not to the extent of the electroplated samples. For the electroplated samples, the electrolytic samples seemed to outperform the electroless samples slightly. The copper coatings had higher MEC values compared to Ni or Ni/Cu. Unexpectedly, the oxidized electroless CuCF sample had a higher MEC value than the reduced form. This is unexpected because generally as copper gets oxidized it performs worse because higher oxidation state leads to less electrons oscillating; therefore, it attenuates electromagnetic energy more poorly. This indicates that oxidation of the metal may play a more minor role. These samples were further investigated, and it was found that they had different amount of copper in the coating. A series of coated samples with different copper loading percentages were measured for their performance values (Figure 9). This study revealed that the percent of copper plays a large role in performance with the highest performing sample being a 35 % copper loading. This metal loading is potentially the sweet spot, due to the skin effect. It is at just the right diameter to take advantage of the carbon fiber core underneath and the effect of the copper coating to give maximum scattering and adsorption effects for peak MEC values.

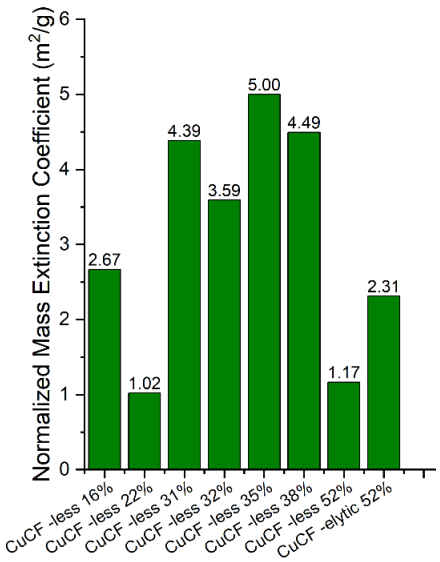

Figure 9. Normalized mass extinction coefficient (MEC) values of electroplated CuCF samples with different copper loadings in the coatings. Where less is electroless plated and elytic is electrolytically plated.

4. CONCLUSIONS

Based on the results discussed above, high performing materials were generated. All materials produced had a higher performance MEC value compared to the currently fielded material for MMW obscuration. The highest performing material overall was the electroless plated CuCF with 35 % copper loading. Not only were high performance materials discovered, but light was shed on the key factors that influence performance. It was determined that the metal type, application method of the metal, the percent loading of the metal, and the continuity/uniformity of the coating play major roles in performance. Oxidation of the metal seems to play a more minor role, which is a promising result for the shelf stability and lifetime performance of these materials. A method for properly cutting the fibers without causing damage was developed, as well as methods for preparing samples for MMW measurement.

Performance of the fibers is of great importance for obscuration, but equally important is how well these materials will disseminate into a cloud and stay aloft. Future efforts will include further investigation of different percent metal coatings for the electrolytic process for comparison as well as will focus on the dissemination of the fibers under different conditions and how to prevent agglomeration upon release. The materials will be scaled up and performance in the cloud will be measured using a MMW dispersion chamber. Ultimately, the material will be transitioned into a dissemination device with the goal of being fielded for the soldiers to utilize.

ACKNOWLEDGMENTS

Funding was provided by the U.S. Army via the In-house Laboratory Independent Research Program (PE 0601101A Project 91A) at the Combat Capabilities Development Command Chemical Biological Center. We acknowledge the support of Prof. Mark Mirotznik for providing the MMW measurement instrumentation. We also acknowledge John Davies for his initial work on implementing a design of experiments protocol.

REFERENCES

[1] Ye, M.; Li, Z.; Wang, C.; Han, A. Preparation, characterization, and millimetre wave attenuation performance of carbon fibers coated with nickel-wolfrma-phosphorus and nickel-cobalt-wolfram-phosphorus. *Mater. Res. Bull.* **2016**, *76,* pp 247–255.

[2] Liu, S.; Xie, Q.; Li, Y.; Bao, L.; Zhang, Z. Surface metalized carbon fibers prepared through ultrasonic pre-treatment for high-quality coating and outstanding millimeter wave stealth performance. *J. Alloys Compd.* **2024**, *1006*, p 176234.
[3] Van Vleck, J.H.; Bloch, F.; Hamermesh, M. Theory of radar reflection from wires or thin metallic strips. *J. Appl. Phys.* **1947**, *18*, pp 274–294.
[4] Bruce, C.W.; Jelinek, A.V.; Alyones, S. Millimeter Wavelength Prime Resonance Spectra for High and Low-Conductivity Fibrous Aerosols. *IEEE Trans. Antennas Propag.* **2022**, *70* (7), pp 5693–5698.
[5] Tai, C.T. Electromagnetic back-scattering from cylindrical wires. *J. Appl. Phys*. **1952**, *23*, pp 909–916.
[6] Cassedy, E.; Fainberg, J. Back scattering cross sections of cylindrical wires of finite conductivity. *IRE Trans. Antennas Propag.* **1960**, *8* (1), pp 1–7.
[7] Mei, K.K. On the integral equations of thin wire antennas. *IEEE Trans. Antennas Propag*. **1965**, *13* (3), pp 374–378.
[8] Chatterjee, A.; Volakis, J.L.; Kent, W.J. Scattering by a perfectly conducting and a coated thin wire using a physical basis model. *IEEE Trans. Antennas Propag*. **1992**, *40* (7), pp 761–769.
[9] Waterman, P.C. Scattering, absorption, and extinction by thin fibers. *J. Opt. Soc. Amer. A.* **2005**, *22* (11), p 2430.
[10] Waterman, P.C.; Pederson, J.C. Scattering by finite wires of arbitrary epsilon, mu, and sigma. *J. Opt. Soc. Amer. A.* **1998**, *15* (1), pp 174–184.
[11] Waterman, P.C.; Pedersen, J.C. Electromagnetic scattering and absorption by finite wires. *J. Appl. Phys*. **1995**, *78* (2), pp 656–667.
[12] Waterman, P.C.; Pedersen, J.C. Scattering by finite wires. *J. Appl. Phys*. **1992**, *72* (2), pp 349–359.
[13] Alyones, S.; Bruce, C.W.; Buin, A. Numerical Methods for Solving the Problem of Electromagnetic Scattering by a Thin Finite Conducting Wire. *IEEE Trans. Antennas. Propag*. **2007**, *55* (6), pp 1856–1861.
[14] Alyones, S.; Bruce, C.W. Electromagnetic scattering and absorption by randomly oriented fibers. *J. Opt. Soc. Amer. A*. **2015**, *32* (6), p 1101–1108.
[15] Alyones, S.; Bruce, C.W. Electromagnetic Scattering by Finite Conducting Fiber: Limitation of a Previous Published Code. *J. Electromagn. Waves Appl*. **2011**, *25* (7), pp 1021–1030.
[16] Skolnik, M.I. An introduction to radar. *Radar Handbook*; McGraw-Hill, **1962.**
[17] Siegel, E.; Labus, J. Scheinwiderstand von antennen. *Hoch.:Tech. u. Elek. Akus.* **1934**, *43*, p 166.

This page left intentionally blank

Synthetic bioprinted ocular and dermal model for toxicological characterization

Priscilla E. Lee[a]*, Susan K. Kozawa[a,b], Samantha E. Sarles[a], Jennifer A. Lee[a,c]
[a]U.S. Army Combat Capabilities Development Command Chemical Biological Center, Research & Operations Directorate, 8198 Blackhawk Rd, Aberdeen Proving Ground, MD 21010
[b]Oak Ridge Institute for Science and Education, 1299 Bethel Valley Rd, Oak Ridge, TN 37830
[c]Defense Threat Reduction Agency, 8725 John J. Kingman Rd, Fort Belvoir, VA 22060

ABSTRACT

Bioprinting living cells with synthetic, biocompatible polymers can provide the capability to develop customizable three-dimensional organ models that offer an alternative to traditional animal testing methods for toxicity assessment warfare agents. Bioprinting relies on similar principles as additive manufacturing technology with the primary difference that these printers use living cells and compatible biomaterials to build three-dimensional biological structures. This technology enables printing of multiple cell types in three dimensional layers, providing a more physiologically relevant model than traditional *in vitro* cell models, which are conventionally in a monoculture and monolayer format. Because bioprinting is a novel technology, there are challenges with structural integrity, cell viability and functionality, and validation. In year one, this project sought to use in-house polymer chemistry and customizable biomaterials to create a viable bioprinted organ eye model. Results provided a baseline for complex, bioprinted organ models that will be used to evaluate agents of interest using established techniques. Formulation modifications have been synthesized and characterized for their elastic modulus and cell viability. The bioprinted models can be applied to a wide range of application, including assessing routes of entry for chemical and biological threats and as a platform for risk assessments with respiratory protection devices.

Keywords: Bioprinting, bioinks, toxicology, hydrogels, biomaterials, crosslink density

BLUF: Bioprinting with custom, in-house bioinks will allow for tunable properties and mission relevant models. This will advance downstream analysis previously unattainable.

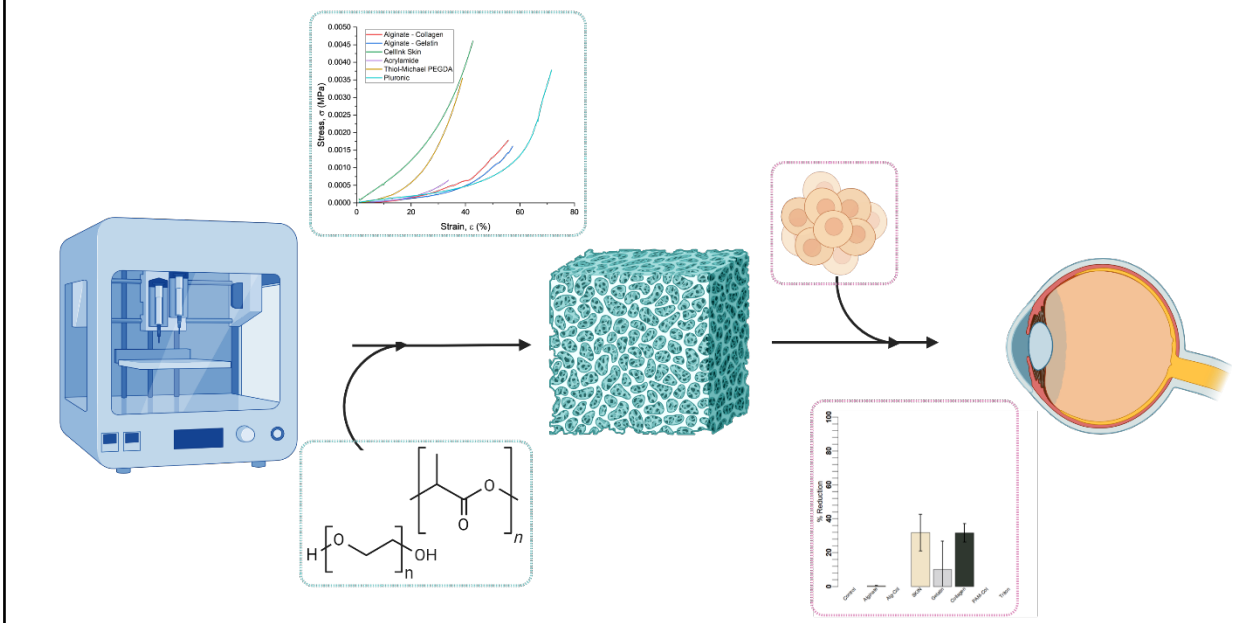

1. INTRODUCTION

1.1. Research problem:

The field of toxicology has advanced from solely relying on animal models to developing and utilizing *in vitro* (alternative to animal) models. Traditional animal models (*in vivo*) present significant limitations, including high monetary cost and intense labor necessary to keep operational models running.[1] In recent years, two-dimensional (2D) human cell models have been utilized for better physiological relevance for assessing human toxicity. These models have been used to help bridge the gap of better emulating the human body, but still lack the physical three-dimensional (3D) relevance necessary to better mimic organ function.[2] 3D *in vitro* platforms, or microphysiological systems, have emerged as a better alternative to *in vivo* and 2D *in vitro* models by providing better physiological relevance. In the past few years, the U.S. Army Combat Capabilities Development Command Chemical Biological Center has become a leader in the microphysiological systems space, specifically focusing on organ-on-a-chip (OOC) technology and organoids for toxicology purposes.[3] These microphysiological systems have been well-established for toxicity testing but lack the customizable aspect as OOC platforms are commercially based and organoids lack a biomaterial component. Recently, the Center has invested in bioprinting technology, which combines traditional additive manufacturing techniques with biological components to create customizable organ models, seen in Figure 1. Bioprinting allows the user to select the cells, biocompatible materials, and additives to develop 3D organ models for their specifications. There is a need for customizable materials that can be utilized for bioprinting, but also for toxicology assessment of the warfighter. The ability to adjust the model to account for factors such as variations in tissue thickness and the effect of aging in the future is important. Understanding the components in the biomaterials used and how to manipulate them is essential to accurately model these variabilities to effectively study experimental conditions, such as transport through tissue. When evaluating the existing and emerging threats of the warfighter, the eyes and the skin are organs of interest as they are focal points of exposure.

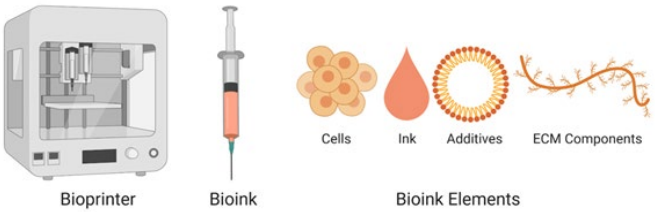

Figure 1. Essential components of bioprinting.[4]

1.2. Current state of the technology:

The field of bioprinting is relatively novel with significant progress in the last decade. All the current bioprinting work at U.S. Army Combat Capabilities Development Command Chemical Biological Center is reliant on commercially available materials, which are costly, and material formulations are kept as trade secret. This project has enabled the development of a pipeline for synthesizing in-house materials for bioprinting organ models relevant to toxicology assessment, ensuring the Center will be a government leader in this field.

1.3. Project objectives:

The primary objective for FY24 (year 1) was to bioprint a synthetic ocular model with a synthetic polymer and corneal epithelial cells. The main subtasks from this year's objective were:

- Formulating various hydrogels (completed in year one)
- Developing a method to assess cellular viability (completed in year one)
- Printing a synthetic hydrogel (in-progress)
- Incorporating corneal cells into printed gel (not started)

1.4. Exit criteria:

For the first objective in this project, criteria for success includes a printable structure and cellular viability. The bioprinted model must be able to maintain mechanical structure after the bioprinting process. Cellular viability must

be at least 70 % when cells are implemented on the bioprinted construct. Additionally, successful immunohistochemistry for cellular function is another success point for the bioprinted model.

- Milestone #1: Printability of Material
  - Go/No-Go: Can the in-house synthetic material extrude on the BIO X bioprinter and maintain structure after printing?
- Milestone #2: Biocompatibility of Material
  - Go/No-Go: Are cells from a human cell line at least 70 % viable on the printed synthetic material?
  - Go/No-Go: Are primary corneal epithelial cells at least 70 % viable on the printed synthetic material?

1.5. Hypothesis:

Customizable biocompatible polymer development for bioprinted skin and eye models would enable a physiologically relevant model amenable to more downstream testing methods.

2. YEAR 1 ACCOMPLISHMENTS

2.1. Summary of project progress:

The hydrogel formulation was developed through an iterative process, transitioning from an ultraviolet (UV) crosslinking chemistry to a thiol-Michael addition reaction, seen in Figure 2. While the original acrylamide synthesis provided controllable mesh sizes with known chemistries, the rate of polymerization is not as controllable as the thiol-Michael addition. This improves the printability of the hydrogel by controlling the rate of polymerization with pH and temperature and allows the gel to maintain its shape during the printing process. The increase in viscosity from this polymerization strategy is regulated by the number of thiol groups conjugated to the crosslinker. Modifying collagen to incorporate thiol groups, this enables dual functionality within a single component and reduces the overall number of components required.[6] By understanding and controlling the crosslinking density, the synthetic tissue models can better replicate varying tissue thicknesses from different regions of the body. A protocol to measure the elastic modulus and toughness of the gels was established using compression dynamic mechanical analysis (DMA). This enables a more accurate mimicry of native tissue properties and assesses the hydrogel's printability. The BIO X bioprinter was purchased and personnel were trained to use the system. The printability of initial thiol-Michael formulations was tested on the BIO X, yielding promising results. A cytotoxicity assay was developed to assess cytocompatibility of biomaterials that may be used for bioprinting organ models. Several natural, synthetic, and hybrid materials were tested to assess potential cellular viability of candidate formulations with primary human fibroblasts as a validation cell type and then with corneal epithelial cells (CECs). Additionally, CEC culture has been started and optimized, as ocular cells have not been utilized for *in vitro* toxicology at the center before.

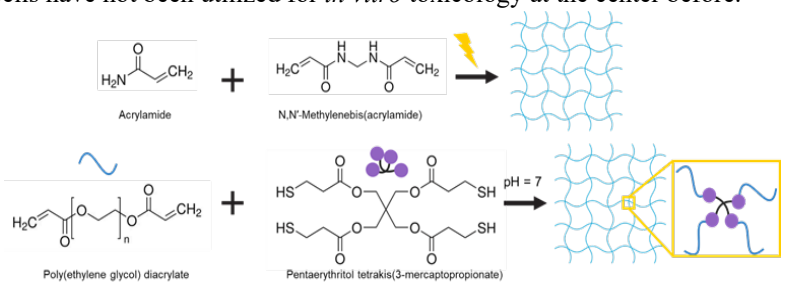

Figure 2. Reaction scheme of hydrogel formulations of a polyacrylamide system (top) and thiol-Michael addition for poly(ethylene glycol) (bottom).

2.2. Project challenges and lessons learned:

The project workflow begins with hydrogel synthesis, followed by gel characterization and cell viability testing, and then printability assessment, before finally incorporating cells into the printing process. This workflow was iterative, with each step depending on the others, leading to longer than expected timelines. There was some troubleshooting

and optimization with primary human corneal epithelial cell culture. Aspects such as seeding surface area, passage limits, and staining protocols were identified and finetuned for optimal culture (Figure 3).

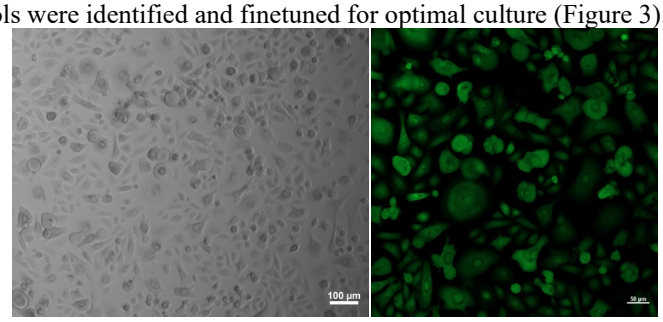

Figure 3. Primary corneal epithelial cells (P2) imaged in brightfield (left, scale bar: 100 µm) and with live/dead staining (right, scale bar: 50 µm). Cell maintenance and seeding has been optimized during FY24.

To streamline the process, the BIO X will be used solely to assess printability, while rheological analysis will be applied to better optimize printability before using the printer. Rheology and other core characterization techniques will be conducted with collaborators at the University of Delaware. Hydrogel formulation, characterization and bioprinting knowledge will also be leveraged. The hydrogel synthesis was shifted from a UV crosslinking system to a chemical crosslinking system to increase viscosity during printing. A methodology to assess mesh size of the gel and polymer volume fraction using PEGDA. For the remainder of year 1's objectives, commercially available bioprinting materials can be harnessed to ensure the development of a functional ocular model for assessing toxicity. Initially using other bioprinter systems was challenging to correlate methodology with the BIO X. The BIO X is currently located in surety lab spaces equipped for cell culture, so personnel access is limited to those who are in the Chemical Personnel Reliability Program (CPRP). Future lab access will be coordinated as team members have joined the CPRP. Another challenge encountered has been the lack of sourcing powdered collagen. The team has tried ordering from multiple vendors; however, this item has been backordered for over six months. Mitigations include using collagen in solution and obtaining the intended form via dialysis and lyophilization.

2.3. Data:

2.3.1 Compressive analysis

Compression DMA was utilized to evaluate elastic moduli of the materials. The Young's modulus was calculated from 2–5 % strain using Origin Pro graphing software. The yield stress was calculated by plotting the elastic modulus at a 2 % offset and the intersection between the two indicates the yield stress. All formulations in this study had significantly lower elastic moduli than literature values,[7] as seen in Figure 4a. This will be mitigated by increasing the crosslinking density of the formulation.[6]

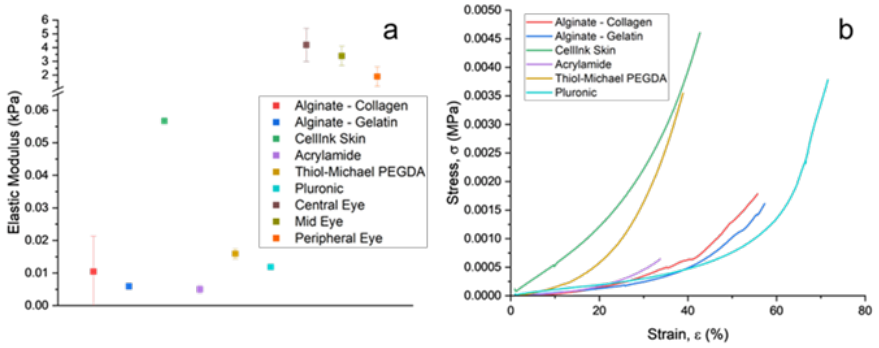

Figure 4. Compression dynamic mechanical analysis on formulations tested. In a) the elastic modulus of the samples compared to literature[7] (n = 1–4) and b) a representative curve for stress strain of the formulations tested.

2.3.2 Cellular viability

For assessing toxicity of various hydrogels and materials, both quantitative (alamarBlue® assay) and qualitative (live/dead imaging) measures were utilized. Cellular viability was assessed using primary human fibroblasts (P7) (Figure 5). Fibroblasts exhibited the highest attachment to gelatin and collagen, with no attachment to commercial

substrate, CELLINK Skin. This assay was repeated with CECs and the best viability was shown with collagen, gelatin, and CELLINK Skin.

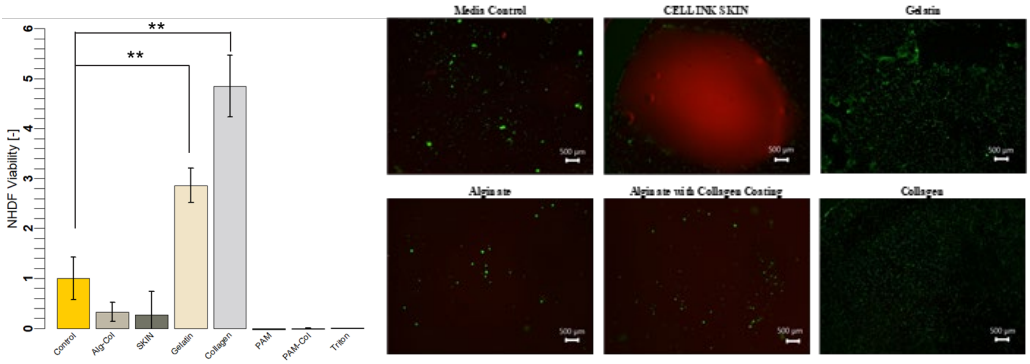

Figure 5. Cellular viability of primary fibroblasts (P7) assessed with alamarBlue® assay and normalized to samples of tissue culture plastic (left). Live/dead stained images with Calcein AM (Green)/Ethidium Bromide (Red) for the various materials tested for cell viability scale bars are 500 µm (right).

3. FUTURE DIRECTIONS

The first year of this project consisted of establishing a new bioprinter capability and a workflow of assessing cellular viability for bioprinting materials. The schedule was delayed due to the iterative process of hydrogel synthesis and characterization as well as limited access to necessary equipment. To account for these risks, expertise from academic collaborators will be utilized and commercially available materials can be used to complete the first year's objectives. As the field of bioprinting is novel, there are numerous stakeholders in the bioprinting community, including academia, industry, and other government partners. For future directions, external customers, such as the Defense Threat Reduction Agency, has shown interest in customizable organ models for assessing chemical and biological threats.

ACKNOWLEDGMENTS

Funding was provided by the U.S. Army via the In-house Laboratory Independent Research Program (PE 0601101A Project 91A) at the Combat Capabilities Development Command Chemical Biological Center.

REFERENCES

[1] Hartung T. Thoughts on limitations of animal models. *Parkinsonism Relat. Disord.* **2008**. *14* (2), pp S81–S83.
[2] Kapałczyńska, M.; Kolenda, T.; Przybyła, W.; Zajączkowska, M.; Teresiak, A.; Filas, V.; Ibbs, M.; Bliźniak, R.;
[3] Goralski T.D.P.; Jenkins C.C.; Angelini D.J.; Horsmon J.R.; Dhummakupt E.S.; Rizzo G.M.; Simmons, B.L.; Liem, A.T.; Roth, P.A.; Karavis, M.A.; Hill, J.M.; Sekowski, J.W.; Glover, K.P. A novel approach to interrogating the effects of chemical warfare agent exposure using organ-on-a-chip technology and multiomic analysis. PLoS ONE. **2023**. *18* (2), e0280883.
[4] Panda, S.; Hajra, S.; Mistewicz, K.; Nowacki, B.; In-Na, P.; Krushynska, A.; Mishra, Y.K.; Kim, H.J. A focused review on three-dimensional bioprinting technology for artificial organ fabrication. *Biomater. Sci*. **2022**. *10* (18), pp 5054–5080.
[5] Kapałczyńska, M.; Kolenda, T.; Przybyła, W.; Zajączkowska, M.; Teresiak, A.; Filas, V.; Ibbs, M.; Bliźniak, R.; Łuczewski, Ł.; Lamperska, K. 2D and 3D cell cultures - a comparison of different types of cancer cell cultures. *Arch. Med. Sci.* **2018**. *14* (4), pp 910–919.
[6] Holmes, R.; Yang, X.-B., Dunne, A.; Florea, L.; Wood, D.; Tronci, G. Thiol-ene photo-click collagen-PEG hydrogels: Impact of water-soluble photoinitiators on cell viability, gelation kinetics and rheological properties. *Polymers (Basel, Switz.)*. **2017**. *9* (6), p 226.
[7] Mikula, E.R.; Jester, J.V.; Juhasz, T. Measurement of an Elasticity Map in the Human Cornea. *Invest. Ophthalmol. Visual Sci*. **2016**. *57* (7), pp 3282–3286.

This page left intentionally blank

Cryptographically protected bioproduction strains

David C. Garcia[a,b], Casey B. Bernhards[a]*
[a]U.S. Army Combat Capabilities Development Command Chemical Biological Center, Research & Operations Directorate, 8198 Blackhawk Rd, Aberdeen Proving Ground, MD 21010
[b]Precise Systems, 22290 Exploration Dr, Lexington Park, MD 20653

ABSTRACT

Protecting intellectual property relevant to national interests is an ongoing challenge requiring forethought and redundant levels of security. As biological production continues to expand in relevance to the development of mission critical accelerants, chemical precursors, and fuels, our ability to safeguard these systems from espionage and theft will need to expand in kind. Biological production inherently relies on microbial bioproduction strains that can be stolen and regrown with easily duplicated methodologies and expertise, such that introducing safeguards to prevent the acquisition and culturing of these strains will be essential to maintaining control over crucial intellectual property. To this end, we propose the development of bioproduction organisms with lock and key growth phenotypes that can only be activated using non-canonical (i.e., unnatural) amino acids and orthogonal tRNA synthetase/tRNA pairs, which serve as the keys and locks, respectively.

Keywords: Biomanufacturing, bioproduction, biocontainment, genetic code expansion, non-canonical amino acids, directed evolution

1. INTRODUCTION

As the role of biological production strains continues to expand for domestic manufacturing, so too will their importance to supply chains crucial to national security needs. The ability to produce fuels, chemicals, and even building materials presents a novel opportunity to establish a biomanufacturing ecosystem with billions of dollars in economic impact.[1] However, while our ability to engineer new and bioproduction organisms has only continued to advance, our ability to protect those strains from espionage, misuse, and theft has severely lagged. The goal of this work is to begin addressing those challenges by taking advantage of the tools of synthetic biology to place barriers between strains of critical importance to Department of Defense missions and those that would misuse them.

Recoded strains are organisms engineered to be completely missing one of the triplet DNA sequences, known as codons, which code for the 20 canonical amino acids found across life.[2] Strains with the TAG stop codon completely removed from the genome, for instance, have effectively been used for various applications including preventing viral infections, integrating non-canonical amino acids (ncAAs) into proteins, and creating effective auxotrophies in *Escherichia coli*.[3–5] Auxotrophies specifically occur when the deleted codon in a recoded genome is placed back into an essential gene along with a tRNA synthetase/tRNA pair that adds an ncAA at that codon's new position. However, an alternative strategy can be followed wherein stop codons are strategically added without recoding. While this may cause deleterious effects to cell growth, it substantially eases the burden of genetic engineering while allowing for the creation of the lock and key auxotrophy. In both cases, growth of the strain is prevented when the specific ncAAs are not provided exogenously, as the cell cannot make ncAAs. *Vibrio natriegens* (*V. nat*) is a promising bacterial strain to expand these efforts due to its prominence as the fastest replicating lab strain, its relevance for industrial applications, and our ability to engineer large sections of its genome simultaneously.[6,7] *V. nat* functions both as a potentially critical biological tool and as a fertile ground from which to characterize the physiology of an organism with important implications as a biosecurity platform.

In this study, the mechanisms for creating *V. nat* strains capable of being secured with auxotrophic growth will be explored to understand the biological principles of bioproduction chassis with security in mind. This work will use a *V. nat* strain as a base to produce and elucidate the phenotypes of subsequent mutants with ncAA auxotrophies (Figure 1). These mutated strains will then be used to explore methodologies to more easily produce tRNA synthetase/tRNA pairs for specific ncAAs that can be used as models for strains that can only be grown in the presence of their respective ncAA.[8,9] Our aim is to demonstrate that we can understand how to engineer organisms relevant to

bioproduction efforts with bespoke security measures for both benchtop and pilot scale bioproduction studies. We anticipate this work will be foundational in the field of biosecurity and advance both our understanding of the fundamental principles dictating cellular growth in *V. nat* as well as the mechanisms by which we can modify *V. nat* towards productive functions.

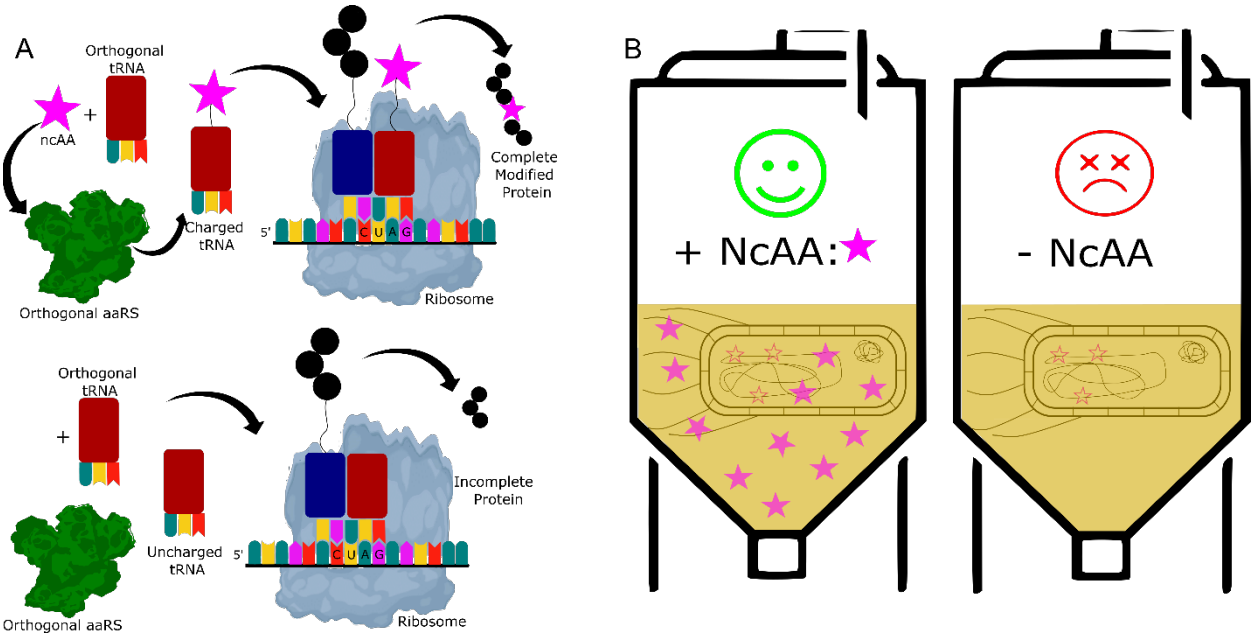

Figure 1. Overview of proposed strategy for securing bioproduction strains. (A) NcAAs (pink stars) (keys), are charged using tRNA synthetase (aaRS)/tRNA pairs (locks) and used as protein building blocks when the codon added by the researcher is present. (B) In the absence of the ncAA, an auxotrophy prevents proper cell growth as the codon added into the genome cannot add an amino acid and complete the protein. Stolen strains would fail to grow in the absence of the proper key, their ncAA.

2. METHODOLOGIES

2.1 Genome engineering

2.1.1 Strain growth

V. nat (ATCC 14048) was grown at 37 °C in LBv2 or LB3 media for liquid cultures and plates. LBv2 is LB-Miller medium supplemented with v2 salts (LB-Miller: 10 g/L tryptone, 5 g/L yeast extract, and 10 g/L NaCl; v2 salts: 204 mM NaCl, 4.2 mM KCl, and 23.14 mM $MgCl_2$). LB3 was made using LB-Miller supplemented with 2 % NaCl. Antibiotic stocks were used at the following final concentrations: carbenicillin: 25 µg/mL, kanamycin: 200 µg/mL, chloramphenicol: 2 µg/mL for plates and 4 µg/mL for liquid cultures. For long-term storage as glycerol stocks at -80 °C, cells were first washed in fresh LB before the addition of glycerol (~15–20 % w/v final). Strains used for genomically integrated superfolder green fluorescent protein (sfGFP) expression experiments were grown in LB3 media, optical density was measured at 600 nm (OD_{600}), and sfGFP expression was measured using excitation and emission wavelengths of 488 nm and 510 nm, respectively.

2.1.2 Assembly of NT-CRISPR plasmids and recombination selection

NT-CRISPR is a genome engineering method combining natural transformation and CRISPR-Cas9 counterselection for direct mutations, deletions, or additions to the genome of *V. nat*.[10] *V. nat* can naturally incorporate extracellular DNA into its genome by homologous recombination, termed Multiplex Genome Editing by Natural Transformation (MuGENT).[7] The recombination process is facilitated by the transformation of transfer DNA (tDNA) into the cells via chemical signal. *V. nat* genomic DNA was used to PCR amplify tDNA with necessary TAG stop codons directly incorporated into the primers. Genomic DNA was isolated using the Wizard® Genomic DNA Purification Kit

(Promega). Gibson assembly was used to anneal tDNA fragments containing TAG stop codons into a carrier plasmid, pST_140_LVL2 cam. *E. coli* cells were transformed with tDNA plasmids using a heat shock method, plated on LB agar medium containing chloramphenicol (25 µg/mL), and incubated at 37 °C overnight. PCR using the 5′ and 3′ ends of the left and right homology arms, respectively, was used to amplify the tDNA from the carrier plasmid. CRISPR-Cas9 expression was performed using guide RNAs directly assembled into plasmid NT4_Addgene 179335 using Golden Gate assembly. CRISPR-Cas9 counterselection mediated MuGENT was performed as previously described.[10] Briefly, precultures of *V. nat* were grown overnight at 30 °C in LBv2 medium supplemented with 4 µg/mL chloramphenicol and 100 µM isopropyl-β-D-1-thiogalactopyranoside (IPTG) to induce production of Tfox. Natural transformation was started by adding 3.5 µL of the precultures (OD_{600} of ~9–11) to 350 µL Instant Ocean® Sea Salt with 100 µM IPTG. A total of 10 ng of tDNA with homologous flanking DNA was then added, briefly vortexed, and incubated statically at 30 °C for 5 hours. CRISPR-Cas9 induction was started by addition of 1 mL of LBv2 medium containing 200 ng/mL anhydrotetracycline (aTc) to the MuGENT cultures. Following a 30 °C incubation for 1 hour with shaking at 250 rpm, 100 µL of the cells were plated on LBv2 agar plates with 2 µg/mL chloramphenicol and 200 ng/mL aTc.

2.2 Cell-free extract production and testing

2.2.1 NcAA cell-free extract production

Cells (Syn61Δ3(ev5)) were grown in 1 L of 2 × YTPG media (pH 7.2) in a 2.5 L Tunair shake flask and incubated at 34 °C and 220 rpm to an OD_{600} of 3.0. Cells were pelleted by centrifuging for 15 minutes at 5,000 × g and 4 °C, washed three times with cold S30 buffer (10 mM tris-acetate pH 8.2, 14 mM magnesium acetate, 60 mM potassium acetate, 2 mM dithiothreitol), and stored at -80 °C. The thawed cells were suspended in 0.8 mL of S30 buffer per 1 g of wet cell mass. The cells were then lysed by sonication, thawed, and suspended cells were transferred into 1.5 mL microcentrifuge tubes and placed in an ice-water bath to minimize heat damage during sonication. The cells were lysed using a Q125 Sonicator (Qsonica, Newtown, CT) with 3.175 mm diameter probe at frequency of 20 kHz and 50 % amplitude. For each 1.4 mL sample, the input energy during sonication was monitored and ceased at ~944 Joules. The lysate was then centrifuged once at 12,000 RCF at 4 °C for 10 minutes. A run-off reaction was performed by incubating at 37 °C and 250 rpm, followed by a second centrifugation (10,000 RCF at 4 °C for 10 minutes). The extract was then aliquoted and flash frozen.

2.2.2 Cell-free protein synthesis reactions

All cell-free protein synthesis reactions were performed using a pJL1 plasmid containing a T7-expressed sfGFP. All DNA was prepared using Qiagen miniprep kits. Cell-free protein synthesis reactions contained 30 % v/v lysate and PANOx-SP buffer, as described in detail previously.[13] Briefly, each 1,000 nL reaction was assembled using an Echo 525 Acoustic Liquid Handler (Beckman Coulter, Indianapolis, IN). Each reaction consisted of 300 nL of cell-free extract, 400 nL of PANOx-SP buffer, 50 nL DNA, and varying concentrations of magnesium, potassium, and water based on extract needs. The final reagent concentrations used in the PANOx-SP buffer are listed in Table 1.

Table 1. Energy mixture components for PANOx-SP base reactions.

Component	PANOx-SP Final Concentration	Component	PANOx-SP Final Concentration
Magnesium	12 mM	tRNA	170.6 µg/mL
Potassium glutamate	130 mM	20 Amino acids	2 mM
Ammonium glutamate	10 mM	PEP	33 mM
Magnesium acetate	3.7 mM	NAD	0.33 mM
Potassium acetate	6.2 mM	CoA	0.27 mM
Tris acetate	5.67 mM (pH 8.2)	Spermidine	1.5 mM
HEPES	7.5 mM (pH 7.4)	Putrescine	2 mM
ATP	1.2 mM	Oxalic acid	4 mM
GTP	0.85 mM	T7 RNA polymerase	100 µg/mL
CTP	0.85 mM	RNase inhibitor	1.2 U/µL
UTP	0.85 mM	DTT	0.5 mM
Folic acid	0.072 mM		

3. RESULTS

3.1 Introduction of TAG stop codons into genomically integrated *sfGFP*

3.1.1 Assembly of tDNA plasmid for introduction of TAG codons into genomically integrated sfGFP

To further understand incorporation ncAAs into *V. nat,* we acquired strains with genomically integrated sfGFP. The strategy below, as opposed to creating an increased burden on the cell and an incentive to remove the mutation or making the cell unviable, provides a fluorescent reporter to measure the effective use of an ncAA incorporation. The initial effort centered around the creation of tDNA constructs to recombineer the TAG codons into the sfGFP regions at amino acid position 150. The regions to be changed maintain all the same amino acids as the wild type but add a stop codon before the end of the protein (Figure 2). Using the methods described in Section 2.1.2, tDNA was successfully created and verified for four different regions (Figures 3 and 4). A total of five strains with sfGFP genes integrated into the genome were used for the following work, heretofore labeled *V. nat* sites 2, 4, 5, 6, and 7. The different sites indicate different regions of the genome of *V. nat* where the sfGFP genes were introduced along with an IPTG inducible promoter and constitutively expressed *lacI* gene. A successful recombination of the TAG stop codon into *V. nat* site 2 was produced for subsequent experiments testing ncAA-dependent expression of sfGFP.

Figure 2. Representative strategy for addition of TAG stop codon to genomically integrated sfGFP. Top: DNA with TAG codon added at amino acid position 150 to express sfGFP-150TAG. Middle: Wild type version of the genomically integrated sfGFP. Bottom: Zoomed in region of DNA showing the precise genetic change made because of the recombination.

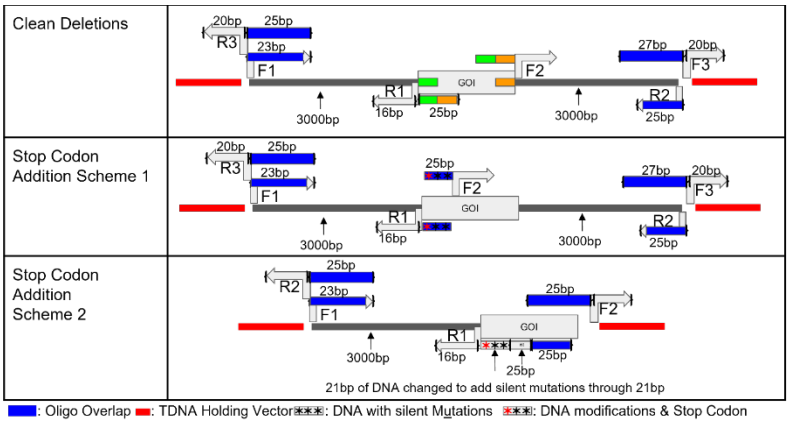

Figure 3. Schemes designed for creating tDNAs for genetic modifications of the *V. nat* genome. F1–3, forward primers; R1–3, reverse primers; GOI, gene of interest.

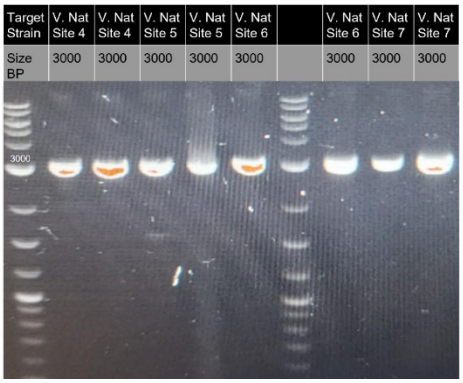

Figure 4. Gel image of PCR of individual homology arms of the tDNA. A purified PCR of the fully assembled tDNA, as per our previous strategy, was used as the template for the gel above. Data for *V. nat* site 2 not shown as the mutant was already made (Figure 2).

3.1.2 Expression of ncAA-dependent sfGFP

We first tested if the expression of the sfGFP protein off the genome was robust and effective. We found that even modest induction of the gene using 100 µM IPTG led to significant sfGFP expression compared to the baseline with no IPTG (Figure 5, Left). Following the introduction of a TAG stop codon into the sfGFP of the *V. nat* strain site 2, we tested if the addition of the TAG stop codon completely removed the expression of the protein in the absence of the ncAA and orthogonal tRNA synthetase and tRNA. We found that no amount of IPTG induced expression of the protein indicating that the TAG stop codon successfully stalled the expression of the sfGFP (Figure 5, Right).

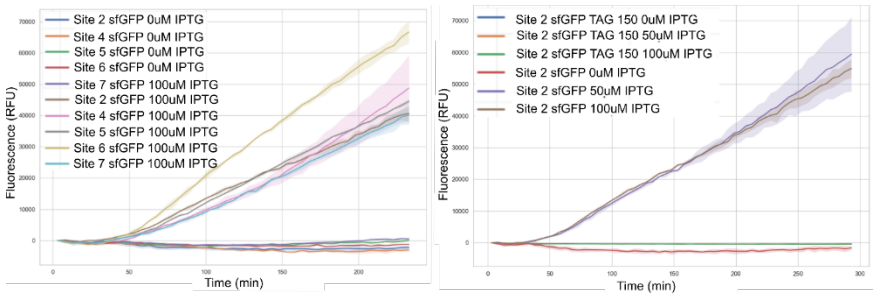

Figure 5. Fluorescence data for expression of sfGFP in *V. nat* strains. Left: Strains were grown with and without the inducing chemical (IPTG) at 37 °C. Right: *V. nat* with TAG codon incorporated at amino acid position 150 in sfGFP grown with increasing concentration of IPTG at 37 °C.

Following successfully showcasing the ability to halt sfGFP expression using an integrated TAG stop codon, we sought to rescue the mutation through the addition of orthogonal tRNA synthetase and tRNA that would introduce the ncAA Boc-Lys-OH into the protein. The tRNA synthetase MmPylRS(IPYE) and the tRNA pylT were cloned into a *V. nat*-specific plasmid pRAGE, but the MmPylRS was found to have a significant number of mutations following its transformation into *V. nat* (Figure 6). It is unclear if this occurred during cloning or following transformation. One potential cause could be the strain itself mutating the protein to remove a deleterious coding region. Regardless, this requires further investigation and mitigation, as a method of rescuing the TAG mutation by successfully adding Boc-Lys-OH into the ncAA-dependent sfGFP is required. One potential mitigation is the use of codon-optimized tRNA synthetases, as this could limit the burden on the cell when expressing the synthetase. Another option is to remove constitutive expression of the tRNA synthetase so that it becomes burdensome in a controllable manner.

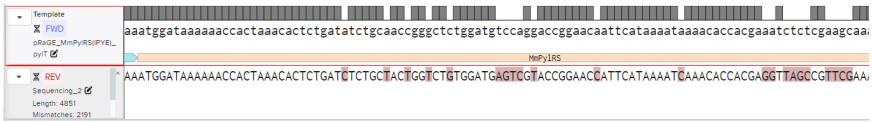

Figure 6. DNA sequence alignment of plasmid containing MmPylRS tRNA synthetase. Top: Expected DNA template sequence for plasmid containing a constitutively expressed tRNA synthetase and tRNA. Bottom: A significant number of mismatches (DNA bases highlighted in red) can be seen in the sequenced plasmid that was introduced into our *V. nat* strain containing the TAG stop codon at amino acid position 150.

3.2 Salt calibration and expression of sfGFP in Syn61Δ3(ev5)

Cell-free protein synthesis systems as a technology have dramatically expanded their use as fundamental and applied research tools. Their open nature and relative simplicity provide a flexible platform that lends itself to applications varying from biofuel to molecular machine production. Given the difficulties of successfully introducing auxotrophies, we decided to create a cell-free system that will allow us to test the use of orthogonal tRNA synthetases as well as serve as a platform bed for the introduction of ncAAs into specific proteins. This was accomplished using a cell-free system derived from a strain with three codons removed from the genome, specifically Syn61Δ3(ev5), a genomically recoded strain with no TCG, TCA, or TAG codons[14] (Figure 7, Left). The use of Syn61Δ3(ev5) allows for the multiplexing of not just orthogonal tRNA synthetases and tRNAs, but also the use of multiple ncAAs. In our initial work, we successfully grew the strain and detected expression of sfGFP under a T7 promoter. As with all cell-free extracts, magnesium and potassium titrations were needed to find the optimal reaction conditions for the extract (Figure 7, Right). While not all reagents were properly dispensed by our automated acoustic liquid handler, as noted by the absent expression at 80 mM potassium, we saw a trend wherein high potassium or high magnesium were ideal for the extract in the absence of the other salt. This is the first successful extract made with the Syn61Δ3(ev5) strain, and future improvements will seek to increase the expression of the basic reporter protein, sfGFP, and test the synthesis of proteins essential to cell survival for successful introduction of ncAAs.

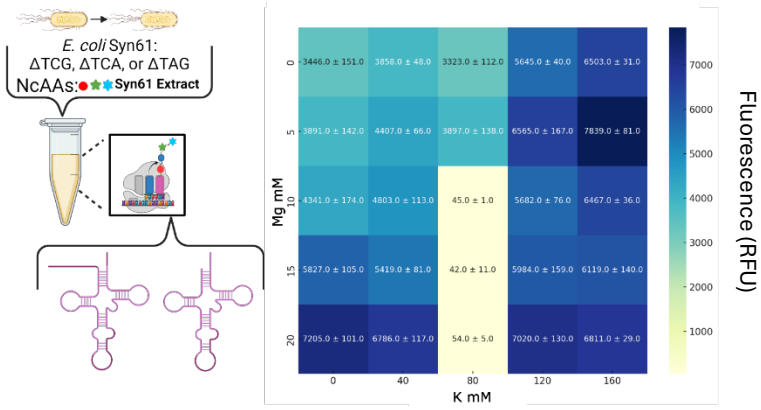

Figure 7. Preparation of a cell-free protein synthesis extract derived from Syn61Δ3(ev5) cells. Left: Extract made with Syn61Δ3(ev5) lacks the genetic machinery to incorporate amino acids into three separate codons. Right: Magnesium and potassium salt calibration performed to test activity of the extract and optimize their concentrations to maximize extract activity. Standard deviations are derived from quadruplicate experiments.

4. CONCLUSIONS

This report describes the progress towards producing cryptographically protected strains through the introduction of ncAA auxotrophies in the bioproduction strain *Vibrio natriegens*. In previous reports, we identified key proteins for the potential disruption of growth functions that would illicit a strong auxotrophic effect and performed modeling to find key amino acids within these proteins for strict auxotrophies. However, work to create lethal auxotrophies proved challenging. To further our efforts to more effectively test the necessary machinery to introduce deadly auxotrophies, we tested the expression of sfGFP from the genome with and without the presence of a TAG stop codon. Additionally, we are developing a method of introducing ncAAs into cell-free produced proteins to more effectively test the machinery required to introduce lethal auxotrophies, specifically orthogonal tRNA synthetases and tRNAs. While we have not yet been able to rescue the expression of sfGFP with orthogonal tRNA synthetases and tRNAs, these pieces have given us a set of tools toward testing orthogonal genetic code expansion machinery in *V. nat*. Together, these pieces will enable our ability to further test the genetic elements and ultimately produce and test cryptographic protection as a tool for securing biological productions strains relevant to national security and key supply chains.

ACKNOWLEDGMENTS

We thank Dr. Tanya Tschirhart from the U.S. Naval Research Laboratory for providing strains and valuable technical discussions, and Charles Sanfiorenzo from the California Institute of Technology for providing expertise on bioinformatic methods. We also thank Dr. B Thuronyi from Williams College and Dr. Matthew Lux from the U.S. Army Combat Capabilities Development Command Chemical Biological Center for helpful discussions in support of this work. Funding was provided by the U.S. Army via the In-house Laboratory Independent Research Program (PE 0601101A Project 91A) at the Combat Capabilities Development Command Chemical Biological Center.

REFERENCES

[1] Hodgson, A.; Maxon, M.E.; Alper, J. The U.S. Bioeconomy: Charting a Course for a Resilient and Competitive Future. *Ind. Biotechnol.* **2022**, *18* (3), pp 115–136.

[2] Lajoie, M.J.; Rovner, A.J.; Goodman, D.B.; Aerni, H.-R.; Haimovich, A.D.; Kuznetsov, G.; Mercer, J.A.; Wang, H.H.; Carr, P.A.; Mosberg, J.A.; Rohland, N.; Schultz, P.G.; Jacobson, J.M.; Rinehart, J.; Church, G.M.; Isaacs, F.J. Genomically Recoded Organisms Expand Biological Functions. *Science.* **2013**, *342* (6156), pp 357–360.

[3] Oza, J.P.; Aerni, H.R.; Pirman, N.L.; Barber, K.W.; ter Haar, C.M.; Rogulina, S.; Amrofell, M.B.; Isaacs, F.J.; Rinehart, J.; Jewett, M.C. Robust production of recombinant phosphoproteins using cell-free protein synthesis. *Nat. Commun*. **2015**, *6*, p 8168.
[4] Rovner, A.J.; Haimovich, A.D.; Katz, S.R.; Li, Z.; Grome, M.W.; Gassaway, B.M.; Amiram, M.; Patel, J.R.; Gallagher, R.R.; Rinehart, J.; Isaacs, F.J. Recoded organisms engineered to depend on synthetic amino acids. *Nature*. **2015**, *518* (7537), pp 89–93.
[5] Nyerges, A.; Vinke, S.; Flynn, R.; Owen, S.V.; Rand, E.A.; Budnik, B.; Keen, E.; Narasimhan, K.; Marchand, J.A.; Baas-Thomas, M.; Liu, M.; Chen, K.; Chiappino-Pepe, A.; Hu, F.; Baym, M.; Church, G.M. A swapped genetic code prevents viral infections and gene transfer. *Nature*. **2023**, *615* (7953), pp 720–727.
[6] Lee, H.H.; Ostrov, N.; Wong, B.G.; Gold, M.A.; Khalil, A.S.; Church, G.M. Functional genomics of the rapidly replicating bacterium Vibrio natriegens by CRISPRi. *Nat. Microbiol.* **2019**, *4* (7), pp 1105–1113.
[7] Dalia, T.N.; Hayes, C.A.; Stolyar, S.; Marx, C.J.; McKinlay, J.B.; Dalia, A.B. Multiplex Genome Editing by Natural Transformation (MuGENT) for Synthetic Biology in Vibrio natriegens. *ACS Synth. Biol*. **2017**, *6* (9), pp 1650–1655.
[8] Zhang, M.S.; Brunner, S.F.; Huguenin-Dezot, N.; Liang, A.D.; Schmied, W.H.; Rogerson, D.T.; Chin, J.W. Biosynthesis and genetic encoding of phosphothreonine through parallel selection and deep sequencing. *Nat. Methods.* **2017**, *14* (7), pp 729–736.
[9] Bryson, D.I.; Fan, C.; Guo, L.-T.; Miller, C.; Söll, D.; Liu, D.R. Continuous directed evolution of aminoacyl-tRNA synthetases. *Nat. Chem. Biol*. **2017**, *13* (12), pp 1253–1260.
[10] Stukenberg, D.; Hoff, J.; Faber, A.; Becker, A. NT-CRISPR, combining natural transformation and CRISPR-Cas9 counterselection for markerless and scarless genome editing in Vibrio natriegens. *Commun. Biol*. **2022**, *5* (1), p 265.
[11] Wannier, T.M.; Nyerges, A.; Kuchwara, H.M.; Czikkely, M.; Balogh, D.; Filsinger, G.T.; Borders, N.C.; Gregg, C.J.; Lajoie, M.J.; Rios, X.; Pál, C.; Church, G.M. Improved bacterial recombineering by parallelized protein discovery. *Proc. Natl. Acad. Sci. U.S.A.* **2020**, *117* (24), pp 13689–13698.
[12] Kelley, L.A.; Mezulis, S.; Yates, C.M.; Wass, M.N.; Sternberg, M.J.E. The Phyre2 web portal for protein modeling, prediction and analysis. *Nat. Protoc.* **2015**, *10* (6), pp 845–858.
[13] Kwon, Y.C.; Jewett, M. High-throughput preparation methods of crude extract for robust cell-free protein synthesis. *Nat Sci Rep.* **2015**, *5*, p 8663.
[14] Nyerges, A.; Vinke, S.; Flynn, R.; Owen, S.V.; Rand, E.A.; Budnik, B.; Keen, E.; Narasimhan, K.; Marchand, J.A.; Baas-Thomas, M.; Liu, M.; Chen, K.; Chiappino-Pepe, A.; Hu, F.; Baym, M.; Church, GM. A swapped genetic code prevents viral infections and gene transfer. *Nature.* **2023***, 615* (7953), pp 720–727.

Sporulated phage: towards the goal of "ready and waiting" phage decon

Courtney E. Love*, Anna M. Crumbley
U.S. Army Combat Capabilities Development Command Chemical Biological Center, Research & Operations Directorate, 8198 Blackhawk Rd, Aberdeen Proving Ground, MD 21010

ABSTRACT

Bacteriophage are viruses that infect and kill bacteria that have the capacity to serve as a non-corrosive decontamination or detection tool. Antibiotic resistance has opened the door for phage to be leveraged as a treatment for drug resistant bacterial infections or hospital infection mitigation of difficult to treat bacteria. Polyvalent phage, capable of targeting multiple bacterial strains, may have additional advantages for action against bacteria linked at the species, genus, or family level. Here, we seek to utilize computational and experimental techniques to identify phage that target multiple bacterial species and modify them for enhanced field applications including incorporating a colorimetric tag to improve visibility of a contaminated area. Additionally, we plan to enclose tagged bacteriophage inside natures armor: bacterial spores. Co-germinating bacteria and phage has been shown to protect the phage genomic material against common degradation risks such as heat, UV radiation, and pH fluctuations. Here, we report the groundwork development of computational and experimental methods that will inform phage-spore cocktail design for decontamination, as well as ways to utilize phage as a detection technique for alternate applications.

Keywords: *Bacillus anthracis*, bacteriophage, polyvalent, Basic Local Alignment Search Tool, surrogate, biosafety, biothreat

1. INTRODUCTION

Using phage as a decontamination tool could enable targeted biothreat elimination without materiel degradation. With the global rise of antibiotic resistance, bacteriophage are being increasingly explored as an alternative weapon in the antimicrobial arsenal, both for direct phage therapy and as targeted decontamination in hospitals.[1–3] One phage, Bacillus gamma (γ), is used by the Centers for Disease Control and Prevention as a confirmational diagnostic tool to distinguish between closely-related *Bacillus* species and pathogenic *B. anthracis*, although false positives have been reported.[4] Phage have also been developed at commercial scales and approved by the Food and Drug Administration as food safety control tools to address risks by *Listeria*, *Shigella*, and others in frozen foods.[5–7]

Classical experimental methods for phage isolation screening typically involve challenging solid and liquid environmental samples against laboratory strains in hope of a match.[8] Screening results are heavily influenced by the collection of available strains, the source of the environmental sample, collection-related events, and lab factors such as temperature, phage to bacteria inoculation ratios, and mutations to the laboratory strains over time. Finding phage active against biothreat strains adds a layer of complexity as high-risk strains are not available for screening in most laboratories. Thus, lower-risk surrogate strains are often utilized for phage isolation, e.g., *B. anthracis* str. Sterne as an alternative to *B. anthracis* str. Ames. This reduces risk; however, the differences between the strains may result in a phage active against a surrogate strain that does not interact with the biothreat strain.

Advances in DNA sequencing and computational biology methodologies speed up the search for phage.[8–10] Access to increasingly cost-effective sequencing technologies and advances in bioinformatics analysis tools and machine learning algorithms provide additional approaches for a phage investigator to use when investigating the potential to expect phage-microbe interactions, with multiple implementations accessible using command-line and web-based tools.[9] Alignment-based methods utilize shared virus-host sequences left by evolutionarily-distant previous phage infections as evidence of the potential for reinfection by similar phage, while alignment-free methods typically utilize codon-usage bias to identify phage with high likelihood of adapting to survival in a certain host microbes.[9] Machine learning methods use a variety of data inputs, often including both sequence alignment and codon bias data in their black-box approach.[8] Regardless of computational approach, experimental validation screens continue to remain the

field standard, with computational approaches requiring both initial experimental isolation and laboratory-based DNA sequencing.

Both experimental and computational screens can have bias during phage-host matching, often defining the strain used to isolate the phage as the "host," followed by testing the isolated phage against other strains.[9] Historically, phage were thought to only target one specific microbe, often at the species or strain level;[10] however, identification of polyvalent phage, defined as phage infecting multiple hosts at the genus level or higher, was reported as early as 1944.[11] Polyvalent phage are thought to target more broadly-available receptors on microbes, with a greater chance of experimental isolation and better likelihood of taking action against multiple microbes of interest, a powerful benefit when looking for biothreat targets using attenuated and surrogate microbes.

In addition to influence by laboratory and computational bias, phage stability during storage also plays a critical role in host screening and development of phage as a decontamination tool. Unstable phage are typically discarded and not subject to further study, even if their performance is otherwise promising.[12] As unprotected DNA particles, phage can be sensitive to UV light, temperature, and solution pH.[13] Regardless of storage method, phage viability and performance can vary over time.[14] Recent research also indicates that phage can be encapsulated for storage. Engineered encapsulation techniques, including the use of polymers, nanoparticles, liposomes, and calcium alginate have been reported to increase stability of phage.[12] Phage can also be encapsulated by sporulating microbes, where phage genomes are stored with the microbial genome during the spore formation process.[15] When a spore germinates, phage replicate, and, in the case of lysogenic phage, eventually break the host microbe's newly grown cell and are released into the environment. Spores represent a promising encapsulation method for phage stability as bacterial spores are stable against environmental extremes including pH, temperature, and UV radiation.[16]

Lastly, and the focus of this second year of our study, is the desire for a visual indicator of phage presence as a biological indicator or to differentiate between phages in a mixture. Research has reported the use of red fluorescent proteins to follow the path phage take through a mammal's body to inform the medical field on how the body's tissues circulate phages over time.[18] Phage cocktails utilize multiple phages to curtail bacterial variation or evolution;[19,20] however, the generation of these cocktails has historically been through trial-and-error: the most lethal combination is explored in further studies. If phage display technology can be incorporated into phage cocktail evaluation, we can understand how the cocktail components interact with each other and the host over time, enhancing the field's knowledge of phage kinetics and phage-host interactions.

2. MATERIALS AND METHODS

2.1 Plasmid design and assembly

Eight plasmid designs were created using the dual-expression *E. coli* and *Bacillus subtilis/megaterium* plasmids pCT5-1.8 and pCT5-2.0 (Addgene catalogue #119871 and catalogue #119872) as the vector backbones.[21] The sfGFP in these plasmids was exchanged with the head decoration protein of SP01 (NCBI),[17] APS-APS solubility linker (NCBI),[17] Fluorescent Protein (ATUM),[22] and 6x His Tag (NCBI),[17] as depicted in Figure 1.

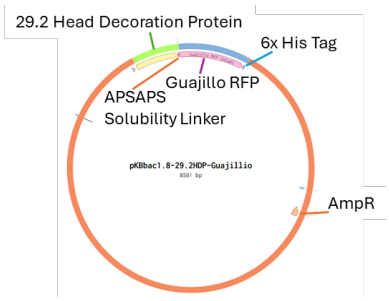

Figure 1. Plasmid design diagram of the pCT5-1.8 backbone with labeled insertions.

Four variations of the head decoration protein were designed as contingency plans from the source bacteriophage, SP01, published on NCBI: location 98292-98863 bp, 98349-98863 bp, 98368-98863 bp, and 98368-99030 bp. Primers were designed in Benchling and ordered from Integrated DNA Technologies.[23] Those primer sequences are listed and annotated in Table 1.

Table 1. Plasmid and insert sequence label and corresponding DNA sequence.

Sequence Title	DNA sequence
P1 - pCT5-bac1.8 Plasmid FWD-V3HDP	GTAGCACGGGTAGCCGTCACCACCACCACCACCACGTTAAAAGTCTCGTAAAGCGTTCTATCAATAACCC
P2 - pCT5-bac1.8 Plasmid REV-V3HDP	ATCTAATATTAATATCAGATCACAGGGAAAGGCATGTTTGTCCTCCTTATTAGTTAATCATAATACAAAC
P3 - NC_011421.1_CBCSequence FWD-V3HDP	GTTTGTATTATGATTAACTAATAAGGAGGACAAACATGCCTTTCCCTGTGATCTGATATTAATATTAGAT
P4 - NC_011421.1_CBCSequence REV-V3HDP	CTTGCTCACCATTGATGGTGCTGATGGTGCTAGAAGGATGGATATCTGCTGACAGAGTAATGACC
P5 - FPB-61-441 FWD_Edited-V3HDP	AGATATCCATCCTTCTAGCACCATCAGCACCATCAATGGTGAGCAAGGGTGAGGAAC
P6 - FPB-61-441 REV-V3HDP	ACGAGACTTTTAACGTGGTGGTGGTGGTGGTGACGGCTACCCGTGCTACCCG
P7 - pCT5-bac1.8 Plasmid REV-V3HDP	GCGTCTGCCTTCCTCGACCTTAGCATTAACATCATGTTTGTCCTCCTTATTAGTTAATCATAATACAAAC
P8 - NC_011421.1_CBCSequence FWD-V3HDP	GTTTGTATTATGATTAACTAATAAGGAGGACAAACATGATGTTAATGCTAAGGTCGAGGAAG
P9 - NC_011421.1_CBCSequence REV-V3HDP	TGCTCACCATTGATGGTGCTGATGGTGCTAGAAGGATGGATATCTGCTGACAGAGTAATGACC
P10 - FPB-61-441 REV-V3HDP	TACGAGACTTTTAACGTGGTGGTGGTGGTGGTGACGGCTACCCGTGCTACCCG
P11 - NC_011421.1_CBCSequence FWD-V3HDP29.2Test	GTTTGTATTATGATTAACTAATAAGGAGGACAAACATGATGTTAATGCTAAGGTCGAGGAAGG
P12 - NC_011421.1_CBCSequence REV-V3HDP29.2Test	TTGCTCACCATTGATGGTGCTGATGGTGCATGCCTATGTACCGTATTGCTGAACAAAGTACTTT
P13 - FPB-61-441 FWD-V3HDP29.2Test	ATACGGTACATAGGCATGCACCATCAGCACCATCAATGGTGAGCAAGGGTGAGGA
P14 - FPB-61-441 REV-V3HDP29.2Test	GTGGTGGTGGTGGTGACGGCTACCCGTGCTACCCGGACCAGCGGTACCATC
P15 - pCT5-bac1.8 Plasmid FWD-V3HDP	GTAGCACGGGTAGCCGTCACCACCACCACCACCACGTTAAAAGTCTCGTAAAGCGTTCTATCAATAA
P16 - pCT5-bac1.8 Plasmid REV-V3HDP	TTAGCATTAACATCATGAATATACTTAAATAACACGTTTGTCCTCCTTATTAGTTAATCATAATACAAAC
P17 - NC_011421.1_CBCSequence FWD-V3HDP	GTTTGTATTATGATTAACTAATAAGGAGGACAAACGTGTTATTTAAGTATATTCATGATGTTAATGCTAAGGT
P18 - NC_011421.1_CBCSequence REV-V3HDP	CTCACCATTGATGGTGCTGATGGTGCTAGAAGGATGGATATCTGCTGACAGAGTAATGACC
P19 - FPB-61-441 FWD-V3HDP	AGATATCCATCCTTCTAGCACCATCAGCACCATCAATGGTGAGCAAGGGTGAGG
P20 - 030624_GUAJILLO FWD PRIMER	AGCTGTACATGGAAGGCACGGT
P21 - 030624_GUAJILLO REV PRIMER	ACCATCGACCGCGGAATTGCTG
P22 - 030624 FWD BACKBONE PRIMER	ACTAGAGGAGCTCATGCCGGCG
P23 - 030624 REV BACKBONE PRIMER	AAATCTGGAGCCGGTGAGCGTG
P24 - GUAJILLO FWD PRIMER	ATGGTGAGCAAGGGTGAGG
P25 - BACKBONE REV PRIMER	GTTATTGATAGAACGCTTTACGAGACTTTTAAC
P26 - BACKBONE FWD DASHER	CTGGACACGTATCAGTAACACCACCACCACCACCAC
P27 - Backbone REV Dasher	TTCCGTCAATGCCGTCATTGATGGTGCTGATGGTGC
P28 - (Dasher GFP) FWD	GCACCATCAGCACCATCAATGACGGCATTGACGGAA
P29 - Cindy Lou CFP and Dasher GFP REV Primer	TAACGTGGTGGTGGTGGTGGTGTTACTGATACGTGTCCAGATCA
P30 - Backbone FWD Cindy Lou	CTGGACACGTATCAGTAACACCACCACCACCACCAC
P31 - Backbone REV Cindy Lou 98368	GATCTTCTTCGTAAACAATTTGGCACCAGACGACAT
P32 - (CindyLouCFP) FWD	GCACCATCAGCACCATCAATGTCGTCTGGTGCCAAA
APS - APS Solubility Linker	GCACCATCAGCACCATCA
Head Decoration Protein 98368-98863 bp	TAGAAGGATGGATATCTGCTGACAGAGTAATGACCAGCTTCTCTATCCAAATCCTTACGGTAATAGTGACGAATATCATCGCCTTCAGCTAATTGAGCCGCTACATTTTCATAGTATAGACGTGCTTTTTCAAACTCGTCTTCCTTAAAGACTTCATCTACTAGAGGACGAACCTCTACTTCCTCAGTTACCCAGATATGATCATCATAATCTCCAGTTGCTTCTGGGTTACGTCCACGTACTAAGACAGGTAACTTTTCTGGAACGTCATACGTAGGAACAGTTACTTTTTGACCCGGTTCTGCTGTCTTAGGATGCACAGGGATGTAAGGTACTTCCTCTTCCCCTACCTTGCACAACAGGATATGCAGTAACCCGATAAGATGTAGACGTTACTTCTTGAGTATCTGGGTCAGTTGTTTCTTCTTTATCAAGAGCGACTCGTACAACGTCAGATAGGTAGCGTCTGCCTTCCTCGACCTTAGCATTAACATCA

For plasmid pKB, the head decoration protein and APS-APS solubility linker were amplified by primers P8 and P9. The Guajillo RFP and His tag were amplified by Primers P5 and P10; the vector backbone and deletion of the sfGFP utilized P1 and P7.

For plasmid pKBu, primers P3 and P4 amplified the head decoration protein and APS-APS solubility linker; primers P5 and P6 amplified the RFP and His tag; and primers P1 and P2 amplified the backbone.

For plasmid pKBα, primers P11 and P12 amplified the head decoration protein and APS-APS linker; primers P13 and P14 amplified the RFP and His tag; and primers P1 and P7 amplified the backbone.

For plasmid pKBΔ, primers P17 and P18 amplified the head decoration protein and APS-APS linker; primers P19 and P7 amplified the RFP and His tag, and primers P15 and P16 amplified the backbone.

The amplified DNA was purified using Invitrogen E-Gel™ CloneWell™ II Agarose Gels (Catalog # G661818), then assembled using the established protocol in the New England Biolabs DNA HiFi Cloning Kit (Catalog # E5520S).

2.2 Plasmid transformation, culturing, and extraction

The assembled plasmids were chemically transformed into *E. coli* using the provided NEB 5-alpha or 10-beta competent *E. coli* cells following the kit protocol. Cell dilutions of 1x, 7x, and 70x SOC media were plated on ampicillin plates and grown overnight at 37 °C. Ten colonies were picked from the plates the following day to conduct colony PCR using the SuperFi Green PCR Master Mix standard protocol (Invitrogen Catalog # 12369010) and the primers flanking the insert of interest. Colonies positive for this insert were grown overnight shaking at 37 °C; each overnight culture was preserved in glycerol and a portion was used for a plasmid miniprep (QIAprep Spin Miniprep Kit, Qiagen Catalog # 27104).

2.3 Preparation of electrocompetent cells

Electrocompetent *Bacillus subtilis* cells were prepared as previously reported.[21] In short, *B. subtilis* cells from -80 °C glycerol stocks that were inoculated into 4 mL of LB medium and cultured at 37 °C overnight. The overnight culture was inoculated into 50 mL LB medium and cultured at 37 °C until the optical density at 600 nm was approximately 1.0. Cells were pelleted by centrifugation at 2500 x g for 10 minutes at 4 °C and washed with 40 mL of pre-chilled and filter-sterilized electroporation buffer consisting of 25 % PEG 6000 and 0.1 M sorbitol. Cells were harvested by centrifugation at 2500 x g for 1 hour at 4 °C. 1 mL of electroporation buffer was added to resuspend the cell pellet, which was aliquoted at 100 µL and stored at -80 °C until use.

2.4 Electroporation

To insert plasmids into the host *B. subtilis* cells, we followed the reported protocol: 100 µL of competent cell mixture was mixed with 5 µL of purified plasmid (50 ng/µL in H_2O), transferred to 0.1 cm gapped electroporation cuvette, and incubated on ice for 2 minutes. Cells were subjected to one electric pulse at 2.5 kV and immediately following, 0.45 mL of LB media was added, and cells were transferred to a sterile tube. Cells were recovered at 37 °C for 2–3 hours in a shaking incubator then spread onto pre-warmed LB agar plates containing carbenicillin and incubated at 37 °C until colonies appeared. Colonies were then screened for the insert using colony PCR with primers P20 and P21, P22 and P23, or P24 and P25 to confirm. Positive colonies were preserved in glycerol and used for phage infection.

2.5 Phage infection

Glycerol stocks of *B. subtilis* containing the engineered plasmid were mixed with 2 mL of LB broth and grown overnight with shaking at 37 °C. 100 µL of culture was mixed with 50, 100, or 200 µL of SP01 phage and 4 mL of molten TSA top agar and overlaid on carbenicillin plates. Plates were incubated overnight at 37 °C. Plaques were picked and mixed with 100 µL of SM buffer. Plaques were then confirmed by PCR to uptake the RFP using primers P20 and P21. Positive plaques were serially diluted; dilutions were overlaid on LB plates with log-phase *B. subtilis* in a 10:250 v:v ratio in 4 mL molten TSA top agar. This process was repeated for a total of three rounds of purification. After the third round of purification, isolated plaques were picked from plates and mixed with 100 µL of SM buffer. The RFP gene was confirmed primers P20 and P21, and positive phage samples were used for expansion and plate reader assays.

2.6 Phage expansion

Phages samples were expanded to 5 mL by mixing 50 µL of phage, 4 mL of LB media, and 1 mL of *Bacillus subtilis* culture and shook overnight at 37 °C. The samples were spun at 3000 x g for 20 minutes, filtered through a 0.22 µm filter, and confirmed for the fluorescent protein by both PCR and plate reader assay (described below). Down selected phage samples were then expanded to 30 mL utilizing 300 µL of phage, 25 mL of LB media, and 5 mL of *Bacillus subtilis* culture. Samples were then centrifuged, filtered, and tested on a plate reader.

2.7 Confirmation of presence of RFP and fluorescence in phage samples

Fluorescence plate reader assays were conducted to confirm the fluorescence of the phage samples. In each well of a sterile 96-well black bottom plate was a different variation of 100 µL total volume with or without 2 µL bacterial culture and with or without 5 µL phage sample. Control wells of the bacterial culture without phage addition was subtracted from each sample well. The experiment ran for approximately 24 hours, incubating at 37 °C with shaking, measuring fluorescence every 10 minutes at 554 nm excitation and 584 nm emission wavelengths. Triplicate wells were averaged and plotted as fluorescence intensity over the *B. subtilis* control over time.

2.8 Plasmid design and construction with Cindy Lou CFP and Dasher GFP

To incorporate additional fluorescent proteins into additional phages, we utilized the backbone pKB006 with the Cindy Lou CFP and Dasher GFP genes purchased from ATUM. We removed the Guajillo RFP segment of the plasmid (Primers P30 and P31) and replaced it with either the CFP (P29 and P32) or GFP (P28 and P29) as desired. The protocols described above for assembly, transformation into *E. coli*, plasmid extraction, transformation into *B. subtilis*, and phage infection and testing were replicated. The fluorescent proteins were detected on the plate reader at 400 nm excitation, 495 nm emission for CFP and 505 nm excitation, 525 nm emission for GFP.

2.9 Bacterial strains and bacteriophages

Bacterial strains and bacteriophages were obtained from American Type Culture Collection, Biodefense and Emerging Infections Research Resources Repository (BEI Resources), or from in-house strain collections. Strains, phage, and recommended media are detailed in Table 2. Incubation temperatures are 37 °C unless otherwise noted.

Table 2. Strains and phage evaluated experimentally in this work.

Bacterial strains				
Species	**Strain**	**Label**	**Source**	**Media**
Bacillus cereus	03BB102	BACI234	In-house/UCC	TSA/TSB
Bacillus cereus	D17	BACI262	In-house/UCC	TSA/TSB
Bacillus cereus	4342	BACI263	In-house/UCC	TSA/TSB
Bacillus cereus	E33L (Zebra killer)	BACI267	In-house/UCC	TSA/TSB
Bacillus thuringiensis	Al Hakam	BACI229	In-house/UCC	TSA/TSB
Bacillus pumilus	-	BEI NRS605	BEI	TSA/TSB (30 °C)
Bacillus subtilis	subsp. Subtilis (Ehrenberg)	ATCC 27370	ATCC	Enriched Nutrient Agar/Broth
Bacillus anthracis	Sterne	BACI012	In-house/UCC	TSA/TSB
Bacillus subtilis	NRS 231	BACI033	In-house/UCC	TSA/TSB
Bacillus anthracis	Delta Sterne	BACI056	In-house/UCC	TSA/TSB
Bacillus thuringiensis	Kurstaki	BACI204	In-house/UCC	TSA/TSB
Bacteriophage				
Phage	**Label**	**Known Host**	**Source**	**Media**
B. subtilis SP01	Phage 27370-B1	*B. subtilis* subsp. Subtilis (Ehrenberg)	ATCC	Enriched Nutrient Agar/Broth, Top agar 0.5%
B. subtilis PMB12	Phage HM-616	*B subtilis* subsp. Subtilis (Ehrenberg)	BEI	LB Lennox+10mM $MgSO_4$ Agar/Broth, Top agar 0.7% (30 °C)
B. anthracis Sterne Cornwall phage	BaSTCΦ	*B. anthracis* Sterne	USMA WP, C. Kovacs	TSA/TSB, Top agar 0.6%

2.10 Phage sequencing

DNA extractions of phage solutions were completed as previously described.[24] In short, phage solution was treated with DNase I and RNase A for 90 minutes at 37 °C without shaking; the enzymes were quenched using 0.5 M EDTA. Next, phage capsids were digested using Proteinase K incubated at 56 °C for 90 minutes. This solution proceeded through the Qiagen DNeasy blood and tissue kit protocol for animal blood or cells, starting at the step for adding AL buffer. DNA was double eluted at the last step. The bacteriophage library was prepared using Illumina's Nextera XT kit and the indexes were incorporated during 15 cycles of amplification. The quality of the library was determined by Qubit and Bioanalyzer analysis. The library was diluted to 13.3 pM and sequenced on a MiSeq using Illumina's MiSeq v2 Reagent Kit. SAMtools (v1.15.1) was used to generate the consensus sequence and coverage statistics.

3. RESULTS & DISCUSSION

3.1 Host screening of environmentally sourced phage

Bacteriophage isolated by our collaborator Dr. Christopher Kovacs at the United States Military Academy West Point, BaSTCΦ, was evaluated for polyvalent behavior using the methods described in our FY23 report and included here under the agar-based screening heading. The isolation host for this phage was *B. anthracis* Sterne, and Figure 2, below, shows plaque formation on three different species of *Bacillus*: *cereus, pumilus,* and *thuringiensis*. This phage was also screened against the remaining strains in Table 2, but this data is not shown here.

Figure 2. Plaque formation of BaSTCΦ phage on three different *Bacillus* species.

3.2 BaSTCΦ sequencing

To verify our sequence-overlap methodology from FY23, we extracted genomic DNA from a concentrated sample of BaSTCΦ and received sequencing results from Illumina sequencing and assembly performed in the BioDefense Branch at the U.S. Army Combat Capabilities Development Command Chemical Biological Center. This phage sample genomic sequence is 98.7 % similar to a previously published sequence for Bacillus phage "Nachito" (OP380492.1).[17]

3.3 Plasmid assembly

Once plasmids were assembled using the methods listed above and all components were confirmed to be present and in the desired order via plasmid PCR testing, three different versions of the plasmid were transformed into *B. subtilis* and used for phage infection. Those three versions are indicated in the table below as V1, V3, and V7.

Table 3. Plasmid builds, indicating the name, backbone, head decoration protein, and fluorescent protein for each version; also indicates which versions were used for phage infection, which phage it was combined with, and if fluorescence was confirmed.

	Name	Plasmid Backbone21	Head Decoration Protein (HDP)	XFP	Phage Infection?	Fluoresces?
V1	pKBu01-010	pCT5-bac1.8	98292-98863 bp	Guajillo (RFP)	Yes – SP01	Yes
V2	pKBΔ01-010	pCT5-bac1.8	98349-98863 bp	Guajillo (RFP)	--	--
V3	pKB01-010	pCT5-bac1.8	98368-98863 bp	Guajillo (RFP)	Yes – SP01	Yes
V4	pKPB01-010	pCT5-bac1.8	98368-99030 bp	Guajillo (RFP)	--	--
V5	pKBu011-020	pCT5-bac2.0	98292-98863 bp	Guajillo (RFP)	--	--
V6	pKBΔ011-020	pCT5-bac2.0	98349-98863 bp	Guajillo (RFP)	--	--
V7	pKB011-020	pCT5-bac2.0	98368-98863 bp	Guajillo (RFP)	Yes – SP01	Yes
V8	pKPB011-020	pCT5-bac2.0	98368-99030 bp	Guajillo (RFP)	--	--
V9	pKBγ001-010	pKB006	98368-98863 bp	Cindy Lou (CFP)	Yes – BaSTCΦ	Yes
V10	pKBδ001-010	pKB006	98368-98863 bp	Dasher (GFP)	Yes – HM-616	Yes

After the initial phage infection with the *B. subtilis* + plasmid on LB-carbenicillin plates, any resulting plaques were then passaged onto *B. subtilis* without the plasmid on LB plates to confirm that any resulting PCR screens would not pick up on plasmid from the bacterial lawn. A sample of the phage purification plates are shown in Figure 3, first displaying the small plaques on the first infection plate, a gel of the PCR products of plaque solution in the presence of RFP-flanking primers, then displaying how further passages result in more and larger plaques. This procedure was repeated for each passage until three had been completed and we had a plate-purified phage sample with PCR-confirmed fluorescent protein insert.

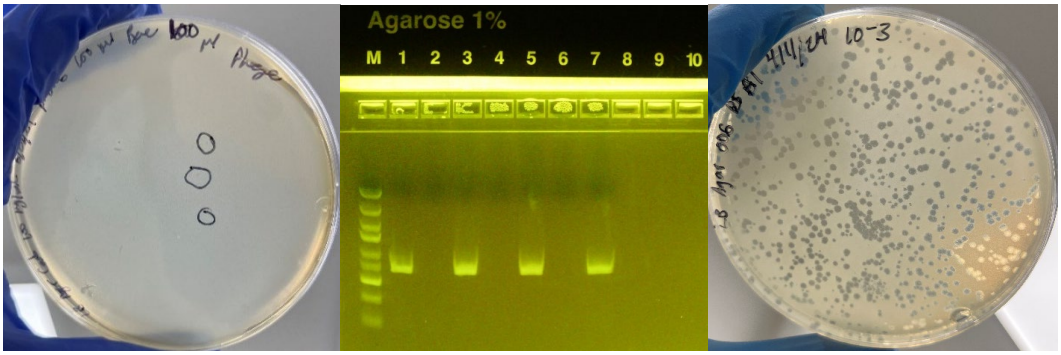

Figure 3. Left: Plaque formation on plasmid-containing *Bacillus subtilis* lawn; Center: gel image of PCR products indicating the presence of RFP in the plaque solution; Right: second passage of phages on *Bacillus subtilis* not containing the plasmid.

This process was repeated for two different colored proteins in the same plasmid backbone that had been successful for RFP, shown as V9 and V10 in Table 3. These plasmids were also PCR-verified for all insert pieces and transformed into *B. subtilis* for phage infection. BaSTCΦ was infected with the Cindy Lou CFP-containing plasmid and HM-616 was infected with the Dasher GFP-containing plasmid. A sample of the double-agar overlay assays, showing many uniform plaques, and PCR confirmation of the GFP and CFP genes in those plaques is given in Figure 4.

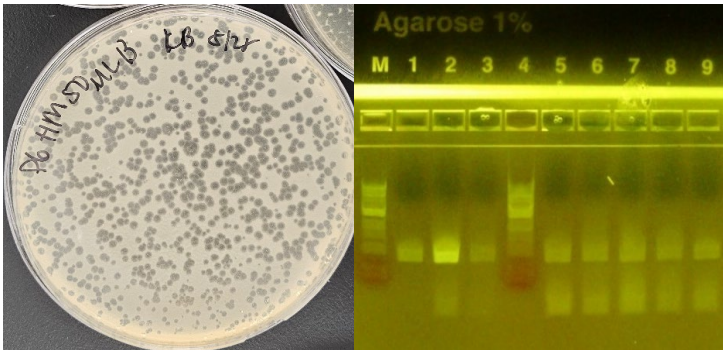

Figure 4. Left: Double-agar overlay plate of HM-616+GFP on LB agar with *B. subtilis*. Right: Gel image lanes 1–3 are GFP-flanking PCR products of different phage isolation samples; lanes 5–9 are CFP-flanking.

Phage samples that indicated the presence of RFP via PCR were utilized for plate reader assays to monitor the fluorescence signal overnight in the presence of *B. subtilis*. If these samples contained and expressed RFP, the fluorescence signal (excitation at 554 nm and emission at 584 nm) would increase over the course of the experiment. The graph in Figure 5 is the result of 13 triply purified phage samples in triplicate incubated with *B. subtilis* at 37 °C and probed for fluorescence every 10 minutes. The signals of the replicate wells were averaged, and the *B. subtilis* control signal was subtracted. Of these 13 samples, eight displayed higher fluorescence intensity than the culture background under these conditions. Samples that displayed lower fluorescence intensity result in a curve that dips below the x axis. The eight higher samples were retained for future experiments.

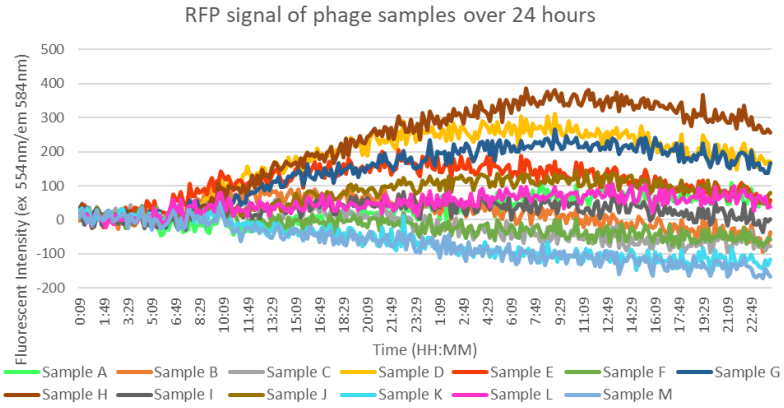

Figure 5. Plate reader data of fluorescence intensity measurements of RFP signal over time.

Once the HM-616 and BaSTCΦ phages were infected with GFP and CFP, respectively, and confirmed via PCR, we completed one plate reader experiment with all three phages in one well with *B. subtilis*. While this experiment was performed as the one in the previous figure, these phage samples are not normalized to the same PFU/mL count per well and the GFP and CFP phages have not been purified. These results, however, confirm that it is possible to track each of the excitation and emission wavelengths for the three fluorescent proteins simultaneously and observe a change over the course of 24 hours, as observed in Figure 6.

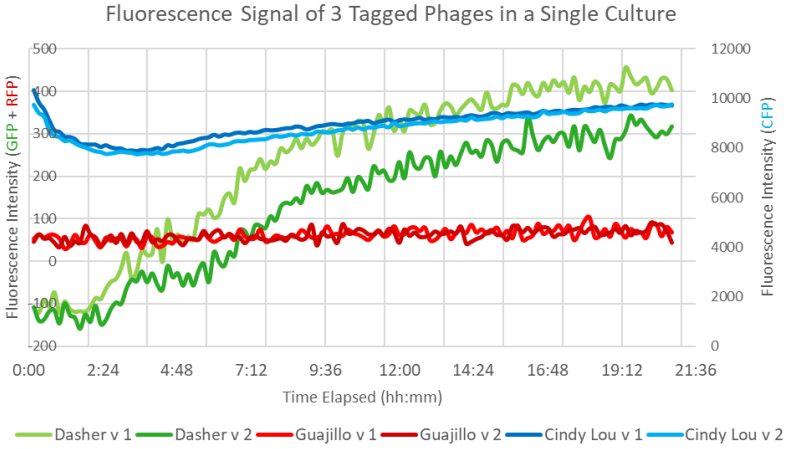

Figure 6. Plate reader data of fluorescence intensity measurements of RFP, CFP, and GFP signal over time.

3.4 Plasmid sequencing

Plasmids for each of the fluorescent protein builds were sequenced at Plasmidsaurus. The results were annotated with the same sequences as in the plasmid builds in Benchling. Figure 7 contains one RFP (A), GFP (B), and CFP (C) plasmid sample result. These plasmids do include each of the correct inserts: head decoration protein, linker, fluorescent protein, and His tag in the predicted location, see Table 3 for components of each version of the plasmid build. The fluorescent protein sequences are sourced from the manufacturer, ATUM. The AmpR sequence was present in the Addgene vector and is noted here as an internal control for sequencing since we had not made any modifications near that portion of the vector. The two custom portions of the vector are the APS-APS solubility linker and the head decoration protein sourced from the SP01 phage sequence, from 98368-98863 bp (Table 1).

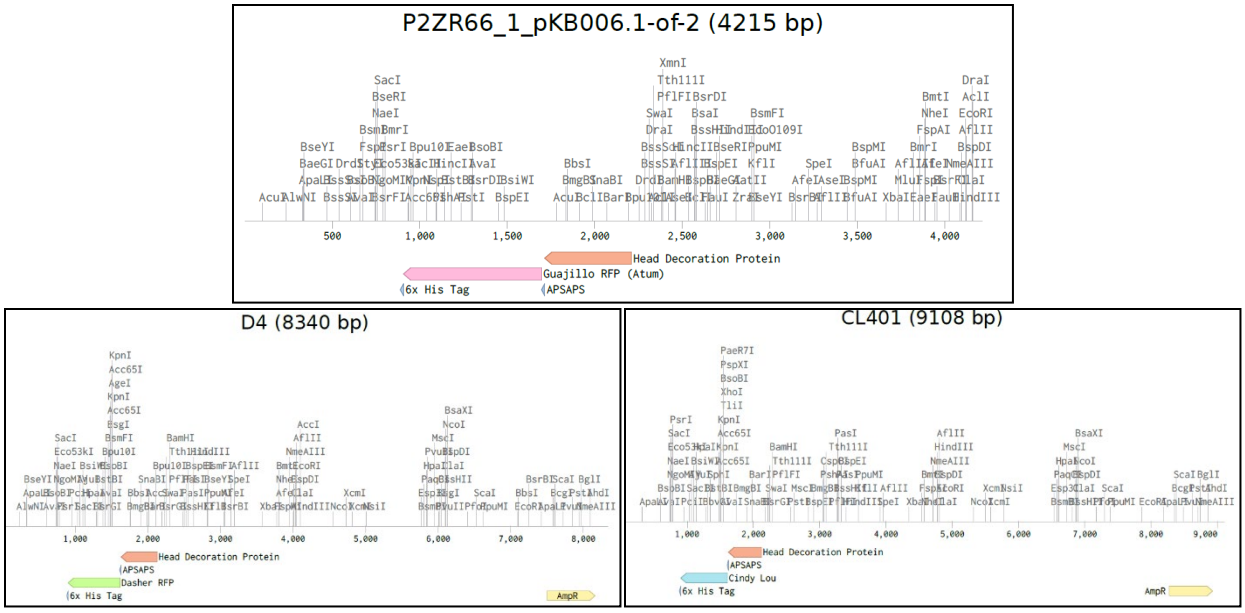

Figure 7. Plasmid sequencing diagram indicating the presence of desired insertions; Top: RFP plasmid, V3; Bottom Left: GFP plasmid, V10; Bottom Right: CFP plasmid, V9.

4. CONCLUSIONS

Here, we describe efforts to introduce fluorescent protein expression into a bacteriophage genome by fusing XFP to the Hoc protein on the phage capsid. When the bacteriophage infects a host cell with the engineered plasmid, the altered head decoration protein sequence can be mistaken for the native protein and produced upon DNA replication inside the cell. We describe the use of a singular head decoration protein for infection of different phages to gain this functionality with minimal plasmid redesign required. Through PCR and fluorescence screening of plaques, we have obtained three different phages with three different fluorescent proteins to track how phage ratios change over time. The synthetic biology and screening techniques have been successfully replicated in another institution. We will continue efforts to stabilize the tagged bacteriophage and utilize protein chromatography to purify our bacteriophage mixtures to complete our kinetics studies of phage population dynamics over time. The lag phase and burst size of these altered phages will inform the timing of our future sporulation objectives. Additionally, we will continue our sequence analysis of the phage genomes to determine if the gene insertions are reproducible across infections and if any alterations to our pathway are necessary.

ACKNOWLEDGMENTS

Funding was provided by the U.S. Army via the In-house Laboratory Independent Research Program (PE 0601101A Project 91A) at the Combat Capabilities Development Command Chemical Biological Center. Thank you to the Army Educational Outreach Program for sponsoring our intern, Katrina Bucci, for her laboratory and primer design support. Thank you to the United States Military Academy West Point Department of Chemistry & Life Science leadership for project support and continued collaboration. Thank you to Kelley Betts for continual graphic and poster design and report editing.

REFERENCES

[1] Crown, K. Bacteriophage Host-Range Expansion to Include Two Strains of Clostridium Sporogenes. Ph.D. Dissertation, University of New Mexico, Albuquerque, NM, **2014**. https://digitalrepository.unm.edu/biol_etds/20.

[2] Reuter, M.; Kruger, D.H. Approaches to optimize therapeutic bacteriophage and bacteriophage-derived products to combat bacterial infections. *Virus Genes*. **2020**, *56* (2), pp 136–149.
[3] Knoll, B.M.; Mylonakis, E. Antibacterial bioagents based on principles of bacteriophage biology: an overview. *Clin. Infect. Dis*. **2014**, *58* (4) pp 528–534.
[4] Kolton, C.B.; Podnecky, N.L.; Shadomy, S.V.; Gee, J.E.; Hoffmaster, A.R. Bacillus anthracis gamma phage lysis among soil bacteria: An update on test specificity. *BMC Res. Notes*. **2017**, *10* (1), pp 4–9.
[5] Kim, S.-H.; Adeyemi, D.E.; Park, M.-K. Characterization of a New and Efficient Polyvalent Phage Infecting *E. coli* O157:H7, *Salmonella* spp., and *Shigella sonnei*. *Microorganisms*. **2021**, *9* (10), p 2105.
[6] Kim, M.H.; Kragl, F.J.; Anderson, B.G. *The 1000 L Scale-up Production And Purification Of Bacteriophages Against Escherichia Coli O157: H7*; ECBC-TR-1441; U.S. Army Edgewood Chemical Biological Center: Aberdeen Proving Ground, MD, **2017**; UNCLASSIFIED Report.
[7] Kim, M.H.; Kragl, F.J.; Anderson, B.G. *Batch Modeling Of A Bacterial Host And Its Bacteriophage Population Dynamics Unclassified // For Official Use Only / Propin*. ECBC-TR-1425; U.S. Army Edgewood Chemical Biological Center: Aberdeen Proving Ground, MD, **2017**; UNCLASSIFIED Report.
[8] Versoza, C.J.; Pfeifer, S.P. Computational Prediction of Bacteriophage Host Ranges. *Microorganisms*. **2022**, *10* (1), p 149.
[9] Andrade-Martínez, J.S.; Camelo Valera, L.C.; Chica Cárdenas, L.A.; Forero-Junco, L.; López-Leal, G.; Moreno-Gallego, J.L.; Rangel-Pineros, G.; Reyes, A. Computational Tools for the Analysis of Uncultivated Phage Genomes. *Microbiol. Mol. Biol. Rev*. **2022**, *86* (2).
[10] Boeckaerts, D.; Stock, M.; Criel, B.; Gerstmans, H.; De Baets, B.; Briers, Y. Predicting bacteriophage hosts based on sequences of annotated receptor-binding proteins. *Sci. Rep.* **2021**, *11*, pp 1–14.
[11] Fouts, D.E.; Rasko, D.A.; Cer, R.Z.; Jiang, L.; Fedorova, N.B.; Shvartsbeyn, A.; Vamathevan, J.J.; Tallon, L.; Althoff, R.; Arbogast, T.S.; Fadrosh, D.W.; Read, T.D.; Gill, S.R. Sequencing *Bacillus anthracis* Typing Phages Gamma and Cherry Reveals a Common Ancestry. *J. Bacteriol*. **2006**, *188* (9), pp 3402–3408.
[12] Yu, P. Polyvalent Bacteriophages: Isolation, Modification, and Applications in Environmental Systems. Ph. D. Dissertation, Rice University, Houston, TX, **2017**. https://scholarship.rice.edu/handle/1911/105568.
[13] Alonzo, L.F.; Jain, P.; Hinkley, T.; Clute-Reinig, N.; Garing, S.; Spencer, E.; Dinh, V.T.T.; Bell, D.; Nugen, S.; Nichols, K.P., Le Ny, A.-L.M. Rapid, sensitive, and low-cost detection of *Escherichia coli* bacteria in contaminated water samples using a phage-based assay. *Sci. Rep*. **2022**, *12*, pp 1–11.
[14] Schade, A.L.; Caroline, L. The Preparation of a Polyvalent Dysentery Bacteriophage in a Dry and Stable Form. *J. Bacteriol.* **1944**, *46* (5) pp 243–251.
[15] Gabiatti, N.; Yu, P.; Mathieu, J.; Lu, G.W.; Wang, X.; Zhang, H.; Soares, H.M.; Alvarez, P.J.J. Bacterial Endospores as Phage Genome Carriers and Protective Shells. *Appl. Environ. Microbiol.* **2018**, *84* (18), pp 1–12.
[16] Riesenman, P.J.; Nicholson, W.L. Role of the Spore Coat Layers in *Bacillus subtilis* Spore Resistance to Hydrogen Peroxide, Artificial UV-C, UV-B, and Solar UV Radiation. *Appl. Environ. Microbiol.* **2000**, *66* (2), pp 620–626.
[17] *National Center for Biotechnology Information (NCBI).* https://www.ncbi.nlm.nih.gov/ (accessed 22 November 2023).
[18] Kaźmierczak, Z.; Majewska, J.; Milczarek, M.; Owczarek, B.; Dąbrowska, K. Circulation of Fluorescently Labelled Phage in a Murine Model. *Viruses.* **2021**, *13*, p 297.
[19] Yoo, S.; Lee, K.; Kim, N.; Vu, T.N.; Abadie, R. Yong, D. Designing phage cocktails to combat the emergence of bacteriophage-resistant mutants in multidrug-resistant Klebsiella pneumoniae. *Microbiol. Spectrum.* **2023**, *12* (1), e0125823.
[20] Ling, C.; Jiqiang, F.; Tingwei, Y.; Quan, L; Shengjian, Y.; Haoran, Z.; Jinfang, Y.; Deng, D.; Shuqiang, H.; Yingfei, M. Isolation and Characterization of Specific Phages to Prepare a Cocktail Preventing Vibrio sp. Va-F3 Infections in Shrimp (Litopenaeus vannamei). *Front. Microbiol.* **2019**, *10* (15), p1467205.
[21] Seo, S.O.; Schmidt-Dannert, C. Development of a synthetic cumate-inducible gene expression system for Bacillus. *Appl. Microbiol. Biotechnol.* **2019**, *103*, pp 303–313.
[22] Protein Paintbox, *ATUM*. https://www.atum.bio/protein-paintbox/ (accessed 25 September 2024).
[23] Custom Primers, *Integrated DNA Technologies (IDT)* https://www.idtdna.com/pages/products/qpcr-and-pcr/custom-primers (accessed 25 September 2024).
[24] Jakŏciūné, D.; Moodley, A. A Rapid Bacteriophage DNA Extraction Method. *Methods Protoc.* **2018**, *1* (3), p 27.

DNA origami for the modification of nerve agent degrading enzymes

Steven P. Harvey[a]*, Grant Knappe[b], Jeffrey Gorman[b], Mark Bathe[b]
[a]U.S. Army Combat Capabilities Development Command Chemical Biological Center, Research & Operations Directorate, 8198 Blackhawk Rd, Aberdeen Proving Ground, MD 21010
[b]Massachusetts Institute of Technology, Bathe Nanolab
77 Massachusetts Ave, Building 16, Room 223, Cambridge, MA 02139

ABSTRACT

Chemical warfare agents can be broken down in a multitude of ways, including through enzyme-mediated degradation. However, enzymes are subject to several limitations including stabilization and lagging catalytic rates. To overcome these limitations and improve catalytic efficiency, we sought to incorporate DNA origami into enzyme-mediate chemical degradation, specifically by conjugating the phosphotriesterase enzyme to a DNA icosahedron structure. In this study, two different chemical approaches were utilized to yield active enzymes with varying reductions in activity. In addition, we were also able to attach polyethylene glycol to the resulting nanostructure and utilize its performance in similar assays.

Keywords: DNA origami, enzymes, conjugation chemistry, chemical nerve agent, catalysis

BLUF: DNA origami can be used to stabilize and group together active enzymes. In this study, DNA origami will be used to stabilize and link together phosphodiesterase enzymes in a proof-of-concept study to demonstrate how DNA origami can improve decontamination in a controlled laboratory environment.

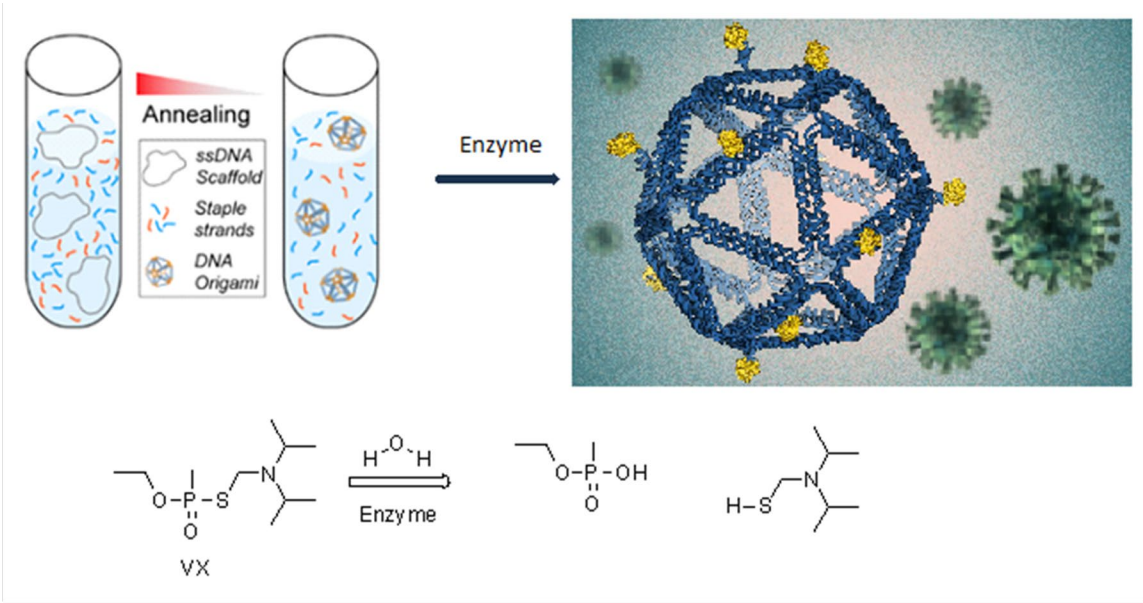

1. INTRODUCTION

1.1 Research problem:

Previously, enzyme mutants have been constructed that yield increased activity against nerve agents, in particular V-series agents. Specifically, reversed enzyme stereospecificity has been shown to increase favor activity against more toxic chemical agent enantiomers.[1] There have also been correlative improvements in agent activity with structurally-related simulants.[1] DNA origami offers a complementary approach which, if successful, could offer a means to improve the catalytic activity of multiple enzymes with activities relevant to the Army's mission. This work is consistent with the U.S. Army Combat Capabilities Development Command Chemical Biological Center's mission to "provide innovative chemical, biological, radiological, nuclear and explosive (CBRNE) defense capabilities to enable the Joint Warfighters' dominance on the battlefield and interagency defense of the homeland."

1.2 Current state of the technology:

DNA origami has several areas of potential utility. With respect to nanofabrication, DNA origami enables 10^{12} products of a single reaction to be produced in a short period of time. DNA origami can also improve catalysis by tethering together multiple components of an enzyme cascade to minimize diffusion of the intermediary products and can be utilized in the non-covalent Watson-Crick base pairing to create a molecular machine with moving parts.[1–3] Typically, origami starts with a circular ssDNA strand known as scaffold DNA, which is "stapled" at strategic points with complementary ssDNA which creates the basic nanostructure for the building blocks for many different structures.[4] In the field of chemical defense, a library of enzyme mutants that catalyze different chemical nerve agents are built and evaluated to determine the best combination of mutations and stabilization strategy. DNA origami offers the potential to further modify and possibly improve these and other enzymes of significance to the Army's biomanufacturing initiative.

1.3 Project objectives:

In the first year of this project, an icosahedral DNA structure was conjugated to at least one organophosphorus (OP)-catalyzing enzyme without destroying the enzyme's activity. In year two, nanopoarticles will be conjugated with polyethylene glycol and/or polylysine along the DNA structure to protect against DNAase degradation. In the third and final year of work, multiple, orthogonal groups of enzymes will be attached to the DNA nanoparticles to increase the range of activity. The accomplishments achieved in the first year of this effort include the identification of two separate chemistries for conjugation (azide and tetrazine reactions), both of which yielded active, conjugated phosphotriesterase enzymes. The tetrazine reaction was also used to attach polyethylene glycol to the nanoparticle.

1.4 Exit criteria:

The primary go/no go point in year one was the successful conjugation of DNA to an enzyme that retains activity which was successfully met. We are confident we can broaden the utility of this technology from the early success of this project moving forward. Most importantly, going forward it will be essential to successfully stabilize the structure and to attach multiple enzymes for a broad range of activity.

1.5 Hypothesis:

We hypothesize the application of DNA origami to OP-hydrolyzing enzymes will stabilize and/or activate those enzymes conjugated to the origami structure and potentially alter their stereospecificity.

2. YEAR 1 ACCOMPLISHMENTS

2.1 Summary of project progress:

A DNA icosahedron structure has successfully been generated attached to phosphotriesterase enzymes which retain activity against VX and GB. The resulting nanoparticles were also attached to polyethylene glycol to improve stabilization (stabilization has not yet been tested). Increased stabilization is an important step in enabling additional decontamination capabilities and increasing the shelf life of existing capabilities.

2.2 Project challenges and lessons learned:

Through year one of funding, we have not encountered any significant risks though we were initially concerned that the possible conjugation chemistries may inactivate the enzyme. However, the three reactions that have been conducted yielded two active PTE enzymes, with at least one enzyme being capable of attachment of polyethylene glycol to the nanoparticle.

2.3 Data:

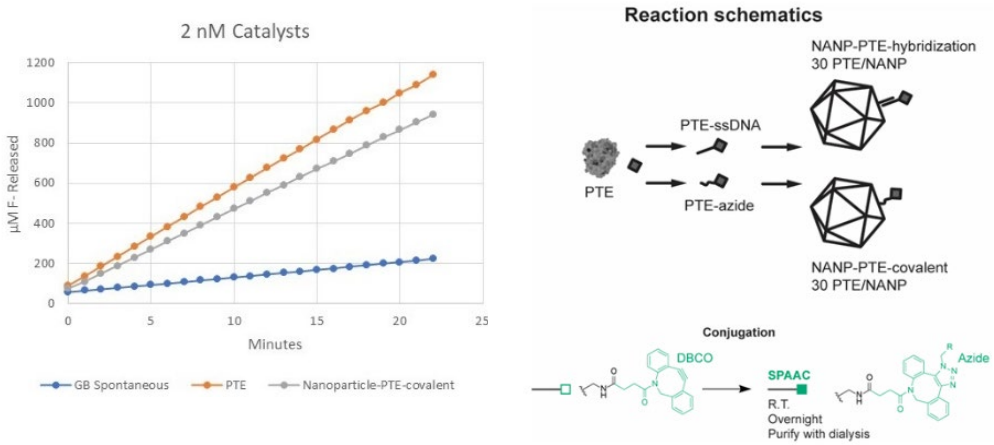

Figure 1. Reaction schematics of ssDNA and azide chemistries used to conjugate PTE to icosahedral DNA structure.

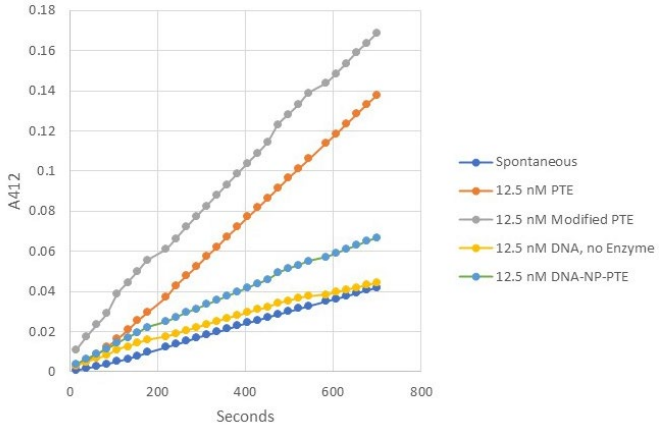

Figure 2. VX activity of tetrazine conjugated PTE with attached DNA and polyethylene glycol compared to relevant controls.

3. FUTURE DIRECTIONS

Looking to year two of the project, we plan to evaluate the azide and tetrazine chemistry to attach DNA to the organophosphorus acid anhydrolase. We will also conduct thermal stability studies on the conjugated enzymes and compare their relative stability to native enzymes. We also plan to incorporate the enzymes into the interior of the icosahedron for protection and possible effects on activity. Because we now have positive conjugation/activity data, we plan to seek out other possible stakeholders that may be interested in this technology including the Army's biomanufacturing initiative.

ACKNOWLEDGMENTS

Funding was provided by the U.S. Army via the In-house Laboratory Independent Research Program (PE 0601101A Project 91A) at the Combat Capabilities Development Command Chemical Biological Center. G.A.K., J.G. and M.B. were also supported by MIT core center grants (P-30-ES002109, NIEHS; P30-CA14051, NCI) and G.A.K. was additionally supported by the National Science Foundation under a Graduate Research Fellowship 4000189657.

REFERENCES

[1] Wamhoff, E-C.; Ronsard, L.; Feldman, J.; Knappe, G.A.; Hauser, B.M.; Romanov, A.; Case, J.B.; Sanapala, S.; Lam, E.C.; St. Denis, K.J.; Boucau, J.; Barczak, A.K.; Balazs, A.B.; Schmidt, A.G.; Lingwood, D.; Bathe, M. Enhancing antibody responses by multivalent antigen display on thymus-independent DNA origami scaffolds. *Nat. Commun*. **2024**, *15* (1), p 795.

[2] Chen, C.; Luo, X.; Kaplan, A.E.K.; Bawendi, M.G.; Macfarlane, R.J.; Bathe, M. Ultrafast dense DNA functionalization of quantum dots and rods for scalable 2D array fabrication with nanoscale precision. *Sci. Adv.* **2023**, *9* (32), eadh8508.

[3] Hart, S.M.; Gorman, J.; Bathe, M.; Schlau-Cohen, G.S. Engineering Exciton Dynamics with Synthetic DNA Scaffolds. *Acc. Chem. Res.* **2023**, 56 (15), p 2051.

[4] Falkovich, R.; Danielson, E.W.; Perez de Arce, K.; Wamhoff, E-C.; Strother, J.; Lapteva, A.P.; Sheng, M.; Cottrell, J.R.; Bathe, M. A synaptic molecular dependency network in knockdown of autism- and schizophrenia-associated genes revealed by multiplexed imaging. *Cell Rep.* **2023**, *42* (5), p 112430.


CBAMMS
PROJECTS

Influence of atmosphere on the reaction properties of Al/Zr/TiO_2 thermites

Steven W. Dean[a], Amee L. Polk[b]*, Dakota G. Scott[a], Michael R. Flickinger[c,d], Jill B. Harland[b]
[a]U.S. Army Combat Capabilities Development Command Army Research Laboratory, Army Research Directorate, 459 Mulberry Point Dr, Aberdeen Proving Ground, MD 21005
[b]U.S. Army Combat Capabilities Development Command Chemical Biological Center, Research & Operations Directorate, 8198 Blackhawk Rd, Aberdeen Proving Ground, MD 21010
[c]Department of Materials Science and Engineering, Johns Hopkins University, 3400 North Charles St, Baltimore, MD 21218
[d]Hopkins Extreme Materials Institute, Johns Hopkins University, 3400 North Charles Street, Baltimore, MD 21218

ABSTRACT

We investigated the influence of different atmospheres on the reaction of a low-gas generating, non-expanding thermite formulation composed of ball-milled Al:Zr fuel and TiO_2 (anatase) oxide powders combined in a stoichiometric ratio. These thermite materials have applications as heat sources in confined geometries where gas generation and sample expansion would be detrimental. We measured burn rates, reaction temperatures, and reaction products of uniaxially compacted samples laser ignited in air, vacuum, Ar, and N_2. Samples in air burned close to the adiabatic reaction temperature, while vacuum, Ar, and N_2 atmospheres resulted in lower temperatures. Ar samples quenched upon removal of the laser energy. Air, vacuum, and N_2 samples all propagated at approximately 2.2 mm/s. A two-stage reaction front was observed in both air and N_2 samples, while only a single reaction front was seen in the N_2 samples. All atmospheres resulted in no expansion of the compact during reaction. Al and Zr oxides were detected in all samples, with crystalline phases of the nitrides of Zr and Ti also recorded for samples ignited in N_2.

Keywords: Thermite, intermetallic, planetary mill, titanium dioxide, environmental chamber

1. INTRODUCTION

Thermites are a class of self-propagating, high-temperature synthesis reactions, characterized by the oxidation-reduction of a metal fuel and an oxide. Many reactions belong to this set, with the most widely recognized and commercially used being that of Al and oxides of iron.[1,2] While this composition has been extensively used in railroad welding for the last century, additional applications for thermite reactions have come forth, including pyrotechnic delays, propulsion, disablement, chemical and biological warfare agent decontamination, plug and abandonment of oil wells, heating, and enhanced energetic formulations.[3–7] This wide variety of applications leads to a requirement for intelligent design of thermite formulations to best meet each specific need.

A common focus has been producing thermites capable of high volumetric gas generation to increase pressure within a system, by using oxides such as CuO and leveraging their reaction products.[8] There are a set of applications that require just the opposite, such as heating within a sealed vessel or minimization of visual signatures due to gas/spark production. Previous work explored a set of formulations designed to react in the condensed phase, allowing for minimization of these situationally undesirable reaction attributes.[9]

In this research, the selected fuels include Al (for its low cost and high energy density) and Zr (which rapidly oxidizes in the condensed phase). Additionally, TiO_2 was chosen for its very low adiabatic reaction temperatures with either Al and Zr, 1,479 °C[10] and 1,463.76 °C[11] respectively, well below the boiling point of Al.[12] This reaction limits the production of Al vapor, keeping the reaction in the condensed phase. Arrested reactive ball milling was chosen for thermite preparation as this method lends itself to production of useable quantities of materials with tunable microstructures and reactivities via adjustment of milling parameters.[13–15] The Al and Zr were first milled together to

increase the intermetallic reaction between the metals and thus lower the ignition threshold.[13, 16–21] The composite fuel was subsequently milled with TiO_2. We refer to this process as dual stage milling.

In a previous study, this dual stage milled Al/Zr/TiO_2 thermite was uniaxially compacted into pellets and ignited resulting in the identification of a two-phase reaction.[9] The dual stage reaction consisted of a distinct initial "dark" reaction front followed by a "luminous" reaction front. This unique propagation was attributed to the formation of Al-Zr intermetallics, with the dark front resulting from the reaction of the Al and Zr to form Al-Zr intermetallic species, and the luminous front being the oxidation of the intermetallic and remaining fuel. This initial formation of intermetallic species in the "dark" reaction is believed to help stabilize the pellet and reduce expansion as the "luminous" reaction propagates through.

To gain a better understanding of the reaction propagation of this thermite, compacts were laser ignited in one of four different atmospheres: Ar, N_2, vacuum, and air. Here, air is the control environment, identical to the conditions in the previous research. Vacuum was chosen to remove the possibility of oxidation reactions occurring with atmospheric oxygen versus the oxygen available in the TiO_2. Ar provided an inert environment while maintaining atmospheric pressure. Past work has indicated N_2 plays a role in the reaction properties of Al and Zr, with the diffusion of N impacting the likelihood of microexplosions – higher concentrations of N lead to more microexplosions.[22] Thus, N_2 was selected as an environment likely to produce a different reaction outcome in the thermite.

2. EXPERIMENTAL

2.1 Material synthesis

Thermites were milled using commercial Al (Alfa Aesar, 99.5 % pure, -325 mesh), Zr (Atlantic Equipment Engineers, 99.5 % pure), -20 to +60 mesh, and TiO_2 (Aldrich, >99 % pure, -325 mesh, anatase).[9] The Al and Zr were processed in a planetary ball mill (Retsch, PM400) in air and sieved to <75 μm following methods detailed elsewhere.[19] These Al-Zr composite fuels and were loaded under Ar into custom made hardened steel vials with a total internal volume of 186 mL. Powders were loaded with 40 mL of hexanes (Fisher Chemical, 98.5 % pure) as a process control agent and 9.525 mm 440 stainless steel milling balls at a ball to powder ratio of 3. The milling cycle consisted of four 15-minute active milling sessions separated by 30-minute rest cycles at 350 RPM for a total mill time of one hour. The sample vials were air cooled during the milling process. The formulation, referred to as (Al:Zr):TiO_2_2S, consists of the composition 28at%Al 28at%Zr 47at% TiO_2 chosen for its noted two-stage reaction.[9] The powder lots used in this work were characterized for morphology, microstructure, ignition temperature, and reaction properties in previous work.[9]

Powders were formed into compacts using a uniaxial load press (Denison) with a force indicator (Dillon, FI-127) and load cell (Dillon, SGMC 5,000 lb). Compacts were consolidated in a custom Elizabeth Carbide 7.37 mm diameter ram/die set[9] with 0.5 ± 0.05 g of thermite powder loaded into the die and compressed for 10 seconds under a normal stress of approximately 104.5 MPa. This resulted in compacts with a length of 4.57 ± 0.3 mm. Based on the calculated theoretical maximum density for this formulation, the average density of the compacts is 60 %.

2.2 Characterization of thermite compacts

Thermite compacts were loaded into the environmental chamber and the chamber was evacuated and backfilled with the desired environment. Four environments (air, vacuum, Ar, and N_2) were tested in triplicate. For Ar and N_2 atmospheres, the chamber was evacuated and backfilled three times before sample ignition. The minimum pressure reached during evacuation, both for atmospheric changeout and for tests performed in vacuum, was approximately 1 kPa. Compacts were top-ignited using a high rep-rate pulsed Nd:YAG laser (Coherent, Avia NX-65, 65 W, 532 nm, 150 kHz, 40 ns/pulse). A mechanical shutter was used to block the low-energy idler pulses continuously emitted by the laser, while allowing high-energy pulse trains to pass when triggered. Samples were ignited with a 3 second high-energy pulse train. The 3.5 mm beam was not focused onto the sample. Four-color pyrometry, time resolved spectroscopy, and filtered high-speed video were used to characterize reaction temperatures and burn rates (Figure 1).

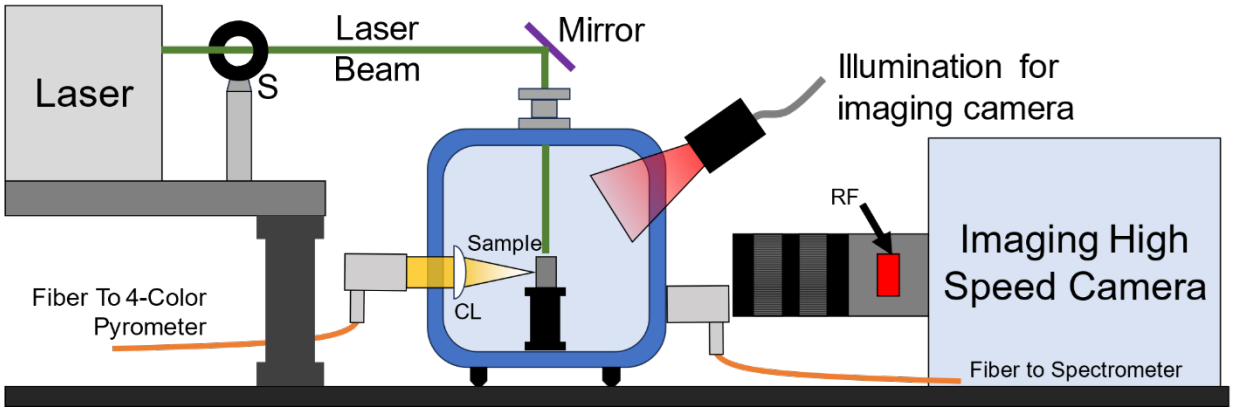

Figure 1. Experimental configuration for studying controlled environment reaction propagation in the powder compacts. S: shutter, RF: red bandpass filter, CL: cylindrical lens

A compact UV-VIS-NIR spectrometer (Avantes, AvaSpec-ULS4096CL-EVO-UA-10) was used to obtain broad emission spectra of the sample during reaction. Light from the sample was collected with a 400 µm, 0.22 NA fiber optic cable. The spectrometer was operated in continuous read mode, with spectra taken every 10 ms.

Spectral information was gathered using a custom, fiber coupled four-color pyrometer which collected emitted light from the sample using a reflective fiber collimator (Thorlabs, RC08SMA-P01), focused onto a 1 mm slit near the center of the compact with a cylindrical lens. Light entering the pyrometer is split into four beams using short-pass dichroic beam-splitters. The beams are then filtered with a 10 nm full-width half-max bandpass filter to either 600 nm, 770 nm, 900 nm, or 1,000 nm. Each beam of filtered light was focused onto a variable gain Si photodiode (Thorlabs, PDA100A2). The narrow bandpass filters inside the pyrometer exclude the red light from the LED used for high-speed video illumination. Reported temperatures of the sample are a weighted average over the whole field of view generated by the 1 mm slit. A schematic of the pyrometer showing the distribution of light to each photodiode is presented in Figure 2.

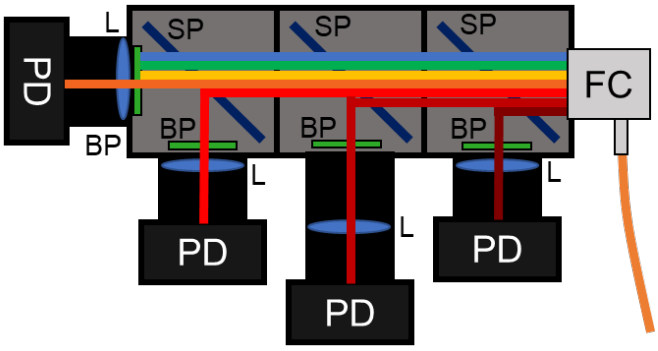

Figure 2. Schematic showing light distribution inside the four-color pyrometer. FC: Fiber collimator, SP: short-pass dichroic beam-splitter, BP: bandpass filter, L: lens, PD: photodiode.

Three-color imaging pyrometry was used to obtain spatially and temporally resolved temperature maps of the reacting samples. This technique leverages commonly available color cameras, with the addition of a triple-pass filter (TPF), to generate temperature maps from thermally emitting subjects.[23] The TPF limits light entering the optical system to tight (10 nm full-width half-max) bands and reduces cross talk between the red, green, and blue passbands of the native color filter built into the image sensor. The system can be calibrated with variable temperature sources, like lamps or blackbodies, or with a single blackbody and three monochromatic sources (red, green, and blue lasers or LEDs). Calibration corrects any remaining crosstalk between the color channels and provides intensity correction that compensates for other potential errors in the image system, like sensor response or optical transmission. Once calibration factors are known, images or videos taken with the camera/TPF system can be analyzed to calculate temperatures on a pixel-by-pixel basis. Subjects of interest must radiate in the visible portion of the electromagnetic spectrum, limiting the systems usefulness to systems with temperatures greater than approximately 1000 K.

Monochromatic high-speed video was used to determine sample burn rates. A digital high-speed camera (Photron, Fastcam SA-Z) recorded the ignition event at 500 frames per second, at a resolution of 1024 x 1024 pixels and a shutter speed of 1 µs. A 70–300 mm zoom lens, combined with 40 mm of extension tubes, was used to image the reacting sample. A red bandpass filter (Thorlabs, FBH650-40) mounted inside the lens extension tubes, limited light emission from the sample from saturating the camera. A red LED (Ushio, SugarCube Red), with an emission spectra aligned to the bandpass filter, was used provide external illumination of the sample. Light from the LED passed through a liquid light guide to a set of collimating optics used to direct the LED light onto the sample.

Analysis of both emission spectra and four-color pyrometry data proceeded in a similar fashion, based on methods used by Weismiller et al. and others.[24–29] The intensity response of both the spectrometer and pyrometer were calibrated using a stabilized tungsten lamp with a known spectral intensity distribution (Thorlabs, SLS201L). For each time step of spectral data (selected spectral band for the spectrometer, four photodiode signals from the pyrometer), the temperature was determined from the slope of a plot of C_2/λ versus $-Ln(I*\lambda^5)$, where C_2 is the second radiation constant ($C_2 = 1.4388 \text{ X } 10^{-2}$ m*K), λ is the wavelength of light, and I is the calibrated light intensity measured at that wavelength. Python scripts were written to execute these calculations.

Temperature calculations using the spectrometer only used a portion of the measured wavelength range in temperature calculations to avoid contributions from external light sources like the laser (532 nm) and the LED illumination source (~650 nm), and atomic emission features from impurities like Na (~589 nm) and K (~770 nm). The four-color pyrometer includes a bandpass filter centered at 770 nm. The selection of this filter for the four-color pyrometer was inadvertent and based on considerations related to available optics more than on atomic emission features. Comparison between temperatures determined with all four pyrometer colors and only three (dropping the 770 nm channel) result in almost identical values. This is likely not due to K atomic emission being a relatively minor contributor to total emitted light compared to the thermal emission from the sample at the same wavelength.

After ignition, the samples were allowed to cool in their respective atmospheres, collected, and imaged using a Keyence Elemental Analyzer Series VHX-7000 digital microscope to visually assess variations in the post reacted compacts. Energy dispersive x-ray spectroscopy information was collected from random sample locations to give an idea of the species present on the surface of the reacted compact. Scanning electron microscope images were collected in backscattered mode at 3500x magnification using a Thermo Scientific Helios G4 UC Focused Ion Dual Beam Instrument equipped with a monochromated electron beam for scanning electron imaging and Tomahawk ion column.

Additionally, post reaction crystalline phases were analyzed using X-ray diffraction (Malvern Panalytical, Aeris Compact Diffractometer with PIXcel 1D detector at 40 kV and 8 mA with Cu-Kα radiation). The reacted compacts were mounted on low background Si discs and scanned from 10° to 90° 2θ with a step size of 0.01° and 21.675 seconds per step. Samples were run 8 times and a simple sum average of the 8 scans was performed. The resulting patterns were analyzed using HighScore Plus4 software.

3. RESULTS AND DISCUSSION

3.1 Compact morphologies

All compacts were noted to have no expansion after reaction, regardless of ambient atmosphere. Compacts were allowed to cool in the chamber prior to venting, then collected for analysis. The external surfaces of the compacts are visually distinct, indicating the different atmospheres lead to formation of different species, phases, or ratios of those phases within the pellets, as seen in Figure 3.

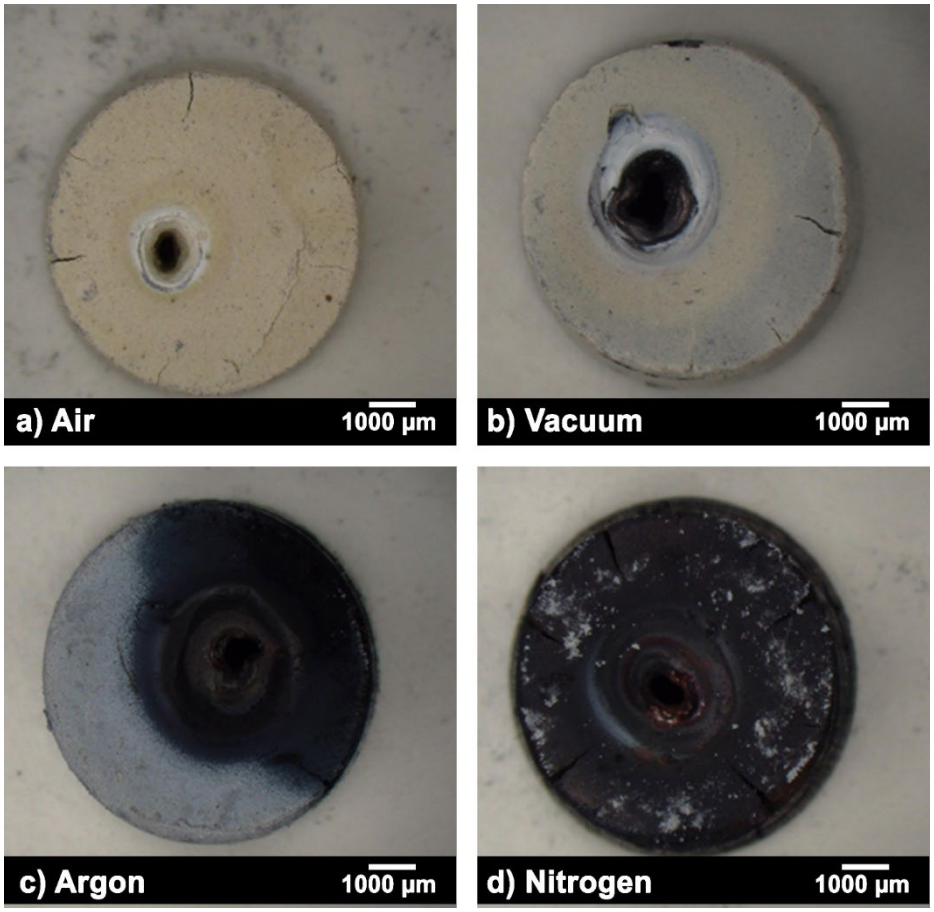

Figure 3. Microscope images of post-reacted compacts in a) air, b) vacuum, c) Argon, d) Nitrogen.

Impingement from the laser on the compact produced its own set of reactions which are not considered in this work. As no optics were used to focus or shape the laser, samples burned in a less-than-ideal wrap around propagation, leading to difficulty in determining the exact moment of ignition. Due to this, ignition delay was not assessed for these compacts. Samples burned in air (Figure 3a) reacted identically to previous research.[9] Those burned in vacuum appear similar to the samples burned in air, however the exterior is slightly grayer (Figure 3b). Quenching of the reaction occurred in all three Ar samples as heat losses to the Ar overwhelmed the propagation of the thermite, clearly seen in the split color appearance of the pellet in Figure 3c. The upper right side of the sample, which did react, is markedly different than the air sample, indicating a different combination of end products. Like the Ar samples, the samples burned in N_2 display a blue-black appearance (Figure 3d). Unlike the Ar samples, the N_2 samples did not quench. Of note, the inside of both the air and vacuum samples display the same blue-black appearance as the Ar and N_2 samples, indicative of the impact of the air on the pellet's surface reactions.

In looking at these samples under 3500x magnification using backscattered electrons (BSE), there are distinct morphology differences between the surfaces (Figure 4). Samples ignited in air (Figure 4a) have large grains interspersed with much finer particles. These finer particles appear as bright white spots in the BSE image and thus are likely Zr containing as Zr has the highest atomic number within the sample. Samples ignited under vacuum (Figure 4b) display no distinct large grains, but rather varying patches of less defined fine particles with interspersed pores. In Figure 4c, the reacted portion of the compact is shown, which appears to have a fine particulate/pore matrix with larger particles familiar of the Al-Zr composite fuel starting material. These larger particles display microstructures and overall particle sizes similar to the data collected from the characterization of these unreacted loose powders, with bright white inclusions in a darker gray matrix.[9] Figure 4d is similar to the reacted portion of Figure 4c, having a fine particulate/pore matrix with interspersed larger particles. In contrast to Figure 4c, the larger particles do not display microstructures akin to the unreacted Al:Zr composites, but instead appear more uniform based on contrast due to atomic number.

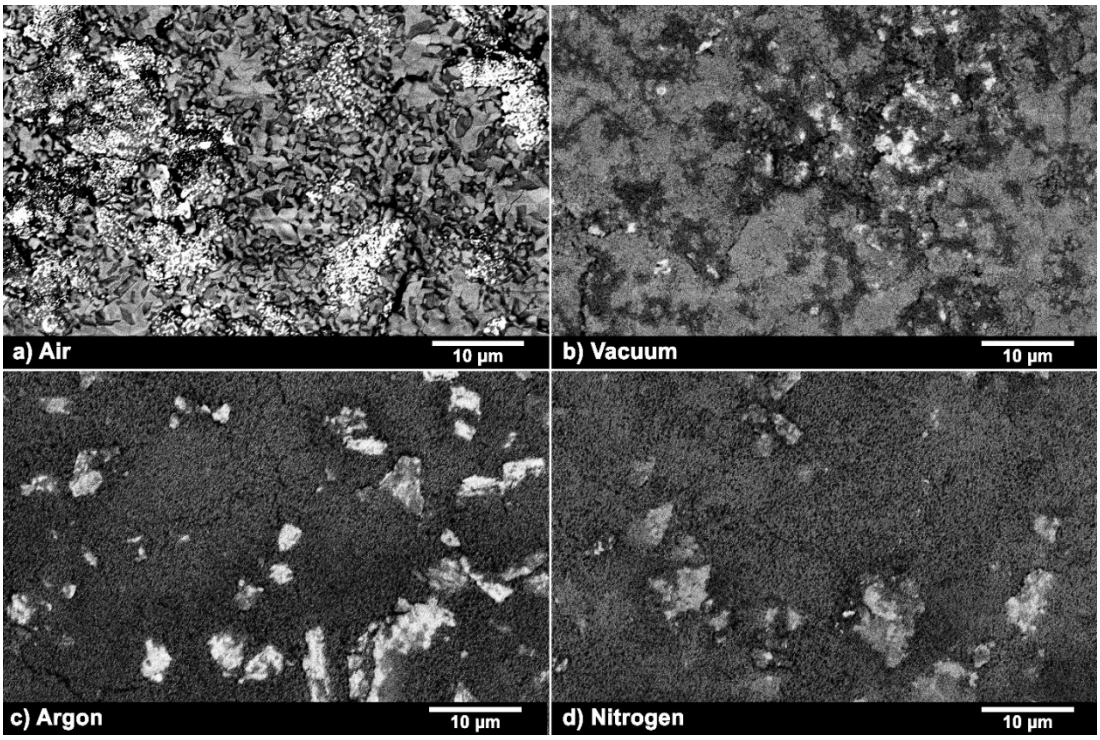

Figure 4: BSE SEM surface images of post reaction compacts at 3500x magnification in the following environments (a) air, (b) vacuum, (c) Argon, (d) Nitrogen.

Prior to compaction, unreacted loose thermite powder was analyzed using XRD, this data is presented in previous work.[9] As expected, the phases of the individual components anatase TiO_2, Al, and Zr are seen in the scan. Additionally, small ZrC peaks are observed, an outcome of the milling procedure used for material preparation. The crystalline phases seen in the post reacted samples in air include rutile TiO_2, Al_2O_3, Ti/Al oxides, and both monoclinic and tetragonal ZrO_2. Tetragonal ZrO_2 is stable at temperatures between 1443 K and 2643 K, below which it reversibly transitions to monoclinic unless stabilized.[30] Tetragonal ZrO_2 can be retained at room temperature by the addition of dopants into the ZrO_2 lattice, where Al_2O_3 can act as a dopant species.[31] Al and Zr metals are not visualized as crystalline phases, indicating they are either fully reacted into other species or are amorphous.

Similar to the air sample, in the vacuum sample crystalline phases of rutile TiO_2, Al_2O_3, Ti/Al oxides, and both monoclinic and tetragonal ZrO_2 are observed. Additionally, crystalline phases of Zr are present. We attribute the presence of Zr to the lack of access to available oxygen for complete reaction of the Zr. It is likely that oxygen from the air is contributing to the oxidation of the metals in the air sample.

The samples reacted in Ar quenched upon removal of the laser and, thus, only the portion of the compact in contact with the laser reacted. Due to this, unreacted anatase TiO_2 and Zr crystalline phases are observed, as well as the ZrC typically seen as a milling contaminant. Zr and Al oxides are also present. In contrast to the air and vacuum samples, no crystalline rutile phase of TiO_2 is detected.

As expected, different crystalline phases are seen in the N_2 sample, a direct result of the atmosphere on the reaction. The rutile phase of TiO_2 is observed, as well as Al_2O_3, monoclinic ZrO_2, and tetragonal ZrO_2. Crystalline phases of the nitrides of Ti and Zr are also present, as both Ti and Zr are enthalpically favorable to react with N_2 when available.

3.2 Properties of self-propagating reactions in compacts

Results from the three temperature analysis methods are given in Table 1. For both spectrometer and four-color pyrometer derived temperatures, samples ignited in air have the highest average burn temperature. This is likely the result of the reaction of the outer layer of the compacts with ambient air. Good agreement in temperature is seen between the temperatures recorded with the spectrometer and four-color pyrometer. These data show air samples tracking with the adiabatic temperatures for the stoichiometric reactions of the individual metal fuels with TiO_2: 1,479 °C for Al + TiO_2[10] and 1,463.76 °C for Zr + TiO_2.[11] The lower average temperatures seen in the other samples are likely due to convective losses to the other atmospheres and lack of additional oxidation.

In comparing the video pyrometry data to the other two methods, there is consistency amongst all methods for samples ignited in air. However, samples ignited in vacuum, Ar, and N_2 all report significantly higher temperatures than the spectrometer and four-color pyrometer. The user settings for the video pyrometry changed for the air samples versus the vacuum, Ar, and N_2. This gave a different calibration for the air samples from the other environments, as the other environments were recorded using the camera's default settings while the air samples were recorded using custom user settings to remove any image enhancement features of the camera. This difference in camera configuration is assumed to be the reason samples reacted in vacuum, Ar, and N_2 are consistently skewed by approximately 300 °C from the other methods.

Table 1. Temperatures recorded by different diagnostic methods in each environment.

Sample Atmosphere	Spectroscopy Temperature (°C)	4-Color Pyrometry Temperature (°C)	Video Pyrometry Temperature (°C)
Air	1494 ± 12	1537 ± 20	1614 ± 59
Vacuum	1382 ± 34	1258 ± 40	1657 ± 51
Ar	1303 ± 94	1333 ± 23	1737[†]
N_2	1333 ± 22	1385 ± 101	1740 ± 32

[†]**Only one trial resulted in usable video for analysis**

Average burn rates and time to visible ignition propagation for the self-propagating reactions in the thermite compacts were determined by analyzing the high-speed videos of each compact. Burn rates were calculated using ImageJ[32] to convert each video into a pseudo-streak image using published methods.[9,33] Pseudo-streak images were created using every 500th frame of the high-speed video (two frames per second). Points fitted to the burn front versus time of the image and were used to determine a slope from which the average burn rate was calculated. The burn rates for the three samples in each group were averaged to give the data presented in Table 2.

Table 2. Average burn rates and times to visible reaction propagation for each environment.

Sample Atmosphere	Average Burn Rate (mm/s)	Propagation Delay (s)
Air	2.20 ± 0.31	0.45 ± 0.06
Vacuum	2.52 ± 0.52	0.64 ± 0.10
Ar*	5.23 ± 0.25	2.13 ± 0.31
N_2	2.21 ± 0.13	0.76 ± 0.13

***Samples ignited in Ar quenched once the laser turned off.**

Average burn rates for air, vacuum, and N_2 are all similar, and are recorded to be slightly faster than observed in previous work.[9] This increased rate is likely driven by the longer laser pulse (three seconds versus a half of a second in previous work), which was increased due to poor ignition in the Ar environment. As evidenced by the Ar samples, the laser increases the burn rate, which slows once removal of the laser occurs. The Ar samples have a significantly higher burn rate, but quench almost immediately after the laser is disengaged indicating the laser is driving the reaction and, thus, not self-propagating.

Delay time to visible propagation of the first reaction front was calculated from the start of laser initiation until the reaction front can be seen on the camera facing side of the compact. This analysis assumes that the reaction front is evenly propagating from the top of the compact, which does not match exactly with observations, but allows for a reasonable approximation to be made for comparisons between the samples. Air has the shortest propagation delay, likely driven by the oxygen in the atmosphere assisting the reaction. Vacuum and N_2 are similar in time to visual propagation delay. Results from the Ar samples are far longer than the other environments, again attributed to the difficulty in igniting the sample under this condition.

Compacts burned in air exhibit minimal expansion and the same dark reaction front preceding the luminous reaction front behavior observed in previous work.[9] Compacts burned in vacuum also exhibit a dark reaction front, with a less distinct luminous reaction following the dark front. The N_2 environment samples did not display the two-stage reaction as seen in air and vacuum, but rather a single luminous front. This is easily attributed to the different reaction products forming on the surface of the compact, namely the nitride compositions. No conclusions could be made for samples burned in Ar due to quenching. Additionally, no samples showed expansion of the compact during reaction. Several samples did crack, most likely due to expansion of gases trapped within the compact during compaction.

4. CONCLUSION

The objective of this work was to further evaluate the Al:Zr:(TiO_2) formulation developed to eliminate gas production and compact expansion during self-propagation. This was achieved by laser igniting the thermite under four different environments: air, vacuum, Ar, and N_2. Samples were evaluated for burn rate, burn temperature, propagation delay, and reaction products.

Samples ignited in air have higher recorded burn temperatures via four-color pyrometry and spectroscopy, and track with the adiabatic reaction temperatures of Al:TiO_2 and Zr:TiO_2. Samples ignited in vacuum, Ar, and N_2 are lower than those recorded for the samples in air which we attribute to convective losses to their environments. Burn rates and propagation delays were similar for air, vacuum, and N_2 samples. Ar samples quenched and, thus, were suspect for evaluation.

Expansion of the compacts was not seen for any environment. Air and vacuum both demonstrated the two-stage reaction seen in previous work, while N_2 samples exhibited a single luminous reaction front. Reaction products were similar for air, vacuum, and Ar, being a mix of oxides of the starting constituents. Samples burned in N_2 had reaction products of oxides and nitrides, as would be expected. The formation of nitrides is attributed to the loss of the two-stage reaction front in these samples.

This study evaluates a small number of atmospheres on the reaction of a minimally expanding thermite formulation and highlights the importance of environment on the reaction properties. Future research is planned to investigate the product formation during reaction, to better resolve the mechanism leading to the two-stage reaction behavior. Understanding these mechanisms will allow for optimization of this system to better direct future formulation development.

ACKNOWLEDGMENTS

The authors wish to thank Warren Gardner, Michael Kauzlarich, Richard Benjamin, and William Sickels for their technical support and editorial assistance. Funding was provided by the U.S. Army via the Chemical Biological Advanced Materials Manufacturing Program (PE 0601102A Project VR9) at the Combat Capabilities Development Command Chemical Biological Center.

REFERENCES

[1] Deppeler, J.H. Physical properties of thermit welds. *Weld J.* **1922**, p 33.
[2] Deppeler, J.H. Rail joint welding of main line track by thermit process. *Weld J.* **1929**, p 58.
[3] Agarwal, P.P.K.; Matsoukas, T. Nanoenergetic materials: enhanced energy release from boron by aluminum nanoparticle addition. *ACS Omega*. **2022**, *7* (30), pp 26560–26565.
[4] Vralstad, T.; Saasen, A.; Fjaer, E.; Oia, T.; Ytrehus, J.D. Plug & abandonment of offshore wells: Ensuring long-term well integrity and cost-efficiency. *J. Pet. Sci. Eng.* **2019**, *173*, pp 478–491.
[5] Sharma, M.; Sharma, V. Superiour performance of multi-layer graphene assisted Al/$Bi2O_3$ nanothermite for small-scale propulsion applications. *J. Energ. Mater*. **2024**, pp 1–21.
[6] Wu, T.; Zachariah, M.R. Silver ferrite: a superior oxidizer for thermite-driven biocidal nanoenergetic materials. *RSC Adv.* **2019**, *9* (4), pp 1831–1840.
[7] Guo, S.; Focke, W.W.; Tichapondwa, S.M. Al-Ni-NiO pyrotechnic time-delays. *Propellants, Explos., Pyrotech.* **2020**, *45* (4), pp 525–685.
[8] Monk, I.; Schoenitz, M.; and. Dreizin, E.L. Combustion of a rapidly initiated fully dense nanocomposite Al-CuO thermite powder. *Combust. Theory Modell.* **2019**, *23* (4), pp 651–673.
[9] Polk, A.L.; Dean, S.W.; Flickinger, M.R.; Chintersingh, K.A.; Scott, D.G.; Valdes, E.R.; Fisher, K.R.; Weihs, T.P. Microstructure and reaction properties of titanium dioxide based thermites using Al-Zr composite fuels, *Combust. Flame*. **2024**, *262*, p 113343.
[10] Fischer, S.H.; Grubelich, M.C. *Theoretical energy release of thermites, intermetallics, and combustible metals;* Sandia National Lab. (SNL-NM), Albuquerque, NM, **1998**, UNCLASSIFIED Report (AC04-94AL85000).
[11] Fried, L.E. *CHEETAH 1.0 users manual*; Lawrence Livermore National Lab, 1994; UNCLASSIFIED REPORT (UCRL-MA-117541).

[12] Lynch, P.; Fiore, G.; Krier, H.; Glumac, N. Gas-phase reaction in nanoaluminum combustion, *Combust. Sci. Technol.* **2010**, *182* (7), pp 842–857.
[13] Wainwright, E.R.; Weihs, T.P. Microstructure and ignition mechanisms of reactive aluminum-zirconium ball milled composite metal powders as a function of particle size. *J. Mater. Sci.* **2020**, *55* (29), pp 14243–14263.
[14] Woodruff, C.; Wainwright, E.R.; Bhattacharia, S.; Lakshman, S.V.; Weihs, T.P.; Pantoya, M.L. Thermite reactivity with ball milled aluminum-zirconium fuel particles. *Combust. Flame*. **2020**, *211*, pp 195–201.
[15] Dreizin, E.L.; Schoentiz, M. Mechanochemically prepared reactive and energetic materials: a review, *J. Mater. Sci.* **2017**, *52,* pp 11789–11809.
[16] Barron, S.C.; Kelly, S.T; Kirchhoff, J.; Knepper, R.; Fisher, K.; Livi, K. J.T.; Dufresne, E.M.; Fezzaa, K.; Barbee, T.W.; Hufnagel, T.C.; Weihs, T.P. Self-propagating reactions in Al/Zr multilayers: anomalous dependence of reaction velocity on bilayer thickness. *J. Appl. Phys*. **2013**, *114* (22), p 223517.
[17] Lakshman, S.V. Gibbins, J.D.; Weihs, T.P. Evaluating the effect of microstructural refinement on the ignition of Al-Mg-Zr ball-milled powders, *Powder Technol*. **2021**, *379*, pp 447–456.
[18] Lakshman, S.V.; Gibbins, J.D.; Wainwright, E.R.; Weihs, T.P. The effect of chemical composition and milling conditions on composite microstructure and ignition thresholds of Al-Zr ball milled powders. *Powder Technol*. **2019**, *343*, pp 87–94.
[19] Polk, A.L.; Chintersingh, K.A.; Flickinger, M.R; Valdes, E.R.; Gardner, W.L.; Weihs, T.P. Effect of composition and process control agents on the microstructure and ignition properties of ball-milled Al-Zr powders. *Powder Technol*. **2023**, *427*, p 118729.
[20] Stamatis, D.; Wainwright, E.R.; Lakshman, S.V.; Kessler, M.S.; Weihs, T.P. Combustion of explosively dispersed Al-Mg-Zr composite particles, *Combust. Flame*. **2020**, *217*, pp 93–102.
[21] Wainwright, E.R.; Inouye, M.; Niu, M.; Chintersingh, K.; Weihs, T.P. Comparing the ignition and combustion of ball-milled Al-based composites with Ti, Zr, and Mg additives, *J. Energ. Mater*. **2023**, *41* (1), pp 43–62.
[22] Wainwright, E.R.; Lakshman, S.V.; Leong, A.F.; Kinsey, A.H.; Gibbins, J.D.; Arlington, S.Q.; Sun, T.; Fezzaa, K.; Hufnagel, T.C.; Weihs, T.P. Viewing internal bubbling and microexplosions in combusting metal particles via x-ray phase contrast imaging, *Combust. Flame*. **2019**, *199*, pp 194–203.
[23] McNesby, K.; Dean, S.; Benjamin, R.; Grant, J. Anderson, J. Densmore, J. Imaging pyrometry for most color cameras using a triple pass filter. *Rev. of Sci. Instrum*. **2021**, *92* (6), p 063102.
[24] Weismiller, M.R.; Lee, J.G.; Yetter, R.A. Temperature measurments of Al containing nano-thermite reactions using multi-wavelength pyrometry. *P. Combust. Inst.* **2011**, 33 (2), pp 1933-1940.
[25] Ward, T.S.; Trunov, M.A.; Schoenitz, M.; Dreizin, E.L. Experimental methodology and heat transfer model for identification of ignition kinetics of powdered fuels. *Int. J. Heat Mass Transfer*. **2006**, *49* (25–26), pp 4943–4954.
[26] Moore, D.S.; Son, S.F.; Asay, B.W. Time-resolved spectral emission of deflagrating nano-Al and nano-MoO_3 metastable interstitial composites. *Propellants, Explos., Pyrotech*. **2004**, *29* (2), pp 106–111.
[27] Goroshin, S.; Mamen, J.; Higgins, A.; Bazyn, T.; Glumac, N.; Krier, H. Emission spectroscopy of flame fronts in aluminum suspensions. *Proc. Combust. Inst.* **2007**, *31* (2), pp 2011–2019.
[28] Blobaum, K.J.; Wagner, A.J.; Plitzko, J.M.; Van Heerden, D.; Fairbrother, D.H.; Weihs, T.P. Investigating the raction path and growth kinetics in CuOx/Al multilayer foils. *J. Appl. Phys*. **2003**, *94* (5), pp 2923–2929.
[29] Ng, D.; Fralick, G. Use of a multiwavelength pyrometer in several elevated temperature aerospace applications. *Rev. Sci. Instrum*. **2001**, *72* (2), pp 1522–1530.
[30] Huang, H.J.; Wang, M.C. The phase transformation and stability of tetragonal ZrO_2 prepared in a silica bath, *Ceram. Int*. **2013**, *39* (2), pp 1729–1739.
[31] Rao, P.; Iwasa, M.; Wu, J.; Ye, J.; Wang, Y. Effect of Al_2O_3 addition of ZrO_2 phase composition in the Al_2O_3-Zr_2 system. *Ceram. Int*. **2004**, *30* (6), pp 923–926.
[32] *Image J Image Processing and Analysis in Java*. https://imagej.net/ij/.
[33] Parker, G.R.; Asay, B.W.; Dickson, P.M. Note: A technique to capture and compose streak images of explosive events with unpredictable timing, *Rev. of Sci. Instrum*. **2010**, *81* (1), p 016109.

This page left intentionally blank

Determination of the influence of tunable chemical environment in MOF-polymer composites on the absorption of linear nonpolar toxic compounds

Chase B. Thompson[a], Melissa S. Hulet[a], Matthew A. Browe[b], Adam R. Hinkle[c], Ivan O. Iordanov[b], Brent A. Mantooth[b], Gregory W. Peterson[b], Thomas P. Pearl[b]*
[a]Leidos, 11951 Freedom Dr, Reston, VA 20190
[b]U.S. Army Combat Capabilities Development Command Chemical Biological Center, Research & Operations Directorate, 8198 Blackhawk Rd, Aberdeen Proving Ground, MD 21010
[c]DCS Corporation, 4696 Millennium Dr, Suite 450, Belcamp, MD 21017-1561

ABSTRACT

This study addresses the chemical environment at the interfaces in metal-organic framework-polymer composites and their role in mass transport behavior for molecular contaminants. To achieve this, a systematic understanding of chemical interactions and polymer chain behavior at metal-organic framework-polymer interfaces is crucial. Work presented here focuses on treating process factors, specifically solvent blends, to control dispersal of UiO-66-NH_2, a prototypical metal-organic framework, in common polymers. The approach invokes the use of self-consistent field theory in conjunction with Hansen solubility parameters to predict conditions that will result in good or bad dispersal of metal-organic framework crystals in solution-cast thin films. Scanning electron microscopy shows composition-dependent dispersion of UiO-66-NH_2 based on predicted solvent blends, demonstrating the utility of the proposed method. Differential scanning calorimetry and broadband dielectric spectroscopy measurement reveal mechanical property and polymer chain dynamics correlations with the processing conditions. Computational modeling complements the experimental efforts by examining metal-organic framework and polymer properties at the molecular scale in metal-organic framework-polymer composites using atomistic simulations. A hybrid force field arrangement is under development that integrates the metal-organic framework, polymer, and solvent interactions into the modeling approach.

Keywords: Metal-organic frameworks, polymer composites, interfaces, chemical permeability

1. INTRODUCTION

For protective coatings, barrier materials, and permeable membranes used in protection and hazard mitigation applications, which are often composed of polymers or polymer composites, there is a need to better understand how to control (i.e., to suppress or enhance) mass transport. Previous work has treated the interaction of toxic chemicals and respective simulants with polymeric materials in order to promote development of more efficacious decontamination processes as well as to contribute to the design of coatings materials (e.g., low gloss paints) to enhance chemical resistance.[1] These composites involve the dispersal of solids in polymer matrices to impart specific material properties. Consistently, there has been great difficulty in designing materials of this type with increased resistance to specific compounds, such as linear nonpolar chemicals. In parallel efforts, metal-organic frameworks (MOF) and MOF-polymer composites have been developed and characterized to establish new materials with customizable functionalities and structures, including the ability to specifically address chemical hazards.[2,3] It would be advantageous to utilize these types of structures to develop new types of barrier materials, but advances in control and tuning of chemical permeation for composites depend on understanding the role of interfacial structures in transport that arise from mixing dissimilar materials.

The dispersion of solids or particles and the chemical and physical environments associated with polymer-particle interfaces have been shown to significantly drive the overall chemical transport properties of a composite.[4] The underlying structure-property relationships of polymer composites influence transport of incoming analytes, which are informed by the properties of the penetrant chemical and the nature of dispersal of solids in the composite. Nonpolar molecular species are readily soluble in certain polymer matrices and exhibit entrainment within surface

and bulk layer textures. These challenges exist for a broad class of polymer composites where the solids dispersed in host polymer matrices introduce spatially localized variations in the density and voids in the binder system that can facilitate transport. Molecular size, shape, and functionality of the penetrant chemical are major factors that impact transport and solubility in bulk polymers. A systematic study of these interactions is necessary to design and optimize novel polymer composites that can serve as strong barriers to chemical absorption, including protective paint coatings (as much as 50 µm thick) and conformal thin films (less than 1 µm thick). Interfaces between MOF solids and polymer chains in composites present a key challenge since defects often form due to the general incompatibility between nanoparticles and polymers.[5,6] Several approaches are available for enhancing the compatibility between MOFs and polymers,[7] thereby reducing interfacial defects, but an understanding of how to process these types of materials with control over defect structures is still lacking.

In this project, we demonstrated the utility in using a computationally efficient mean field theory in combination with solubility parameters to predict the adsorption and depletion of a polymer layer on a MOF surface, see Figure 1.[8] This allowed a determination of solvent-mediated dispersion of UiO-66-NH_2 in select polymers, polystyrene (PS), poly(methyl methacrylate) (PMMA), and poly(butadiene) (PB), when films were cast from a solution of MOF, polymer, and solvent. This level of prediction for the contribution of solvent in processing conditions has the potential to inform production of other composite materials and provides a means of assessing the role of defect structure in mass transport due to solvent-induced variations in MOF-polymer interfaces. Furthermore, we have been able to measure different properties of these types of films both experimentally and computationally, to capture the effect of solvent in mechanical properties of MOF-polymer films as well as quantify how polymer chain behavior varies as a function of interface formation.

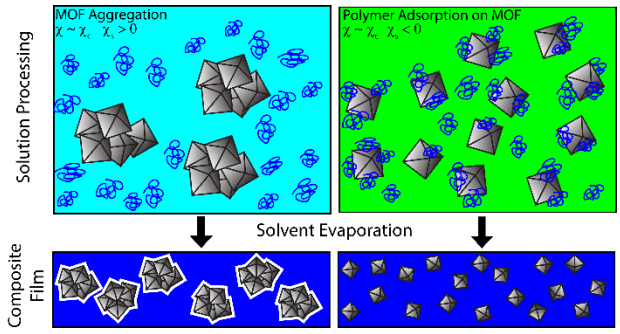

Figure 1. Illustration of using solubility parameters in conjunction with polymer adsorption theory to tune MOF-polymer-solvent combinations to control interface types (adapted from reference 8).

2. MATERIALS AND METHODS

2.1 Materials

For this proof-of-concept study, UiO-66-NH_2 was prioritized as the principal MOF since it is well-characterized, employed in the relevant application areas,[2,3,9] can be synthesized with controlled crystal shapes and sizes less than 200 nm (which is important for thin films such that crystals do not transverse the film), and is one of the most stable MOFs known.[10] NuMat Technologies (Skokie, IL) provided UiO-66-NH_2 for producing composites, as well as other Zr-based MOFs for turbidity measurements as part of STTR, ManTech, and IBAS programs. Details on dispersal of UiO-66-NH_2 in two high glass transition temperature (T_g) polymers (PS and PMMA) were published previously as part of this program.[8] Elastomeric composites were prepared using PB with a molecular weight of approximately 200 kg/mol and a density of 0.9 g/mL. The photoinitiator phenylbis(2,4,6-trimethylbenzoyl)phosphine oxide (BAPO) was used to cure PB films by photopolymerization, a means of locking in the polymer chain structure after MOF integration. Photopolymerization reactions were conducted in an Anycubic Wash & Cure station equipped with an irradiation source with a wavelength of 405 nm. All solvents used in turbidity measurements and in MOF-polymer film processing were procured from Sigma Aldrich/Supelco (HPLC or ACS reagent grade) and used as received with no further purification.

2.2 Experimental

Composite films consisting of approximately 10 wt% UiO-66-NH_2 in PS, PMMA, and PB were prepared by solution casting. Similar to the steps for producing PS and PMMA composites,[8] PB films were prepared with either chloroform or chloroform/methanol blends to promote different MOF dispersal states. All PB films were prepared with 2 wt% BAPO (in reference to polymer mass). After drying in a desiccator, PB films and composites were irradiated for 20 minutes to promote covalent crosslinking. The compositions of the polymer solutions were based on self-consistent field theory (SCFT) calculations and Hansen solubility parameters (HSP) and the same practice used for PS and PMMA was employed here with regards to control over vapor liquid equilibrium to prevent significant changes in the solvent composition in the films as a function of cure time. Films were either drop cast or drawn down from MOF-polymer-solvent solutions. A Phenom GSR desktop scanning electron microscope (SEM) was used to assess the dispersion of UiO-66-NH_2 in each polymer. A 1 cm × 1 cm sample of the composite was mounted on an Al stub using double-sided tape, then sputter coated with gold before imaging. Accelerating voltages between 5–15 kV were used with a 10 mm nominal working distance. Differential scanning calorimetry (DSC) (TA Discover Series DSC) or dynamic mechanical analysis (DMA) (TA DMA 850) measured glass transition temperature and mechanical properties of composites. Broadband dielectric spectroscopy (BDS) (custom built instrument, National Institute of Standards and Technology (NIST)) was performed on a select set of both glassy and elastomeric composite films for initial determinations of differences in polymer chain relaxation dynamics resulting from using solvent blends for casting films. For assessment of solubility parameters for Zr-based MOFs, time-resolved turbidity measurements of MOF powders mixed in probe solvents (high borosilicate glass vials with screw caps) were performed using an Apera Instruments TN400 portable turbidity meter kit with an 850 nm wavelength light emitting diode source.[8]

2.3 Computational

This work aimed to develop a hybrid scheme in Large-scale Atomic/Molecular Massively Parallel Simulator molecular dynamics code that uses a mixture of computational approaches to capture interactions in all three distinct regions of a MOF-polymer-solvent composite system. This includes a molecular mechanics (MM3) force field for MOF-MOF interatomic interactions, a universal force field for MOF-polymer and MOF-solvent pairs, and a class II polymer consistent force field to account for polymer-polymer, solvent-solvent, and polymer-solvent combinations. Quantum chemical vibrational frequency calculations and QuickFF tool[11] were used to determine force field parameters to differentiate bulk MOF from MOF interface and molecular dynamics simulation to explore the interfaces in MOF-polymer composite materials as a function of polymer, MOF, and solvent properties. Additional details on computational methods and tools used for molecular simulation are described in the Results and Discussion Section.

3. RESULTS AND DISCUSSION

3.1 Using solubility parameters and self-consistent field theory for MOF-polymer film processing

Recent work has used SCFT to study the adsorption/depletion behavior of homopolymers in solution near the critical point of the polymer solution where phase separation begins to occur (i.e., the extremal point of the spinodal curve).[12] Of particular interest in this work is the concentration of a monodisperse polymer as a function of distance from a solid surface, which has previously been studied for several different systems.[13–16] For the purpose of interrogating polymer adsorption on porous solids like MOF crystals, SCFT calculations were performed in this program with the freely available SFBox code, which provides a numerical implementation of the Scheutjens-Fleer lattice-based SCFT.[13,17,18] The calculations are specified by the polymer chain length, N, bulk polymer volume fraction, φ_b, polymer-solvent interaction parameter, χ (equivalent to the Flory-Huggins interaction parameter), and the interaction parameter χ_s, which quantifies the relative polymer-solid and solvent-solid interactions ($\chi_s < 0$ indicates the polymer interacts more strongly with the solid than does the solvent and vice versa for $\chi_s > 0$). With a given system specification, the SFBox code outputs $\varphi(z)$, which is a profile of polymer volume fraction, φ, as a function of distance, z, (in lattice units) from the solid surface.

Rational selection of the solid + polymer + solvent system such that it exists near the bulk solution critical point with $\chi_s < 0$ has been explored in this program as a viable processing method for producing composites with improved properties. This strategy was applied to control the dispersion of UiO-66-NH_2 in PS and PMMA, from single crystallites to agglomerated clusters, as a function of predicted solvent composition. Previously, the position of the solubility sphere for UiO-66-NH_2 in Hansen solubility parameter space (δ_D, δ_P, δ_H) was determined through Hansen

Solubility Parameters in Practice (HSPiP) software to be δ_D=13.9, δ_P=11.7, δ_H=11.8.[8] The Hansen solubility parameters describe the dependence of molecular, polymer, and nanoparticle properties like solubility and diffusion on dispersion (δ_D, van der Waals), polarity (δ_P, related to dipole moment), and hydrogen bonding (δ_H) type chemical interactions. Using HSPs available in the HSPiP software for PS (δ_D = 18 MPa$^{0.5}$, δ_P = 5 MPa$^{0.5}$, and δ_H = 5 MPa$^{0.5}$) and PMMA (average of top 5 results in the database: δ_D = 17.3 MPa$^{0.5}$, δ_P = 8.2 MPa$^{0.5}$, and δ_H = 7.6 MPa$^{0.5}$), the interaction parameters ($\chi = \chi_{sol-pol}$ and $\chi_s = \chi_{pol-MOF} - \chi_{sol-MOF}$) for each polymer and UiO-66-NH$_2$ dispersed in different solvent blends were computed using the following equation,[19,20]

$$\chi_{ab} = \frac{\bar{V}_r}{RT}[(\delta_D^a - \delta_D^b)^2 + 0.25(\delta_P^a - \delta_P^b)^2 + 0.25(\delta_H^a - \delta_H^b)^2]. \quad (1)$$

The superscripts a and b refer to the components of the mixture (polymer, MOF, or solvent), and $\bar{V}_r$ is a reference molar volume. For interaction parameters in which the solvent is one component, $\bar{V}_r$ is the molar volume of the solvent or the average of the solvent mixture, while for the MOF-polymer interaction parameter, $\bar{V}_r$ is the molar volume of a monomer unit. For PS, chloroform/hexane mixtures were explored for improved dispersion of UiO-66-NH$_2$ compared to using pure chloroform. For PMMA, acetone/hexane mixtures were used to improve UiO-66-NH$_2$ dispersion while acetonitrile/ethanol (ACN/EtOH) mixtures were used to purposely cause agglomeration of UiO-66-NH$_2$ crystallites. Except for the pure chloroform case for PS, the compositions of the solvent mixtures were adjusted such that the solvent-polymer interaction parameter computed from the HSPs was $\chi = \chi_c$ = 0.57 (critical polymer concentration) and χ_s could either be positive or negative.[8] SCFT calculations verified how excess adsorbed polymer, Γ_{ex}, depends on χ_s, where adsorption or depletion maxima would occur roughly at the critical polymer concentration in solution.[12] When casting thin films from these solvent blend-optimized solutions, steps were taken to control the vapor headspace during drying to prevent variances in MOF density throughout the thickness of the films.[8]

A similar approach was taken for defining solution blend conditions for dispersal of UiO-66-NH$_2$ in PB, see Figure 2. Photopolymerization to induce crosslinking was used to trap the MOF arrangement in the lower T_g polymer for either MOF-polymer or polymer-solvent favored conditions.

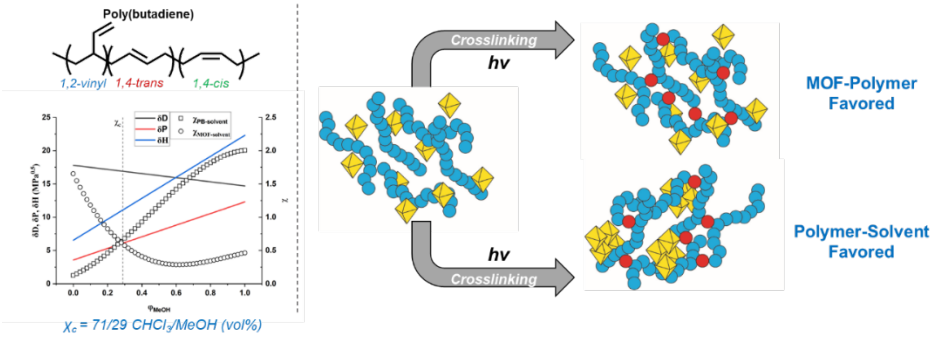

Figure 2. Producing elastomeric composites with poly(butadiene) using a chloroform/methanol blend optimized to result in the correct balance of interaction parameters. A rapid light-induced crosslinking step was included to lock the structures in place.

Briefly, the procedure for generating composites of PB with 10 wt% UiO-66-NH$_2$ is included here. First, 0.63 g (0.7 mL) of polymer is weighed and added to a vial. For a nanocomposite, a larger overall volume is required to disperse the MOF. A total of 5 mL of either chloroform or chloroform/methanol blends is then added to the polymer based on the ratios shown in Table 1 along with 0.012 g BAPO photoinitiator (2 wt% of polymer), followed by continuous, multi-hour stirring.

Table 1. Solvent ratios for PB films with and without UiO-66-NH$_2$.

Sample No.	Sample Name	Solvent A	Solvent B
1	PB ($CHCl_3$)	$CHCl_3$ (10 mL)	--
2	PB-MOF ($CHCl_3$/MeOH)	$CHCl_3$ (8.10 mL)	MeOH (1.90 mL)
3	PB ($CHCl_3$)	$CHCl_3$ (5 mL)	--
4	PB-MOF ($CHCl_3$/MeOH)	$CHCl_3$ (4.05 mL)	MeOH (0.95 mL)

For samples with MOF, 0.063 g of UiO-66-NH_2 (10 wt% of polymer) is added into a separate vial along with 5 mL of the solvent ratio listed in Table 1. To mix thoroughly, the MOF-solvent solution is ultrasonicated using a sonicating probe (80 % amplitude, 10 s ON and 20 s OFF for 3 cycles) until visual confirmation showed that the MOF is fully suspended in solution. The MOF-solvent solution is added to the stirring polymer solution, which is then homogenized to ensure that the MOF and polymer are well mixed. MOF-polymer-solvent solutions are poured into Teflon molds and placed in a desiccator for drying films. Located in the desiccator for each film would be a solvent reservoir to control the vapor composition and minimize significant changes in the solvent blend concentration profile in the films as they dried. From calculations of chloroform/methanol vapor-liquid equilibrium data,[21] solvent reservoirs are set-up to give equal mole fraction of solvents in the headspace for drying films (e.g., 10 mL $CHCl_3$ or 1.7 mL $CHCl_3$/8.3 mL MeOH). Films dry overnight in the dark and are then cured with an LED source to minimize heating. The cure state for both sides of the films from photopolymerization is confirmed using FTIR based on alkene stretch conversion.

3.2 Characterization of MOF dispersal and film properties: glassy and rubbery composites

For PS and PMMA, SEM images of the resulting composite films with 10 wt% UiO-66-NH_2 are shown in Figure 3. As predicted by SCFT calculations using HSPs to estimate interaction parameters, UiO-66-NH_2 forms agglomerates in PS when cast in pure chloroform and in PMMA when cast in the ACN/EtOH mixture. Improved dispersion of UiO-66-NH_2 was observed in PS when cast in a chloroform/hexane mixture and in PMMA when cast in an acetone/hexane mixture. Quantitative image analysis was also performed to estimate the size of the UiO-66-NH_2 particles/agglomerates in each composite using the Fiji distribution of ImageJ (v. 1.53e). In the PS-based composite cast in pure chloroform, the area-averaged agglomerate size was 1.75 µm, while for the composite cast in the chloroform/hexane mixture the particle size was 0.26 µm, which is the approximate size of individual UiO-66-NH_2 crystallites. In the PMMA-based composite cast in the ACN/EtOH mixture the area-averaged particle size was 0.77 µm while for the composite cast in the acetone/hexane mixture the particle size was 0.31 µm. Measurement of glass transition temperature for the composites revealed important tradeoffs between increased polymer adsorption but reduced chain entanglements for the composite films cast with the poorer solvent quality for the polymer.[8]

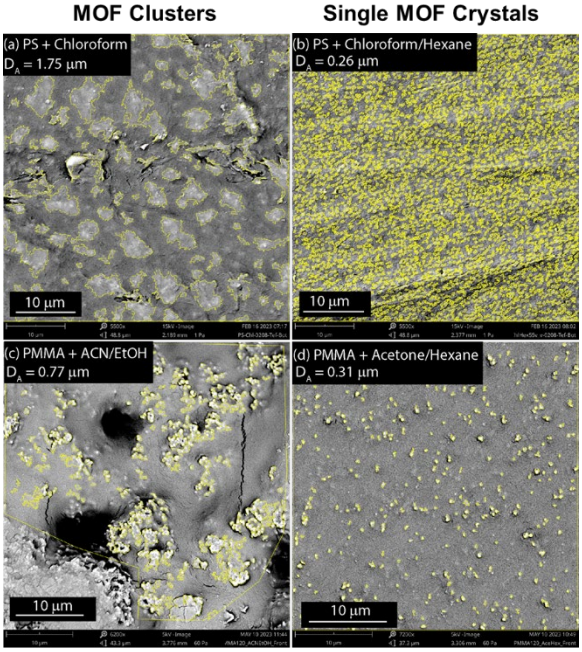

Figure 3. SEM images of solution cast composite films containing 10 wt% UiO-66-NH_2: (a) PS cast in pure chloroform, (b) PS cast in a 32 vol% chloroform/hexane mixture, (c) PMMA cast in a 27 vol% ACN/EtOH mixture, and (d) PMMA cast in a 70 vol% acetone/hexane mixture (adapted from reference 8).

Further evidence of differences in polymer chain interactions as a function of thin film processing can be measured in BDS, which probes the movement of electronic dipoles (e.g., dipolar molecules) in the presence of an oscillating electric field, E. Frequency dependent permittivity, ε, or dissipation factor, $tan\delta$, is analyzed and generally, lower/higher polymer chain mobility is associated with longer/shorter relaxation times, τ, where $f_{relaxation}$

corresponds to a peak in $tan\delta(f)$ and $\tau \sim \frac{1}{2\pi f_{relaxation}}$. Temperature dependent measurements for $tan\delta(f)$ allow for confirmation and comparison of relaxation modes. Longer polymer relaxation time was observed for PS/UiO-66-NH_2 using a solvent blend ($CHCl_3$/hexane) compared to an unoptimized solvent ($CHCl_3$). Temperature dependent measurements confirm tracking of the same polymer relaxation mode. Differences observed in response during the BDS heating cycle are either due to film thickness change/deformation or annealing of the composite; linear increase in $\log(\tau)$ with lower temperature is expected. Results suggest greater degree of interaction of PS polymer chains with UiO-66-NH_2 MOF crystals when films were cast from solvent blends that promoted MOF-polymer interactions. This is evidenced by the increase in relaxation times in these materials, where favorable adsorption of the polymer to the MOF surface would retard relaxation time as reported in other polymer composites.[22] Materials with a larger number of defects due to agglomeration/clustering of MOF solids reflect shorter relaxation times possibly due to the limited adsorption of polymer to the MOF surface.

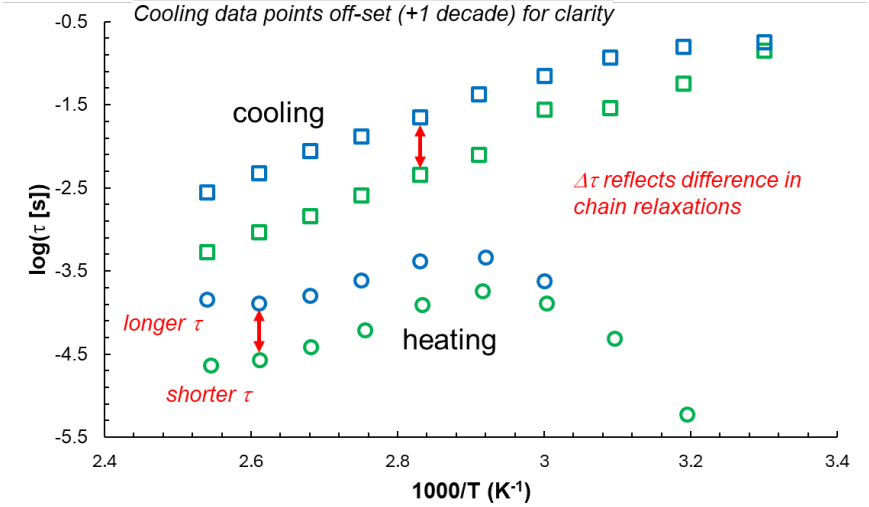

Figure 4. Broadband dielectric spectroscopy measurements for PS and 10 wt% UiO-66-NH_2 cast in either chloroform/hexane (blue) or chloroform (green). BDS data collection and analysis courtesy of Dr. Avery Baumann, NIST.

For the UiO-66-NH_2-poly(butadiene) films, process steps were developed to successfully cast and cure films in controlled solvent environments of either CH_3Cl or CH_3Cl/MeOH. Fourier transform infrared spectroscopy was used to confirm that photopolymerization was complete through the thickness of the films. An attempt was made to measure dielectric relaxation time with BDS on these films but the resonances were too high in frequency (very short τ) at room temperature and lower temperature measurements are necessary to confirm permittivity trends. Future work will explore modifications to the available instrumentation at NIST to increase the temperature range to resolve responses for softer materials. Upcoming measurements on UiO-66-NH_2-poly(butadiene) films produced with different solvent blends will use SEM to assess MOF dispersal and clustering, DSC to verify changes in glass transition temperature, DMA to determine crosslink density and relaxation behavior, and thermogravimetric analysis to confirm MOF loading and degradation temperature. These measurements will allow for a comparison with the work performed on PS and PMMA composites.

3.3 Measurement of solubility parameters for Zr-based MOFs

Turbidity measurements with probe solvents were performed on a range of Zr-based MOFs with different linker chemistries, MOF topologies, and crystal sizes to determine the viability for estimating solubility parameters. SEM, powder X-ray diffraction, N_2 isotherm for Brunauer-Emmett-Teller surface area, and thermogravimetric analysis measurements were performed to investigate if correlations could be drawn between fit Hansen solubility parameters and crystal properties.

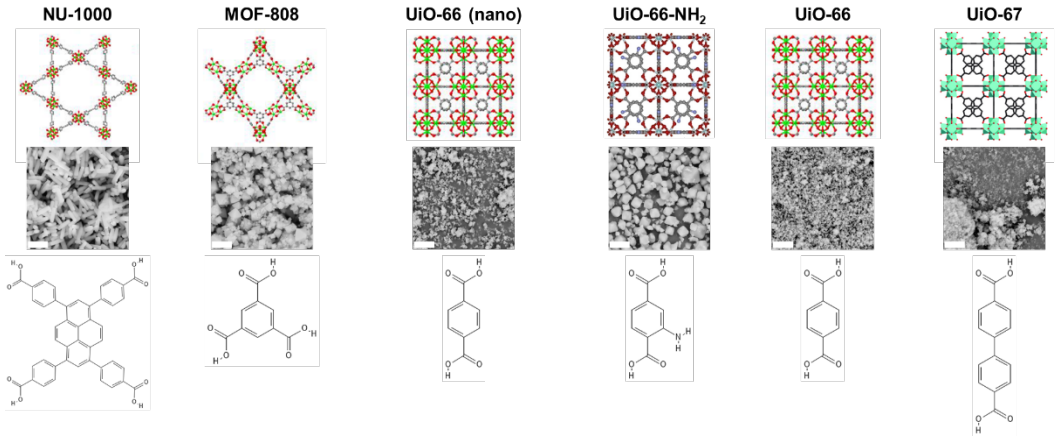

Figure 5. Set of Zr-based MOFs used for evaluating crystal property associations with turbidity-derived solubility parameters.

Time-dependent turbidity measurements were performed both for short (three hours) and long (seven days) term settling to determine rankings of solvent affinity for each of the MOF crystals shown, in a similar fashion to what was done previously for 200 nm UiO-66-NH_2 crystals.[8] All rankings were done by visual group of turbidity trends using concentration-corrected turbidity values and select corrections of rankings were made to avoid errors in HSPiP fits. Despite maintaining a common metal node chemistry, i.e., Zr, surveying such a wide variety of particle sizes and types resulted in several different challenges with regards to identification of clear trends, and it is possible that turbidity as invoked is not sensitive enough to the variations in crystal chemistry and structure. However, a few initial observations could be made from the data. All MOFs save NU-1000 show similar solubility sphere radius values between 9–11.2 (note that values of R<5 exist for polymers like poly(3,4-ethylenedioxythiophene) polystyrene sulfonate or polyvinyl chloride) and NU-1000 also shows high δH value, which could also lead to drop in sphere radius. Across these MOFs, unique solubility profiles in solvents persist despite similar chemistry; there are similar δD values with most apparent changes in δP and δH values. Furthermore, and interestingly, UiO-66 (nano) and UiO-66 show distinct Hansen behavior, which suggests that the MOF crystal size can influence turbidity-based solvent compatibility rankings. An initial attempt was made to determine if Hansen parameters tracked with MOF properties, and preliminarily, it appears there is an association of specific surface area with δD as shown in Figure 6. Follow-on experiments on components of the MOFs (e.g., nodes and linkers separately) and alternate means of producing rankings for HSPiP are currently being considered.

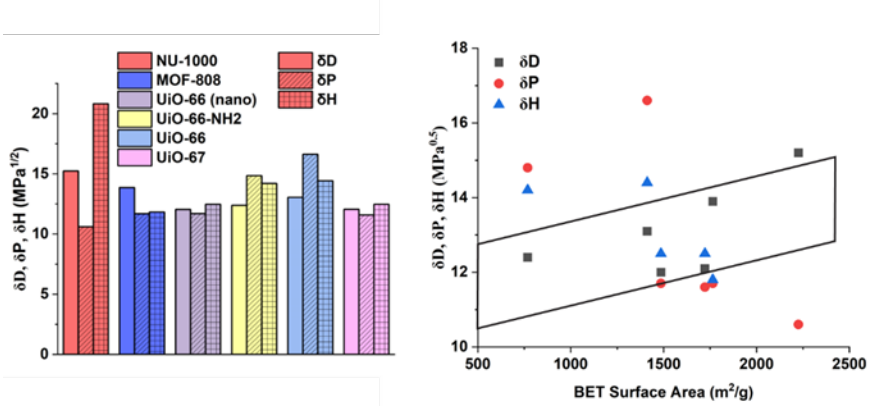

Figure 6. Solubility parameters for Zr-based MOFs and a composite plot of solubility parameters versus specific surface area for each MOF.

3.4 Computational modeling of MOF-polymer interfaces

Computational modeling using atomistic simulations is being used to ultimately examine transport properties at the molecular scale within interfaces in MOF-polymer composites. This follows from past work done for functionalized

silica-polyurethane systems.[23] The aim here is to determine how to theoretically model the interface in a composite with MOF particles where special attention is given to the MOF-polymer interface and surface morphology of the MOF. From this model, the goal is to then calculate diffusivities and study the transport of different chemical species through the porous interface and to probe how and why different properties of the MOF and polymer influence the transport. Recent work has revealed a strong dependence of the structure of the composite on the interfacial connectivity,[21] which in turn can greatly affect permeability and selectivity in the presence of diffusive penetrants.[4,24]

The objective herein is to develop a hybrid force field arrangement that integrates the MOF, polymer, and solvent interactions into a single set of interactions. Presently no single, "off-the-shelf" force fields are available that can treat both Zr-MOF frameworks and other inorganic molecular structures. A universal, robust set of interaction parameters for MOF structures by themselves also does not exist. There are three regions and sets of interactions: the MOF, the bulk polymer (far from the MOF), and the MOF-polymer interface. In this project the specific coupling of the various components has been achieved such that the MOF-MOF interactions are handled via an MM3 force field, the MOF-polymer and MOF-penetrant interactions via Universal force field parameters, and the polymer-polymer and polymer-solvent via a class II polymer consistent force field. An MM3 force field has been shown to accurately predict material properties of UiO-66 such as its bulk modulus and has previously been used in modeling diffusion of acetone and isopropanol in that MOF.[25,26]

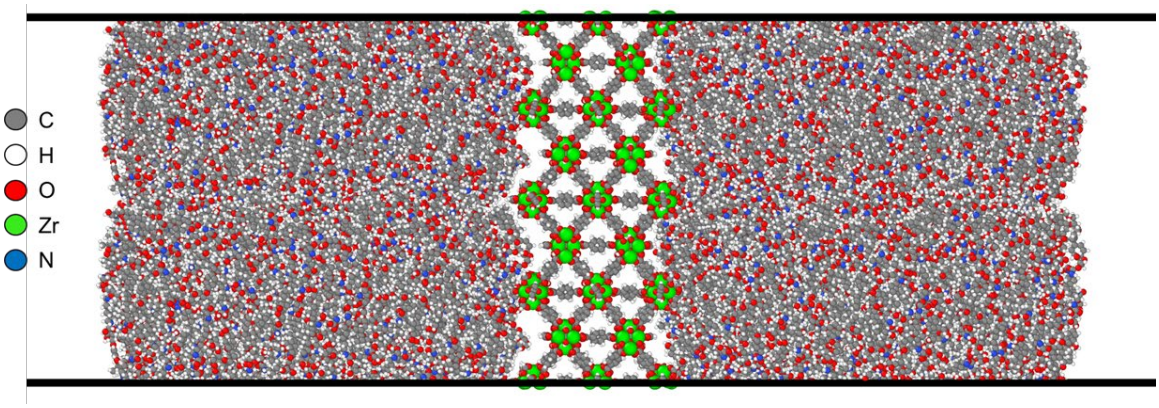

Figure 7. Simulation box that reflects the integrated force field for UiO-66, polyurethane, and hexane.

Figure 7 illustrates the initial introduction of the different components into a simulation cell, i.e., MOF (UiO-66), polymer (polyurethane), and a solvent (hexane, 10 wt%). This involves the use of the hybrid force field framework to capture interactions coupling the distinct species of the system. Modeling is currently focused on combinations of different termini of UiO-66 (base structure for MOF used experimentally) and previously studied, select polymers (polyurethane and polyhydroxyurethane) with linear solvents (hexane and hexanol) to quantify the mass density at the interface, polymer rigidity, porosity, and percolation of voids and other defects. Comparisons of these properties in fully relaxed and equilibrated structures will be made to those of the bulk polymer, and these results will inform subsequent calculations of transport of chemical species. Figure 8 shows the structures for different MOF termini as part of the combination of simulations to assess the impact of MOF surface chemistry in polymer depletion/adsorption at the interface.

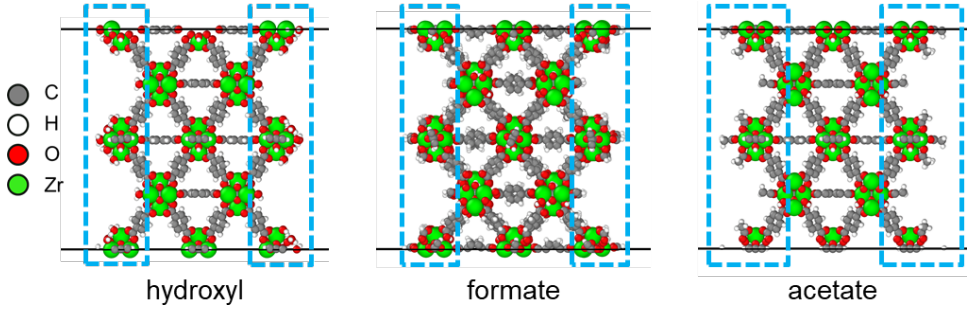

Figure 8. Variable termini for UiO-66 MOF.

4. CONCLUSIONS AND FUTURE WORK

An approach for generating MOF-polymer composites with variable MOF dispersion in the polymer using tuned solvent blends was established. These model systems illustrate the ability to control polymer chain interactions with the MOF periphery and to generate structures that are hypothesized to exhibit distinct mass transport properties. Hansen solubility parameters of the MOF UiO-66-NH_2 were used in conjunction with the Scheutjens-Fleer SCFT formulation to study the adsorption/depletion behavior of glassy (polystyrene and poly(methyl methacrylate)) and rubbery polymers (poly(butadiene)) on the surface of UiO-66-NH_2 crystallites. This work shows the potential utility of using HSPs in conjunction with SCFT to identify solvents/blends to control MOF-polymer interactions and the resulting dispersion of MOF crystallites. To complement the continuum level calculations based on SCFT, a hybrid framework has been established for atomistic simulations to capture MOF-polymer-solvent structures using molecular dynamics. The developed approach is extensible to a wide variety of MOF-polymer composites and will be instrumental in understanding chemical penetrant behavior at complex interfaces.

Future work will be pursued on multiple research fronts. First, it would be useful to apply the methods laid out in this work to other MOF-polymer systems of interest as well as treat the dispersion of other functional solid inclusions, e.g., low dimensional materials like graphene, MXenes, melanin. Second, solubility parameter measurements for MOFs and other functional solids can be assessed with measurements that do not depend on turbidity. This could include a combination of nanoindentation measurements with MOF crystals attached to force spectroscopy cantilevers and other means of measuring forces between particles as a function of chemical environment.[27] Third, additional characterization of the polymer structure and chain dynamics at the MOF interface compared to the bulk would provide a more complete picture of how tuning the three-way MOF-polymer-solvent interactions influences the final state of the composite film.[28] Lastly, chemical mass transport measurements in MOF-polymer composite films using quartz crystal microbalance and Fourier transform infrared-attenuated total reflectance spectroscopy can characterize sorption of a penetrant chemical into different bulk polymers and probe penetrant-polymer interactions.[29,30] This will allow for a determination of the influence of MOF dispersal type on transport behavior for specific types of penetrant chemicals, e.g., hexane, chlorohexane, dicholorohexane, and 2-chloroethyl ethyl sulfide.

ACKNOWLEDGMENTS

The authors thank colleagues in Decontamination Sciences and Protective Materials Development Branches at the U.S. Army Combat Capabilities Development Command Chemical Biological Center who supported this effort. Further, we thank Dr. Avery Baumann (NIST Functional Polymers Group) for performing BDS measurements and analysis. Funding was provided by the U.S. Army via the Chemical Biological Advanced Materials Manufacturing Science Program (PE 0601102A Project VR9) at the Combat Capabilities Development Command Chemical Biological Center.

REFERENCES

[1] Cooley, K.A.; Pearl, T.P.; Varady, M.J.; Mantooth, B.A.; Willis, M.P. Direct measurement of chemical distributions in heterogeneous coatings. *ACS Appl. Mater. Interfaces.* **2014**, *6* (18), pp 16289–16296.

[2] Peterson, G.W.; Browe, M.A.; Durke, E.M.; Epps, T.H. Flexible SIS/HKUST-1 mixed matrix composites as protective barriers against chemical warfare agent simulants. *ACS Appl. Mater. Interfaces* **2018**, 10 (49), pp 43080–43087.

[3] Peterson, G.W.; Wang, H.; Au, K.; Epps, T.H. Metal-organic framework polymer composite enhancement via acyl-chloride modification. *Polym. Int.* **2021**, *70* (6), pp 783–789.

[4] Keskin, S.; Altinkaya, S.A. Review on computational modeling tools for MOF-based mixed matrix membranes. *Computation.* **2019**, *7* (3), p 36.

[5] Denny, M.S.; Moreton, J.C.; Benz, L.; Cohen, S.M. Metal-organic frameworks for membrane-based separations. *Nat. Rev. Mater.* **2016**, *1* (12), p 16078.

[6] Semino, R.; Moreton, J.C.; Ramsahye, N.A.; Cohen, S.M.; Maurin, G. Understanding the origins of metal-organic framework/polymer compatibility. *Chem. Sci.* **2018**, *9* (2), pp 315–324.

[7] Kalaj, M.; Bentz, K.C.; Ayala, S.; Palomba, J.M.; Barcus, K.S.; Katayama, Y.; Cohen, S.M. MOF-polymer hybrid materials: from simple composites to tailored architectures. *Chem. Rev.* **2020**, *120* (16), pp 8267–8302.

[8] Varady, M.J.; Schenning, C.S.; Thompson, C.B.; Mantooth, B.A.; Peterson, G.W.; Pearl, T.P. Solvent selection guided by self-consistent field theory for improved dispersion of metal–organic frameworks in polymers. *ACS Appl. Polym. Mater.* **2024**, *6* (1), pp 888–895.
[9] Palomba, J.M.; Wirth, D.M.; Kim, J.Y.; Kalaj, M.; Clarke, E.M.; Peterson, G.W.; Pokorski, J.K.; Cohen, S.M. Strong, ductile MOF-poly(urethane urea) composites. *Chem. Mater.* **2021,** *33* (9), pp 3164–3171.
[10] DeCoste, J.B.; Peterson, G.W.; Jasuja, H.; Glover, T.G.; Huang, Y.G.; Walton, K.S. Stability and degradation mechanisms of metal-organic frameworks containing the $Zr_6O_4(OH)_4$ secondary building unit. *J. Mater. Chem. A.* **2013**, *1* (18), pp 5642–5650.
[11] Vanduyfhuys, L.; Vandenbrande, S.; Verstraelen, T.; Schmid, R.; Waroquier, M.; Van Speybroeck, V. QuickFF: A program for a quick and easy derivation of force fields for metal-organic frameworks from ab initio input. *J. Comput. Chem.* **2015**, *36* (13), pp 1015–1027.
[12] Zhang, P.F. Critical Depletion, Adsorption, and Intersurface Interaction in Polymer Solutions: A Mean-Field Theory Study. *Macromolecules.* **2021**, *54* (8), pp 3790–3799.
[13] Fleer, G.J.; Cohen Stuart, M.A.; Scheutjens, J.M.H.M.; Cosgrove, T.; Vincent, B. *Polymers at Interfaces*. Springer Science & Business Media: Berlin, Germany, **1998**; p 496.
[14] Postmus, B.R.; Leermakers, F.A.M.; Stuart, M.A.C. Self-consistent field modeling of poly(ethylene oxide) adsorption onto silica: The multiple roles of electrolytes. *Langmuir.* **2008**, *24* (5), pp 1930–1942.
[15] Tuinier, R.; Fleer, G.J. Concentration and solvency effects on the pair interaction between colloidal particles in a solution of nonadsorbing polymer. *Macromolecules.* **2004**, *37* (23), pp 8764–8772.
[16] Vanderlinden, C.C.; Vanlent, B.; Leermakers, F.A.M.; Fleer, G.J. Adsorption of polymers on heterogeneous surfaces. *Macromolecules.* **1994**, *27* (7), pp 1915–1921.
[17] Scheutjens, J.; Fleer, G.J. Statistical-theory of the adsorption of interacting chain molecules. 1. partition-function, segment density distribution, and adsorption-isotherms. *J. Phys. Chem.* **1979**, *83* (12), pp 1619–1635.
[18] Scheutjens, J.; Fleer, G.J. Statistical-theory of the adsorption of interacting chain molecules. 2. train, loop, and tail size distribution. *J. Phys. Chem. A* **1980**, *84* (2), pp 178–190.
[19] Barton, A.F.M. *CRC Handbook of Polymer-Liquid Interaction Parameters and Solubility Parameters*. CRC Press: Boca Raton, FL, **1990**.
[20] Hansen, C.M. *Hansen Solubility Parameters: A User's Handbook, 2nd ed.* CRC Press: Boca Raton, FL, **2007**.
[21] Hiaki, T.; Kurihara, K.; Kojima, K. Vapor-liquid equilibria for acetone+ chloroform+ methanol and constituent binary systems at 101.3 kPa. *J. Chem. Eng. Data.* **1994**, *39* (4), pp 714–719.
[22] Holt, A.P.; Griffin, P.J.; Bocharova, V.; Agapov, A.L.; Imel, A.E.; Dadmun, M.D.; Sangoro, J.R.; Sokolov, A.P. Dynamics at the polymer/nanoparticle interface in poly(2-vinylpyridine)/silica nanocomposites. *Macromolecules.* **2014**, *47* (5), pp 1837–1843.
[23] Hinkle, A.R.; Browe, M.A.; Iordanov, I.O.; Mantooth, B.A.; Pearl, T.P.; Varady, M.J. Effect of interfacial regions and surface functional groups on chemical transport in polymer-particle composites. *J. Phys. Chem. C.* **2023**, *127* (23), pp 11231–11239.
[24] Ozcan, A.; Semino, R.; Maurin, G.; Yazaydin, A.O. Modeling of gas transport through polymer/MOF interfaces: a microsecond-scale concentration gradient-driven molecular dynamics study. *Chem. Mater.* **2020**, *32* (3), pp 1288–1296.
[25] Wardzala, J.J.; Ruffley, J.P.; Goodenough, I.; Schmidt, A.M.; Shukla, P.B.; Wei, X.; Bagusetty, A.; De Souza, M.; Das, P.; Thompson, D.J.; Karwacki, C.J.; Wilmers, C.E.; Borguet, C.P.; Rosi, N.L.; Johnson, J.K. Modeling of diffusion of acetone in UiO-66. *J. Phys. Chem. C.* **2020**, *124* (52), pp 28469–28478.
[26] Mhatre, C.V.; Wardzala, J.J.; Shukla, P.B.; Agrawal, M.; Johnson, J.K. Calculation of self, corrected, and transport diffusivities of isopropyl alcohol in UiO-66. *Nanomaterials.* **2023**, *13* (11), p 1793.
[27] Palomba, J.M.; Saygin, V.; Brown, K.A. Experimental observation of metal–organic framework–polymer interaction forces and intercalation. *Chem. Commun.* **2023**, *59* (3), pp 290–293.
[28] Baumann, A.E.; Beaucage, P.A.; Vallery, R.; Gidley, D.; Nieuwendaal, R.C.; Snyder, C.R.; Ilavsky, J.; Chen, F.; Stafford, C.M.; Soles, C.L. Assessing composite structure in metal-organic framework-polymer mixed-matrix membranes. *Chem. Mat.* **2024**, *36* (6), pp 3022–3033.
[29] Boyne, D.A.; Varady, M.J.; Lambeth, R.H.; Eikenberg, J.H.; Bringuier, S.A.; Pearl, T.P.; Mantooth, B.A. Solvent-assisted desorption of 2,5-lutidine from Polyurethane films. *J. Phys. Chem. B.* **2018**, *122* (7), pp 2155–2164.
[30] Varady, M.J.; Boyne, D.A.; Pearl, T.P.; Lambeth, R.H.; Mantooth, B.A. Composition-dependent multicomponent diffusivity of 2,5-lutidine with acetonitrile in polyurethane. *Polymer.* **2019**, *180*, p 121697.

Developing design rules for CBRN-relevant additive manufacturing systems by probing network structure and system free volume

Chase B. Thompson[a,b], Susan K. Kozawa[a,c], and Kristian M. Van de Voorde[a]*
[a]U.S. Army Combat Capabilities Development Command Chemical Biological Center, Research & Operations Directorate, 8198 Blackhawk Rd, Aberdeen Proving Ground, MD 21010
[b]Leidos, Inc., 11951 Freedom Dr, Reston, VA 20190-5640
[c]Oak Ridge Institute for Science and Education, 1299 Bethel Valley Rd, Oak Ridge, TN 37830

ABSTRACT

Photopolymerization additive manufacturing has gained traction as a platform to produce high performance materials in areas such as tissue engineering and soft robotics. However, a gap in the current knowledge remains on how minute variations during resin formulation can impact the properties of these crosslinked, 3D printed parts. In this study, a series of model resins were printed with varied printing settings to connect the influence of the manufacturing process to the resulting properties of the printed parts. Thermomechanical properties and transport properties were the primary focus. An impact on the connectivity and heterogeneity was observed as the layer size of the induvial slices changed. Larger layer depth parts have a bimodal tanδ curve. Moreover, the effective crosslinking density was dependent on the manufacturing parameters. Manipulation of the effective crosslinking density was a variation in the network-structure. This aspect of the polymer structure was found to correlate to properties such as mechanical, aging, and transport. Additionally, this work explores utilization of structure-property dynamics to manipulate macroscopic behavior such as actuation. Overall, these findings highlight the need for an understanding of the polymerization pathways utilized in resin 3D printing as the foundation towards predicting thermomechanical and functional properties of crosslinked systems.

Keywords: additive manufacturing, 3D printing, advanced manufacturing, vat polymerization, digital light processing, polymer networks.

1. INTRODUCTION

Additive manufacturing (AM) of soft materials has emerged as a technique capable of rapidly producing complex geometries with a wealth of material chemistries and physical properties.[1,2] Of the available 3D printing technologies, vat photopolymerization processes such as digital light processing (DLP) 3D printing offers high spatial resolution, short printing times, material tunability, and robust mechanics. Likely the most familiar and accessible vat polymerization AM method is stereolithography, popularized by such familiar names as Formlabs and Anycubic. Vat polymerization utilizes liquid polymer resins that are crosslinked using radiation, UV, or visible light to produce solid parts. The vat polymerization relies on the precise projection of light to polymerize a layer of photosensitive resin into the desired shape, with spatial resolution determined by the voxel.[3] Layer thickness, layer cure time, and post-cure conditions all dictate the specific polymerization pathway of each print layer, with factors such as light penetration and total dosage determining how these print parameters translate to polymerization kinetics.[3–5] Consequently, the printer as well as the resin formulation dictate the resulting properties of the manufactured part.

Recently, several research efforts have been conducted to better understand the effect of the printer on the resulting mechanical properties.[6,7] While the connection of specific printer parameters to the resulting printed part have been established, a lack of understanding on how and to what extent each of the parameters contributed to the bulk properties still existed. To fill this gap, this project focused on vat polymerization-based additive manufacturing methods that considered structure-property relationships that arise from tuning different aspects of the printing process utilizing commercially available resins.

In the initial focus of this project, the influence of print properties, e.g., layer thickness, cure time, etc., on mechanical properties of a commercially available resin to facilitate future explorations of how those properties are affected by network structure. During this investigation, drastically different mechanical properties were measured for parts manufactured with the same resin at different printer settings. Those variations in mechanical properties were

determined to be the result of different microstructures within the printed parts. To further elucidate information on the microstructure, a complete understanding of the resin formulation is required. As a result, the focus of the second year of this project was on the development of a series of model resins. These resins had two key components of the formulation that were varied: the functionality of the crosslinker (*f*, 2 or 4) and the concentration of the photoinitiator. Increasing both the photoinitiator concentration (from 0.2 mol% to 1.0 mol%) and the crosslinker functionality allows for control over the connectivity and heterogeneity of the resulting prints and a better opportunity to understand the overall microstructure of the print. Printed parts were manufactured at the same printing parameters and the resulting network topology was investigated. Primarily, dynamic mechanical analysis (DMA) was utilized to characterize the network topology of the prints. During this investigation, significantly different structures and properties were observed across the series of resins. Utilizing a crosslinker with a higher functionality resulted in an increase in inhomogeneities. Additionally, an 'ideal' concentration of photoinitiator was determined as it enabled an optimized number of effective crosslinks to form during the printing process.

To conclude this program, the final year of effort focused on investigating the effect of varying printing properties within a model resin system. These printed parts were then probed via DMA and dye elution studies to correlate the variations in printing parameters to the bulk properties. The photopolymerization of thermoset acrylates proceeds by initiation, propagation, and termination as described by typical free radical polymerizations; however, the gelation of the network, caused by the formation of a system-spanning continuous crosslinked structure, substantially influences the polymerization kinetics due to a loss in mobility. Factors such as light dosage and light penetration also play a role in the photopolymerization kinetics and can result in polymerization fronts that drive differences in local gelation behavior.[11,12] The rapid onset of gelation in free radical thermosetting (meth)acrylate resins yields distinct differences in the local and global crosslink densities within the network.[8,13] This heterogeneity in chain connectivity results in regions of high crosslink density, termed microgels, that are separated by long strands with fewer crosslink junctions.[14] Network heterogeneity is influenced by several factors including monomer concentration, crosslinker functionality, and monomer reactivity.[14,15] These structures have a profound impact on the bulk properties of the network. In this work, we will connect the manufacturing process to the chemistry so future, mission-specific formulations can be generated with a high confidence as the observed trends set in place formulation-design principles.

2. MATERIALS AND METHODOLOGY

2.1 Materials

All chemicals were purchased from Millipore Sigma and used as received unless stated otherwise. The 2-propanol used in this work was purchased from Fisher Scientific and used as received.

2.2 General methods

2.2.1 Resin formulation

During this investigation, a total of eight resins were formulated for DLP 3D printing. The primary formulation utilized a calculated amount of 2-hydroxyethyl acrylate (HEA) and poly (ethylene glycol) diacrylate (PEGDA-575) at a molar ratio of 9:1 (HEA to PEGDA). The monomer (HEA) and the crosslinker (PEGDA) was added to an amber jar equipped with magnetic stirring and vigorously mixed. The initiator, phenylbis(2,4,6-trimethylbenzoyl) phosphine oxide (BAPO), was weighed and added into the mixture in an amount of 0.5 mol% of total acrylate content in the resin. Similarly, a resin was formulated that only used HEA (no PEGDA). For some studies within this investigation, both Rodamine 6G and Sudan III were utilized as a dye and were added at a wt % of 0.002. The Rodamine 6G dye was mixed into the resins that were later studied under florescent microscopy, and Sudan III dye was used during the brief study into actuation behavior of hygromorphic bilayers. The remaining six model resin formulations were the same mixtures that were studied the previous year, and then served as the passive layer in the actuating bilayer prints. Calculated amounts of *tert*-butyl acrylate and *n*-butyl acrylate were mixed in an amber jar equipped with magnetic stirring. Afterwards, either 1,6-hexanediol diacrylate or pentaerythritol tetraacrylate were added as crosslinkers in calculated amounts to ensure that the resulting resin contained 7:2:1 *tert*-butyl acrylate:*n*-butyl acrylate :crosslinking acrylate functional groups. The formula was adjusted so that there were a constant number of crosslinking functional groups in resins consisting of 1,6-hexanediol diacrylate (difunctional, 2F) or pentaerythritol tetraacrylate (tetrafunctional, 4F) crosslinker. After the base resin is thoroughly mixed, BAPO was weighed out and added into the mixture in an amount of 0.2, 0.5, or 1.0 mol% of total acrylate content in the resin. Afterwards, the resin was mixed

thoroughly and added to the print vat or stored in a chemical refrigerator. Each of the model resins were well mixed such that a homogenous, optically transparent solution was generated.

2.2.2 3D printing

All printing was conducted on an Anycubic Photon M3 printer. Rectangular specimens were prepared for most tests (either 20 mm x 5 mm x 1 mm LWT, or 20 mm x 5 mm x 0.5 mm LWT). For the HEA-PEGDA and HEA specimens, layer cure times were set to either 10 seconds or 14 seconds, and the layer depth alternated between 50 μm and 100 μm. Additionally, bilayers were generated using set parameters of 12 seconds and 100 m. The two distinct layers were formed through the implementation of a vat exchange process. First, the passive layer was printed from the 2F and 4F resin series; then the printer was paused, and the vat was removed. A vat containing HEA was mounted to the printer, and the print was allowed to continue for the remaining time. Printed samples were briefly washed with 2-propanol from a squirt bottle, patted dry with a Kim wipe, and sandwiched between 2 glass slides held closed with binder clips for post-curing. UV post curing was conducted in an Anycubic Wash and Cure Plus machine for 20 minutes such that both sides of the printed specimen were evenly cured.

2.2.3 Dynamic mechanical analysis

The thermal characteristics of printed parts were determined using a TA Instruments 850 Dynamic Mechanical Analyzer operating in tension mode with film clamps. For measurement of the glass transition temperature and rubbery plateau, samples were subjected to an isochronal temperature ramp. Samples were deformed to a strain of 0.1 % at an oscillation frequency of 1 Hz across a temperature range of -40–60 ºC at a ramp rate of 3 ºC/minute. Each sample run was repeated in triplicate and analysis was performed in the Trios software.

2.2.4 Dye elution

To investigate the transport properties, a dye elution study was completed. The HEA-PEGDA specimens were printed with a single layer containing the fluorescent dye. The localization of the dye was done through the vat exchange process during the printing step. Rodamine 6G was elected as it was not photobleached from the UV exposure that was used while the part was printed. These fluorescent specimens were then fixed to a glass slide with super glue such that the layer stack was normal to the glass slide. Initial images were taken with a fluorescent microscope at 4x and 10x. The original area that was imaged was recorded to enable the same area to be imaged throughout the study. The mounted samples were then placed into a turbulent water bath at room temperature. At regular intervals, the samples were removed from the bath, dried by blotting with a Kim wipe, and re-imaged at 10x magnification.

An additional transport study was also done on the HEA-PEGDA samples via UV-vis spectroscopy. Here, rather than observing the dye leach into other layers like in the previous study, the focus was on measuring the concentration of the dye that leached into the turbulent water bath. The samples used here had dye in each of the printed layers. A total of 1 g of the HEA-PEGDA specimens were placed into a 15 mL falcon tube with 10 mL of water. The falcon tubers were then placed on a roller to allow the water to continually wash over the specimen. At regular time intervals, 2 mL of water was removed from the falcon tubes, and 2 mL of fresh water was added back to the containers to maintain a consistent concentration of specimen in water utilized. The washed water was then placed in a cuvette and analyzed via UV-vis spectroscopy. The absorbance spectra were recorded between 200–800 nm. The spectra of each aliquot had a baseline correction before it was imported into a data analysis software, Origin Pro. The singular peak in each of the tests was observed that correlated Rodamine 6G, and the peak was integrated. The integrated value for the sequential time points was added to the integral of the time point prior to its measurement.

2.2.5 Curvature

Bilayer prints were imaged to calculate their radius of curvature. Rectangular bilayer prints were place on the bottom of a single well plate with their short ends adhered to the side of the dish with an adhesive to establish an anchoring point. Samples were arranged in such a way that the print layers were normal to the camera lens (Canon EOS Rebel T3 camera with a EFS 18-55 SLR lens). Distilled water was then added to the bilayers and images were captured every minute for the first 30 minutes of the experiment, followed by once every 15 minutes for the remaining 150 minutes of the actuation experiment to track the change in bilayer curvature as a function of time. The displacement of the films was measured using the Kappa plugin available for ImageJ. The radius of curvature (κ) was calculated according to equation (1) where ρ is the radius of the circular arc measured from the displacement experiments.

$$\kappa = \frac{1}{\rho} \tag{1}$$

3. RESULTS

3.1 Sample printing

DLP 3D printing is a complex process in which photopolymerization is used to print objects in a layer-by-layer fashion; different aspects of the resin chemistry will strongly influence the properties of the printed part. Understanding how the covalent crosslinks develop during the print process is vital for the expanded use of 3D printing as an on-demand manufacturing technique and for developing highly functional and reproducible parts. To study how network connectivity influences print properties, a model resin was first developed for various printing parameters. HEA was selected as the monomer due to its previous established success as a 3D printable resin, hydrophilicity, and unique ability to crosslink with itself under specific criteria. Poly(ethylene glycol) diacrylate (M_n-575) was used as the crosslinker. For the model resins, it was critical the reaction during the 3D printing process represent as many as possible acrylate-based resin formulations. Additionally, the hydrophilicity was important to allow for simplistic experimental conditions during the transport property investigations. The HEA-PEGDA resin formulation (Figure 1) was mixed with a ratio of 9:1 (HEA to PEGDA), and an initiator content of 0.5 mol% of total acrylate was added. Initiator (BAPO) content was determined from the success of the model resins from the previous year of this program. This resin was the primary focus of this year, and as such, it was printed with a range of printing parameters. The layer exposure was set to either 10 seconds or 14 seconds, and the layer thickness was set to either 50 µm or 100 µm. In total, the primary sample matrix of four distinctly different HEA-PEGDA specimens were evaluated. Additionally, a resin with only HEA was also printed at similar conditions to compare thermomechanical properties. Finally, hygromorphic bilayers were printed, where HEA was used to generate the active layer. The passive layers were formed from the model resin series that was the focus of the previous year's investigation.

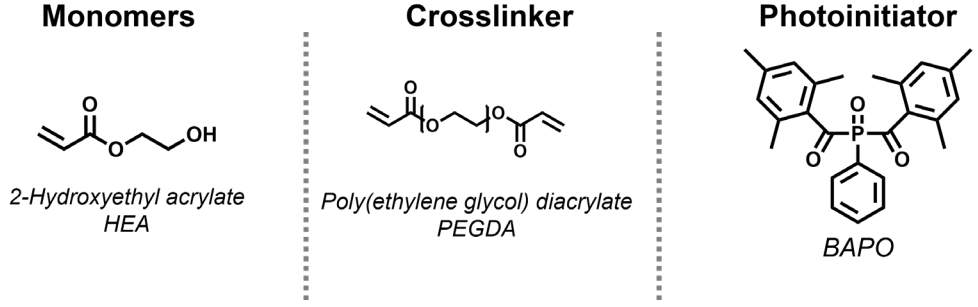

Figure 1: Components of model resins.

3.2 Thermal properties

The prints were subjected to DMA to establish how small changes in the print formulation influence the thermal properties. The shape of the tanδ curve offers insight into the structure and connectivity of thermoset networks. While the position of the peak can be used to estimate the T_g of a system from the α relaxation, the peak full width half

maximum (FWHM) is related to the distribution of chain motions in a system and, therefore, the heterogeneity of the network. A sample with a greater tanδ FWHM is more heterogeneous than a narrower peak as described by the Gaussian distribution of segmental motions during the α relaxation process.[18,19] The tanδ curves for the HEA-PEGDA print series are illustrated in Figure 2A. An interesting difference in the shape of these curves between the 100 µm and 50 µm prints is immediately apparent. In the 50 µm series, the tanδ curve was a single, broad peak, and the FWHM was similar (14 sec: 23.3 ± 3.4 °C, 10 sec: 21.1 ± 1.4 °C), and the T_g was relatively similar (14 sec: 8.91 ± 0.76 °C, 10 sec: 7.05 ± 0.34°C). This indicates there was a minimal effect of the layer cure time on the overall formation of the network when a smaller cure depth was utilized. Comparatively, the tanδ curves from the 100 µm series were significantly different than their 50 µm counterparts. In the 100 µm series, a bimodal distribution of chain relaxation was observed from the tanδ curves. In thermosets, a biomodal distribution can indicate the presents of two distantly different networks. While the intended network for this formulation was linear HEA chains connected to PEGDA junctions, there was an alternative reaction pathway that could have occurred. Other researchers have observed HEA crosslinking itself such that HEA forms both the linear chains and the junction points. These junction points tend to form in a highly irregular pattern throughout the network. Consequently, the biomodel tanδ curves observed in the 100 µm series is likely due to part of the network consisting of HEA chains connected to PEGDA and other regions in the network consisting of HEA crosslinking with itself (Table 1).

Table 1. DMA data for the acrylate systems sample sets. [a]Determined from the peak of the tanδ curve.

	[a]T_{g1} (°C)	[a]T_{g2} (°C)	FWHM (1) (°C)	FWHM (2) (°C)	Area Ratio (1 to 2)	ν_e x 10^{-3} (mol/m^3)
14 sec-100 µm	-5.31 ± .84	9.46 ± 1.6	23.3 ± 3.4	7.86 ± 0.48	2.25 ± 0.18	761 ± 14
10 sec-100 µm	-10.4 ± 1.5	5.73 ± 1.7	21.1 ± 1.4	10.6 ± 0.47	1.12 ± 0.078	765 ± 11
14 sec-50 µm	-	8.91 ± 0.76	-	17.8 ± 0.42	-	702 ± 25
10 sec-50 µm	-	7.05 ± 0.34	-	18.8 ± 1.1	-	690 ± 22
Batch Cure	-9.4 ± 3.2	-	-	-	-	156 ± 23
HEA-10-100	-11.3 ± 2.7	-	-	-	-	13 ± 8.9

To determine the relative amount of the network that was formed from HEA to PEGDA versus HEA alone, the tanδ curves were fit and separated into two separate, unimodal peaks. These single peaks were then integrated, and the ratio of peak one (lower temperature peak) to peak two (higher temperature peak) was determined. In the 14 sec-100 µm specimen tested, the area of the peak one was twice as large as the area of peak 2 (2.25 ± 0.18). However, in the 10 sec-100 µm specimen, the areas were near equivalent (1.12 ± 0.078). Peak two is the apparent peak that was observed in the 50 µm series, so that likely correlates to the HEA-PEGDA network. To confirm the peak to network correlation, an HEA resin with no PEGDA was 3D printed at 10 sec-100µm (Figure 2B). The tanδ curve generated from the HEA formulation was a single peak that correlated to peak one. From this, we determined that the HEA self-crosslinking reaction is favorable if the layer thickness is larger. Furthermore, when longer exposure times are implemented, this side reaction is even more favorable as the ratio of the two peaks was twice as large in the 14 sec-100 µm samples. Here, a clear significant effect on the printing parameters was highlighted, and we wanted to test these 3D printed parts to a film that was produced from a simple film casting-bulk cure method. A sample of comparable dimensions was produced from the HEA-PEGDA resins and tested via DMA (Figure 2B). The tanδ of the batch cured sample was a single, broad peak. Interesting, the peak of this broad curve was at the lower temperatures, which indicated a high presence of HEA self-crosslinking.

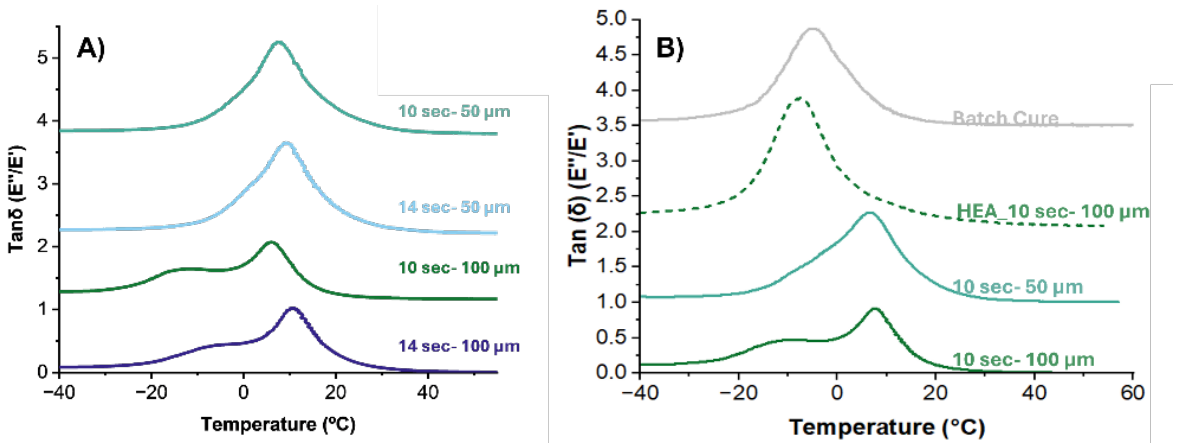

Figure 2: Representative tanδ curves of A) HEA-PEGDA systems printed with different parameters and B) a batched cured sample, HEA, and two HEA-PEGDA systems

In addition to observing the network topology through the analysis of the tanδ curves, DMA was also used to calculate the effective crosslinking density (ν_e) using equation (2):

$$\nu_e = \frac{E'}{3RT} \tag{2}$$

Where E' is the plateau storage modulus at temperature T and R is the universal gas constant.[20] The increase in effective crosslink density, while not being a result of the overall conversion of the network, may be influenced by network defects like dangling chain ends or loops that do not contribute to the overall elasticity of the thermoset network.[15] All of the 3D printed systems had a very similar effective crosslinking density (~ 0.7 mol/m^3). However, there was a statistical increase in the effective crosslinking density of ~0.06 as the layer thickness increased. This increasing is likely the result of the 100 µm series having a high content of HEA that crosslinks with itself.

3.3 Dye elution

To understand transport properties of the 3D printed HEA-PEGDA series, a dye elution study was conducted. Samples were printed with a vat exchange method such that a single layer incorporated a fluorescent dye, Rhodamine 6G. These single dye layer prints were washed for up to 90 minutes and periodically removed and imaged (Figure 3). From these micrographs, the dye can be observed to leach out into the neighboring layers. After only 30 minutes, it was evident that the dye had eluted into each of the layers for each of the HEA-PEGDA samples. Due to challenges in normalizing the florescence of the image, quantitative analysis was not able to be done from the imaged obtained.

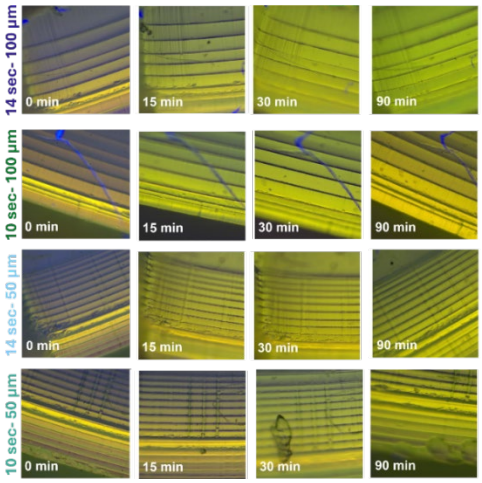

Figure 3: Florescent microscope images of HEA-PEGDA samples that contain a single layer of fluorescent, water soluble dye at various time points when the samples were washed.

An additional dye elution study was done using UV-Vis spectroscopy. During this study, 3D printed parts were printed with the HEA-PEGDA resin formulation with dye in each of the layers. The fluorescent samples were washed in falcon tubes at a consistent concentration. Aliquots of the washing solvent, water, were taken periodically and tested via UV-vis spectrometry to determine the comparative concentrations of dye. The peak from the individual spectra was integrated, and the absorbance was calculated and plotted against time (Figure 4A). While most of the samples have a consistent trend in the amount of dye that was measured over time the 10 sec-50 µm appeared to be an outlier. To elucidate the relationship between the printing parameters and the transport properties, the integrated absorbance was plotted against the effective crosslinking density (Figure 4B). In this simplistic plot, it was apparent that a higher effective crosslink density yields a lower amount of dye eluted. This structure-property correlation is to be expected as a network that has more junction sites that are well distributed are more likely to generate higher tortuosity.

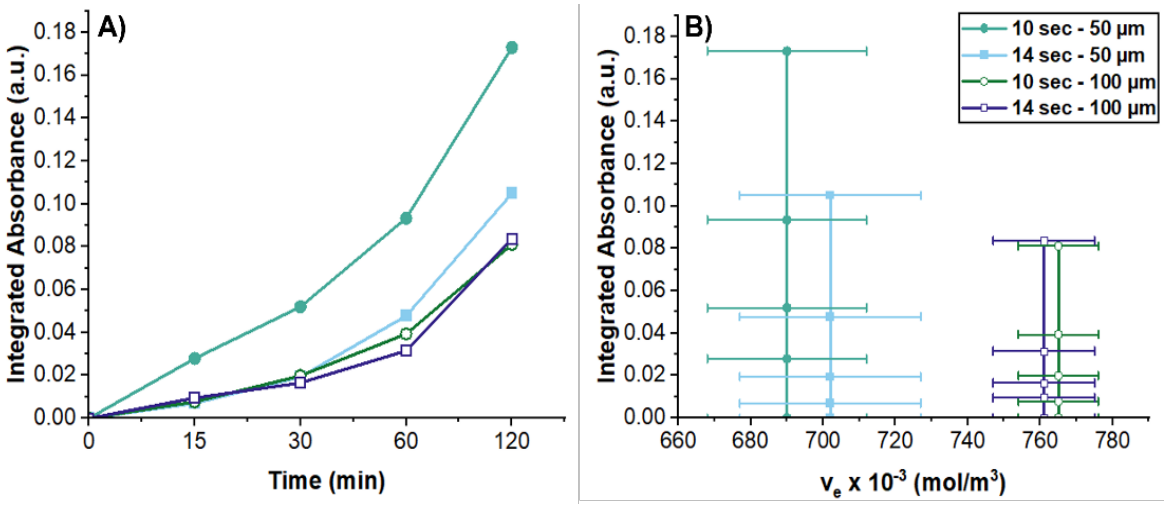

Figure 4: A) Integrated absorbance of dye eluted into water from samples over time. B) Relationship depiction of integrated absorbance and the effective crosslinking density.

3.4 Curvature

Additive manufacturing has garnered attention as a platform to produce stimuli-responsive functional materials because of the control of sample geometry and chemistry available in 3D printing. One area of interest is the printing of shape-changing actuators. Vat photopolymerization 3D printing can easily produce bilayer actuator architectures through simple vat exchange during the print, enabling for unique crosslinking chemistries to be incorporated into shape morphing soft robots. To demonstrate the utility of fine-tuning the thermal and mechanical properties of our 3D printed samples, we set out to incorporate these model resins as the passive layer in a hygromorphic actuator. The active layer consists of HEA loaded with 1 mol% BAPO as photoinitiator and Sudan III as a dye as adapted from prior literature. The passive layer resin was printed first. At 50 % completion, the print was paused and the passive resin vat containing either 2F or 4F resin was replaced with the active HEA resin formulation; printing was then resumed until completion. After washing and post-curing, the bilayer samples were submerged in distilled water at room temperature. In all cases, the swelling of the HEA layer caused the samples to curl inward toward the passive layer as described in typical hygromorphic bilayers (Figure 5). Water uptake studies of the different prints demonstrates that none of the passive layer prints take up any water while the active HEA layer shows a marked water uptake of 223 % of the initial mass.

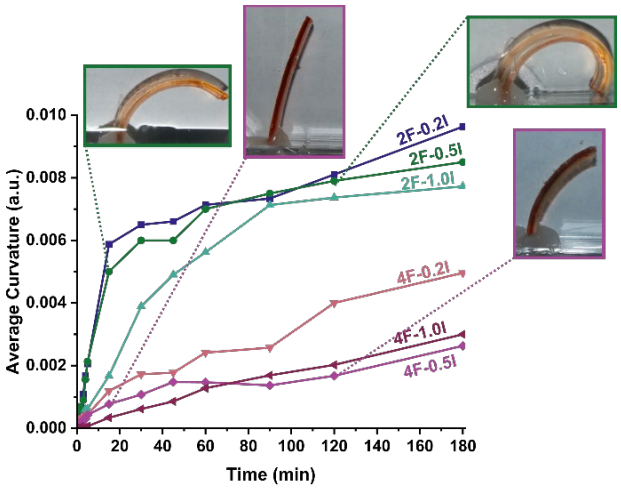

Figure 5: Radius of curvature over time for the bilayer prints.

To track the response time of the different actuators as well as how changes in network connectivity influenced the overall shape change, the bilayer prints were imaged with a high-speed camera over a series of time points over a two-hour long experiment. Displacement of the bilayer prints was first measured and plotted as a function of submersion time and used to calculate the radius of curvature, κ. The evolution of κ over time is plotted in Figure 5, highlighting the differences between the sample sets in their response to actuation behavior. The 2F samples overall show a much higher curvature than their 4F counterparts. This is easily attributable to the changes in crosslink density between the samples. The 4F samples, while more inhomogeneous and displaying higher values of stress and similar E_y values, have a great number of effective crosslinks as measured by DMA. Furthermore, the 4F samples were also shown to have a greater cooperativity derived from the increased slope in the a_T versus T_g/T plots, indicating a greater coupling between polymer strands. For the strands to deform during actuation, the crosslink junctions fluctuate to accommodate applied stressed as described by the phantom network model. However, as crosslink functionality is increased, these junction fluctuations are repressed and more closely match the 'fixed junction' assumption of the affine network model. In our printed samples here, the limited mobility of crosslink junctions, and, therefore, the strands that are attached to them, causes a more pronounced actuation behavior in the 2F samples series when compared to 4F.

Within the different printed sample series there are also noticeable differences in the curvature response. In the 2F series, the 2F–0.2I shows the greatest deformation as well as the most rapid actuation response. This is explained by the lower value of ν_e calculated for 2F–0.2I when compared to other samples. With less elastically effective strands in the network, there is less resistance to the stress imposed by the active HEA layer during swelling. The 4F bilayer print series has similar trends to those noted in the 2F bilayers. As would be expected by the dramatic differences in T_g and tensile properties, the 4F–0.5I resists actuation much more greatly than the other samples in the 4F series due to the reduced inhomogeneity resulting in great elasticity and the highly coupled crosslink strands contained in the network as measured from TTS experiments.

4. CONCLUSION

Research conducted in FY24 made significant strides in elucidating the relationship between resin formulation, printing parameters, and the resulting material properties of 3D printed parts. By systematically varying the printing parameters of interest, we demonstrated that these factors have a profound impact on network heterogeneity, mechanical properties, and functional behavior. DMA revealed that thicker prints (100 μm) produced exhibited bimodal tanδ curves, indicative of the formation of multiple network structures. This network heterogeneity was linked to an alternative crosslinking pathway, particularly in the HEA system, which was more prevalent at higher layer thicknesses. In contrast, thinner prints (50 μm) exhibited more uniform networks and lower glass transition temperatures, highlighting the critical role of both layer thickness and crosslinker functionality in dictating material behavior.

The dye elution studies further underscored the importance of network connectivity, showing that resins with higher effective crosslink densities—particularly the 100 µm resins—exhibited significantly lower rates of dye diffusion, suggesting a more tortuous and impermeable network structure. This result is crucial for applications requiring controlled permeability, such as filters or barrier materials. Additionally, the bilayer curvature experiments demonstrated clear differences in actuation performance between 2F and 4F systems. The 2F resins showed faster and more pronounced curvature responses, attributed to the increased mobility of polymer strands at crosslink junctions, whereas 4F systems exhibited more constrained actuation due to their higher crosslink density and reduced chain mobility.

Overall, the findings from this effort demonstrate the intricate balance required between resin formulation and 3D printing parameters to achieve specific performance characteristics in printed materials. With the observed trends in the structure-property relationships, we can form basic formulation design rules (Figure 6). These guidelines will enable a more streamlined innovation pathway towards mission specific 3D printing research. These results provide a robust framework for developing additive manufacturing systems capable of producing high-performance, mission-critical parts for CBRN-relevant applications. As an example, the next generation of respirators for CBRN protection may be produced via additive manufacturing. Additionally, the additive manufacturing process may be done in a 'forward deployed' setting. Understanding the significant materials characteristics that are readily varied when seemingly minute changes are done will be beneficial in ensuring quality control in these respirators. Future work will build on these findings to refine formulation strategies towards specific desirable properties and further optimize the functional properties of 3D printed materials for diverse defense-related applications.

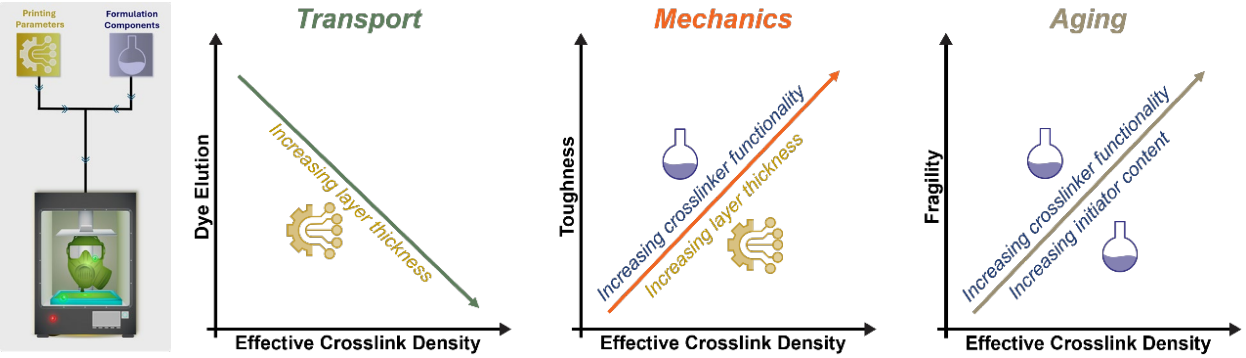

Figure 6: Structure-property relationships established through this program.

ACKNOWLEDGMENTS

Funding was provided by the U.S. Army via the Chemical Biological Advanced Materials Manufacturing Program (PE 0601102A Project 91A) at the Combat Capabilities Development Command Chemical Biological Center.

REFERENCES

[1] Boydston, A.J.; Cao, B.; Nelson, A.; Ono, R.J.; Saha, A.; Schwartz, J.J.; Thrasher, C.J. Additive manufacturing with stimuli-responsive materials. *J. of Mat. Chem. A*. **2018**, *6*, pp 20621–20645.

[2] Ge, Q.; Jian, B.; Li, H. Shaping soft materials via digital light processing-based 3D printing: A review. *Forces Mech.* **2022**, *6*, p 100074.

[3] Bagheri, A.; Jin, J. Photopolymerization in 3D Printing. *ACS Appl. Polym. Mater.* **2019**, *1*, pp 593–611.

[4] Sahrir, C. D.; Ruslin, M.; Lee, S. Y.; Lin, W. C. Effect of various post-curing light intensities, times, and energy levels on the color of 3D-printed resin crowns. *J. Dent. Sci.* **2023**, *19* (1), pp 357–363.

[5] Schittecatte, L.; Geertsen, V.; Bonamy, D.; Nguyen, T.; Guenoun, P. From resin formulation and process parameters to the final mechanical properties of 3D printed acrylate materials. *MRS Commun.* **2023**, *13 (3),* pp 357–377.

[6] Uzcategui, A.C.; Higgins, C. I.; Hergert, J.E.; Tomaschke, A,E.; Crespo-Cuevas, V.; Ferguson, V.L.; Bryant, S.J.; McLeod, R.R.; Killgore, J.A. Microscale Photopatterning of Through-Thickness Modulus in a Monolithic and Functionally Graded 3D-Printed Part. *Small Sci.* **2021**, *1*(3), p 2000017.
[7] Higgins, C.I.; Brown, T.E.; Killgore, J.P. Digital light processing in a hybrid atomic force microscope: In Situ, nanoscale characterization of the printing process. *Addit. Manuf.* **2021**, *38*, p 101744.
[8] Elliott, J.E.; Bowman, C.N. Kinetics of primary cyclization reactions in cross-linked polymers: An analytical and numerical approach to heterogeneity in network formation. *Macromol.* **1999**, *32* (25), pp 8621–8628.
[9] Lovell, L.G.; Berchtold, K.A.; Elliott, J.E.; Lu, H.; Bowman, C.N. Understanding the kinetics and network formation of dimethacrylate dental resins. *Polym. for Adv. Technol.* **2001**, *12* (6), pp 335–345.
[10] Wen, M.; Scriven, L.E.; McCormick, A.V. Kinetic gelation modeling: Kinetics of cross-linking polymerization. *Macromol.* **2003**, *36* (11), pp 4151–4159.
[11] Terrones, G.; Pearlstein, A.J. Effects of kinetics and optical attenuation on the completeness, uniformity, and dynamics of monomer conversion in free-radical photopolymerizations. *Macromol.* **2001**, *34* (26), pp 8894–8906.
[12] Reid, A.; Jackson, J.C.; Windmill, J.F.C. Voxel based method for predictive modelling of solidification and stress in digital light processing based additive manufacture. *Soft Matter*. **2021**, *17* (7), pp 1881–1887.
[13] Jangizehi, A.; Schmid, F.; Besenius, P.; Kremer, K.; Seiffert, S. Defects and defect engineering in Soft Matter. *Soft Matter*. **2020**, *16*, pp 10809–10859.
[14] Seiffert, S. Origin of nanostructural inhomogeneity in polymer-network gels. *Polym. Chem.* **2017**, *8*, pp 4472–4487.
[15] Lin, T.S.; Wang, R.; Johnson, J.A.; Olsen, B.D. Topological Structure of Networks Formed from Symmetric Four-Arm Precursors. *Macromol.* **2018**, *51* (3), pp 1224–1231.
[16] Anseth, K.S.; Bowman, C.N.; Peppas, N.A. Polymerization kinetics and volume relaxation behavior of photopolymerized multifunctional monomers producing highly crosslinked networks. *J. Polym. Sci., Part A*, **1994**, *32* (1), pp 139–147.
[17] Anseth, K.S.; Anderson, K.J.; Bowman, C.N. Radical concentrations, environments, and reactivities during crosslinking polymerizations. *Macromol. Chem. and Phys.* **1996**, *197* (3), pp 833–848.
[18] Young, J.S.; Kannurpatti, A.R.; Bowman, C.N. Effect of comonomer concentration and functionality on photopolymerization rates, mechanical properties and heterogeneity of the polymer. *Macromol. Chem. Phys.* **1998**, *199* (6), pp 1043–1049.
[19] Jones, B. H.; Alam, T. M.; Lee, S.; Celina, M.C.; Allers, J.P.; Park, S.; Chen, L.; Martinez, E.J.; Unangst, J.L. Curing Behavior, Chain Dynamics, and Microstructure of High T g Thiol-Acrylate Networks with Systematically Varied Network Heterogeneity. *Polymer.* **2020**, *205*, p 122783.
[20] Yu, J.W.; Jung, J.; Choi, Y.M.; Choi, J.H.; Yu,J.; Lee, J.K.; You, N.H.; Goh, M. Enhancement of the crosslink density, glass transition temperature, and strength of epoxy resin by using functionalized graphene oxide co-curing agents. *Polym. Chem.* **2016**, *7* (1), pp 36–43.

Structure-property relationships dictating pressure drop and particle capture in emulsion-templated polymer foams

Chase B. Thompson[a,b], Gregory W. Peterson[b]*
[a]U.S. Army Combat Capabilities Development Command Chemical Biological Center, Research & Operations Directorate, 8198 Blackhawk Rd, Aberdeen Proving Ground, MD 21010
[b]Leidos Inc., 1750 Presidents St, Reston, VA 20190, United States

ABSTRACT

Porous polymers remain a key platform for the design of next-generation respirators. Emulsion-templated foams are a versatile, scalable platform that show promise for tunable particle capture and pressure drop properties, but there have been no widespread studies that correlate air flow through these materials to their chemistry and morphology. This project seeks to establish structure-property relationships in a series of high internal phase emulsion polymer foams in relation to how these materials capture and retain particulate matter. We have found that increasing the porosity of a series of hydrophobic phase emulsion polymer foams decreases the pressure drop across the foam. Moreover, the pressure drop behavior was correlated to Darcy's law describing flow through a porous medium. Deviations from Darcy's law were found for foams with porosities between 75–80 %, indicating that drag forces are playing a substantial role in flow through these less porous materials.

Keywords: Polymerized high internal phase emulsions, porous polymer, aerosol capture, pressure drop

BLUF: Emulsion-templated foams offer a versatile platform for creating porous, soft materials, but there is no unifying study that quantifies air flow through polymerized high internal phase emulsions and how it relates to their morphology/chemical structure. This study aims to identify key structure-property relationships that govern aerosol uptake and pressure drop in a library of emulsion-templated foams.

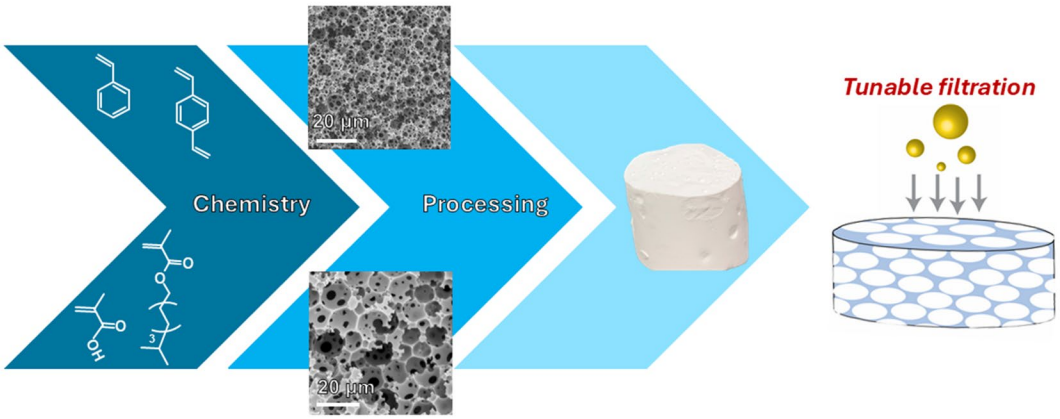

1. INTRODUCTION

1.1 Research problem:

Porous polymers serve as our primary platform for aerosol protection. High internal phase emulsion foams (polyHIPEs) have shown promise as scalable and versatile filtration platforms, but there have been no widespread quantitative studies that relate the structure-property relationships of polyHIPEs to their aerosol filtration capabilities.

1.2 Current state of the technology:

PolyHIPEs have seen widespread use in separation science and water purification, resulting in a diverse set of available chemistries and processing techniques to control the polyHIPE morphology. This chemical toolbox allows us to finely tune the properties of the polyHIPE, polarity, primary pore size, and pore connectivity, to establish relationships between foam structure and pressure drop/particle capture. The U.S. Army Combat Capabilities Development Command Chemical Biological Center (DEVCOM CBC) has an established expertise in studying both porous materials and aerosol particulate capture. The available subject matter expertise and instrumentation available at DEVCOM CBC means that we are capable of synthesizing polyHIPE foams and testing them in-house for expediated measurements and precision tuning of material properties.

1.3 Project objectives:

- Develop structure-property relationships in polyHIPEs for aerosol capture and pressure drop
- Expand chemical library to enhance chemical affinity for aerosol deposition and enhance foam mechanic

1.4 Exit criteria:

- Develop a precision understanding of the effects of polyHIPE chemistry and structure on aerosol uptake properties
- Identify potential polyHIPE candidates for technology transition/application in prototypes for next-generation aerosol capture technologies

1.5 Hypothesis:

Increasing the porosity of a polyHIPE will result in a decrease in the pressure drop (ΔP) across the foam. Larger primary pores will decrease the ΔP across the foam but will have little effect on the aerosol capture properties. Larger pore throats will result in a decrease in the ΔP at the cost of higher aerosol penetration, but increasing the density of the interconnecting pore throats without changing their size will reduce ΔP without sacrificing particle uptake properties.

2. YEAR 1 ACCOMPLISHMENTS

2.1. Summary of project progress:

In the first year of funding, we established a custom polyHIPE formulation that generates stable emulsions while still allowing for processing of the foam for testing; this was achieved by adding a small amount of flexible monomer into the base formulation. Furthermore, we optimized scalability of these monoliths by curing the material inside of resin 3D printed molds, allowing for control over the dimensions and shape of the final foam without changing the size distribution of the foam pores. We also synthesized a series of foams with different porosities and measured the pressure drop across them, fitting the measured quantities to existing empirical models to back out values for permeability and drag forces.

2.2. Project challenges and lessons learned:

This project is highly reliant on access to scanning electron microscopy (SEM) for measurement of the pore morphology. The primary SEM used for this imaging was inaccessible due to needing repairs for most of the summer (May 2024–September 2024) resulting in delays in some of the efforts in needing to access an older SEM on post. The microscope has since been repaired, allowing work to resume as usual starting next fiscal year. There were

difficulties in establishing methods to tune the pore morphology/interconnecting pore dimensions using published techniques. In the future, more screening methods will be chosen and carried out on small scales in parallel to enhance throughput before scaling the techniques into full-sized samples for testing.

2.3. Data:

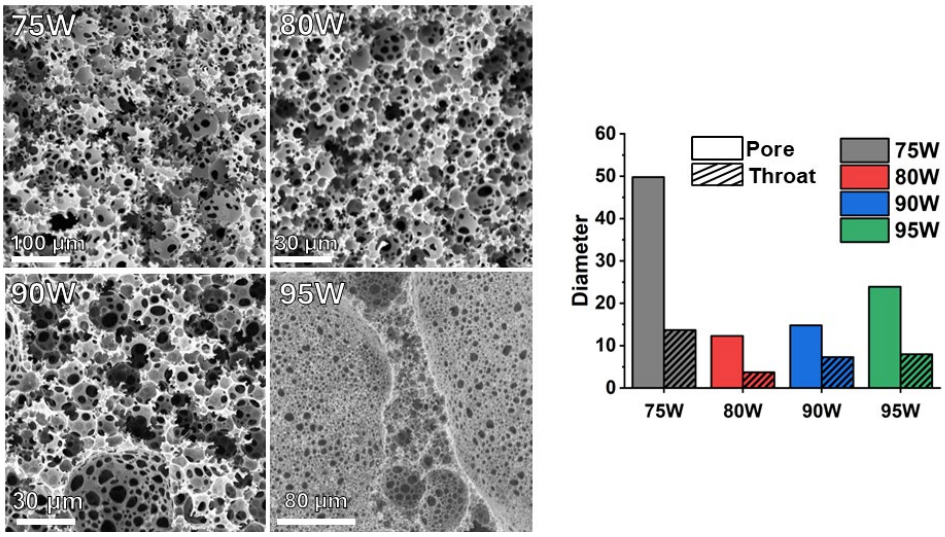

Figure 1: Electron micrographs of polyHIPE foams with differing porosities (left). Number-average pore and pore throat diameters for foams (right). Nomenclature: XXW where XX is the vol% of water in the HIPE (the remainder is the reactive oil phase). Tuning the water/oil content provided control over both foam porosity and pore dimensions.

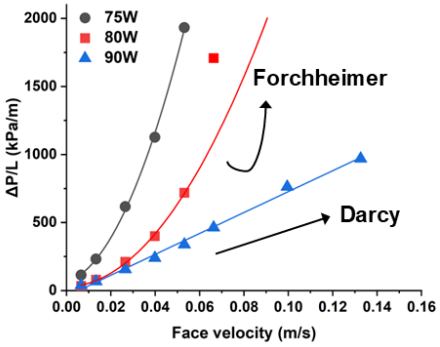

Darcy's Law: $\frac{\Delta P}{L} = \frac{\mu}{K} v$

Darcy-Forchheimer: $\frac{\Delta P}{L} = \frac{\mu}{K} v + \rho \beta v^2$

Sample	K (m^2)	β (m^{-1})	R^2
75W	3.65×10^{-12}	461.4	0.999
80W	7.46×10^{-11}	194.6	0.998
90W	2.36×10^{-12}	--	0.995

Figure 2: Pressure drop versus face velocity plots with accompanying Darcy and Darcy-Forchheimer fits. The table lists permeability (K) and inertial coefficient (β) values derived from fitted data. Decreasing porosity led to increases in the foam pressure drop, and deviations from Darcy's law in 75W and 80W can be attributed to drag forces from contact of the flowing air with the pore wall. This demonstrates that porosity plays a critical role in determining air flow properties, and that we may find tradeoffs between pressure drop and foam mechanics in future efforts.

3. FUTURE DIRECTIONS

In the first year of funding, we designed a model polyHIPE for pressure drop and aerosol capture measurements and developed a methodology for scaling the foams into larger geometries for testing. Pressure drop tests revealed trends in the air flow properties that could be fitted using established empirical equations. In the next steps, the sample set of the current formulation will be expanded to include tunable pore size at a single established porosity to test how changes in pore size alone contribute to changes in pressure drop and aerosol capture. Furthermore, aerosol capture will be quantified using a salt challenge to quantify how pore morphology dictates protection capabilities of the synthesized foams. We will continue to fit data from pressure drop measurements to established empirical equations to derive mathematical values that can be used to understand flow through these porous mediums to optimize properties for desired aerosol capture applications. An established collaborator will also provide biomass monomers for incorporation into the foams to tune mechanical properties and foam polarity. It is expected that at the end of this program, these foams will be able to be applied in the areas of personal and collective protection or bioaerosol sampling for next-generation CBRN defense materials.

ACKNOWLEDGMENTS

Funding was provided by the U.S. Army via the Chemical Biological Advanced Materials Manufacturing Program (PE 0601102A Project VR9) at the Combat Capabilities Development Command Chemical Biological Center. We would also like to thank Ms. Melissa Betz for assistance in running the pressure drop experiments. We are grateful for Dr. Susan Kozawa for designing and printing the sample insert in the 8130 and to Mr. Cody Kendig and Mr. Dan Barker for helpful conversations surrounding aerosol capture measurements for foam samples.

REFERENCES

[1] Zhang, S.; Chen, M.; You, Y.; Zhu, Y. Mechanism of Interconnected Pore Formation in High Internal Phase Emulsion-Templated Polymer. *ACS Macro Lett*. **2024**, *13* (8), pp 903–907.
[2] Kalisa, E.; Saini, A.; Lee, K.; Mastin, J.; Schuster, J.K.; Harner, T. Capturing the Aerobiome: Application of Polyurethane Foam Disk Passive Samplers for Bioaerosol Monitoring. *ACS EST Air.* **2024**. *1* (5), pp 414–425.
[3] Foudazi, R. HIPEs to PolyHIPEs. *React. Funct. Polym.* **2021**, *164*, p 104917.
[4] De Soricellis, G.; Rinaldi, F.; Tengattini, S.; Temporini, C.; Massolini, G.; Mandracchia, D.; Milanese, C.; Casero, F.; Calleri. E. Synthesis of Hydrophilic Polymeric Supports with Poly-HIPE Structures Based on Acrylates for Pharmaceutical Applications. *ACS Appl. Polym. Mater.* **2023**, *5* (3), pp 2113–2123.
[5] Choudhury, S.; Connolly, D.;White, B. Supermacroporous polyHIPE and cryogel monolithic materials as stationary phases in separation science: A review. *Anal. Methods*. **2015**, *7* (16), pp 6967–6982.
[6] Zhao, B.; Gedler, G.; Manas-Zloczower, I.; Rowan, S.J.; Feke, D.L. Fluid transport in open-cell polymeric foams: effect of morphology and surface wettability. *SN Appl. Sci*. **2020**, *2*, p 189.
[7] Mhatre, S.V.; Mahajan, J.S.; Epps, T.H.; Korley, L.S.T.J. Lignin-derivable alternatives to petroleum-derived non-isocyanate polyurethane thermosets with enhanced toughness. *Mater. Adv*. **2022**, *4*, p 110–121.
[8] Üzüm, G.; Akln Özmen, B.; Tekneci Akgül, E.; Yavuz, E. Emulsion-Templated Porous Polymers for Efficient Dye Removal. *ACS Omega*. **2022**, *7* (185), pp 16127–16140.
[9] Henning, L.M.; Abdullayev, A.; Vakifahmetoglu, C.; Simon, U.; Bensalah, H.; Gurlo, A.; Bekheet, M.F. Review on Polymeric, Inorganic, and Composite Materials for Air Filters: From Processing to Properties. *Adv. Energy Sustainability Res*. **2021**, *2*, p 2100005.
[10] Jiang, Q.; Menner, A.; Bismarck, A. Robust macroporous polymers: Using polyurethane diacrylate as property defining crosslinker. *Polymer*. **2016**, *97*, pp 598–603.

Molecular modeling of toxic industrial chemicals on metal-organic frameworks for next-generation filtration applications

Matthew A. Browe[a]*, Adam R. Hinkle[a,b], Ivan O. Iordanov[a], Sergio Garibay[a,c], Wesley O. Gordon[a]
[a]U.S. Army Combat Capabilities Development Command Chemical Biological Center, Research & Operations Directorate, 8198 Blackhawk Rd, Aberdeen Proving Ground, MD 21010
[b]DCS Corporation, 4696 Millennium Drive, Suite 450, Belcamp, MD 21017
[c]Leidos, Inc., 1750 Presidents Street, Reston, VA 20190

ABSTRACT

Reactive molecular dynamic simulations were performed against derivatives of zirconium-based metal-organic frameworks UiO–66 and metal-organic framework (MOF)–808 to elucidate design strategies for improving reactivity against toxic industrial chemicals for filtration applications. Separate simulations were used to examine methodologies by imparting reactivity to the cluster via hydroxyl group incorporation from activation in HCl solution and imparting reactivity to the organic ligand via functional groups. Selected high-performing materials were evaluated using infrared spectroscopy and breakthrough testing methods. Results showed greater sulfur dioxide removal from formate-modulated MOF–808 activated in 5.5 M HCl relative to 0.2 M HCl activation and greater hydrogen sulfide removal from cyano-functionalized UiO–66 compared to baseline UiO–66 and amine-functionalized UiO–66, all consistent with predictions from simulations. These results show molecular simulation is useful to design strategies for toxic industrial chemical removal in metal-organic frameworks and provides rationale for trends employed in future studies.

Keywords: Monte Carlo, molecular dynamics, metal-organic frameworks, molecular simulation, adsorption, chemical reaction, ReaxFF

1. INTRODUCTION

Removal of toxic industrial chemicals is a concern in military filtration applications. Their high vapor pressure precludes removal via noncovalent interactions such as physical adsorption, requiring a variety of reactions be used in filtration media for removal of threats. Currently fielded filtration media, such as metal-incorporated activated carbon, cannot adequately address the full spectrum of chemical threats. Metal-organic frameworks (MOFs) have been extensively investigated for this purpose[1] as their high surface area, porosity, and tunable properties enable a range of reactions to be incorporated for chemical removal. Additionally, zirconium-based MOFs are of high interest due to their stability under a range of environmental and synthetic conditions,[2] a deficiency common with other MOFs.

Among the zirconium MOFs, UiO–66 and MOF–808 have been extensively studied in the literature.[3] These MOFs can be tuned physically and chemically for enhancing guest molecule removal. The UiO-66 MOF, in particular, can be modified through induced defects in its structure, in which a linker molecule is removed and the resulting site is terminated through either a formate group (in the traditional formic acid synthesis) or hydroxyl groups.[4] The UiO–66 family of MOFs can vary through functionalization of the linker, as represented by UiO–66–NH_2 where an amine moiety is incorporated onto the benzene dicarboxylic acid linker through synthesis variation, using aminoterephthalic acid instead of terephthalic acid.[2] The MOF–808 can be chemically modified through modulator incorporation on the node, a feature not available on pristine UiO–66 as all possible node sites are bonded to linker molecules.[5]

This effort aims to build on previous work to determine the effect of chemical modifications of zirconium-based MOFs on reactions against guest molecules of interest. Chemical reactions can be evaluated using molecular dynamic simulations incorporating reactive force fields (ReaxFF5), which allow for explicit bond breaking and formation phenomena. Experimental efforts were incorporated to evaluate high-performing materials from simulations. Results can be used to guide design strategies towards improving and optimizing these materials for filtration applications.

2. METHODS

Crystallographic information files for UiO–66 and MOF–808 came from the Cambridge Structural Database website. Defects were induced into UiO–66 at a density of two missing benzene dicarboxylic acid ligands per unit cell using the Avogadro molecular editor. The resulting structure was optimized with the Quantum Espresso code[6] using the "relax" option of the pw.x executable of Quantum Espresso. Simulation settings used a kinetic energy cutoff distance of 60 Ry for wavefunctions, a kinetic energy cutoff distance of 480 Ry for charge density, Gaussian smearing with a degauss parameter of 0.002, the semiempirical Grimme's DFT–D2 van der Waals dispersion correction, the BFGS (Broyden–Fletcher–Goldfarb–Shanno) quasi-newton algorithm for ion dynamics, and a mixing factor of 0.7. Default settings were used for convergence.

Molecular dynamics simulations were conducted using the LAMMPS code.[7] In the codes for production runs analyzing the HCl solution activation process of MOF–808 and formate-terminated-missing-ligand-defective UiO–66, a 2 x 2 x 2 unit cell simulation domain was utilized. For other screening runs on toxic industrial chemical reactivity of ligand-functionalized UiO–66 and MOF–808 materials, a 1 x 1 x 1 unit cell simulation domain was used. The ReaxFF[5] reactive force field jz0c02930,[8] trained on the zirconium-based MOF MIL–140C was used for UiO–66 and MOF–808, as it was parameterized and trained on structurally similar materials to the MOFs used in this study. A Langevin thermostat was used in the micro-canonical ensemble with a time step of 0.1 fs in all simulations. In the simulations, each atom is assigned a unique identifier number, with its bonding explicitly tracked roughly every 0.01 % of the total simulation time, including all bonds and the identifier number of the atoms that it is bonded. This information was then converted by a postprocessing code into time-dependent species population data to quantify reaction product data.

Nitrogen isotherm measurements were performed for selected MOF powder samples at 77 K using a Micromeritics ASAP 2420 Multi-Port Surface Area and Porosimetry Analyzer. Samples were heated at 120 °C for 24 hours prior to analysis. Attenuated total reflectance Fourier transform infrared (ATR-FTIR) spectra of selected MOF powders was obtained using a FTIR spectrometer (Tensor 27, Bruker Optics Inc., Germany) equipped with a platinum ATR accessory, a room-temperature deuterated triglycine sulphate (DTGS) detector, and a KBr beamsplitter. A wavenumber range of 400–4000 cm^{-1} was scanned at a resolution of 2 cm^{-1}.

Diffuse reflectance infrared Fourier transform spectra (DRIFTS) of selected MOF powders against toxic industrial chemicals of interest were collected with a Nicolet 6700 (Thermo Fisher Scientific Nicolet, Waltham MA) spectrometer equipped with an infrared source, a mercury—cadmium—telluride detector, and a KBr beam splitter. A background spectrum was first collected with 1024 scans per spectra. Sample data was then collected at 1024 scans per spectra with a collection length of 727 seconds. The resolution was kept at 2.0 cm^{-1} with levels of zero filling kept at zero.

A detailed schematic of the DRIFTS setup at the U.S. Army Combat Capabilities Development Command Chemical Biological Center has been previously described.[9] About 20 mg of the MOF powder sample of interest was loaded into a 6 mm porous ceramic cup, which was then dried over 1 day at room temperature in a N_2(g) purge before loading into the DRIFTS cell (Pike Technologies DiffusIR environmental cell). The DRIFTS cell was then evacuated under high vacuum for approximately 100 minutes at room temperature. After evacuation, a nitrogen flow of 20.0 mL $minute^{-1}$ at 1 atm was introduced to equilibrate the chamber and to eliminate adventitious hydrocarbons and residual humidity before reactant gas introduction. The cell was configured as a continuous-flow system, where inlet gas flowed from the bottom of a porous ceramic cup and through the packed bed before filling the chamber and exiting through the side outlet tube of the cell. The purge flow was maintained long enough for the DRIFTS baseline to stabilize (~1 hour), indicating that the sample had equilibrated with the purge gas. Next, vapor was introduced into the system by diverting the nitrogen flow (using a six-way valve) through a saturator cell containing a chemical reservoir. Hydrogen sulfide chemical was then introduced from the system from a pressurized ballast. After chemical feed introduction, infrared spectra were recorded every minute for 60 minutes at an average of 128 scans and a resolution of 2 cm^{-1}. Difference spectra are plotted by subtracting the IR spectrum of the powder material before chemical exposure (after nitrogen purge) from the postexposure spectra.

Micro-breakthrough experiments were conducted on selected MOF powders using an internally developed system. Analyte (limited to sulfur dioxide or hydrogen sulfide for this study) was injected into a ballast and pressurized; this chemical mixture was mixed with an air stream containing the required volumetric flow rate to achieve a concentration of 1,000 mg/m^3 for each chemical. The completely mixed stream then passed through a sorbent bed submerged in a temperature-controlled water bath. The sorbent bed is filled on a volumetric basis in a 4 mm internal diameter tube to

a height of 4 mm resulting in approximately 10 mg of MOF material being used for each test. The sample bed was constructed of glass so the bed height could be measured. The samples were regenerated in dry air at 120 °C for 1 hour. In all cases, the effluent stream then passed through a continuously operating HP5890 Series II gas chromatograph equipped with a flame photometric detector for sulfur-containing gases such as hydrogen sulfide and sulfur dioxide. All the data were plotted on a normalized time scale of minutes per gram of the adsorbent. The underlying theory utilized for calculating the dynamic capacity to saturation has been described previously.[10]

3. RESULTS AND DISCUSSION

Analysis of results for reactive molecular dynamics simulations of HCl activation of MOF–808 and UiO–66 focused on resulting surface chemistry speciation (Figure 1). The metal oxide cluster component of MOFs could be chemically modified to produce hydroxyl species of varying coordination environment of the oxygen atoms, resulting in species of varying Bronsted acidity that could participate differently in neutralizing reactions based on the chemical probe.[11] Analogously, the functional group substitution on the ligand could affect reaction chemistry.

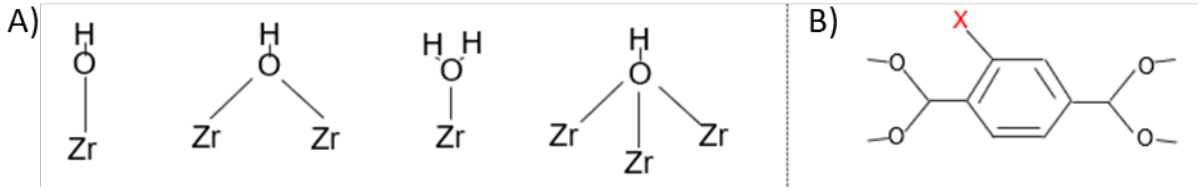

Figure 1. A) Types of hydroxyl groups formed on zirconium oxide clusters of UiO–66 and MOF–808 after HCl activation. B) Example functional group substitution site on ligand of UiO–66, labeled with a red X.

Setup of the starting systems for HCl activation reaction of formate-terminated MOF–808 and missing ligand-defective, formate-terminated UiO–66 (Figure 2). Formate modulator species present in both structures are circled in yellow. These MOFs present varying physical properties, formate group density, and formate group accessibility for study on the differentiation of the HCl activation dynamics. Representative cluster models of the formate modulation geometry and density of the MOF–808 and UiO–66 systems are shown in Figure 3.

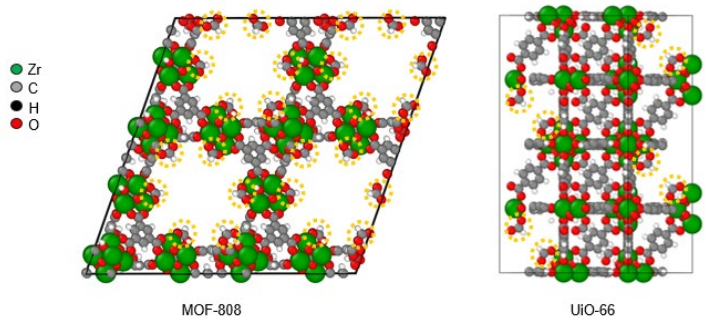

Figure 2. Formate-modulated MOF–808 used in HCl activation simulations (left). Missing-ligand defective UiO–66 with formate termination of defects used in HCl activation simulations (right).

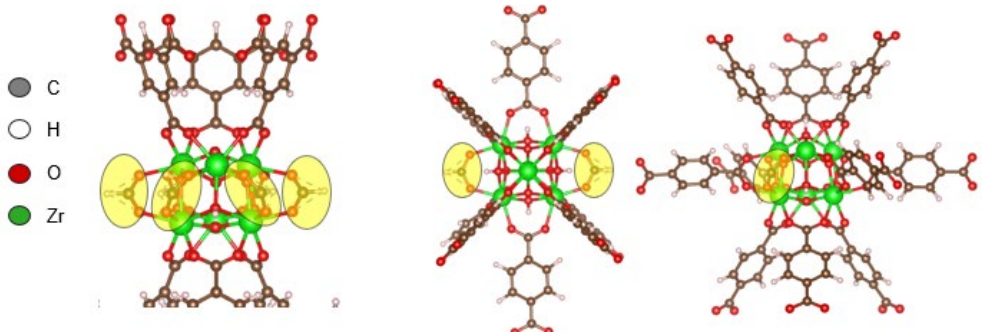

Figure 3. Formate modulation on MOF–808 (left) and on UiO–66 with two formate-terminated missing linker defects per unit cell (middle, right).

A cluster model of the MOF–808 metal oxide component is shown in Figure 4 (left), and the full MOF–808 system saturated with HCl solution is shown in Figure 4 (right). Among the relevant species tracked in the simulations include μ_3–OH species, circled in blue in Figure 4, and formate species, circled in orange in Figure 4. An example HCl activation mechanism determined from these simulations is shown in Figure 5. Starting from the left, hydrogen from an HCl molecule is transferred to the oxygen atom or a nearby free water molecule. Concomitantly, a hydrogen from the free water molecule is transferred to an oxygen atom of a formate group, leading to partial desorption of the formate species (center). The formate species then fully detaches as formic acid from the metal oxide cluster of MOF–808 and the nearby μ_3–OH species migrates to a μ_1–OH configuration on the zirconium atom where the formic acid species last detached from. Finally, the hydrogen of the free formic acid then translates to the μ_1–OH species, forming a μ_1–OH_2 species.

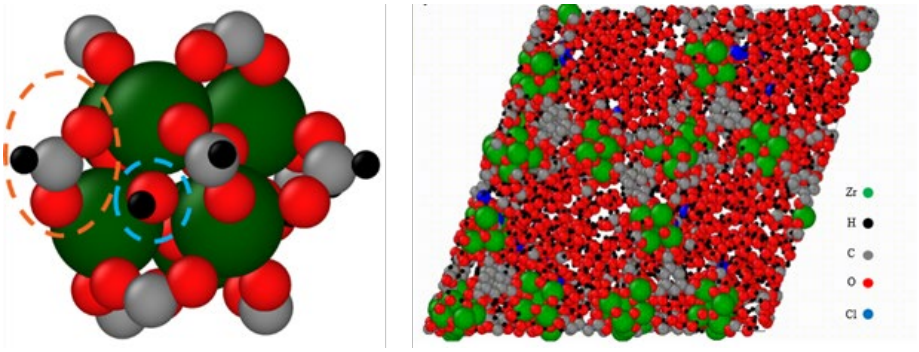

Figure 4. MOF–808 cluster with formate modulator and μ3-OH group circled (left) and MOF–808 with its pores saturated with HCl solution (right).

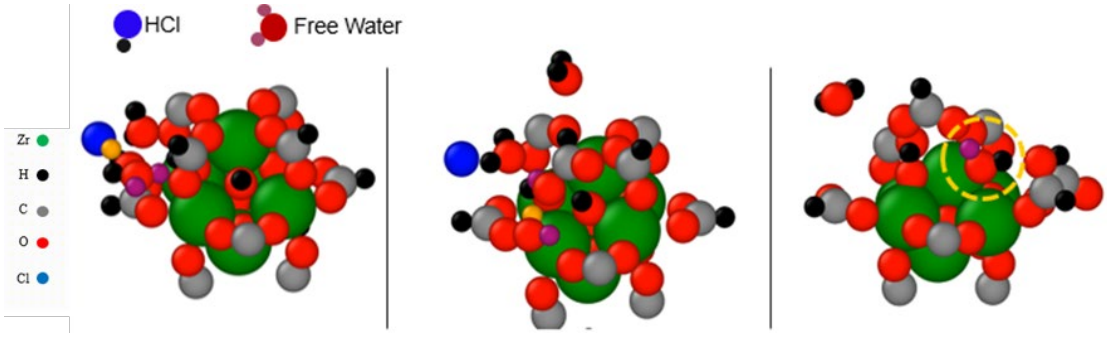

Figure 5. HCl activation mechanism determined from reactive molecular dynamics simulations on MOF–808. Participating hydrogen atoms on the HCl and free water molecules are distinctly colored yellow and purple, respectively. Starting configuration (left). Dissociation of HCl, proton transfer to H_2O, and protonating formate group as formic acid (center). μ_3–OH transition to μ_2–OH, partial desorption of second formate (right).

Reaction product species quantification was then performed on a system scale for run times up to equilibrium, around 15 ns in this case. Fates of the formate species included remaining fully attached, being partially desorbed (only one oxygen atom bonded to a zirconium atom), being fully desorbed as a formate group, and being fully desorbed as a formic acid group, depicted in the left of Figure 6. It is considered that the ideal scenario is being fully desorbed as a formic acid group, as this frees all zirconium sites for hydroxyl speciation from neighboring water molecules and leaves the desorbed product in a neutrally charged state with a lower propensity for subsequent reaction. The presence of hydroxyl groups on the MOF surface following activation include formation of tri-bridging OH species, bi-bridging OH species, terminal-OH species, and terminal-OH_2 species, depicted in the right of Figure 6. The specific identity of the hydroxyl group and local bonding environment of the oxygen atom may influence guest molecule reactivity, depending on the specific chemical target. Example depiction of the quantification of these reaction products for MOF–808 at low (0.2 M) and high (5.5 M) HCl concentrations at 300K is shown in Figure 7. Results show that, at high HCl concentrations, free formic acid species increase and all other formate derivative species (fully and partially attached formate, free formate anion species) decrease, which is considered a more favorable activation condition.

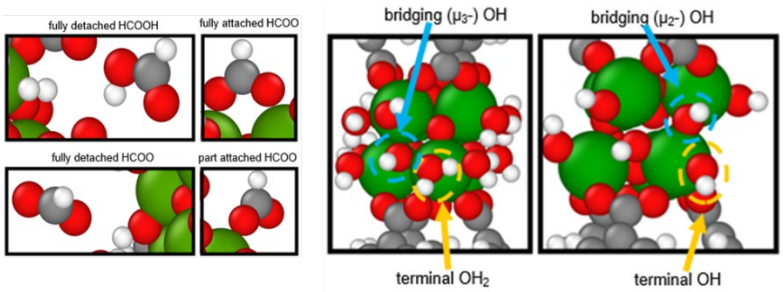

Figure 6. Species identification for (left) formate-derivative species and (right) hydroxyl-derivative species formed on MOF–808 and UiO–66 metal oxide clusters from HCl activation.

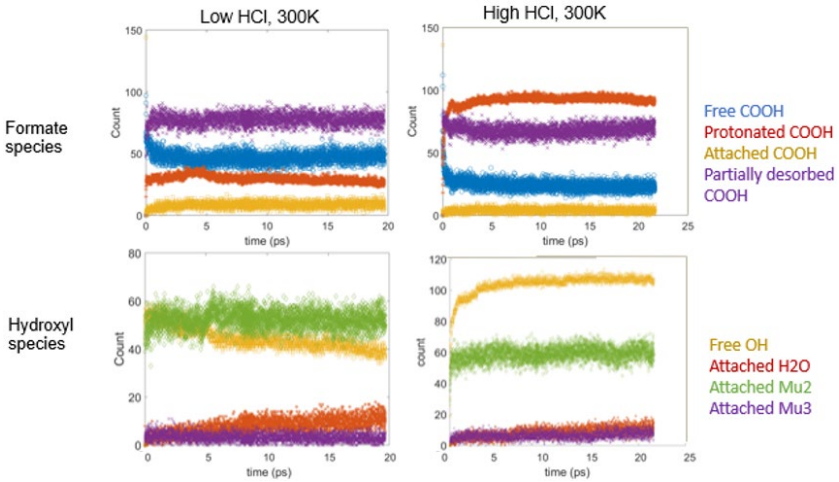

Figure 7. Example species statistics for formate-derivative moieties and hydroxyl-derivative moieties on MOF—808 at 300K under low HCl concentration (0.2 M, left column) and high HCl concentration (5.5 M, right column).

Equilibrated formate species and hydroxyl species quantification data is summarized in Figures 8, 9, and 10 for all systems evaluated. A few general trends are observed. The ratio of bridging to terminal hydroxyl species on the surface of the MOFs increases with increasing HCl concentration for all materials, with a greater effect on MOF–808 than UiO–66. Additionally, in general, the ratio of free formate to attached formate species increases with increasing HCl concentration for all MOFs, with a greater ratio observed for UiO–66 than MOF–808. An exception to this is seen with the highest HCl concentration in UiO–66 at 300K. This may be related to the ability of HCl molecules to efficiently access formate sites in UiO–66 at the highest concentration; trajectory analysis and further simulations representing a rewashing of HCl in the system are finishing to clarify this trend.

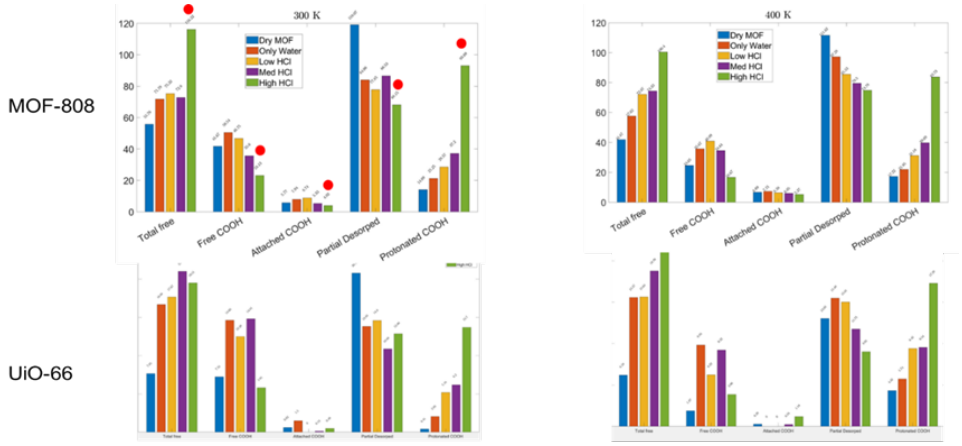

Figure 8. Summary of formate group equilibrium statistics for MOF–808 and UiO–66 during HCl activation simulations at 300K and 400K. Optimal formate removal conditions for MOF–808 are labeled with a red circle, and optimal formate removal conditions for UiO-66 are labeled with an orange circle.

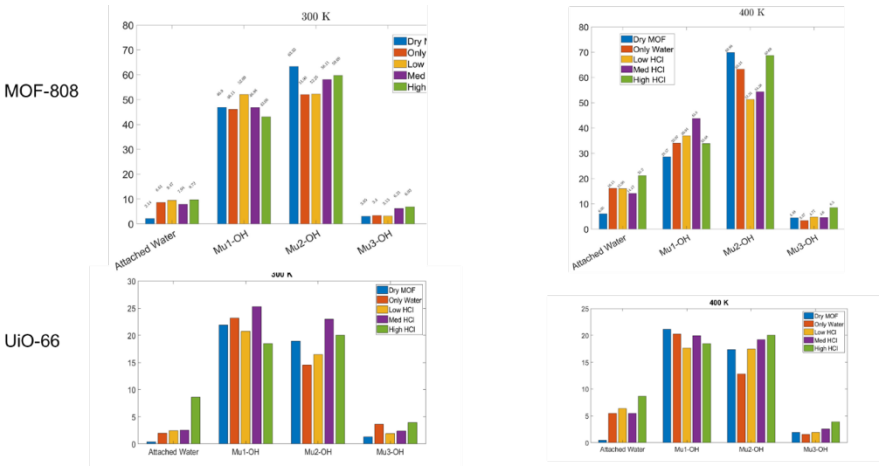

Figure 9. Summary of hydroxyl group equilibrium statistics for metal oxide cluster surfaces of MOF–808 and UiO–66 during HCl activation simulations at 300K and 400K.

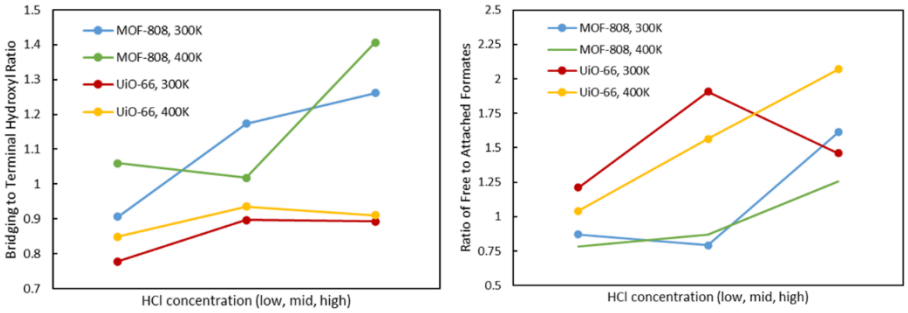

Figure 10. Formate group and hydroxyl group summary data for MOF–808 and UiO–66.

High-performing results from MOF–808 species were then selected to evaluate against toxic chemical removal performance. Sulfur dioxide is known to react with hydroxylated zirconia surfaces readily[9] and was chosen as a probe molecule of interest for reaction against formate-modulated MOF–808 samples. Two activation conditions, 0.2 M HCl and 5.5 M HCl at 300K, were selected to pursue for formate-modulated MOF–808, as they represented upper and lower bounds of total free surface hydroxyl species and total detached formates. Simulations showed that 5.5 M HCl-activated MOF–808 at 300K had the greatest formate removal efficacy and surface hydroxyl concentration, and this material was expected to perform better against sulfur dioxide than the 0.2 M HCl-activated material. Results, shown in Figure 11, are consistent with this hypothesis and confirm greater sulfur dioxide capacity of the 5.5 M HCl-activated material. The unactivated formate-modulated MOF–808 (MOF–808–FA) showed the highest capacity but had the lowest initial breakthrough time. The shape of the breakthrough curve, with rapid initial breakthrough followed by attenuation of the effluent concentration, suggested a pressure buildup fault in the system for that particular test; these data trends could be resolved through replication. Likely, the unactivated MOF–808–FA will show the lowest average loading of the three materials after replication and removing outlier data, which is consistent with expected surface chemistry trends predicted from simulation.

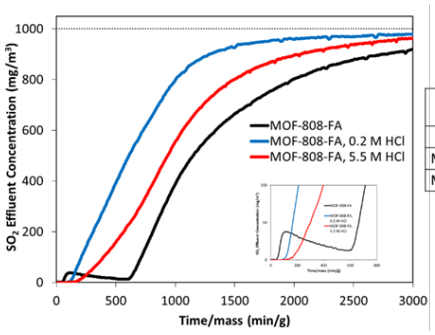

Sample	SO_2 loading (mol/kg)
MOF-808-FA	0.467
MOF-808-FA, 0.2 M HCl	0.231
MOF-808-FA, 5.5 M HCl	0.344

Figure 11. Sulfur dioxide microbreakthrough data for formate-acid-modulated MOF–808 at conditions from simulation.

Physical and chemical properties of the MOF–808–FA samples were measured and are depicted in Figures 12 and 13. The 0.2 M HCl-activated MOF–808–FA sample showed the highest surface area and micropore volume by far, yet it had the lower sulfur dioxide loading compared to the 5.5 M HCl-activated sample. This is consistent with significantly different surface chemistry being present in the two samples and may be due to a high density of partially-detached formate modulators in the 0.2 M HCl-activated sample. Figure 13 shows infrared spectra data, and wavenumber regions assigned to COO stretching vibrational modes, particularly around 1500 cm^{-1}, show increased fractional transmittance of the 5.5 M HCl-activated sample, which may reflect higher degree of formate removal. Additional analysis using tools such as solid state ^{1}H nuclear magnetic resonance spectroscopy may clarify this trend. Additionally, vibrational frequency computation of representative cluster models of MOF–808, shown in Figure 14, may clarify assigning wavenumber regions of interest for identifying and differentiating hydroxyl species and formate species observed in simulation.

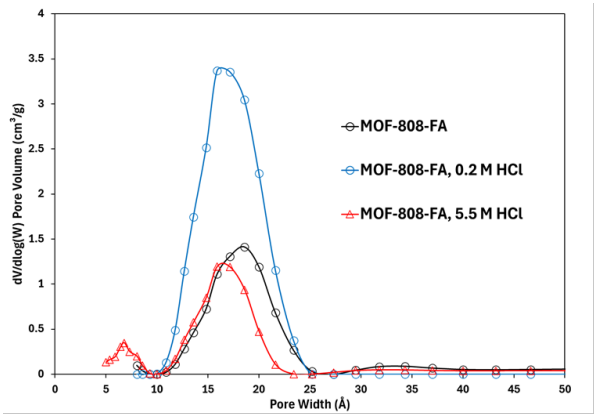

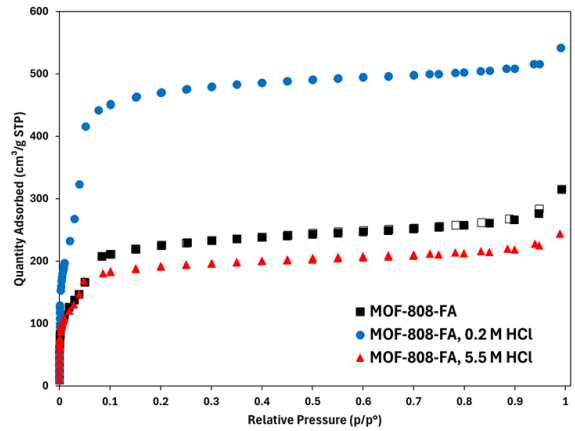

Sample	SO_2 loading (mol/kg)	BET Surface Area (m^2/g)	Micropore Volume (cm^3/g)
MOF-808-FA	0.467	781	0.218
MOF-808-FA, 0.2 M HCl	0.231	1639	0.564
MOF-808-FA, 5.5 M HCl	0.344	688	0.215

Figure 12. Pore size distribution computed from nitrogen adsorption isotherms on formate-modulated MOF–808 materials (upper left). Nitrogen adsorption isotherms at 77 K on formate-modulated MOF–808 materials (upper right). Summary of physical properties of formate-modulated MOF–808 materials and comparison to sulfur dioxide loading data (lower center).

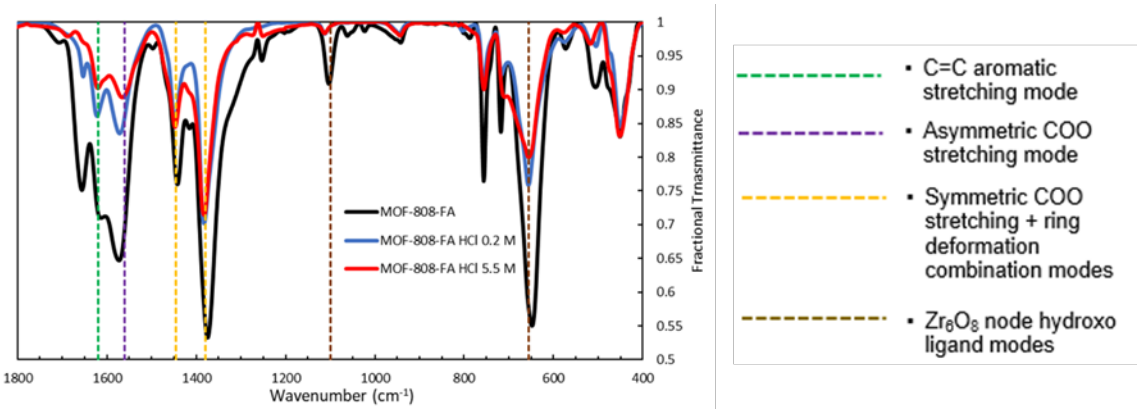

Figure 13. ATR-FTIR spectra of formate modulated MOF–808 materials, with select vibrational mode assignments from literature labeled.

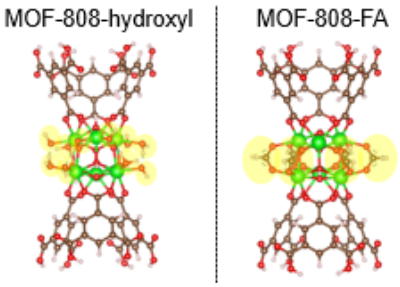

Figure 14. Cluster models of (left) fully terminal-hydroxylated MOF–808 and (right) formate-modulated MOF–808 used in quantum vibrational frequency calculations for assigning wavenumbers and corresponding modes for surface species formed from HCl activation process.

The effect of functionalization of the linker was explored using guest molecule-ligand functionality combinations shown in Figure 15. All simulations consisted of five guest molecules placed in the center of a single unit cell of MOF and run in the micro-canonical ensemble for one nanosecond. Among the data observed, cyano-functionalization showed strong propensity for reaction against hydrogen sulfide. This combination was hence selected for follow-on analysis.

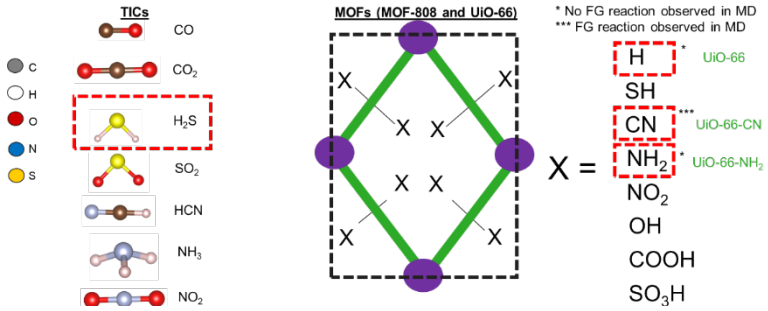

Figure 15. toxic industrial chemicals evaluated in screening ligand-functionalized UiO–66 and MOF–808 derivative reactivity (left) functional groups (FGs) incorporated into ligands on UiO–66 and MOF–808 for screening study (right).

Steric factors appear to play a role in mechanistic data with hydrogen sulfide reaction with cyano functionality. With UiO–66, in contrast to MOF–808, while hydrogen sulfide is still deprotonated by the cyano groups, the proximity of the functional groups seems to favor the HS^- reaction intermediates reacting with each other to form dihydrogen disulfide and then trisulfur (Figure 16). This type of reaction to a higher-molecular-weight product would be favorable for filtration, as such products would have greater propensity for removal via physical adsorption than the reactant toxic molecule due to lower vapor pressure.

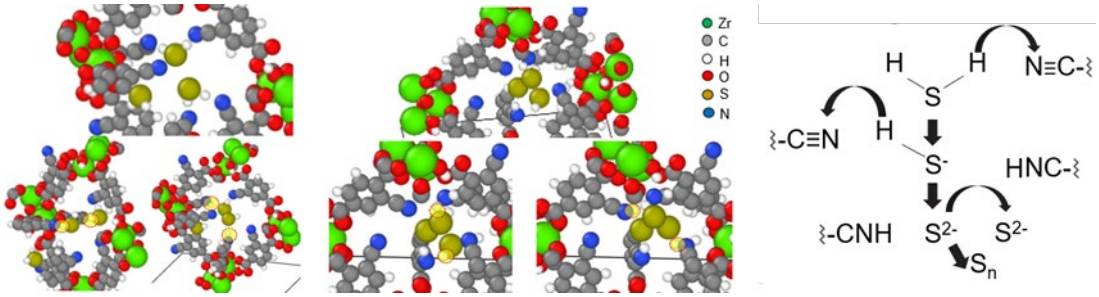

Figure 16. Hydrogen sulfide reaction mechanism observed in simulation with cyano-functionalized UiO–66.

DRIFTS spectra were collected for hydrogen sulfide exposure to UiO–66–CN and are shown in Figure 17. Results show strong negative peaks at 2234 cm^{-1}, indicative of disappearance of cyano group stretching modes and reflecting a reaction of hydrogen sulfide with the cyano functional group of the MOF, consistent with simulations. Further, microbreakthrough data in Figure 18 show a higher sulfur dioxide removal capacity of cyano-functionalized UiO–66 compared to baseline UiO–66 and amine-functionalized UiO-66, further emphasizing higher performance of hydrogen sulfide with the MOF using the cyano functional group.

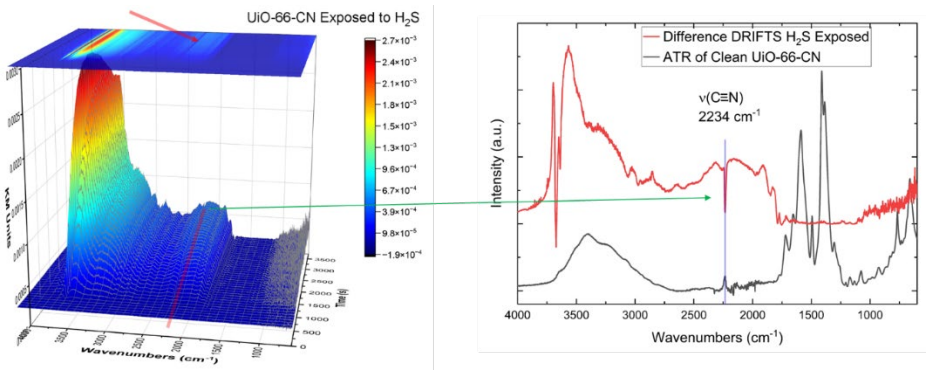

Figure 17. Diffuse reflectance infrared Fourier transform spectra of hydrogen sulfide exposed to cyano-functionalized UiO–66.

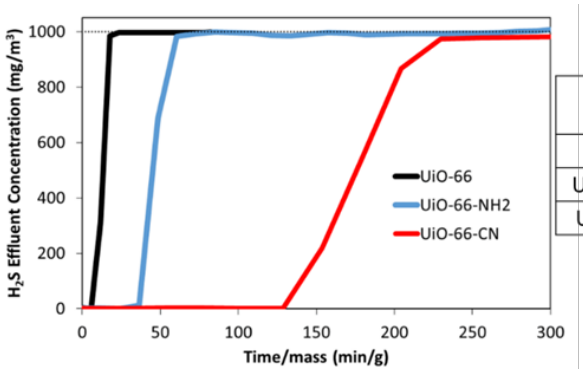

Sample	H_2S Loading (mol/kg)
UiO-66	0.009
UiO-66-NH_2	0.086
UiO-66-CN	0.253

Figure 18. Hydrogen sulfide microbreakthrough data and corresponding loadings for UiO–66 derivatives.

Lastly, comparison of hydrogen sulfide microbreakthrough against cyano-functionalized UiO–66 is shown against historical CBC lab data in Figure 19. Most high-performing MOFs against hydrogen sulfide were copper-containing MOFs, which are notorious for being unstable in the presence of humidity.[12] Among zirconium-based MOFs (UiO–66, MOF–808, and NU–1000, Figure 19), the cyano-functionalized UiO–66 had the highest hydrogen sulfide performance without incorporation of another metal into the structure.

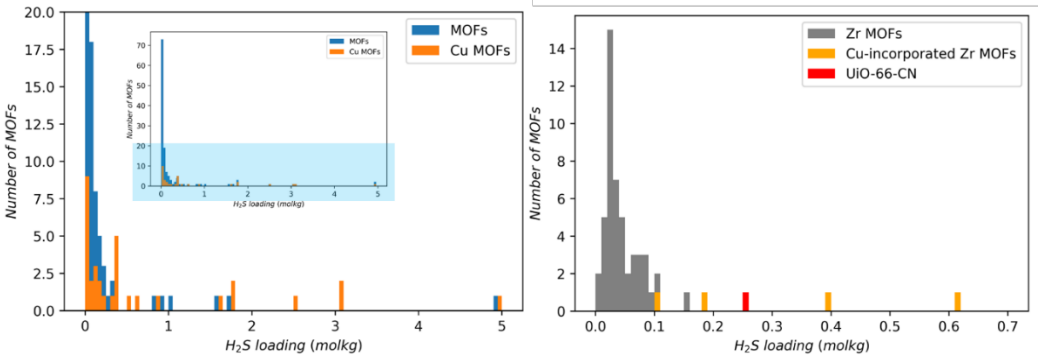

Figure 19. Histogram distribution of hydrogen sulfide loading for all MOFs ever tested in CBC laboratories (left). Histogram distribution of hydrogen sulfide loading for all zirconium-based MOFs ever tested in CBC laboratories (right).

4. CONCLUSIONS

Reactive molecular dynamics simulations have been used to simulate chemical reaction of guest molecules of interest on zirconium-based MOFs UiO–66 and MOF–808, simulating both synthesis conditions and toxic industrial chemical exposure for incorporating design strategies for increasing reactivity of the metal oxide cluster and organic ligand component of the MOF. Reactive molecular dynamics simulations have been performed to determine optimal

conditions facilitating the HCl solution activation removal of formate modulators from MOF–808 and UiO–66. Experimental results collected supported simulation data and showed higher sulfur dioxide removal capacity on the MOF–808 sample for which degree of formate removal was predicted to be greatest. Additionally, imparting cyano functionality on the organic ligand of UiO–66 was predicted to improve hydrogen sulfide reactivity of the structure and was confirmed by experiments.

ACKNOWLEDGMENTS

Funding was provided by the U.S. Army via the Chemical Biological Advanced Materials Manufacturing Program (PE 0601102A Project VR9) at the Combat Capabilities Development Command Chemical Biological Center.

REFERENCES

[1] Bobbitt, N.S.; Mendonca, M.L.; Howarth, A.J.; Islamoglu, T.; Hupp, J.T.; Farha, O.K.; Snurr, R.Q. Metal-Organic Frameworks for the Removal of Toxic Industrial Chemicals and Chemical Warfare Agents. *Chem. Soc. Rev.* **2017**, *46* (11), pp 3357–3385.

[2] Kandiah, M.; Nilsen, M.H.; Usseglio, S.; Jakobsen, S.; Olsbye, U.; Tilset, M.; Larabi, C.; Quadrelli, E.A.; Bonino, F.; Lillerud, K.P. Synthesis and Stability of Tagged UiO-66 Zr-MOFs. *Chem. Mater.* **2010**, *22* (24), pp 6632–6640.

[3] Winarta, J.; Shan, B.H.; McIntyre, S.M.; Ye, L.; Wang, C.; Liu, J.C.; Mu, B.A. Decade of UiO-66 Research: A Historic Review of Dynamic Structure, Synthesis Mechanisms, and Characterization Techniques of an Archetypal Metal-Organic Framework. *Cryst. Growth Des.* **2020**, *20* (2), pp 1347–1362.

[4] Liu, L.M.; Chen, Z.J.; Wang, J.J.; Zhang, D.L.; Zhu, Y.H.; Ling, S.L.; Huang, K.W.; Belmabkhout, Y.; Adil, K.; Zhang, Y.X.; Slater, B.; Eddaoudi, M.; Han, Y. Imaging defects and their evolution in a metal-organic framework at sub-unit-cell resolution. *Nat. Chem.* **2019**, *11* (7), pp 622–628.

[5] Senftle, T.P.; Hong, S.; Islam, M.M.; Kylasa, S.B.; Zheng, Y.X.; Shin, Y.K.; Junkermeier, C.; Engel-Herbert, R.; Janik, M.J.; Aktulga, H.M.; Verstraelen, T.; Grama, A.; van Duin, A.C.T. The ReaxFF reactive force-field: development, applications and future directions. *npj Comput. Mater.* **2016**, *2*, (15011) pp 2057–3960.

[6] Giannozzi, P.; Andreussi, O.; Brumme, T.; Bunau, O.; Nardelli, M.B.; Calandra, M.; Car, R.; Cavazzoni, C.; Ceresoli, D.; Cococcioni, M.; Colonna, N.; Carnimeo, I.; Dal Corso, A.; de Gironcoli, S.; Delugas, P.; DiStasio Jr., R.A.; Ferretti, A.; Floris, A.; Fratesi, G.; Fugallo, G.; Gebauer, R.; Gerstmann, U.; Giustino, F.; Gorni, T.; Jia, J.; Kawamura, M.; Ko, H.-Y.; Kokalj, A.; Küçükbenli, E.; Lazzeri, M.; Marsili, M.; Marzari, N.; Mauri, F.; Nguyen, N.L.; Nguyen, H.V.; Otero-de-la-Roza, L.; Paulatto, L.; Poncé , S.; Rocca, D.; Sabatini, R.; Santra, B.; Schlipf, M.; Seitsonen, A.P.; Smogunov, A.; Timrov, I.; Thonhauser, T.; Umari, P.; Vast, N.; Wu, X.; Baroni, S. Advanced capabilities for materials modelling with QUANTUM ESPRESSO. *J. Phys. Condens. Matter.* **2017**, *29* (46), p 465901.

[7] Thompson, A.P.; Aktulga, H.M.; Berger, R.; Bolintineanu, D.S.; Brown, W.M.; Crozier, P.S.; Veld, P.J.I.; Kohlmeyer, A.; Moore, S.G.; Nguyen, T.D.; Shan, R.; Stevens, M.J.; Tranchida, J.; Trott, C.; Plimpton, S.J. LAMMPS-a flexible simulation tool for particle-based materials modeling at the atomic, meso, and continuum scales. *Comput. Phys. Commun.* **2022**, *271*, p 108171.

[8] Dwivedi, S.; Kowalik, M.; Rosenbach, N.; Alqarni, D.S.; Shin, Y.K.; Yang, Y.J.; Mauro, J.C.; Tanksale, A.; Chaffee, A. L.; van Duin, A.C.T. Atomistic Mechanisms of Thermal Transformation in a Zr-Metal Organic Framework, MIL-140C. *J. Phys. Chem. Lett.* **2021**, *12* (1), pp 177–184.

[9] McEntee, M.; Peterson, G.W.; Balboa, A.; Iordanov, I.; Balow, R.B.; Pehrsson, P.E. Surface Chemistry of Sulfur Dioxide on $Zr(OH)_4$ Powder: The Role of Water. *J. Phys. Chem. C.* **2019**, *123* (28), pp 17205−17213.

[10] Glover, T.G. Peterson, G.W.; Schindler, B.J.; Britt, D.; Yaghi, O. MOF-74 building unit has a direct impact on toxic gas adsorption. *Chem. Eng. Sci.* **2011**, *66* (2), pp 163–170.

[11] Yang, D.; Gaggioli, C.A.; Ray, D.; Babucci, M.; Gagliardi, L.; Gates, B.C. Tuning Catalytic Sites on Zr_6O_8 Metal-Organic Framework Nodes via Ligand and Defect Chemistry Probed with tert-Butyl Alcohol Dehydration to Isobutylene. *J. Am. Chem. Soc.* **2020**, *142* (17), pp 8044–8056.

[12] Gul-E-Noor, F.; Jee, B.; Poppl, A.; Hartmann, M.; Himsl, D.; Bertmer, M. Effects of varying water adsorption on a $Cu_3(BTC)_2$ metal-organic framework (MOF) as studied by ^1H and ^{13}C solid-state NMR spectroscopy. *Phys. Chem. Chem. Phys.* **2011**, *13* (17), pp 7783–7788.

MOF straws: optimizing transport phenomena through the development of design rules for metal-organic framework hollow fibers

Trenton Tovar*[a], Matt Browe[a], Mark Harrison[b], John Mahle[a]
[a]U.S. Army Combat Capabilities Development Command Chemical Biological Center, Research & Operations Directorate, 8198 Blackhawk Rd, Aberdeen Proving Ground, MD 21010
[b]University of Maryland Baltimore County, 1000 Hilltop Cir, Baltimore, MD 21250

ABSTRACT

We aim to develop design rules for the fabrication of metal-organic framework hollow fibers. Using a customizable injection molding process developed and patented in-house, we can control the hollow fiber dimensions (inner diameter, fiber wall, metal-organic framework loading) by tuning a combination of parameters at both the macroscopic and nano scales. With the ability to fine tune fiber dimensions and properties, the transport phenomena (vapor, liquid) through the fibers, and subsequently through fiber arrays can be controlled. The hypothesis is sub divided into three aims: 1) fiber dimensions can be controlled through a combination of nanoscale and macro scale parameter tuning, 2) tuning of the fiber dimension will result in different performance for mass transfer, and 3) multiple fibers can be bundled into an array resulting in air flow through the array that approximates laminar flow to improve filtration from traditional packed beds. Collectively, the testing of this hypothesis will lead to design rules for the fabrication of hollow fibers and fiber arrays. The development of these metal-organic framework hollow fibers has broad implications beyond chemical biological filtration and may serve as a lightweight alternative to conventional filtration media employed across the defense, space, and healthcare industries.

Keywords: Metal-organic frameworks, polymer, composite, filtration, design of experiments

BLUF: We recently developed a new metal-organic framework/polymer composite hollow fiber form factor. We believe that by controlling the hollow fiber morphology, an optimized hollow fiber array can be developed with better mass and heat transfer properties than traditional packed bed sorbents.

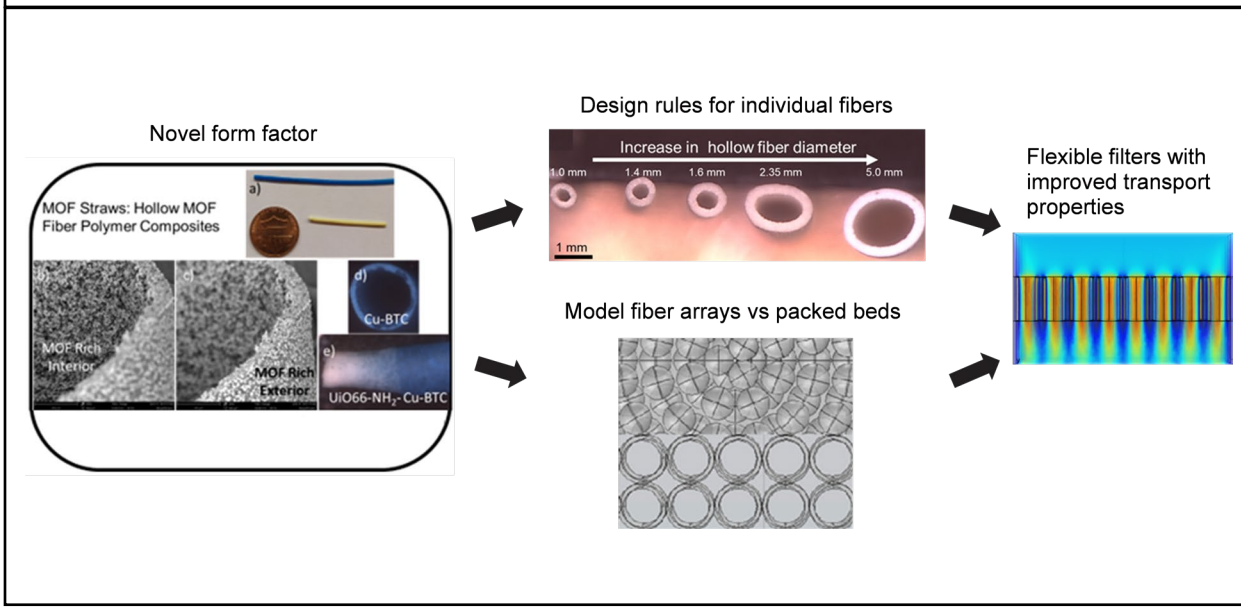

1. INTRODUCTION

1.1 Research problem:

Chemical protective equipment imposes a significant physiological burden on the warfighter.[1] Due to stringent requirements for high-capacity, broad spectrum filtration, mask filters are bulky with significant pressure drop.[2] Filters on the face of the mask can also create a tactical burden, such as rifle sighting.[3] In this project, we aim to develop a flexible filter that can effectively replace the traditional packed bed canisters. A flexible filter could allow mask engineers to design new equipment that reduces the impact of protective equipment on the warfighter.

Metal-organic frameworks (MOFs) have been studied as sorbents to protect from chemical threats.[4] This is due to their high surface areas and modular chemistries that can target specific applications.[5,6] While MOFs are synthesized as powders, MOF/polymer composites have been studied to develop functional materials in the form of membranes, fibers, and beads.[7–9] Recently, a novel hollow fiber MOF/polymer composite form factor was developed and patented in-house. We believe this new form factor could be used to develop a flexible filter with improved air flow while maintaining chemical protection.

1.2 Current state of the technology:

Figure 1 shows the current issue M50 mask and a self-contained breathing apparatus (SCBA). Bulky filters on the face of the M50 and a large CO_2 scrubber/ice pack in the SCBA make both burdensome. A flexible filter that could conform to the user or be placed in the breathing tubes of the SCBA could improve these issues. Developing better protective equipment is critical to the U.S. Army Combat Capabilities Development Command Chemical Biological Center's mission.

Figure 1: M50 mask (left) and SCBA (right)

1.3 Project objectives:

- Objective 1: Development of design rules for controlled morphology of MOF hollow fibers
  - Use design of experiments (DOE) to efficiently vary synthesis parameters and determine importance
  - Characterize fiber dimensions
- Objective 2: Elucidating hollow fiber mass transfer structure-performance relationships
  - Measure sorption capacity, mass transfer rates, and reactivity
  - Correlate to fiber morphology from Objective 1
- Objective 3: Fluid flow modeling, array assembly, and performance assessment
  - Use COMSOL® modeling to predict optimal fiber properties for fiber array design
  - FY25: Bundled fiber array filters undergo tube breakthrough and automated breathing and metabolic simulator testing

1.4 Exit criteria:

- Objective 1: Execute synthesis of DOE sample plan and individual hollow fiber characterization
- Objective 2: Experimentally measure sorption, mass transfer, and reactivity on DOE samples
- Objective 3: Predict optimized fiber array using fluid flow modeling to guide array assembly and testing

1.5 Hypothesis:

MOF hollow fiber morphology can be tuned by a combination of nanoscale and macroscopic parameters to optimize vapor and liquid transport properties. These hollow fibers can be bundled together to create a flexible array with better mass and heat transfer properties than traditional packed bed filters.

2. YEAR 1 ACCOMPLISHMENTS

2.1 Summary of project progress:

For objective one, a DOE plan was developed to minimize the number of individual hollow fibers needed to assess the importance of different synthesis parameters. The synthesis factors are MOF wt%, solution concentration, mold tube size, drying temperature, polymer type, MOF type, and solvent type. Factors one and two both have a continuous range that can vary. Factors three–seven have all three possible options. Trying to execute a sample plan where every possible combination of synthesis factors was tested would result in several thousand samples. With DOE, a plan with 67 samples was developed to determine the relevant factors in hollow fiber synthesis. For each sample, three response variables are tested for which includes the capacity/reactivity, an efficiency metric based on the capacity which is normalized to the active amount of MOF in each sample, the mass transfer rate, and the hollow fiber wall thickness. At the end of year one, 66 of the 67 samples were synthesized and the wall thickness response was characterized by either SEM or optical microscope, completing objective one.

For objective two, several different experiments have been used to measure responses one and two. This is due to the different applications of the three types of MOFs in the DOE plan. For sorption capacity of CO_2 and NH_3, isotherms were measured on a Micromeritics 3flex instrument. CO_2 is of interest due to scrubbing in an SCBA unit while NH_3 is a toxic industrial chemical of interest. Figure 2 shows an example of this data in both raw and normalized forms. The CO_2 sorption of pure MOF CALF-20 is higher than three MOF straws (MS) with varying wt% MOF. When normalized by the amount of MOF in each MS, the two samples made with tetrahydrofuran both reach the same sorption level as CALF-20 indicating a 100 % use of MOF efficiency metric while the MS synthesized in dichloromethane does not. A factor relevance plot shows the relative importance of each MS synthesis variable. The most important factor is MOF percent followed by solvent choice, tube size, and solution concentration which all have similar relevance. Drying temperature and polymer choice have the least relevance. The same analysis can be performed for NH_3 sorption and agent (GD) reactivity.

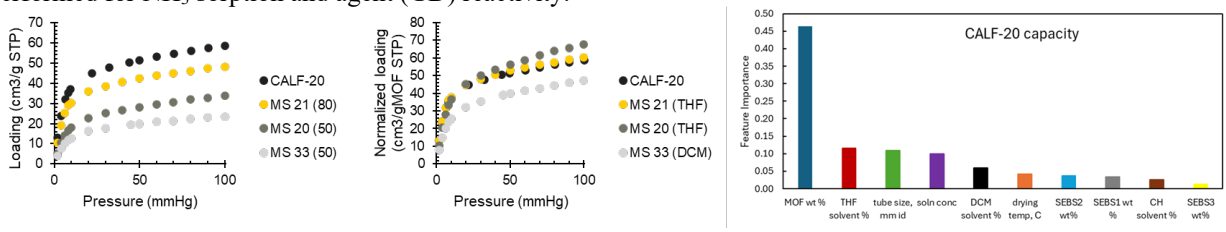

Figure 2: Raw (left) and normalized (middle) CO_2 isotherms and DOE factor importance (right) for CALF-20 MS.

Mass transfer data for CO_2 and NH_3 has been measured via zero-length column (ZLC) and gravimetric uptake methods.[10,11] Figure 3 shows examples of this data. It was found that the formation of MS has a significant impact on the mass transfer of CO_2 but not for NH_3. We hypothesize that this is due to the physisorptive versus chemisorptive nature of the chemicals. NH_3 degrades the structure of the MOF as more chemical reacts with the metal. Thus, when measuring NH_3 uptake rate, it is not mass transfer that is measured but rather the rate of breakdown of the MOF. Capacity and mass transfer measurements are ongoing and objective two is about 66 % completed.

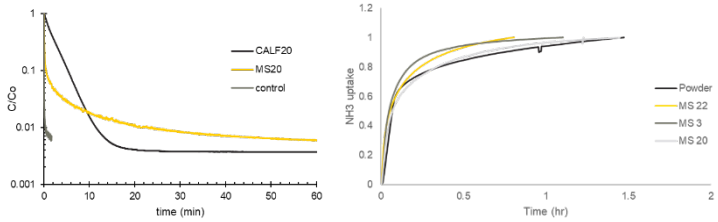

Figure 3: CO_2 ZLC (left) and NH_3 gravimetric uptake (right).

For objective three, hollow fiber arrays were simulated using COMSOL® MultiPhysics computational fluid dynamics software, which uses the finite element method to numerically solve systems of partial differential equations in continuum-level models.[12] Physics of interest for the simulations included pressure drop and chemical species transport through the fibers. Pressure drop computation is a steady-state solution and was solved in isolation to gauge the effect of physical parameters of the fibers. Figure 4 shows how the simulation geometry was set up for various fiber sizes and the pressure drop per length as a function of fiber diameter and flow velocity. Preliminary breaktime profiles were also simulated based on equilibrium sorption isotherms. The goal of this work is to optimize fiber array designs to maximize chemical breaktimes within the constraint of pressure drop requirements. The modeling portion of objective three is 75 % complete.

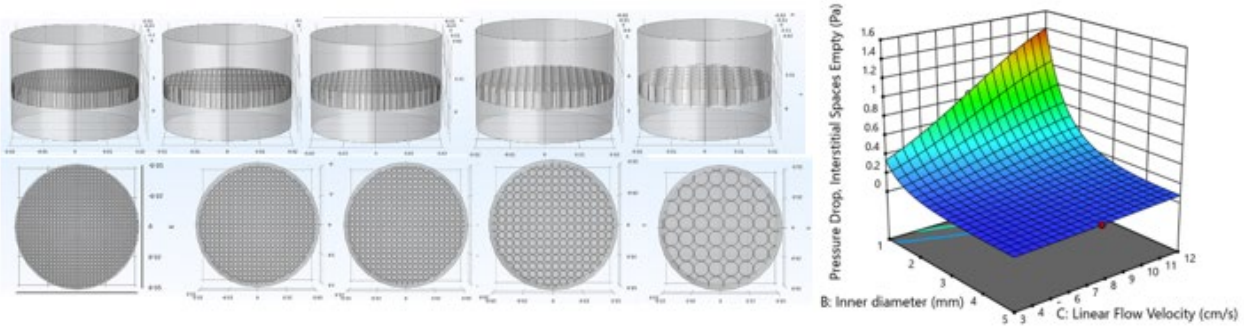

Figure 4: COMSOL® fiber array models (left) and pressure drop profiles (right).

2.2 Project challenges and lessons learned:

A few challenges have been encountered during this research but the risk to project cost or timeframe has been minimal. The SEM instrument used to measure wall thickness was down for several months, but an optical microscope was used in its place. Additionally, a hard-drive crash on the computer used for the ZLC apparatus delayed data collection but is now operational. Currently, the biggest issue is the computational time required for modeling chemical breakthrough on a full fiber array. Scaled down simulations as opposed to full filter modeling is being used to get around this challenge. Currently, the data accumulated from this effort to date supports our hypothesis and adjustments are not needed at this time.

3. FUTURE DIRECTIONS

All experimental measurements for objective two should be completed by the end of Q1 in FY25 along with the modeling for objective three and optimal fiber array designs forwarded for testing. The DOE design rules will be used to produce fibers and test the fiber array designs using NH_3 tube and Automated Breathing and Metabolic Simulator testing. If successful, the project will seek transition to interested stakeholders such as Defense Threat Reduction Agency or Joint Program Executive Office for Chemical, Biological, Radiological and Nuclear Defense.

ACKNOWLEDGMENTS

The authors of this report would like to acknowledge Dr. John Landers who was the original inventor of the MOF hollow fibers and contributed to the project proposal before leaving the U.S. Army Combat Capabilities Development Command Chemical Biological Center. Funding was provided by the U.S. Army via the Chemical Biological Advanced Materials Manufacturing Program (PE 0601102A Project VR9) at the Combat Capabilities Development Command Chemical Biological Center.

REFERENCES

[1] Krueger, G.P.; Banderet, L.E. Effects of chemical protective clothing on military performance: a review of the issues. *Mil. Psychol.* **1997**, *9* (4), pp 255–286.

[2] Harmata, W. Testing filter elements for gas masks. *Scientific Journal of the Military University of Land Forces.* **2021**, *53* (201), pp 464–481.
[3] Merchan, A.; Clemente-Suarez, V.J. Psychophysiological modifications in an assault infantry maneuvre using a chemical, biological, radiological and nuclear personal protective equipment. *BMJ Military Health.* **2019***, 166* (2), pp 62–66.
[4] DeCoste, J.B.; Peterson, G.W. Metal-Organic Frameworks for Air Purification of Toxic Chemicals. *Chem. Rev*. **2014**, *114*, pp 5695–5727.
[5] Li, H.; Eddaoudi, M.; O'Keeffe, M.; Yaghi, O.M. Design and synthesis of an exceptionally stable and highly porous metal-organic framework. *Nature.* **1999**, *402*, pp 276–279.
[6] Long, J.R.; Yaghi, O.M. The pervasive chemistry of metal-organic frameworks. *Chem. Soc. Rev*. **2009**, *38*, pp 1213–1214
[7] Peterson, G.W.; Lu, A.X.; Hall, M.G.; Browe, M.A.; Tovar, T.M.; Epps III, T.H. MOFwich: Sandwiched Metal-Organic Framework-Containing Mixed Matrix Composites for Chemical Warfare Agent Removal. *ACS Appl. Mater. Interfaces.* **2018**, *10*, pp 6820–6824.
[8] Peterson, G.W.; Lee, D.T.; Barton, H.F.; Epps III, T.H.; Parsons, G. N. Fibre-based composites from the integration of metal-organic frameworks and polymers. *Nat. Rev. Mater.* **2021**, *6*, pp 605–621.
[9] Peterson, G.W.; Mahle, J.J.; Tovar, T.M.; Epps III, T.H. Bent-But-Not-Broken: Reactive Metal-Organic Framework Composites from Elastomeric Phase-Inverted Polymers. *Adv. Funct. Mater.* **2020**, *30* (51), pp 2005517.
[10] Brandani, S.; Mangano, E. The zero length column technique to measure adsorption equilibrium and kinetics: lessons learnt from 30 years of experience. *Adsorption.* **2021**, *27*, pp 319–351.
[11] Remi, J.C.S.; Lauerer, A.; Chmelik, C.; Vandendael, I.; Terryn, H.; Baron, G.; Denayer, J.F.M.; Karger, J. The role of crystal diversity in understanding mass transfer in nanoporous materials. *Nat. Mater.* **2016**, *15*, pp 401–406.
[12] COMSOL Multiphysics® v. 6.2. www.comsol.com. COMSOL AB, Stockholm, Sweden.

This page left intentionally blank

Controlling the heterogeneous catalysis of zirconium clusters within a porous SBA-15 scaffold

Ann M. Kulisiewicz[a]*, Sergio J. Garibay[a,b], Trenton B. Tovar[a], Matthew A. Browe[a]
[a]U.S. Army Combat Capabilities Development Command Chemical Biological Center, Research & Operations Directorate, 8198 Blackhawk Rd, Aberdeen Proving Ground, MD 21010
[b]Leidos, Inc., 3465 Box Hill Corporate Center Dr, Abingdon, MD 21009

ABSTRACT

Metal-organic frameworks with Zr-based secondary building units have shown promise as catalytic degraders of chemical warfare agents. The Zr-based secondary building units within these metal-organic frameworks have been determined to be the active site for hydrolysis reactions within these materials. However, reaction rates of Zr metal-organic frameworks vary, indicating the metal-organic framework linker may play a role in the catalytic activity of the metal-organic framework by affecting the environment around the secondary building unit. The metal-organic framework structure variables (e.g., pore size/structure, connectivity, crystal size, functional groups, defects, and monocarboxylic acid modulators) complicate our understanding of the linker's role in the reaction. Here, we explored a simplified secondary building unit system consisting of Zr_6 and Zr_{12} clusters with monocarboxylic acid modulators varying in size and functionality to simulate the environment of the secondary building unit. The Zr clusters were supported on mesoporous silica (SBA-15) functionalized with sulfuric or phosphoric acid groups. The final silica-bound Zr clusters showed enhanced reactivity towards dimethyl nitrophosphate hydrolysis, a nerve agent simulant, compared to the bare Zr clusters and showed differences in catalytic activity based on the chemical environment. In addition, silica scaffolding allowed for the incorporation of adjacent amine moieties on the SBA-15 support to facilitate hydrolysis of dimethyl nitrophosphate under neutral aqueous conditions.

Keywords: Metal-organic framework, catalysis, acid-modified silica

1. INTRODUCTION

Metal-organic frameworks (MOF) have shown immense promise in recent years for the catalytic degradation of chemical warfare agents (CWA).[1–5] MOFs are materials consisting of metal nodes, referred to as secondary building units (SBU), bridged in a crystalline arrangement by organic linkers to create a porous framework. By varying the SBU and linker, a wide array of MOFs can be synthesized with different structural or chemical properties tailored to a specific application. MOFs containing $Zr_6O_4(OH)_4^{12+}$ SBUs have recently shown promise as catalytically active materials for nerve agent hydrolysis.[6–13] This includes UiO-66, UiO-67, NU-1000, NU-901, MOF-808, and many other variants of these structural topologies with functionalized linkers. For each of these MOFs, the hydrolysis reaction mechanism with phosphorous based agents (such as VX and GB) occurs solely on the SBU and does not involve the linker.[14] However, despite having the same reaction site and mechanism, the reaction rate varies greatly based on the MOF and agent combination. Therefore, it can be inferred that the fundamental difference in reactivity among Zr-based MOFs is primarily due to the nature of the linker. While linkers do not participate directly in the hydrolysis reaction, linker topology and functionality can create steric and electronic effects at the SBU which can affect the adsorption and subsequent reactivity of CWAs with the MOF.

Understanding the effect of the linker on the SBU is crucial for elucidating the fundamental differences in reactivity among Zr-based MOFs with CWAs. However, studies regarding the impact of the MOF linker on the chemical environment around the SBU pose a challenge for a variety of reasons. One of the key limitations is the inability to quantify the number of, and access to, active sites within a MOF. Zr-MOFs can have connectivity of six, eight, or 12 linkers per SBU and can have linker defects within that motif at discrete points within the SBU structure, possibly revealing more active Zr-OH sites on the SBU. However, while bulk material defects can be calculated, these point defects, which can greatly influence reactivity, are impossible to detect and quantify.[15] Additionally, these defects can vary from batch to batch making fundamental reactivity studies even more challenging. Due to pore size, it has been hypothesized that certain agents cannot access the interior of some MOFs based on steric constraints limiting reactivity

of these materials to surface sites.[16–18] Therefore crystal size is also a significant factor when it comes to MOF reactivity, with smaller crystal sizes exhibiting faster kinetics. However, crystal size can vary based on synthesis conditions, making it difficult to standardize.

In this study, we seek to understand the effect of the linker on hydrolysis reactivity at the Zr-MOF SBU independent of the topology constraints of the MOF structure. To accomplish this, we have synthesized a suite of materials consisting of zirconium clusters analogous to SBUs used in reactive Zr-based MOFs. These clusters have monocarboxylic acid modulators (MCAM) varying in size and pKa to simulate the MOF linkers independent of the structure and simulate the chemical environment of the SBU within the MOF. The zirconium clusters are then bound to an acid-modified, inert SBA-15 support to control catalyst loading and to determine the effect of catalyst loading on the rate of the hydrolysis reaction of dimethyl nitrophosphate (DMNP), a nerve agent simulant.

2. EXPERIMENTAL METHODS

2.1 Synthesis

2.1.1 Zirconium cluster synthesis

All reagents were purchased from commercial sources and used without further purification. Zr_6 and Zr_{12} clusters were synthesized according to modified literature procedures from Pappas et al.[19] and Bezrukov et al.[20] respectively. Reagents were purchased from commercial sources and used without further purification. Zr_6-acetic acid, Zr_6-glycine, and Zr_{12}-SBUs were synthesized according to modified literature procedures.[2–4]

$[Zr_6(O)_4(OH)_4(H_2O)_8(Gly)_8]$ ·12Cl · $8H_2O$: In an 8-dram vial, 0.403 g (1.25 mmol) of $ZrOCl_2 \cdot 8H_2O$ 0.403 g, 1.25 mmol) was dissolved in 12 mL of H_2O. After solvation, 0.375 g (5 mmol) of glycine and 0.1 mL of 8 mM HCl were added to the vial. The resulting solution was then briefly stirred for 5 minutes and then heated at 98 °C for 4 days to allow for the slow evaporation of water. The resulting gel was then recrystallized with 4–6 mL of hot deionized water held at 100 °C until the volume decreased to 3 mL of water. The vial was removed from the hot plate and allowed to cool. After cooling for 2 hours, the resulting white solid was rinsed with $CHCl_3$ (3 mL x 3).

$[Zr_6(O)_4(OH)_4(AA)_8] \cdot 3Cl \cdot 2H_2O$: A 2.00 g (8.58 mmol) amount of $ZrCl_4$, 5.00 mL of isopropanol, and 3.00 mL (53.0 mmol) of acetic acid were added in succession to a 50 mL round-bottom flask. The resulting mixture was then refluxed under stirring at 120 °C for 1 hour. After cooling to room temperature, the resulting zirconium clusters were filtered and rinsed with acetone.

$[Zr_6(O)_4(OH)_4(BA\text{-}CH_2NH_2)_{10}] \cdot 5Cl$: A 0.140 g (0.927 mmol) amount of 4-(aminomethyl) benzoic acid ($BA\text{-}CH_2NH_2$) was dissolved in 12.0 mL H_2O and added to an 8-dram vial containing 0.100 g (0.070 mmol) of $[Zr_6(O)_4(OH)_4(AA)_8] \cdot 3Cl \cdot 2H_2O$. This mixture was then heated at 50 °C for 30 minutes under stirring and then capped and heated for an additional 18 hours at 80 °C in an oven. The resulting suspension was dried through rotary evaporation.

$[Zr_6(O)_4(OH)_4(BA\text{-}CH_2\text{-}Morph)_{12}] \cdot 5Cl$: A 0.204 g (0.924 mmol) amount of 4-(morpholinomethyl)benzoic acid ($BA\text{-}CH_2$ –Morph) (0.204 g, 0.924 mmol) was dissolved in 12.0 mL H_2O and added to an 8-dram vial containing 0.100 g (0.070 mmol) of $[Zr_6(O)_4(OH)_4(AA)_8] \cdot 3Cl \cdot 2H_2O$. This mixture was then heated at 80 °C for 30 minutes under stirring and then capped and heated for an additional 18 hours at 80 °C in an oven. The resulting suspension was dried through rotary evaporation.

$[Zr_6(O)_4(OH)_4(BA)_{10}] \cdot 2Cl \cdot 2H_2O$: A 2g (8.58 mmol) amount of $ZrCl_4$ (2.00 g, 8.58 mmol), 10.0 mL of isopropanol, and 6.39 g (52.4 mmol) of benzoic acid were added in succession to a 50 mL round-bottom flask. The resulting mixture was then refluxed under stirring at 120 °C for 18 hours. After cooling to room temperature, the resulting solid was then filtered and rinsed with acetone.

$Zr_{12}O_8(OH)_8(AA)_{24}$: A 1.16 g (3.60 mmol) amount of $ZrOCl_2 \cdot 8H_2O$ was dissolved in 1.80 mL of N,N-Dimethylformamide (DMF) in an 8-dram vial. After dissolution, 7.95 mL (139 mmol) of acetic acid was added to the vial and the resulting solution stirred for 5 minutes until the solution turned clear. The vial was then capped and placed in a pre-heated oven at 110 °C for 24 hours. The resulting white crystalline solid was filtered and rinsed with 50 mL of a 1:1 DMF/acetic acid solution. The solid was transferred to an 8-dram vial and solvent exchanged with $CHCl_3$ (3 mL x 3). After the solvent exchange, residual chloroform was removed through evaporation using N_2 at room temperature.

[$Zr_6(O)_4(OH)_4(FA)_8$]: A 1.16 g (3.60 mmol) amount of $ZrOCl_2 \cdot 8\ H_2O$ was dissolved in 1.80 mL of DMF in an 8-dram vial. After dissolution, 5.24 mL (139 mmol) of propanoic acid (5.24 mL, 139 mmol) was added to the vial and the resulting solution stirred for 5 minutes until the solution turned clear. The vial was then capped and placed in a pre-heated oven at 110 °C for 24 hours. The resulting white crystalline solid was filtered and washed with 50 mL of a 1:1 DMF/propanoic acid solution. The solid was transferred to an 8-dram vial and solvent exchanged with $CHCl_3$ (3 mL x 3). After the solvent exchange, residual chloroform was removed through evaporation using N_2 at room temperature.

[$Zr_6(O)_4(OH)_4(PA)_8$]: A 2.00 g (8.58 mmol) amount of $ZrCl_4$, 5.00 mL of isopropanol, and 3.90 mL (53 mmol) of propanoic acid was added in succession to a 50 mL round-bottom flask. The resulting mixture was then refluxed under stirring at 120 °C for 1 hour. After cooling to room temperature, the resulting white crystalline solid was then filtered and rinsed with acetone. After the solvent exchange, residual acetone was removed through evaporation using N_2 at room temperature.

$Zr_{12}O_8(OH)_8(FA)_{24}$: A 2.0 g (8.6 mmol) amount of $ZrCl_4$, 5.0 mL of isopropanol, and 2.0 mL (53 mmol) of formic acid were added in succession to a 50 mL round bottom flask. The resulting mixture was then refluxed under stirring at 130 °C for 18 hours. After cooling to room temperature, the resulting white crystalline solid was then filtered and rinsed with acetone. Residual acetone was removed through evaporation using N_2 at room temperature.

$Zr_{12}O_8(OH)_8(PA)_{24}$: A 2.35 mL (5.22 mmol) amount of $Zr[O(CH_2)_2CH_3]_4$, and 3.13 mL (41.8 mmol) of propanoic acid were added in succession to a 50 mL round bottom flask. The resulting mixture was then stirred for 18 hours at 25 °C. The resulting white crystalline solid was then filtered and rinsed with 50 mL of a 1:4 1-propanol: propanoic acid solution.

2.1.2 Synthesis of sulfuric acid treated SBA-15

Sulfuric acid treated SBA-15 was synthesized according to literature procedures from Crisci et al.[21] A 0.67 g amount of Pluronic 123 was dissolved in 23 mL of 1.6 M HCl at 35 °C. A 1.4 mL amount of tetraethyl orthosilicate (TEOS) and 140 mg NaCl were added and the resulting solution was stirred for 1 hr. The solution was then equally divided into 3 vials. One vial contained only the synthesized solution. For the other two vials, 12 µL of 3-mercapto-trimethoxysilane (MPTMS) was added and to one and 48 µL of MPTMS was added in 12 µL increments every 15 minutes to the other. To each of the three vials, an additional 1.4 mmol of H_2O_2 was added. and the vials were then stirred for 24 hours. Afterwards, all three samples were placed in Parr bombs and heated at 100 °C for 24 hours. After heating, the samples were filtered and washed with water. From each sample, the Pluronic surfactant was removed by refluxing in ethanol. The samples were then washed with ethanol and the removal was repeated. The two samples containing MPTMS were washed with water and suspended in 1 M HCl for 3 hours. The HCl treated samples were filtered and washed with water, dried in air overnight at 60 °C. The samples were then dried under vacuum at 150 °C.

2.1.3 Synthesis of phosphoric acid treated SBA-15

A phosphoric acid functionalized SBA-15 was synthesized following the procedure from Wu et. al.[22] The MPTMS-free sample synthesized in the previous section was first suspended in a 0.2 M H_3PO_4/acetone solution. The mixture was then stirred at 60 °C until all acetone was removed. The sample was then dried in air overnight at 60 °C and then dried under vacuum at 150 °C.

2.1.4 Synthesis of zirconium cluster treated acid functionalized SBA-15

A solution of 70 mg of Zr-SBU cluster dissolved in 12 mL of DMF was added to an 8-dram vial containing 70 mg of either phosphoric or sulfuric acid functionalized SBA-15 and then capped. For the sample containing the sulfuric acid functionalized SBA-15, the vial was heated in an oven at 55 °C while the sample containing phosphoric acid functionalized SBA-15 was heated in an oven at 100 °C; both samples were heated for 18 hours. After heat treatment, the vials were solvent exchanged with fresh DMF and acetone (12 mL x 3).

2.1.5 Synthesis of acid-base functionalized SBA-15

A bifunctional acid-base SBA-15 support was synthesized according to Shao et. al.[23] An amount of 1 g of Pluronic P-123 was dissolved in 40 mL of water and 5 mL of HCl at 40 °C. An amount of 5 mL of TEOS, 200 µL of MPTMS, and 400 µL 3-tert-butyloxycarbonylaminopropyltrimethoxysilane (NHBoc) were then added to the initial solution and stirred for 24 hours. The addition of the tert-butylcarbonyl amine was essential to act as an acid-protecting group on SBA-15-SO_3 to allow for subsequent addition of aminopropyltrimethoxysilane. The solution was then placed in a Parr

bomb and heated for an additional 24 hours at 100 °C. The resulting product was then washed with water followed by removal of P123 with ethanol under reflux. After removing P123, the material was treated with 1 mL H_2O_2 in 10 mL water to oxidize the mercapto groups to sulfonic acid sites. Afterwards, the sample was heated under vacuum at 185 °C for 24 hours to remove the protecting group and leave basic amino sites.

2.1.6 Synthesis of zirconium cluster treated acid-base functionalized SBA-15

A 70 mg amount of Zr_{12}-acetic acid-SBU cluster dissolved in 12 mL of DMF was added to an 8-dram vial containing 70 mg of propylamine-propylsulfuric acid-functionalized SBA-15 and then capped. The vial was heated in an oven at 55 °C for 18 hours. The vials were solvent exchanged with fresh DMF and acetone (12 mL x 3).

2.2 Characterization

2.2.1 SEM-EDX

Scanning electron microscopy (SEM) images were taken with a Phenom GSR desktop instrument. Samples were placed on double-sided carbon tape. Samples were imaged at an accelerating voltage of 15 kV and a working distance of ~10 mm. Energy dispersive X-ray spectroscopy (EDX) was used to map elemental dispersion throughout the composites.

2.2.2 Powder X-ray diffraction

Powder x-ray diffraction (PXRD) patterns were measured on a Rigaku MiniFlex 600 diffractometer equipped with a D/teX Ultra detector with Cu-Kα radiation (λ = 1.5418 Å) over a range of 2θ = 3-50° at a scan rate of 5 deg min^{-1}.

2.2.3 ATR-IR

Attenuated total reflectance-Fourier transform infrared (ATR-FTIR) spectra were measured on a Bruker Tensor 27 spectrometer over the range of 4000–400 cm^{-1} at a resolution of 2 cm^{-1}.

2.2.4 N_2 physisorption

N_2 isotherms were measured using a Micromeritics ASAP 2420 analyzer set at 77 K. Samples were off-gassed at -120 °C under vacuum for approximately 16 hours. The Brunauer-Emmett-Teller (BET) method was used to calculate specific surface area in m^2/g.

2.2.5 X-ray photoelectron spectroscopy experiments

All ***X-ray photoelectron spectroscopy*** (XPS) measurements were performed using a Physical Electronics VersaProbe II photoelectron spectrometer outfitted with an Al Kα x-ray source. The base pressure of the analyzer chamber was $\leq$ 1 x 10^{-9} mbar. High-resolution scans were taken with a pass energy of 23.5 eV and a step size of 0.05 eV. The elemental analysis does not reveal contamination in the studied compounds beyond adventitious carbon, which corresponds to hydrocarbon species present in all air-exposed materials. The peak-fitting procedures were carried out using CasaXPS software using a Shirley-type background.

2.3 Catalysis experiments

A solution (9:1) of H_2O:D_2O (0.9/0.1 mL) was added to a vial containing 8.6–8.7 g (~12 mol%) of cluster modified SBA-15 and then capped. The vial was briefly sonicated for 1 minute and then transferred to a nuclear magnetic resonance (NMR) tube. An amount of 50 μL of N-ethylmorpholine was added to the above solution contained within the NMR tube. An amount of 4 μL (25 μmol) of DMNP was then deposited on the inside wall of the NMR tube. Lastly, the NMR tube was capped and carefully inverted three times to ensure proper mixing and then inserted into the NMR instrument. The progress of DMNP hydrolysis was determined by monitored using ^{31}P NMR.

2.4 Computational modeling of zirconium clusters

Amorphous silica slab models were generated to better understand electronic structure properties of the materials synthesized. A 28 x 28 x 14 Å slab of beta-cristobalite silica was prepared in the Materials Studio molecular editor. The slab was fed into the Large-scale Atomic/Molecular Massively Parallel Simulator molecular dynamics code and subjected to a melt-quench algorithm using a Tersoff interatomic potential for all atoms, a commonly used procedure for preparing an amorphous silica surface. A representative “patch” of silica was cut out of the surface, approximately 100 atoms in total, to minimize computational intensiveness. The patch was modified such that all oxygen atoms contained two bonds and all silicon atoms contained four bonds, satisfying all oxygen bonding with hydrogen atoms and satisfying all silicon bonding with hydroxyl (-OH) groups. The resulting structure was then geometry optimized

and energy minimized using the Gaussian 16 quantum chemistry software at the B3LYP/lanl2dz level of theory. All Zr_6-based clusters were based off a Zr_6O_8 core structure with 24 additional oxygen atoms bonded to the zirconium atoms and protruding to the outer edge of the cluster. These external oxygen atoms were then subjected to different capping chemistries. Previous literature on sulfate group binding to these clusters was used as a guide for modelling bound zirconium clusters to the silica surface.[21, 22] The net result involved removal of the capping group and bonding of oxygen atoms from the functional group to the zirconium atoms of the cluster. A few possible configurations were explored using polarizable continuum implicit solvation models (designating water as the solvent) in Gaussian 16 at the B3LYP/6-31G(d,p) level of theory. In these calculations, the atoms native to the optimized silica patch were fixed to save on computational resources; only the functional groups and zirconium cluster atoms were allowed to move. The mapping of electrostatic potential at constant electron density was then generated in Vesta for bonded and non-bonded zirconium clusters. An isovalue of 0.001 atomic units is commonly used for the contour of constant electron density and was utilized here.[25] Electrostatic potential was mapped from a maximum of 0.05 atomic units (red) to a minimum of -0.05 atomic units (blue) and is loosely considered a metric for identifying regions of guest molecule affinity, with higher electrostatic potential (red) correlating to higher guest molecule affinity.

3. RESULTS

A suite of Zr_6 clusters with MCAMs varying in size and electronic structure were synthesized to be tethered to SBA-15 supports. In addition, Zr_{12} clusters were synthesized based on a recent report in which these clusters were used as MOF precursors and to determine if the dimeric structure imparts any fundamental differences in reactivity.[20] The Zr_6 and Zr_{12} clusters were synthesized through modified literature procedures using excess MCAMs under heating. The PXRD patterns of the synthesized clusters closely resembled that of their simulated patterns derived from their single crystal X-ray diffraction structures. The reactivity of the Zr_6- and Zr_{12}-clusters with DMNP under buffered aqueous conditions was assessed using ^{31}P NMR spectroscopy. As previously reported in Zr-based MOFs, the Zr clusters do not facilitate DMNP hydrolysis under strictly neutral (pH = 7) conditions, requiring basic conditions or an amine co-catalyst for effective reactivity.[24] The use of N-ethylmorpholine buffer engenders the Zr clusters to facilitate DMNP hydrolysis (Figure 1). Presumably, N-ethylmorpholine facilitates the dissociation of mono-carboxylic acids which then induces DMNP access to the resulting Zr-OH and Zr-H_2O catalytic sites for hydrolysis. The Zr_6 clusters fully facilitate the selective hydrolysis of DMNP with half-lives ($t_{½}$) ranging from 8–27 minutes. The suite of Zr_6 clusters also showed a distinct trend with reactivity in terms of pKa with the MCAM with the highest pKa having the fastest kinetics. The larger the pKa of the MCAM, the more easily it can be removed from the cluster. This trend aligns well with the hydrolysis reaction mechanism on the SBU of the MOF, where a Zr-OH or Zr-H_2O site is the initiator for the reaction.[26]

Interestingly, the Zr_{12} clusters perform much faster having a DMNP half-life ranging from 7–12 minutes. This may be attributable to the larger number of available Zr-OH and Zr-H_2O catalytic sites of the Zr_{12} clusters as compared to the Zr_6 clusters (2:1, respectively). To further enhance DMNP hydrolysis with the Zr clusters, HCl-activation was performed to displace the MCAMs from the SBU and generate more active sites available for reaction with DMNP.[25] Both Zr clusters retain their crystallinity after HCl-activation. As expected, the HCl-activated Zr_{12}-(acetic acid) cluster facilitated faster DMNP hydrolysis than the as synthesized Zr_{12}-(acetic acid) cluster under 0.45 M N-ethylmorpholine aqueous conditions ($t_{½}$ = 7 versus 12 minutes, respectively (Figure 1)).

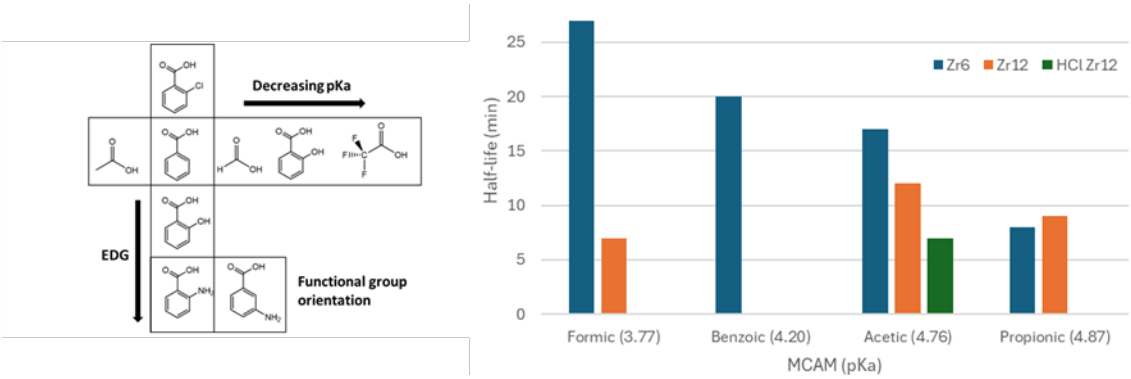

Figure 1. MCAMs used in the synthesis of Zr clusters (left). Half-life of DMNP in 0.45 NEM buffer for Zr6 and Zr12 with synthesized with various MCAMs (right).

To assess the effect of catalyst loading on reactivity, Zr clusters were bound to modified silica particles. Silica particles (SBA-15) were modified with phosphoric acid so the Zr clusters were covalently bound to the porous silica structure similar to a MOF structure. The particles were characterized by ATR-IR and N_2 isotherms to determine crystallinity and porosity respectively. The IR spectrum of phosphoric acid functionalized SBA-15 (P-SBA-15) contain peaks around 1323 cm^{-1} and 626 cm^{-1} corresponding to the P=O and P-OH stretches respectively. After phosphoric acid functionalization, the N_2 adsorption significantly decreases. The observed decrease in porosity might be due to the high degree of residual H_3PO_4 within the pores of P-SBA-15 or a high level of functionalization. Indeed, when P-SBA-15 was utilized for DMNP hydrolysis under 0.45 M N-ethylmorpholine aqueous conditions, residual H_2PO_4 is observed in the ^{31}P NMR spectrum at 2.5 ppm. Interestingly, P-SBA-15 is not selective towards the desired dimethylphosphate (DMP) product and instead primarily and slowly ($t_{½}$ = >220 minutes) generates the undesired P-O-Me cleavage product methyl 4-nitrophenyl phosphate (M4NP). Dissolved Zr_{12}-(acetic acid) was introduced to P-SBA-15 through heating overnight to generate Zr_{12}-SBU-P-SBA-15 and residual clusters were removed through successive solvent exchange. The stretching modes associated with P=O and P-OH in P-SBA-15 shift or decrease after introduction of the Zr_{12}-(acetic acid). More importantly, new C=O stretching modes appear, corresponding to the acetic acid within the Zr_{12}-(acetic acid). However, the stretching modes associated with the Zr-O-H stretches of the cluster at 3390 cm^{-1} completely disappear after introduction into P-SBA-15, presumably through the binding of Zr to the Si centers or phosphoric acid within P-SBA-15. The PXRD of Zr_{12}-SBU-P-SBA-15 does not display crystallinity, possibly due to the relatively low amount of Zr retained in the SBA-15 as the SEM-EDX indicates the Si:P:Zr ratio is 1: 0.5: 0.09 respectively. Remarkably, Zr_{12}-(acetic acid)-P-SBA-15 facilitates the fast ($t_{½}$ = 69 minutes) and selective hydrolysis of DMNP to DMP under 0.45 M N-ethylmorpholine aqueous conditions (Table 2). The stark contrast in DMNP hydrolysis reactivity and selectivity is clearly attributable to the introduction of the Zr_{12}-(acetic acid) clusters into SBA-15.

To determine if the binding method affects catalyst loading and activity, SBA-15 was modified with varying HSO_3 to generate H-SO_3H-SBA-15 and L-SO_3H-SBA-15 (H = high, L = low) for comparison to the P-SBA-15 material. SEM-EDX analysis indicates that H-SO_3H-SBA-15 has a 3.9-fold greater sulfide content than L-SO_3H-SBA-15. The IR spectrum of H-SO_3H-SBA-15 contains a peak at 688 cm^{-1} corresponding to the S-OH stretch. Upon introduction of the Zr_{12}-(acetic acid), the S-OH stretch disappears and new stretches at 1586 cm^{-1} and 1480 cm^{-1} corresponding to the acetic acid within the Zr_{12}-(acetic acid). Like P-SBA-15, H-SO_3H-SBA-15 generates M4NP in the hydrolysis of DMNP in 0.45 M N-ethylmorpholine aqueous conditions. Similar to Z_{12}-(acetic acid)-P-SBA-15, modification of SBA-15 with HSO_3 reduces the porosity and Zr_{12}-(acetic acid)-H-SO_3H-SBA-15 does not exhibit crystallinity. Zr_{12}-(acetic acid)-H-SO_3H-SBA-15 facilitates the fast ($t_{½}$ = 15 minutes) and selective hydrolysis of DMNP to DMP under 0.45 M NEM aqueous conditions (Table 1). There is a 3-fold greater Zr content within Zr_{12}-(acetic acid)-L-SO_3H-SBA-15 than its analog Zr_{12}-(acetic acid)-H-SO_3H-SBA-15 (Si:Zr ratios 1:0.24 and 1: 0.083, respectively). Based on the elemental analysis of their precursors (3.9:1 H- versus L-respectively), H-SO_3H-SBA-15 was expected to have more bound Zr_{12}-(acetic acid) clusters within the pores of SBA-15. XPS data confirms covalent binding of the Zr_{12}-(acetic acid) clusters to the support rather than those bound through weaker interactions. The high resolution O1s XPS spectrum of Zr_{12}-acetic acid L-SO_3H-SBA-15 shows the presence of O species from both the cluster and support and there is change in the S peak intensity.

This dramatic increase in the zirconium content appears to significantly affect hydrolysis as Zr_{12}-(acetic acid)-L-SO_3H-SBA-15 quickly and selectively converts DMNP into DMP under buffered aqueous conditions ($t_{½}$ = 8 min). This increase in hydrolysis activity was found to be reproducible in a subsequent batch of Zr_{12}-(acetic acid)-L-SO_3H-SBA-15. Both Zr_{12}-(acetic acid)-L-SO_3H-SBA-15 and Zr_{12}-(acetic acid)-H-SO_3H-SBA-15 samples show significantly enhanced reactivity over Zr_{12}-SBU-P-SBA-15. Additionally, while the half-life of Zr_{12}-(acetic acid)-L-SO_3H-SBA-15 is similar to the unsupported Zr_{12}-(acetic acid) clusters, Zr_{12}-(acetic acid)-L-SO_3H-SBA-15 contains significantly less Zr on a mass basis and therefore fewer active sites. This suggests that the interaction of the clusters with sulfate groups enhances the catalytic activity. To better understand this trend, Gaussian fits to map the electrostatic potential of the derivatives were performed. It was found that the sulfate modified materials had higher electrostatic potentials than the phosphate modified materials.[26] These larger areas of electrostatic potential indicate a higher potential of non-covalent interaction between the guest molecule (DMNP) and zirconium catalyst which supports the experimental observation of enhanced reactivity of Zr_{12}-(acetic acid)-L-SO_3H-SBA-15 and Zr_{12}-(acetic acid)-H-SO_3H-SBA-15 over Zr_{12}-SBU-P-SBA-15 or unsupported Zr_{12}-(acetic acid).

Since the bound cluster was found to be more active than the unbound cluster, a suite of Zr_6 and Zr_{12} clusters were tethered to L-SO_3H-SBA-15 to determine the effect of the cluster motif and MCAM on reactivity. The reactivity for this set of materials was also assessed in 0.45M N-ethylmorpholine buffered solution with DMNP. The Zr_{12} clusters

showed selectivity and reaction profiles consistent with steric effects, with clusters containing smaller MCAMs exhibiting faster reactivity than clusters containing larger MCAMs (Table 1). As such, Zr_{12}-formic acid-L-SO_3H-SBA-15 exhibited the fastest kinetics while Zr_{12}-(propanoic acid)-L-SO_3H-SBA-15 exhibited the slowest. Zr_{12}-formic acid-L-SO_3H-SBA-15 also has the highest calculated Gibbs free energy of solvation (-36.33 kJ/mol) as compared to Zr_{12}-acetic acid-L-SO_3H-SBA-15 and Zr_{12}-propanoic acid-L-SO_3H-SBA-15 (-21.42 kJ/mol and -18.19 kJ/mol, respectively). It has been previously established that basic conditions are required for the formation of Zr-OH and -H_2O catalytic sites required for hydrolysis. The increased hydrophilicity of Zr_{12}-formic acid-L-SO_3H-SBA-15, as indicated by the Gibbs free energy of solvation, alludes to an increase of water molecules around the MCAM. This increase in water around the cluster can further facilitate the formation of active sites through deprotonation by N-ethylmorpholine buffer and substitution on the cluster.

The Zr_6 clusters showed a difference in reactivity trends and selectivity compared to the Zr_{12} clusters. The Zr_6 clusters bound to SBA-15 showed the formation of a mixture of products with slower reacting clusters forming more of the undesired M4NP product. In addition, Zr_6-formic acid-L-SO_3H-SBA-15 was the slowest performing material despite the free cluster (Zr_6-formic acid) being the fastest performing as compared to the free Zr_6 clusters. However, Zr_6-formic acid-L-SO_3H-SBA-15 also showed the highest Zr:S ratio, indicating the presence of partially bound clusters. These partially bound clusters could impede the simulant from accessing active sites and thus hinder hydrolysis.

Table 1. DMNP hydrolysis of bound Zr clusters in 0.45 M N-ethyl morpholine buffer conditions.

Material	Half-life (minute), DMNP, 0.45 M NEM buffer	DMNP:DMP:M4NP (%, at 18 hours)	Zr:S ratio (SEM-EDX)
P-SBA-15	>220	0.177337963	N/A
Zr_{12}-acetic acid-P-SBA-15	69	0.066030093	N/A
H-SO_3H-SBA-15	>1080	43:14:43	N/A
Zr-SBA-15	>550	34:36:29	0.09:1 (Zr:Si)
SBA-15 + Zr_{12}-acetic acid	69	0.7140625	N/A
Zr_6-acetic acid-L-SO_3H-SBA-15	89	0.268159722	5.6:1
Zr_6-propanoic acid-L-SO_3H-SBA-15	197	0.591157407	5.68:1
Zr_6-benzoic acid-L-SO_3H-SBA-15	407	0.6696875	5.25:1
Zr_6-formic acid-L-SO_3H-SBA-15	717	25:54:21	8.03:1
Zr_{12}-formic acid-L-SO_3H-SBA-15	85	0.35625	4.3:1
Zr_{12}-acetic acid-L-SO_3H-SBA-15	221	31:69:0	2.8:1
Zr_{12}-propanoic acid-L-SO_3H-SBA-15	283	0.80625	1.9:1

While the Zr cluster modified SBA-15 materials show fast, selective activity for DMNP hydrolysis, this activity is limited to buffered conditions. To extend the reactivity of these materials to non-buffered aqueous media, amine moieties were incorporated into the material in two ways that were analogous to previous work, on either the MCAM of the zirconium cluster or directly onto the silica strut.[23, 27–28] To introduce an amine moiety into the material through the MCAM, Zr_6-(BA-CH_2NH_2) and Zr_6-(BA-CH_2-morpholine) were synthesized and incorporated into SBA-15 and the hydrolysis reactivity of the resulting materials was measured under buffered and non-buffered conditions. Although Zr_6-(BA-CH_2-morpholine) showed enhanced reactivity under buffered conditions, neither material showed appreciable reactivity under non-buffered conditions (Table 2).

Two approaches were taken to incorporate a buffering amine moiety onto the silica support. The first approach was to incorporate a buffering polyethyleneimine (PEI) moiety onto SBA-15 to synthesize L-SO_3H-SBA-15-PEI prior to reacting the silica structure with Zr_{12}-(acetic acid) clusters. The resulting material, Zr_{12}-acetic acid-L-SO_3H-SBA-15-PEI, showed improved reactivity in aqueous conditions with double the amount of DMNP degraded in the same amount of time as for Zr_{12}-acetic acid-L-SO_3H-SBA-15. However, while PEI contains amine groups, it also exhibits a much lower pK_a than the N-ethylmorpholine buffer typically used for these reactions.[29, 30] In addition, protonation of the amine groups present on the PEI chains directly affects the basicity of the adjacent amines,

thereby potentially diminishing its buffering activity during the reaction. By incorporating adjacent acid/base groups using a grafting method, adjacent proton sinks can be built onto the material to avoid the buffer activity being diminished during the reaction in addition to ensuring the incorporation of an amine with adequate basicity. While the baseline silica material, L-SO_3H-SBA-15-$(CH_2)_3NH_2$, showed enhanced reactivity under aqueous conditions, it also showed the formation of the undesired M4NP product (Table 2). However, when the material was modified to include Zr_{12}-(acetic acid) clusters, the resulting material, Zr_{12}-acetic acid-L-SO_3H-SBA-15-$(CH_2)_3NH_2$, showed much faster and selective reactivity for DMNP hydrolysis under non-buffered conditions (50 % conversion after 18 hours) with no M4NP formation observed during the reaction.

Table 2. DMNP hydrolysis under aqueous conditions of Zr12-(acetic acid) clusters bound to silica supports modified with buffer molecules.

Material	Half-life (min), DMNP, water	DMNP:DMP:M4NP 18 hours
H-SO_3H-SBA-15	N.R.	100:00:00
L-SO_3H-SBA-15-$(CH_2)_3NH_2$	~20% (18 h)	77:22:01
SBA-15-$(CH_2)_3NH_2$	>1080	73:25:02
Zr_{12}-acetic acid-L-SO_3H-SBA-15	~10% (18 h)	67:33:00
Zr_{12}-acetic acid-L-SO_3H-SBA-15-PEI	~20% (18 h)	80:20:00
Zr_{12}-acetic acid-L-SO_3H-SBA-15-$(CH_2)_3NH_2$	~50% (18 h)	50:50:00

4. CONCLUSIONS/FUTURE WORK

The nature of the MCAM and amount of zirconium in the clusters was a key factor for reactivity. Clusters containing higher zirconium content (Zr_{12}) had enhanced catalytic activity and clusters with MCAMs with higher pKa values had faster reaction rates corresponding to more labile linker molecules and the greater formation of active sites. When clusters were incorporated into SBA-15 modified with acid moieties, analogous reaction rates were observed despite having a fraction of the zirconium content in the particles (approximately 20 %) compared to the free Zr clusters. The individual clusters, and those bound to the SBA-15 support, were characterized by XPS to confirm cluster covalent binding to the surface. The presence of oxygen species from both the cluster and support in the O 1s peak in addition to the consistency of the S 2p peak intensity indicate the clusters are covalently bound to the SBA-15 support. The reactivity profile and data not only indicate that the mesoporous structure does not inhibit hydrolysis, but that hydrolysis is potentially enhanced by immobilization to an inert support. In addition, the tethering method was a key component for the hydrolysis of DMNP by the supported materials with the sulfate modified silica affording enhanced reactivity on the bound zirconium clusters over the phosphate modified silica. Computational data supports this trend by showing an enhanced electrostatic potential on the zirconium clusters bound to the sulfate modified silica compared to the phosphate modified silica indicating an effect on the environment of the clusters caused by the support. Using this modified silica structure template, the catalytic properties of the Zr clusters were further investigated by varying the composition of Zr clusters on the support. The effect of MCAM on cluster reactivity appears to be dependent on both the connectivity of the cluster and the binding mode of the cluster. When the clusters are bound to SBA-15, steric effects of the MCAM play a role in reactivity, with Zr_{12}-formic acid-L-SO_3H-SBA-15 being the fastest performing material. Interestingly, the Zr_6 clusters are an anomaly in the reactivity trend, with Zr_6-formic acid-L-SO_3H-SBA-15 being the slowest material. The amount of zirconium incorporated into the SBA-15 materials also plays a role in the reactivity. While Zr_6-formic acid-L-SO_3H-SBA-15 has the highest ratio of Zr:S, this ratio also indicates there are some partially bound clusters on the surface. This partial binding can affect the selectivity of the hydrolysis reaction and cause the formation of the undesired M4NP product. It has also been demonstrated that these materials are active under neutral aqueous conditions by incorporating adjacent acid (-SO_3) and basic (propyl amine) moieties onto the silica structure. These initial experiments with an adjacent acid-base modified material demonstrate the potential use of this silica platform to optimize zirconia clusters for CWA decontamination under neutral aqueous conditions.

ACKNOWLEDGMENTS

Funding was provided by the U.S. Army via the Chemical Biological Advanced Materials Manufacturing Science Program (PE 0601102A Project VR9) at the Combat Capabilities Development Command Chemical Biological Center. The authors would also like to acknowledge the technical assistance of Dr. Ngon Tran at DEVCOM Army Research Laboratory with the collection of XPS data included in this work.

REFERENCES

[1] Couzon, N.; Dhainaut, J.; Campagne, C.; Royer, S.; Loiseau, T.; Volkringer, C. Porous textile composites (PTCs) for the removal and the decomposition of chemical warfare agents (CWAs) – a review. *Coord. Chem. Rev.* **2022**, *467*, p 214598.

[2] Vellingiri, K.; Philip, L.; Kim, K.-H. Metal-organic frameworks as media for the catalytic degradation of chemcical warfare agents. *Coord. Chem. Rev.* **2107**, *352*, pp 159–179.

[3] DeCoste, J.B.; Peterson, G.W. Metal-organic frameworks for air purification of toxic chemicals. *Chem. Rev.* **2014**, *114* (11), pp 5695–5727.

[4] Liu, Y.; Howarth, A.J.; Vermeulen, N.A.; Moon, S.-Y.; Hupp, J.T.; Farha, O.K. Catalytic degradation of chemical warfare agents and their simulants by metal-organic frameworks. *Coord. Chem. Rev.* **2017**, *346*, pp 101–111.

[5] Mondloch, J.E.; Katz, M.J.; Isley III, W.C.; Ghosh, P.; Liao, P.; Bury, W.; Wagner, G.W.; Hall, M.G.; DeCoste, J.B.; Peterson, G.W.; Snurr, R.Q.; Cramer, C.J.; Hupp, J.T.; Farha, O.K. Destruction of chemical warfare agents using metal-organic frameworks. *Nature Mater.* **2015**, *14* (5), pp 512–516.

[6] Katz, M.J.; Moon, S.-Y.; Mondloch, J.E.; Beyzavi, M.H.; Stephenson, C.J.; Hupp, J.T.; Farha, O.K. Exploiting parameter space in MOFs: a 20-fold enhancement of phosphate-ester hydrolysis with UiO-66-NH_2. *Chem. Sci.* **2015**, *6* (4), pp 2286–2291.

[7] DeCoste, J.B.; Demasky, T.J.; Katz, M.J.; Farha, O.K.; Hupp, J.T.A UiO-66 analogue with uncoordinated carboxylic acids for the broad-spectrum removal of toxic chemicals. *New J. Chem.* **2015**, *39* (4), pp 2396–2399.

[8] Gallis, D.F.S.; Harvey, J.A.; Pearce, C.J.; Hall, M.G.; DeCoste, J.B.; Kinnan, M.K.; Greathouse, J.A. Efficient MOF-based degradation of organophosphorus compounds in non-aqueous environments. *J. Mater. Chem. A.* **2018**, *6* (7), pp 3038–3045.

[9] Moon, S.-Y.; Proussaloglou, E.; Peterson, G.W.; DeCoste, J.B.; Hall, M.G.; Howarth, A.J.; Hupp, J.T.; Farha, O.K. Detoxification of chemical warfare agents using a Zr_6-based metal–organic framework/polymer mixture. *Chemistry – A European Journal.* **2016**, *22* (42), pp 14864–14868.

[10] Moon, S.-Y.; Liu, Y.; Hupp, J.T.; Farha, O.K. Instantaneous hydrolysis of nerve-agent simulants with a six-connected zirconium-based metal–organic framework. *Angew. Chem., Int. Ed.* **2015**, *54* (23), pp 6795–6799.

[11] Islamoglu, T.; Ortuño, M.A.; Proussaloglou, E.; Howarth, A.J.; Vermeulen, N.A.; Atilgan, A.; Asiri, A.M.; Cramer, C.J.; Farha, O.K. Presence versus proximity: the role of pendant amines in the catalytic hydrolysis of a nerve agent simulant. *Angew. Chem.* **2018**, *130* (7), pp 1967–1971.

[12] Liu, Y.; Moon, S.-Y.; Hupp, J. T.; Farha, O.K. Dual-Function Metal–Organic Framework as a Versatile Catalyst for Detoxifying Chemical Warfare Agent Simulants. *ACS Nano.* **2015**, *9* (12), pp 12358–12364.

[13] de Koning, M.; van Grol, M.; Breijaert, T. Degradation of paraoxon and the chemical warfare agents VX, tabun, and soman by the metal-organic frameworks UiO-66-NH_2, MOF-808, NU-1000, PCN-777. *Inorg. Chem.* **2017**, *56* (19), pp 11804–11809.

[14] Conic, D.; Pierloot, K.; Parac-Vogt, T.; Harvey, J. Mechanism of the Highly Effective Peptide Bond Hydrolysis by MOF-808 Catalyst Under Biologically Relevant Conditions. *Phys. Chem. Chem. Phys.* **2020**, *22* (43), pp 25136–25145.

[15] Feng, Y.; Chen, Q.; Jiang, M.; Yao, J. Tailoring the properties of UiO-66 through defect engineering: a review. *Ind. Eng. Chem. Res.* **2019**, *58* (38), pp 17646–17659.

[16] Gibbons, B.; Bartlett, E.C.; Cai, M.; Yang, X.; Johnson, E.M.; Morris, A.J. Defect level and particle size effects on the hydrolysis of a chemical warfare agent simulant by UiO-66. *Inorg. Chem.* **2021**, *60* (21), pp 16378–16387.

[17] Zhao, Y.; Zhang, Q.; Li, Y.; Zhang, R.; Lu, G. Large-scale synthesis of monodisperse UiO-66 crystals with tunable sizes and missing linker defects via acid/base co-modulation. *ACS Appl. Mater. Interfaces* **2017**, *9* (17), pp 15079–15085.

[18] Han, Y.; Liu, M.; Li, K.; Zuo, Y.; Wei, Y.; Xu, S.; Zhang, G.; Song, C.; Zhang, Z.; Guo, X. Facile synthesis of morphology and size-controlled zirconium metal-organic framework UiO-66: the role of hydrofluoric acid in crystallization. *CrystEngComm.* **2015**, *17* (33), pp 6434–6440.
[19] Pappas, I.; Fitzgerald, M.; Huang, X.; Li, J.; Pan, L. Thermally Resolved in Situ Dynamic Light Scattering Studies of Zirconium(IV) complex formation. *Cryst. Growth Des.* **2009**, *9* (12), pp 5213–5219.
[20] Bezrukov, A.A.; Tornroos, K.W.; Le Roux, E.; Dietzel, P.D.C. Incorporation of an intact dimeric Zr_{12} oxo cluster from a molecular precursor in a new zirconium metal-organic framework. *Chem. Commun.* **2018**, *54* (22), pp 2735–2738.
[21] Crisci, A.J.; Tucker, M.H.; Lee, M.-Y.; Jang, S.G.; Dumesic, J.A.; Scott, S.L. Acid-Functionalized SBA-15-Type Silica Catalysts for Carbohydrate Dehydration. *ACS Catal.* **2011**, *1* (7), pp 719–728.
[22] Wu, B.; Tong, Z.; Yuan, X. Synthesis, characterization and catalytic application of mesoporous molecular sieves SBA-15 functionalized with phosphoric acid. *J. Porous Mater.* **2012**, *19*, pp 641–647.
[23] Shao, Y.; Liu, H.; Yu, X.; Guan, J.; Kan., Q. Synthesis, characterization and catalytic activity of acid-base bifunctional materials through protection of amino groups. *Mater. Res. Bull.* **2012**, *47*, pp 768–773.
[24] Troya, D. Reaction Mechanism of Nerve-Agent Decomposition with Zr-Based Metal Organic Frameworks. *J. Phys. Chem. C.* **2016**, *120* (51), pp 29312–29323.
[25] Murray, J.S.; Politzer, P. The electrostatic potential: an overview. *WIREs Comput. Mol. Sci.* **2011**, *1* (2), pp 153–163.
[26] Ploskonka, A.M.; DeCoste, J.B. Insight into organophosphate chemical warfare agent simulant hydrolysis in metal-organic frameworks. *J. Haz. Mat.* **2019**, *375*, pp 191–197.
[27] Garibay, S.J.; Farha, O.K.; DeCoste, J.B. Single-component frameworks for heterogeneous catalytic hydrolysis of organophosphorous compounds in pure water. *Chem. Commun.* **2019**, *55* (49), pp 7005–7008.
[28] Gargiulo, N.; Peluso, A.; Aprea, P.; Pepe, F.; Caputo, D. CO_2 Adsorption on Polyethyleneimine-Functionalized SBA-15 Mesoporous Silica: Isotherms and Modeling. *J. Chem. Eng. Data* **2014**, *59* (3), pp 896–902.
[29] Curtis, K.A.; Miller, D.; Millard, P.; Basu, S.; Horkay, F.; Chandran, P.L. Unusual salt and pH induced changes in polyethylenimine solutions. *PLoS ONE.* **2016**, *11* (9), e0158147.
[30] Ziebarth, J.D.; Wang, Y. Understanding the protonation behavior of linear polyethyleneimine in solutions through Monte Carlo simulations. *Biomacromolecules.* **2010**, *11* (1), pp 29–38.

Functionalization of polymer fibers and particles via incorporation of cell-free protein synthesis

Jennifer A. Lee[a,b]*, Susan K. Kozawa[a,c], Ann M. Kulisiewicz[a], Terry Henderson[a], Steven Blum[a], Kristian M. Van de Voorde[a], Marilyn S. Lee[a]
[a]U.S. Army Combat Capabilities Development Command Chemical Biological Center, Research & Operations Directorate, 8198 Blackhawk Rd, Aberdeen Proving Ground, MD 21010
[b]Defense Threat Reduction Agency, 2800 Bush River Rd, Gunpowder, MD 21010
[c]Oak Ridge Institute for Science and Education, 1299 Bethel Valley Rd, Oak Ridge, TN 37830

ABSTRACT

Smart materials integrate sensing and computation functions to signal the presence of a hazard, decontaminate, or change physical properties in response to stimuli. Equipment with smart materials could expand functionality while reducing size, weight, and power requirements. Cell-free protein synthesis technology presents a novel way to deliver synthetic biology functions with DNA-programmable control to polymer materials as cell-free protein synthesis reagents are stable to polymer casting conditions. In addition, polymers can impact the function of cell-free protein synthesis reactions by providing a protective matrix and controlling exposure to water that affects activation and shelf stability. Polymer fibers created by spinning techniques create high performance materials while particles can protect delicate cargo for delivery capabilities or incorporation into other materials. In this work, we incorporate cell-free protein synthesis reactions into polymer fiber and particle fabrication to understand how morphology of the polymer bio-composite affects cell-free protein synthesis shelf-life and function. Cell-free protein synthesis-polymer fibers prepared by solution blow spinning are characterized for physical characteristics and shelf life. Several methods for preparing active cell-free protein synthesis particles are described. These results illuminate paths forward to improve cell-free protein synthesis-polymer composite performance.

Keywords: Cell-free protein synthesis, polymers, fibers, particles

1. INTRODUCTION

High performance polymers are a critical class of materials integrated into essential gear for the warfighter. These materials are often formed from spun fibers to achieve both strong and resilient physical properties, high surface area to trap contaminants, and controlled porosity for breathability or fluid flow. Innovation in the field of smart materials has achieved much to craft polymers with dynamic properties like mechanical response to light, pH, redox or small molecules, self-cleavage or self-repair, or catalytic composites that degrade contaminants.[1–3] Despite their versatility, the field has yet to design "smart materials" that possess both useful mechanical characteristics and dynamic functions that could enable equipment to alert and protect the warfighter against threats.

Recently, researchers have begun to embed DNA-programmable microorganisms within materials.[4,5] Microbes can produce biomolecules to perform warfighter relevant functions; however, the instability of live organisms can prevent the incorporation of microbes into polymers, which can require organic solvents, heat, or radical polymerization. Previous work demonstrated cell-free systems which offer a solution to this problem.[6] Cell-free protein synthesis (CFPS) reactions utilize crude microbial lysates to enact DNA-programmed functions outside of a living cell.[7] Compared to live cells and purified proteins, CFPS systems are surprisingly stable where CFPS activity is maintained after freeze-drying and exposure to certain polymer casting conditions.[8,9] When CFPS/polymer composites are exposed to water, freeze dried CFPS reagents are re-activated *in situ* to produce sensor gene circuits and functional antimicrobial proteins. Thus far, CFPS/polymer composites have only been demonstrated in a film format using poly lactic-co-glycolic acid (PLGA) and polycaprolactone (PCL) polymers.[9] From this work, solvent screens uncovered solvent compatibility limitations that reduce the range of compatible polymers. Further, the geometry of the cast, distribution of CFPS components, and chemical identity and crystallinity of the polymer can all influence gene

expression and water infiltration within the CFPS-polymer unit.[6] It is important to investigate these effects to approach a design with optimal mechanical and bio-activation characteristics.

This work develops methods to cast CFPS-polymers into fiber and particle morphologies, with the aim of studying the effects of cast geometry on CFPS activity. We hypothesize fiber and particle geometries can be tuned to control reactivation dynamics. Here, we used solution blow spinning (SBS), a straightforward, scalable method in which high speed air jets pull polymer solutions into nonwoven, fiber mats.[10] Because SBS only requires a polymer solution with a volatile solvent, fewer variables will interfere with the function of the system compared to other spinning techniques. These fibers are characterized for shelf life and physical properties. Also, nuclear magnetic resonance (NMR) is used to examine how different solvents may extract some CFPS components during processing. Polymer particles may act as a protective carrier to allow processing with solvents, UV, or other conditions that are incompatible with CFPS activity if applied directly. After stability issues with diblock copolymer vesicles in previous work, this study focuses on functionalizing hydrogel particles using commercial resins, gelatin emulsions, or microfluidics. Continued examination of atomized polymer particles is also described.

2. RESULTS AND DISCUSSION

2.1 Effect of solvent on CFPS composition in CFPS/polymer fibers

Previous studies showed lyophilized CFPS reactions maintain activity following exposure to solvents.[8] This work did not explore exactly which components of a CFPS reaction may be extracted into a solvent to impact recovered activity. We have used chloroform and acetone in our SBS fibers and, thus, explored these solvents further. Here, NMR spectroscopy[11] was used to determine the effect of the solvent choice on the composition of CFPS reactions incorporated into polymers. Because a CFPS reaction is comprised of an extensive list of buffer components and proteins, analysis was limited to sub-mixtures: murine RNAse inhibitor (New England Biolabs, Ipswich, MA), *E. coli* lysate (generated in-house), and a reaction buffer consisting of phosphoenolpyruvate, amino acids, NAD+, oxalic acid, spermidine, and putrescine (PANOx-SP) were compared to the total CFPS reaction.[12] From these spectra, unique features for each sub-mixture can be identified.

To evaluate the effect of solvent exposure during fabrication on final cell free composition, each of the samples were lyophilized and resuspended in acetone or chloroform. Samples were spun down to separate any insoluble (pellet) and soluble (supernatant) components. Samples were dried overnight and suspended in deuterated water for NMR analysis (Figure 1). There was no significant extraction of CFPS components into the supernatant for the total CFPS reaction, *E. coli* lysate, or PANOx-SP reaction buffer for either solvent. Peaks were observed in the supernatant of RNAse inhibitor samples exposed to acetone which correspond to glycerol and makes up 50 % of the buffer in which the RNAse inhibitor is stored. Glycerol has a limited solubility in acetone (1 g/15 mL) but is insoluble in chloroform. The lack of CFPS components extracted into the supernatant coincides with the observation that CFPS activity is not significantly affected by acetone or chloroform exposure. Future experiments using solvents that render lyophilized CFPS reactions inactive (i.e., dimethylformamide or methanol) may have a detectable effect on CFPS composition.

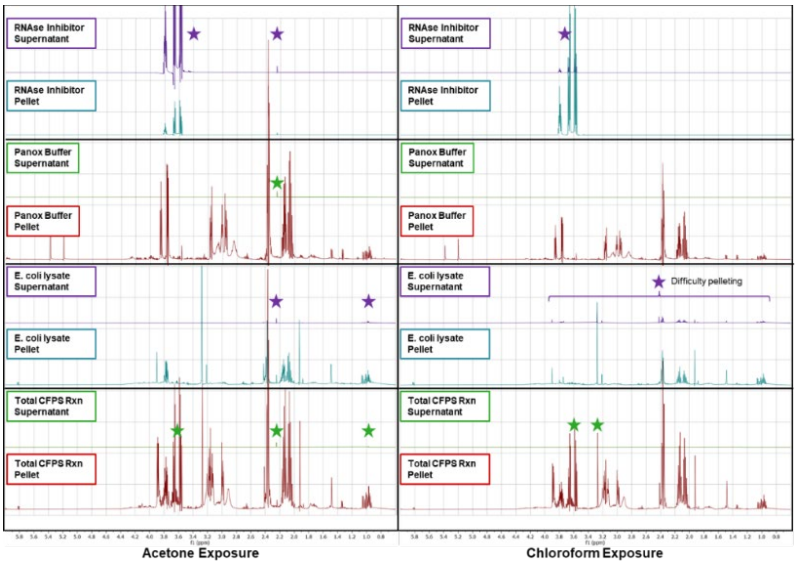

Figure 1. NMR analysis of CFPS content following acetone and chloroform exposure. Stars indicate peaks of substances potentially solubilized into supernatant samples.

2.2 Shelf life of CFPS/polymer fibers

Previous work established the feasibility of using SBS to create CFPS functionalized fibers. In this work, CFPS/polymer fibers were rehydrated with water on the same day of spinning to confirm activity. A question remained whether the cell-free powder encapsulated in polymer fibers could maintain this activity after extended storage. To begin addressing the shelf-stability of CFPS/polymer fibers, fiber samples were evaluated for generation of superfolder green fluorescent protein (sfGFP) fluorescence on the day of spinning (Day 0) and at one week after (Day 7). Increasing in hydrophobicity, polyethylene oxide (PEO), polycaprolactone (PCL), and poly(vinylidene fluoride)-co-hexafluoropropylene (PVDF-co-HFP) fibers were spun. A sample of the CFPS/fiber mat was cut and placed in a plastic dish. Water (10–300 µL) was deposited on top of fiber samples and imaged using a UV light source and single-lens reflex camera equipped with a filter to detect sfGFP fluorescence. Average and maximum fluorescence of fiber samples was measured using FIJI.[13]

PEO fibers did not exhibit fluorescence after rehydration at any time point (data not shown). The PEO formulation used in these experiments requires UV exposure to cross-link the polymer. We speculate that this exposure, in addition to heat emitted by the UV lamp, could have inactivated the lyophilized cell free powder within the PEO fibers. Thus, further optimization is needed to determine a protocol to develop UV cured fibers.

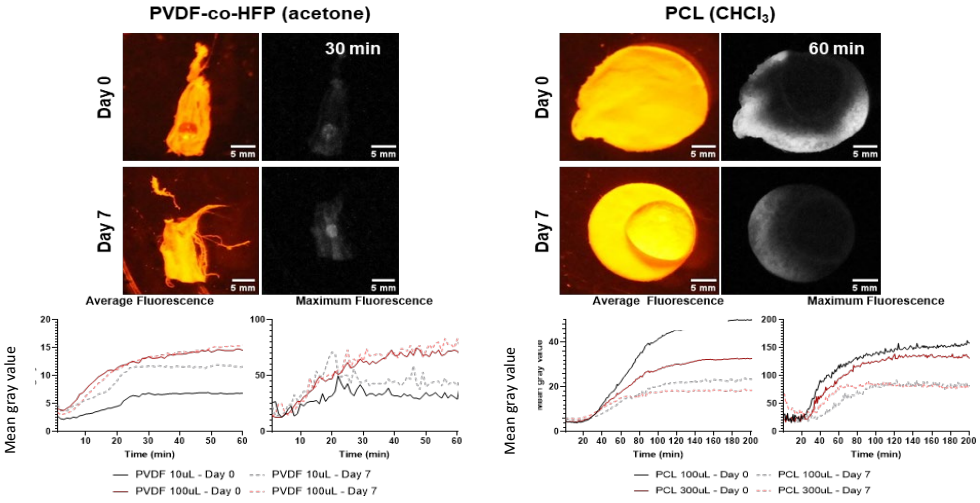

Figure 2. Shelf-life of CFPS/polymer fibers.

Representative shelf-life analysis of PCL and PVDF-co-HFP fiber samples on Day 0 and Day 7 are shown in Figure 2. On Day 0, fluorescence could be observed in both PCL and PVDF-co-HFP fibers with PCL fibers demonstrating ~3x brighter signal overall. While water added to PVDF-co-HFP fibers remained as a droplet on top, water permeated through the more hydrophilic PCL fibers creating a traveling front of cell-free activity that moved to the perimeter of the sample. This behavior could contribute to a higher signal intensity by concentrating the cell-free or expressed sfGFP. Furthermore, the PCL fiber samples were thicker and could have contained more cell-free material to start.

After storage in a desiccator at room temperature for one week, cell-free activity was observed for both fiber samples. There was no loss in signal in PVDF-co-HFP fibers whereas PCL fibers demonstrated a ~50 % decrease in fluorescence compared to Day 0. CFPS reactions contained within PVDF-co-HFP fibers progressed more rapidly, showing an increase in signal at around 10 minutes whereas PCL fibers demonstrated detectable increases in fluorescence at closer to 20 minutes. The slower cell-free activity in PCL fibers could be due to the fluid diffusion throughout the sample as rehydration ratios can significantly affect CFPS reaction speeds.

It is well known that heat and humidity can dramatically affect the performance of lyophilized cell-free samples. Here, fiber samples were stored in a shared cabinet desiccator at room temperature. Shelf-life could be improved by storing fibers in sealed mylar bags containing desiccant and oxygen absorbing pouches. Furthermore, fibers were spun in less-than ideal conditions with humidity levels in the 40–60 % range and temperatures above 75 °F. Engineering controls (portable air conditioning and dehumidifying units) could be used to improve spinning conditions and by extension shelf-life of the resultant CFPS/polymer fibers.

2.3 Physical characteristics of CFPS/polymer fibers

Fourier transform infrared spectroscopy (FTIR) is an analytical technique used to characterize the chemical composition of fibers and other materials, potentially a non-destructive method to evaluate CFPS loading in polymer fibers. The FTIR spectra was collected for lyophilized CFPS and polymer fibers (PEO, PVDF-co-HFP, PCL) with and without encapsulated CFPS (Figure 3A). The spectrum for CFPS powder is depicted in black. Polymer fibers are depicted in solid lines and fibers with CFPS in dotted lines. There were no obvious differences in CFPS/polymer fibers compared to polymer fibers alone, with the exception of the O-H stretch (3550–3200 cm^{-1}) and N-H region (1640 cm^{-1}). These slight differences can be attributed to the presence of amino acids in the CFPS reaction. The lack of CFPS signatures in polymer fibers could be due to the relatively small amount of CFPS in the fibers (1 mL lyophilized powder: 5 mL polymer solution). Spinning fibers with a higher CFPS content and re-evaluating with FTIR could explore this hypothesis and determine a limit of detection for FTIR when evaluating CFPS/polymer fibers.

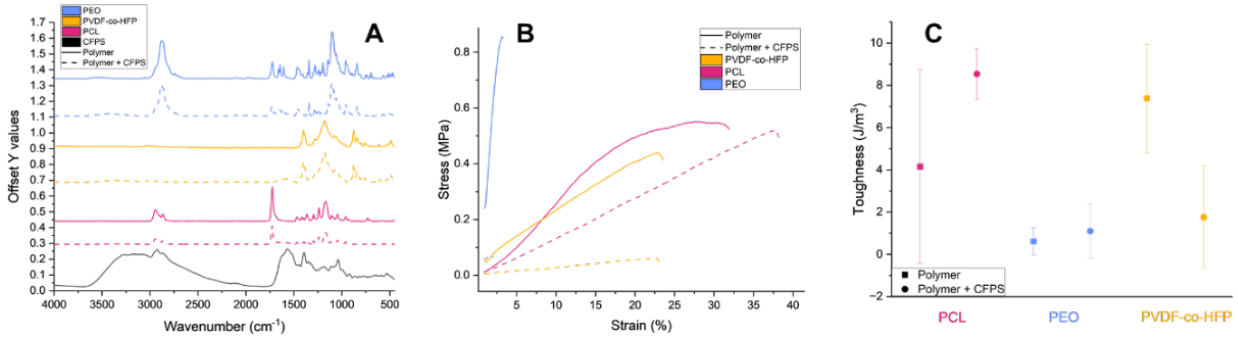

Figure 3. Physical characteristics of fibers. (A) FTIR of lyophilized CFPS reactions and polymer fibers with and without CFPS. (B) Stress/strain curve and (C) toughness of polymer fibers with and without CFPS.

Dynamic mechanical analysis was used to measure the stress/strain response of polymer fibers with and without CFPS (Figure 3B-C). The addition of CFPS to polymer fibers resulted in a decrease in the slope of their stress/strain curves (Young's modulus), indicating these fibers were more easily deformable compared to their pure polymer counterparts. This behavior is expected due to the larger CFPS masses disrupting the polymer chain alignment and fiber structure overall during fiber fabrication. The stress/strain response of pure PCL fibers possessed a curvature as strain increased, indicating strain hardening in these fibers that was not present in PCL/CFPS fibers. While this is also likely due to the interference of the CFPS preventing the formation of crystalline domains when in tension, both the PCL and PCL/CFPS fibers pulled to a similar strain before failure, highlighting the robustness of PCL as a material. PEO fibers were extremely brittle as a crosslinked system with PEO/CFPS fibers failing rapidly compared to PEO alone. In the future, the elasticity of PEO can be tuned by the use of different crosslinkers. PVDF-co-HFP fibers with and without

CFPS both pulled to a similar strain before failure but PVDF/CFPS fibers had a significantly reduced ability to undergo stress compared to polymer alone. While not significant, the presence of CFPS counterintuitively seemed to increase the toughness of PCL and PEO fibers. This is likely due to favorable chain entanglement with the polymers and the CFPS. Alternatively, PVDF/CFPS fibers demonstrated a significant decrease in toughness compared to polymer alone, a result of the voids caused by CFPS and hydrophobic nature of PVDF-co-HFP.

2.4 Resin-based CFPS/polymer particles

A strategy for creating CFPS/polymer particles is to load the liquid CFPS reaction into a pre-existing porous particle such as a hydrogel or resin bead to be frozen and lyophilized before incorporation into polymer solutions for particle fabrication. Commercially available chromatography resin beads, Sephacryl® (S500HR) and Sepharose™ (CL-2B) were selected based on their large pore sizes to test for CFPS/polymer particle fabrication. As these beads are commonly shipped as a slurry, it is necessary to validate the beads can maintain their structure after lyophilization (Figure 4A). Following lyophilization, Sephacryl® beads maintained their shape and ability to absorb liquid cell free while Sepharose™ beads collapsed (not shown); thus, were not used further. Once lyophilized, liquid CFPS reactions were loaded into Sephacryl® beads and the whole bead/CFPS structures frozen and re-lyophilized. The beads were loaded with liquid CFPS reactions. Post-lyophilization, Sephacryl® beads loaded with CFPS reactions maintained their structure and size, with evidence of excess CFPS reaction that was not encapsulated surrounding the beads. Beads were rehydrated with or without sfGFP plasmids and sfGFP fluorescence read on a plate reader to confirm CFPS activity within the beads. Fluorescence was detected in the expected experimental groups (Figure 4B).

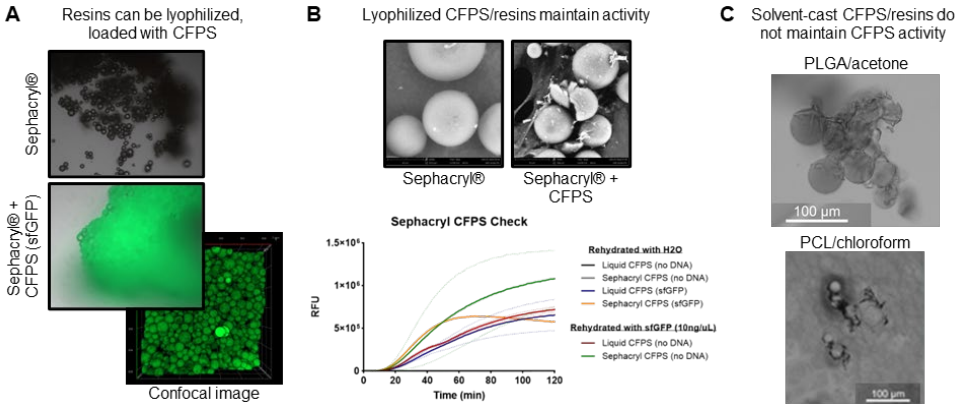

Figure 4. Resin-based particle lyophilization and activity. (A) Lyophilization and loading of Sephacryl® resin beads. Activity of lyophilized (B) and solvent-cast (C) CFPS/resins.

To test the activity of Sephacryl®/CFPS beads in a polymer solution, Sephacryl®/CFPS beads expressing sfGFP were solvent-cast in PLGA (15 wt% in acetone) and PCL (5 wt% in chloroform) films and dried (Figure 4C). Following rehydration with water, both films displayed no detectable fluorescence. Beads in PCL films were shrunken in size, likely due to chloroform exposure during casting. The degradation of the beads could have contributed to the lack of CFPS activity; however, this would not explain the lack of activity in PLGA films. The most likely explanation lies with the physical characteristics of the Sephacryl® beads themselves, as the pore size of the beads may not be large enough to easily accommodate for large biomolecules like ribosomes (~2–4 MDa). The fractionation range for this resin is 4–20,000 kDa MW; however, this metric refers to the separation ability of a packed bed of beads. The bead exclusion limit and pore size would determine if molecules are too large to easily enter the bead itself.

2.5 Nebulization of CFPS/polymer particles

An alternative strategy to creating CFPS/polymer particles follows the same strategy as CFPS/polymer fiber fabrication by lyophilizing a liquid CFPS reaction, grinding it into a fine powder, and resuspending in polymer solution for fabrication into particles. Nebulization is often used to aerosolize medicines that contain biological components such as proteins, antibodies, and liposomes into fine mists or particles. Given this more delicate cargo, there is potential for the use of nebulization to create CFPS/polymer particles. A Patin, at-home nebulizer (Figure 5A) was purchased to test jet nebulization of CFPS/polymer solutions (40–80 KPa) to produce particles (<10 µm). CFPS/PVDF in acetone was nebulized to produce a fine mist, resulting in the capture of CFPS/polymer particles imaged using SEM, proving this technique to be a viable option. However, because the solution reservoir cup must be held upright during operation,

a 50 mL conical tube was inverted over the opening to capture any particles, resulting in a very inefficient collection strategy. There was a notable loss of material as not all the mist deposited properly in the tube. Another limiting factor to this instrument is the solvent tolerance of the reservoir cup where in the presence of acetone the cup degraded, only allowing for one to two runs before it was no longer functional.

Given the potential of nebulization for the creation of CFPS/polymer particles, aerosol subject matter expert Dr. Angela Zeigler (U.S. Army Combat Capabilities Development Command Chemical Biological Center, Sensors, Signatures, and Aerosol Technologies Branch) was consulted for alternative nebulization strategies. A Collison nebulizer (Figure 5B) is an alternative pneumatic strategy to create aerosols for research purposes. A solution of PCL in acetone (5 wt%) was used to attempt nebulization, yet when the instrument was initiated, the temperature of the solution dropped significantly, and the polymer crashed out of solution. It is unclear if the addition of CFPS would further clog the instrument; however, if this strategy is to be successful, a heating element would be needed to inhibit the temperature drop of the solution.

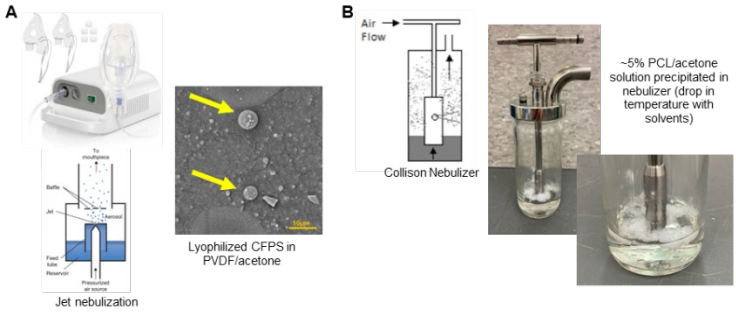

Figure 5. Nebulization of CFPS/polymer particles. (A) Jet nebulization of CFPS/PVDF particles using a commercial, at home nebulizer. (B) Collison nebulization of a PCL/acetone solution resulted in the polymer crashing out of solution.

2.6 Gelatin-based encapsulation

As an alternative to using a commercial hydrogel resin and absorbing CFPS components post-synthesis of the particle, aqueous CFPS may be included with a hydrogel material during particle formation. This restricts the particle preparation methods to conditions compatible with hydrated CFPS. Aqueous solutions must be handled on ice or kept cold to prevent CFPS reactions from proceeding prematurely and consuming the provided resources. Likewise, the CFPS material should not be handled after thawing for more than a few hours, as the components are only completely stable when frozen or dry. Hydrated CFPS is also not tolerant to organic solvents as well as other inhibiting solutes such as high salt or ion concentrations. One hydrogel that may fit these restrictions is gelatin from cold water fish skin, which is molten at room temperature, solidifies at 4 °C, and can be prepared by a variety of means. Emulsion and microfluidic methods were tested in this work.

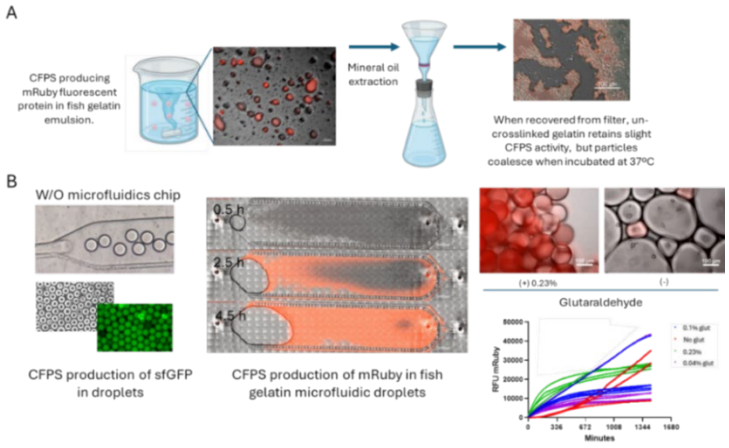

Figure 6. Fish gelatin CFPS particles. (A) Formation of fish gelatin particles with CFPS via emulsion method, (B) Microfluidics CFPS particle generation: microscopy of water-in-oil (W/O) microfluidic chip and GFP-production in CFPS droplets (left), CFPS production of mRuby in fish gelatin droplets (middle), effects of glutaraldehyde crosslinker addition on morphology and mRuby productivity (right).

First, a CFPS gelatin emulsion was formed (Figure 6A) by mixing gelatin into a CFPS solution at room temperature then emulsifying in mineral oil with span80 surfactant. Fish gelatin is chilled at 4 ºC to solidify. CFPS activity was observed in aqueous gelatin droplets suspended in oil. To preserve CFPS particles for storage without a cold chain as well as with stability to downstream particle processing, the particles need to be extracted from the mineral oil and dried. This is accomplished by an organic solvent extraction, filtering out the particles, and air drying. A syloid flow aid was used to prevent particle agglomeration. A dry and flowable CFPS-fish gelatin powder was formed via this method and some CFPS activity was recovered after rehydration of the powder in water. However, microscopy imaging indicated the fish gelatin particles merged into a larger gel phase during incubation, likely since the fish gelatin melts at temperatures above 20 °C. Future work on the emulsion method remains to explore the use of glutaraldehyde crosslinking to stabilize particles or directly solvent-casting the dry particles into polymer.

Another method to form fish gelatin particles is the use of microfluidics (Figure 6B). The 2024 U.S. Army Combat Capabilities Development Command Chemical Biological Center QUEST program establishing microfluidics capability, led by Dr. Jennifer Lee, was leveraged to perform this technique with cell-free cargoes. Dr. Jose Wippold at U.S. Army Combat Capabilities Development Command Army Research Laboratory provided a chip to generate water-in-oil (W/O) droplets approximately 50–100 μm in diameter. We first prepared aqueous CFPS droplets expressing fluorescent protein. Plain CFPS droplets were found to have good activity. Fish gelatin was added to the solution which yielded a good fluorescence signal production, though droplets still could coalesce over time or during drying since the fish gelatin is not solid at warmer temperatures. Low concentrations (0–0.23 %) of glutaraldehyde were added to test whether crosslinking could improve particle stability while avoiding any loss of CFPS activity. Results indicate that 0.23 % glutaraldehyde was most effective at stabilizing the particles, and final fluorescence levels were not significantly affected. Interestingly, the rate of fluorescent protein production was faster with glutaraldehyde under these conditions. Glutaraldehyde will be applied to both emulsion and microfluidic generated fish gelatin particles going forward as methods are tested to embed these particles into solvent-cast polymers.

3. METHODOLOGY

3.1 Reagent and DNA sources

Unless otherwise noted, reagents were purchased from Millipore Sigma, St. Louis, MO. A pY71-sfGFP plasmid (Genbank MT346027) template was utilized for T7-polymerase driven expression of sfGFP via CFPS.[14] The mRuby sequence was inserted in place of sfGFP on the same plasmid backbone (pY71-mRuby) for production of red fluorescence. Plasmid DNA was purified from transformed *E. coli* using a Promega PureYield plasmid midiprep kit, followed by ethanol precipitation, or by a Qiagen gigaprep kit without additional purification.

3.2 Preparation of CFPS reaction mixtures and lyophilization

E. coli lysates were prepared from a Δ*lacZα* derivative of Rosetta 2 (DE3) *E. coli* (Novagen) grown in a 100 L culture scaled up from a flask culture method described previously.[15] CFPS reactions contained 40 % v/v lysate and additional reagents following the PANOx-sp recipe as described in detail previously.[8] mRuby or sfGFP plasmid DNA is added at a concentration of 10 ng/μL while an equivalent volume of water is added for no DNA controls. Reaction solutions are flash frozen in liquid nitrogen, then dried using a shelf-type lyophilizer (SP Scientific, VirTis Wizard 2.0) with a primary overnight drying step at -20 °C. A secondary drying step of at least two hours at 15 °C was then conducted. After removal from the lyophilizer, CFPS powders were stored for minimal time in a desiccator at room temperature, if necessary, prior to treatment or rehydration.

3.3 Solution blow spinning

SBS was completed using a system acquired from the Nonwovens Institute (NC State University, Raleigh, NC). Lyophilized CFPS powders were added to solvent at ratios indicated for each experiment and ground into a fine suspension using a Tenbroeck tissue homogenizer. The CFPS/solvent suspension was then used to dilute a solution of polymer/solvent to the desired final polymer concentration. Polymers used in this report include poly(vinylidene fluoride-co-hexafluoropropylene) (Mw 455,000, 427179-100G, Aldrich), polycaprolactone (Mn ~80,000 440744-500G, Aldrich), and polyethylene oxide (Mv 100,000, 181986-250G, Aldrich). The CFPS/polymer solution was transferred to a 5 mL syringe (14-823-16D, BD 301027, Fisher Scientific) and placed on a syringe pump (New era pump systems, Farmingdale, NY) at a flow rate of 0.3 ml/minute. Compressed air (40–45 psi) was used to pull

CFPS/polymer solutions through a blunt end, 2 inch 18-gauge needle (CU Innovations, Champaign, IL) suspended 250 mm above a perpendicular platform to form fibers.

3.4 Fluorescence and colorimetric imaging and measurement

A Zeiss Axio Observer Z1 inverted microscope with incubation cabinet, automated stage, and auto focusing was used to image fluorescent protein production in particles, films, and fibers. Images were captured with a Plan-Apochromat 10x/0.45 M27 objective or a Plan-Apochromat 63x/1.40 oil DIC M27 objective and an Axiocam 506 camera while samples were incubated at 37 °C. The light source was Colibri 7 with a 475 nm LED used for green fluorescence (sfGFP and background lysate signal) and a 567 nm LED for mRuby. Tiled time course images of each sample were taken using DIC, sfGFP (ex: 480 nm, em: 505 nm, 9 % intensity), and mRuby (ex: 577, em: 603, 100 % intensity) channels. Fluorescent CFPS activity over time was analyzed using FIJI software.[13] A plate reader was used to measure the overall fluorescence of samples producing fluorescent proteins (BioTek Synergy H1 or Neo2). Endpoint measurements were single timepoints without incubation and time course data is captured with incubation at 37 °C.

3.5 Nuclear magnetic resonance spectroscopy

Total CFPS reaction (250 µL), *E. coli* lysate (100 µL), PANOx buffer (87.4 µL), and RNAse inhibitor (2.5 µL) were lyophilized, resuspended and ground in acetone or chloroform, centrifuged at 16,000 x g for 15 minutes. The supernatant and pellet were separated, and solvent evaporated. Samples were rehydrated in deuterated water (1 mL), and added to NMR tubes (Wilmad, 535-PP-8). ^{1}H NMR data acquisitions were recorded at 600 MHz using an Agilent DD2 spectrometer console (Agilent Technologies, Santa Clara, CA) through VnmrJ software (version 4.2, revision A, with patch 4.2_LNX_DDR_107) running on Red Hat Enterprise Linux (release 6.3 (Santiago), Raleigh, NC) computer workstations. The spectrometer was fitted with a Varian 5 mm triple resonance ^{1}H, ^{13}C and ^{15}N probe incorporating an actively shielded *z*–gradient coil (Varian, Inc., Santa Clara, CA). The variable temperature unit thermocouple was calibrated to maintain the sample temperature at 37.0 ± 0.2 °C.

^{1}H free induction decay (FID) data of 16,384 complex points were summations of 32 acquisitions recorded with 10.0 ppm spectral windows, 90 ° read pulses and 75 sec relaxation delays to allow full spin–lattice relaxation and quantitative spectra. To obliterate the HOD signal, FID data sets were recorded without sample spinning using a double pulsed-field gradient spin-echo pulse sequence. Recorded FID data were multiplied by an exponential window function with a line–broadening factor of 0.5 Hz before Fourier transformation into spectra and manual phase correction into pure absorption mode. ^{1}H chemical shifts were referenced to external 3-(trimethylsilyl)-1-propanesulfonic acid in 90 % H_2O/10 % D_2O.

3.6 Resin bead polymer film casting

Polymer films were prepared as described in previous work.[9] The selected polymer is dissolved in an organic solvent as described for individual experiments. The polymer solution is added to the dried CFPS material and ground with a pestle. The CFPS:polymer ratio notation used in the text is the volume ratio of CFPS solution prior to drying compared to the volume of polymer solution added. 10 µL of the suspension is dropped into coverslip-bottom well plates. Polymer films form as solvent evaporates. Films were activated when 200 µL of nuclease free water was added to each well and slides were imaged by microscope as described below.

3.7 Nebulization of CFPS-polymer particles

A commercial, portable nebulizer (Manufacturer: Patin, Model Number MY105) was used to create CFPS/polymer particles (1–5 µm). Polymer solution (3 wt% in acetone, 1:5 CFPS) was added to the reservoir and nebulized. Particles were captured in a 50 ml falcon tube and characterized via scanning electron microscopy.

3.8 Scanning electron micrograph/energy dispersive x-ray

A Phenom ProX scanning electron micrograph/energy dispersive x-ray instrument is used to image samples mounted on aluminum pedestals with double-sided carbon tape. The sample mounted pedestals were then sputter coated with gold using a sputter coater (108 Manual Sputter Coater, Ted Pella, Inc.) prior to imaging. Fiber diameter was quantified from the SEM images using the macro general image fiber tool (GIFT)[16] in the software FIJI.

3.9 Fourier transform infrared spectroscopy

Chemical identification was conducted using a Bruker Tensor 27 attenuated total reflectance fourier-transform infrared instrument. Background and sample spectra are collected using 128 scans across a range of 4000–400 cm^{-1} with a spectral resolution of 4 cm^{-1}. Baseline corrections were conducted with Opus Software. Data was plotted using Origin Pro graphing software.

3.10 Dynamic mechanical analyzer

Fiber bundles were evaluated via tensile testing using a TA Instruments 850 dynamic mechanical analyzer instrument operating in tension mode with film clamps. Fiber bundles were held in place using high grit sandpaper within the clamps. Testing was conducted at a preload force of 0.001 N and a strain rate of 10 %/minunte until failure. Successful failure was only considered if fibers failed between the clamps. The Young's modulus was calculated from 2–5 % strain using Origin Pro graphing software. The yield stress was calculated by plotting the elastic modulus at a 2 % offset and the intersection between the two indicates the yield stress. All samples were measured in triplicate.

3.11 Gelatin emulsion

A 0.27 g/mL stock solution of cold-water fish gelatin (Sigma G7041-100G) was added to CFPS concentrated components, replacing some of the water in the CFPS mixture, to reach a final concentration of 0.1 g/mL fish gelatin while keeping all CFPS components at their usual concentration. A 0.1 g sample of Span 80 was dissolved in 4.375 mL mineral oil. The aqueous gelatin-CFPS solution was added dropwise to the mineral oil mixture with continuous vortexing. The emulsion was then stirred with a magnetic stir bar set to 600 rpm and maintained at 4 ºC for an hour. A sample of the emulsion in oil was then incubated and imaged between slide and coverslip on the microscope as described in Section 3.4. Meanwhile the remaining emulsion was extracted. A total of 3 mL tetrahydrofuran (THF) solvent was combined with 0.125 g of Syloid 244 (Grace Davidson) and vortexed 10 s to suspend. Following the vortexing, 0.3 mL of the THF suspension was added to 1 mL of the fish gelatin emulsion on ice with periodic vortex. Then 5 mL of THF alone was added and stirred at 600 rpm for 1 minute. The mixture was then vacuum filtered through Whatman filter paper (Sigma WHA1541110) in a buchner funnel. The product is rinsed 4x with 5 mL THF, then air dried overnight. Once dry, the sample is collected and broken up with a spatula until a homogeneous and flowable powder is obtained. The product was imaged with the Zeiss microscope both dry and rehydrated to look for morphology and mRuby fluorescence production by CFPS.

3.12 Microfluidics

A fish gelatin and CFPS solution was prepared as described in Section 3.11. This was stored on ice during microfluidic setup. A W/O droplet generator microfluidic chip was prepared by Dr. Jose Wippold according to established photolithography procedures.[17] The outer oil phase was Novec 750 (3M) with 0.3 % Picosurf surfactant (Sphere fluidics). Inner gelatin-CFPS phase and outer oil phase solutions are placed in syringes and syringe pumps push fluid through PTFE tubing to the chip at 100 uL/hr for inner phase and 1000 µL/hr outer phase. Droplets can be collected in a reservoir chip or in a snap cap tube. For glutaraldehyde samples, 25 % glutaraldehyde solution was added to the W/O droplet suspension with vortexing to reach their final concentrations (described in Section 2.6).

4. CONCLUSIONS

This year the solvent-casting process was further characterized by measuring solvent-extracted components of CFPS via NMR, physical characteristics and shelf life of CFPS-fibers produced via SBS were measured, and several CFPS particle generation methods were screened. Remarkably, little of the dry CFPS material is detected in solvent extractions, supporting the stability of this system to solvent processing. Preliminary shelf-life measurements highlight the possibility to recover CFPS activity one week after preparation, and more studies are required to deconvolute variability between samples and conditions. FTIR analysis of fibers did not detect differences due to CFPS incorporation, but mechanical testing indicates fibers containing CFPS are more easily stretched. Particles containing CFPS components were successfully generated using commercial hydrogel resins, nebulized polymer, or gelatin encapsulation methods. Activity have been shown for all but the nebulized particles, but commercial resins and gelatin particles exhibited some hurdles to particle stability during downstream drying and polymer processing. Future work

will continue to refine particle generation methods, characterize CFPS-particle performance, continue fiber characterization, and elucidate the effects of adding polymer shells to fibers and particles to stability and activity.

ACKNOWLEDGMENTS

Funding was provided by the U.S. Army via the Chemical Biological Advanced Materials and Manufacturing Science Program (PE 0601102A Project VR9) at the Combat Capabilities Development Command Chemical Biological Center. Special thanks to Katherine Rhea with assistance from the Biomanufacturing Branch for supplying *E. coli* lysate and CFPS reagents.

REFERENCES

[1] Png, Z.M.; Wang, C.-G.; Yeo, J.C.C.; Lee, J.J.C.; Surat'man, N.E.; Tan, Y.L.; Liu, H.; Wang, P.; Tan, B.H.; Xu, J.W.; Loh, X.J.; Zhu, Q., Stimuli-responsive structure–property switchable polymer materials. *Mol. Syst. Des. Eng.* **2023**, *8* (9), pp 1097–1129.

[2] Wang, S.; Urban, M.W. Self-healing polymers. *Nat. Rev. Mater.* **2020**, *5* (8), pp 562–583.

[3] Peterson, G.W.; Lee, D.T.; Barton, H.F.; Epps, T.H.; Parsons, G.N. Fibre-based composites from the integration of metal–organic frameworks and polymers. *Nat. Rev. Mater.* **2021**, *6* (7), pp 605–621.

[4] Tang, T.-C.; An, B.; Huang, Y.; Vasikaran, S.; Wang, Y.; Jiang, X.; Lu, T.K.; Zhong, C. Materials design by synthetic biology. *Nat. Rev. Mater.* **2020**, *6* (4), pp 332–350.

[5] Liu, A.P.; Appel, E.A.; Ashby, P.D.; Baker, B.M.; Franco, E.; Gu, L.; Haynes, K.; Joshi, N.S.; Kloxin, A.M.; Kouwer, P.H.J.; Mittal, J.; Morsut, L.; Noireaux, V.; Parekh, S.; Schulman, R.; Tang, S.K.Y.; Valentine, M.T.; Vega, S.L.; Weber, W.; Stephanopoulos, N.; Chaudhuri, O. The living interface between synthetic biology and biomaterial design. *Nat. Mater.* **2022**, *21* (4), pp 390–397.

[6] Marilyn S.; Lee, J.A.L.; Biondo, J.R.; Lux, J.; Kuhn, D.L.; Browe, M.A.; Gupta, M.K.; Lux, M.W. Extending Bio-Functionality in Materials via Controlled Polymer Erosion. *FY22 Proceedings of the U.S. Army Combat Capabilities Development Command Chemical Biological Center In-House Laboratory Independent Research and Chemical Biological Advanced Materials and Manufacturing Science Programs.* **2022**.

[7] Silverman, A.D.; Karim, A.S.; Jewett, M.C. Cell-free gene expression: an expanded repertoire of applications. *Nat. Rev. Genet.* **2020**, *21* (3), pp 151–170.

[8] Lee, M.S.; Raig, R.M.; Gupta, M.K.; Lux, M.W. Lyophilized Cell-Free Systems Display Tolerance to Organic Solvent Exposure. *ACS Synth. Biol.* **2020**, *9* (8), pp 1951–1957.

[9] Lee, M.S.; Lee, J.A.; Biondo, J.R.; Lux, J.E.; Raig, R.M.; Berger, P.N.; Bernhards, C.B.; Kuhn, D.L.; Gupta, M.K.; Lux, M.W. Cell-Free Protein Expression in Polymer Materials. *ACS Synth. Biol.* **2024**, *13* (4), pp 1152–1164.

[10] Dadol, G.C.; Kilic, A.; Tijing, L.D.; Lim, K.J.A.; Cabatingan, L.K.; Tan, N.P.B.; Stojanovska, E.; Polat, Y. Solution blow spinning (SBS) and SBS-spun nanofibers: Materials, methods, and applications. *Mater. Today Commun.* **2020**, *25*.

[11] Wei, W.W.; Liao, Y.X.; Wang, Y.F.; Wang, S.Q.; Du, W.; Lu, H.M.; Kong, B.; Yang, H.W.; Zhang, Z.M. Deep Learning-Based Method for Compound Identification in NMR Spectra of Mixtures. *Molecules.* **2022**, *27* (12).

[12] Jewett, M.C.; Swartz, J.R. Mimicking the cytoplasmic environment activates long-lived and efficient cell-free protein synthesis. *Biotechnol. Bioeng.* **2004**, *86* (1), pp 19–26.

[13] Schindelin, J.; Arganda-Carreras, I.; Frise, E.; Kaynig, V.; Longair, M.; Pietzsch, T.; Preibisch, S.; Rueden, C.; Saalfeld, S.; Schmid, B.; Tinevez, J.Y.; White, D.J.; Hartenstein, V.; Eliceiri, K.; Tomancak, P.; Cardona, A. Fiji: an open-source platform for biological-image analysis. *Nat. Methods.* **2012**, *9* (7), pp 676–682.

[14] Bundy, B.C.; Swartz, J.R. Site-specific incorporation of p-propargyloxyphenylalanine in a cell-free environment for direct protein-protein click conjugation. *Bioconjug. Chem.* **2010**, *21* (2), pp 255–263.

[15] Kwon, Y.C.; Jewett, M.C. High-throughput preparation methods of crude extract for robust cell-free protein synthesis. *Sci. Rep.* **2015**, *5*, p 8663.

[16] Götz, A.; Senz, V.; Schmidt, W.; Huling, J.; Grabow, N.; Illner, S. General image fiber tool: A concept for automated evaluation of fiber diameters in SEM images. *Measurement.* **2021**, *177*.

[17] Xia, Y.; Whitesides, G.M. Soft Lithography. *Angew. Chem. Int. Ed. Engl.* **1998**, *37* (5), pp 550–575.

Beyond behavior: identifying correlates of olfactory responses in military working dogs using physiological monitoring and machine learning

Edgar O. Aviles-Rosa[a], Nathaniel J. Hall[a], Jörg Schultz[b], Brian D. Farr[c], Andrea L. Henderson[c], Erin B. Perry[d], Dakota R. Discepolo[d,i,j], Dana M. Pasquale[e], Eric M. Best [f], Debra L. Zoran[g], Caitlin E. Sharpes[h,j], Michele N. Maughan[h,j], Jenna D. Gadberry[h,j], Aleksandr E. Miklos[j], Patricia E. Buckley[j]*

[a]Texas Tech University, 2500 Broadway West, Lubbock, TX 79409

[b]Tier Wohl Team GbR, 97348 Rödelsee

[c]Department of Defense Military Working Dog Veterinary Service, Joint Base San Antonio-Lackland, 1219 Knight St, Building 7602, San Antonio, TX 78236

[d]Southern Illinois University, Department of Animal Science, Food and Nutrition, 1263 Lincoln Dr, Carbondale, IL 62901

[e]Valiant Harbor International LLC, 4800 Hampden Ln, Bethesda, MD 20814

[f]University at Albany, College of Emergency Preparedness, Homeland Security and Cybersecurity, 1400 Washington Ave, Albany, NY 12222

[g]Texas A&M University, College of Veterinary Medicine, 400 Bizzell St, College Station, TX 77843

[h]Precise Systems Inc., 22290 Exploration Dr, Lexington Park, MD 20653

[i]Oak Ridge Institute for Science and Education, 1299 Bethel Valley Rd, Oak Ridge, TN 37830

[j]U.S. Army Combat Capabilities Development Command Chemical Biological Center, Research & Operations Directorate, 8198 Blackhawk Rd, Aberdeen Proving Ground, MD 21010

ABSTRACT

Detection canines serve critical roles to support the military, homeland security and border protection. Like human personnel, dogs are subject to physiological and psychological variables that can influence performance, but the nature and magnitude of these effects are almost entirely unknown. The impact of physical activity on canine olfactory detection ability was assessed using a treadmill with automated olfactometry, the "olfacto-treadmill". Twelve minutes of moderate intensity exercise (trotting) caused a 15–20 % drop in olfactory detection and dogs were detecting odor only at chance levels within 24–33 minutes. Low intensity exercise did not cause a drop in performance, but rather improved over 33 minutes. In a second experiment, dogs transitioned from low-to-high or high-to-low intensity exercise after 23 minutes. When transitioning from high-to-low intensity, dogs rapidly recovered performance at the low intensity, improving performance within minutes. When transitioning from high-to-low intensity exercise, dogs showed a precipitous drop yielding the poorest detection outcomes. Performance drops were associated with increasing core body temperature and an overall >1 °C increase in core body temperature. The results highlight that a combination of monitoring of ongoing exercise intensity, duration, and core body temperature may predict detection canine olfactory capabilities.

Keywords: Detection canines, machine learning, olfaction, physiological status monitoring, accelerometry

1. INTRODUCTION

Within the military and search and rescue enterprises, working dogs are required to engage in substantial physical activity while scanning for trained odors associated with explosives[1] or missing persons.[2] During these tasks, dogs engage in extensive activity, leading to an increase in core body temperature and subsequently cooling behaviors such as panting.[3–11] Previous research has shown that exercising dogs on a treadmill prior to a detection task leads to decreased detection performance,[12–14] presumably through induction of cooling mechanisms that may be incompatible

with scent detection. Dogs cool primarily through evaporative cooling from panting,[14] whereby most of the air inhaled during panting passes through the mouth.[15]

A decrement in olfactory performance during ongoing activity could be due to cooling mechanisms being incompatible with olfaction, but may also be related to more global factors such as fatigue or decline in motivation during ongoing physical activity. Research investigating these mechanisms however, are minimal. Prior research has shown that physical conditioning can improve canine athletes' olfactory performance under moderate exercise,[12] but it's unclear if this improvement is related to more efficient cooling/reduced heat gain and reduced panting, or the dogs are showing less fatigue and maintain higher levels of motivation. Prior researchers have suggested that poor physical conditioning can cause dogs to become demotivated or fatigued, causing search efficacy to drop.[16]

Recently, our team developed a paradigm to assess the effect of ongoing exercise intensity on olfactory sensitivity. A treadmill setup was recently created and published that incorporated an automated olfactometer, allowing odor to be presented while a dog simultaneously exercised on a treadmill.[17] We found a complex relationship between odor concentration, exercise intensity, and exercise duration. When dogs engaged in higher intensity exercise (a trot), dogs' olfactory performance for the lowest concentration odors went from nearly 100 % accuracy in the first 10 minutes of exercise, to nearly 0 % detection accuracy after 20 minutes.[17] Performance during a lower exercise intensity (a walk), detection remained relatively stable across 30 minutes. This study, however, did not evaluate (1) whether the decline at higher exercise intensity and duration correlated with increased core body temperature, (2) whether dogs would quickly recover from performance decrement if the exercise intensity is reduced, and (3) whether advanced analytics with physiological measures can predict when the decrement will occur.

Advanced analytics of physiological status monitoring (PSM) has grown substantially over the last decade. These advancements have demonstrated that monitoring sniffing behavior can distinquish true negatives from false negatives,[18] heart rate monitoring can distinquish between dogs sniffing target odors from controls,[19] PSM monitoring can predict probability of success in a service dog program,[20] and accelerometry can predict canine behavior.[21] Although it was over two decades ago that Gazit and Terkel's work highlighted a clear concern about the effect of exercise and physical fittness on working dogs detection capabilities,[14] it was not until our team developed a novel experimental paradigm in year one (FY23) of this project that it became posible to conduct systematic research synchronizing canine detection performance, exercise intensity, and advanced physiolgoical status monitoring.

The objective of this study was to leverage our unique pradigm,[17] advances in canine PSM, advances in machine learning and artifical intelligence to 1) Integrate machine learning (ML)-based data analysis to lay the groundwork for predictive modeling between PSM and odor-detection performance using our previously collected data set;[17] 2) Correlate enhanced PSM measures with canine odor-detection performance; and 3) Identify the psychological and physiological measures that cause the odor-detection decrement.

2. MATERIALS AND METHODS

2.1 General

The study was conducted at Texas Tech University Canine Olfaction Research and Education (CORE) Lab. All procedures were approved by the Institutional Animal Care and Use Committee. Three dogs (N = 3) between 2–5 years old participated in the study (see Table 1 for demographic information). Owner consent was obtained for the privately owned animal. Charles, who was a pet dog, lived at his owner's residence. Adele and Boomer were housed at the CORE Lab. Boomer and Charles had previous treadmill training experience. Charles also had a history of exercising (e.g., 30-minute runs with his owner weekly) and participated in multiple sessions of strength conditioning exercises each week with his owner (Penn Vet Working Dog Center Fit to Work Program).[22] Dogs were trained to nose-poke an odor port in a go/no-go olfaction task while simultaneously walking (4 km/h) or trotting (8 km/h) on a treadmill (Dog Runner Treadmill Revolution Pro or DogTread Large Dog Treadmill). The treadmill had a manufacturer set incline of 5 %.

Table 1. Demographic information of study dogs.

Dog Name	Sex	Breed	Age in Yrs	Weight	Previous Treadmill Experience
Adele	Spayed female	Belgian Malinois	3.0	22 kg	N
Boomer	Intact male	English Springer Spaniel	2.0	23 kg	Y
Charles	Neutered male	Mixed breed	4.0	20 kg	Y

2.2 Olfacto-treadmill apparatus

An olfactometer was mounted onto a treadmill with a polypropylene panel to assess olfactory sensitivity while simultaneously exercising as previously described (Figure 1).[23] Odor delivery (activation/deactivation of odor valves) was controlled by an automated computer system and the experimenter was always blind to odor status during testing sessions. When an odor valve was activated, air from the odor line (at 2 L/min) entered the odor vial (with either a target odor or diluent odor). The headspace in the jar from the odor vial was carried through a Teflon (PTFE) tube to a Teflon manifold. The headspace was mixed with a continuous air stream (at 8 L/min) where it was transferred to a stainless-steel odor port through a Teflon tube. See Figure 2 for a visual depiction of the odor plume.

Dogs were acclimated to the PSM devices, conditioned and trained to walk and trot on the treadmill as previously described.[17] Similarly, all testing was conducted double blind as previously described.[17]

Figure 1. Charles walking on the olfacto-treadmill apparatus.

Figure 2. A visualization of the odor plume using titanium tetrachloride ($TiCl_4$).

2.3 Physiological status monitoring

2.3.1 Core body temperature

Dogs were given an Anipill core body temperature capsule (Bodycap; Hérouville-Saint-Clair, France) with a small morsel of peanut butter or wet dog food prior to beginning a test session. The capsule was administered at least 30 minutes prior to the start of a session.

2.3.2 Heart rate and heart rate variability

To measure heart rate, a Polar® H10 heart rate monitor (Kempele, Finland) was attached around the dog's chest using the manufacturer's strap and secured using self-adhering elastic bandage wrap (e.g., Juvale Self Adhesive Bandage Wrap). Ultrasound gel (e.g., Aquasonic Ultrasound Gel) was applied to the electrode belt to promote conductivity.

2.3.3 Accelerometer

Dogs wore an Actigraph wGT3X-BT attached to a harness (PetSafe 3 in 1 No-Pull Dog Harness) with two zip ties between the dogs' scapulae. The Actigraph was initiated at 30 Hz. Additionally, 3-axis accelerometry was obtained from the Polar® H10 heart rate monitor using custom software.

2.3.4 Video

All sessions were video recorded using two Razer Kiyo Pro cameras and audio recorded using a TONOR TC30 microphone for the room setup with audio and video recorders.

2.4 Statistical analysis

Proportion correct was calculated as the number of hits and rejections by the number of trials. Proportion correct was calculated over time bins across the period. Core body temperature was measured every minute and averaged over the same time-bins. Heart rate and accelerometry were sampled at 25 Hz and synchronized with behavioral data.

2.5 Machine learning

2.5.1 Predicting detection dog performance

Based on feature forward selection, the top five features (concentration, heart rate, trial count, energy_x, energy_y) were chosen for analysis. A model comparison involving a feed-forward neural network, Random Forest, K-Nearest Neighbor (KNN), Decision Tree, and Naive Bayes classifier showed that Random Forest achieved the highest accuracy. Parameter optimization via grid search resulted in an accuracy of 80 % on unseen test data for the Random Forest classifier.

2.5.2 Gait classification

Spectra from one-second windows of 25 Hz accelerometer data were used to train a neural network with output classes "Trot" and "Walk". Anomaly detection was performed using k-means clustering. The trained network achieved >99 % accuracy. For real-time predictions, the classification pipeline was implemented on an M5 Stick-C Plus device, which reports data and classification results via Message Queuing Telemetry Transport to Amazon Web Service (AWS) Internet of Things Core. Data are stored in AWS Timestream, and a web interface provides device control, real-time monitoring, and data recall.

2.5.3 Markerless pose estimation

DeepLabCut was used to extract frames from video recordings. These frames were manually annotated using Computer Vision Annotation Tool to create training data. The images were used to train the prediction network based on MobileNetV2_1.0. Once trained, the network was used for predictions on a video stream sent via Web Real-Time Communication to a Graphics Processing Unit-accelerated AWS Elastic Comute Cloud instance.

2.5.4 Facial expression classification

The vision capabilities of the OpenAI GPT-4 model are used for annotation of images. Two prompts are available for classification: (1) exhaustion analysis based on "Canine Record of Perceived Exertion (K9-RPE)," and (2) a prompt looking for stress signs. Base64 encoded images and prompts are sent to OpenAI using the LangChain framework. A web interface allows predictions on recorded images or single video frames.

3. RESULTS

3.1 Experiment 1

The purpose of Experiment 1 was to replicate our prior work[17] while including more PSM measures such as core body temperature and accelerometry. Differing from our prior work,[17] we increased reinforcement rate for correct rejections to 100 % reinforcement from 40 %. This was done, because during initial training some dogs began to false alert at low odor concentration because responses were reinforced at a higher frequency than correct rejections (100 % vs. 40 %). Increasing reinforcement for correct rejections reduced false positives and was continued throughout testing. In addition, we only tested dogs with a moderately challenging odor concentration (10^{-4} v/v dilution) to maximize data collection where performance decrements were observed.

Three dogs (Adele, Boomer, and Charles) were tested for 100 trials using 1-bromooctane 10^{-4} v/v. Charles was tested with an additional lower concentration, due to high performance with 10^{-4} v/v. Each session had a random sequence of go and no-go trials, for a total of 50 trials of 1-bromooctane 10^{-4} v/v and 50 trials of the diluent. Each session lasted 32 minutes. Two dogs (Adele and Boomer) completed a total of four sessions. Charles completed a total of eight sessions, with four sessions with 1-bromooctane 10^{-4} v/v and four sessions with 1-bromooctane 10^{-5} v/v. Charles was tested with an additional lower concentration (1-bromooctane 10^{-5} v/v) because he did not show a large decrement in performance at a trot at 1-bromooctane 10^{-4} v/v. Mean accuracy for Charles at 1-bromooctane 10^{-4} v/v was 92 % at a walk, and 91 % at a trot. The walk and trot order of the sessions was counterbalanced for all dogs. Individual dogs alternated between the trot and walk intensities. A dog only completed one session per day. Figure 3 shows Experiment 1 results of proportion correct, core body temperature and heart rate across exercise time.

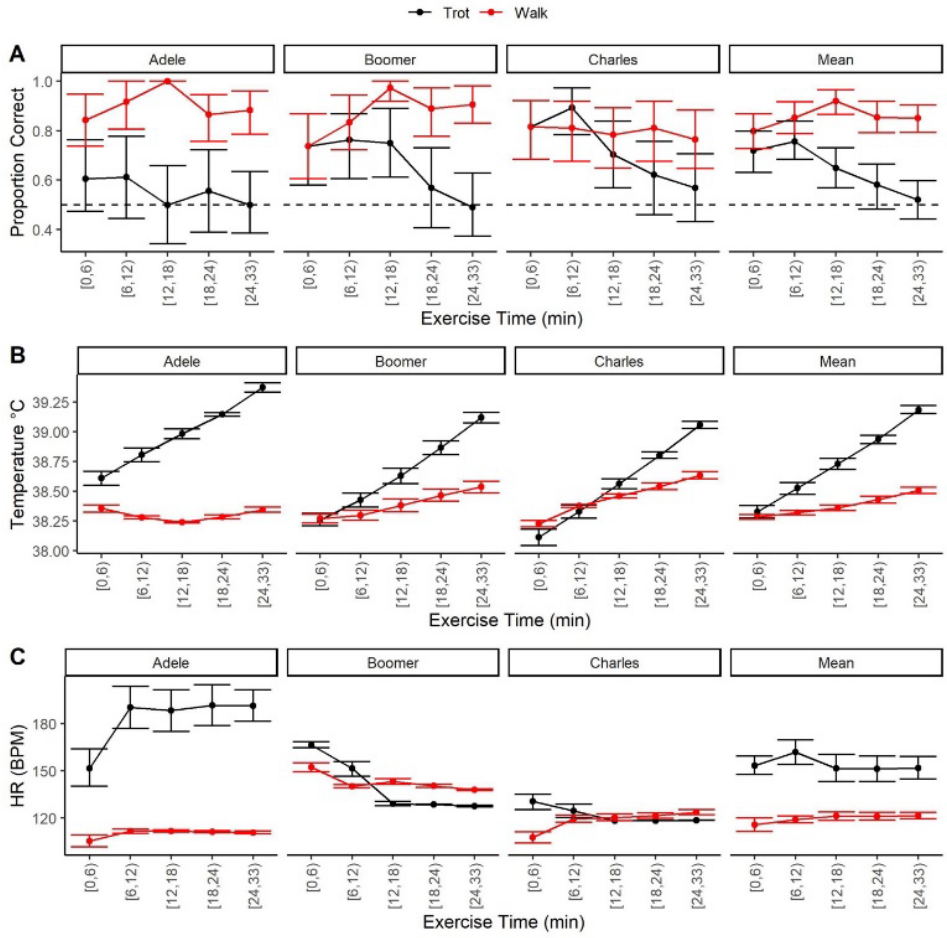

Figure 3. (A) Shows the mean proportion of correct responses across exercise time. (B) Shows mean core body temperature across exercise time. (C) Shows mean heart rate across exercise time. Error bars show 95 % boot strap confidence intervals.

3.1.1 Proportion correct

At a walk, as exercise time increased, olfactory performance remained stable or increased across the session. In contrast, at a trot the mean proportion of correct responses decreased as exercise duration continued (ranged between 71.9 % mean accuracy during minutes 0–6 to chance performance of 51.9 % mean accuracy during minutes 24–33).

3.1.2 Core body temperature

At a walk, mean core body temperature increased slightly and steadily as exercise time increased (mean ranged between 38.3 °C at 0–6 minutes to 38.5 °C at 24–33 minutes). At a trot, mean core body temperature increased at a faster rate and dogs ended exercise with a mean ~1 °C higher body temperature than at the end of the walk sessions. Mean core body temperature ranged between 38.3 °C at 0–6 minutes to 39.2 °C during minutes 24–33.

3.1.3 Heart rate

At a walk, mean heart rate stopped increasing after the first 12 minutes of exercise and remained steady throughout the duration of the exercise session (mean ranged between 116–122 bpm). At a trot, mean heart rate showed an initial increase, then leveled out after 12 minutes (mean ranged between 151–162 bpm). Mean heart rate at a walk always remained lower than at a trot throughout the duration of exercise.

3.2 Experiment 2

Experiment 2 evaluated how a dog's olfactory performance changed after being switched between exercise intensities within a session. We increased the session duration to 45 minutes (140 trials) and introduced a reversal of exercise intensity midway (trial 70/ minute 22.5). All dogs were tested for 140 trials using 1-bromooctane 10^{-4} v/v as a target odor and mineral oil as a distractor odor. The first 70 trials were one condition (walk or trot). After trial 70, the pace was changed to the opposite condition (walk or trot). The walk and trot order was counterbalanced across sessions for all dogs, with consecutive sessions always being different pace configurations (e.g., Session 1: Walk/Trot, Session 2: Trot/Walk). Each session had a random sequence of go and no-go trials, for a total of 70 trials of the target odor (1-bromooctane 10^{-4} v/v) and 70 trials of the diluent. Each session lasted 45 minutes with all dogs completed eight sessions. Prior to moving onto session five, dogs were required to achieve at least 60 % accuracy (greater than chance) during a 100-trial trot session with a higher concentration (1-bromooctane 10^{-2} v/v) to maintain motivation and ensure dogs were still responding to target odor appropriately under both the walk and trot conditions. During the refresher trot sessions, Adele achieved 74 % accuracy, Boomer achieved 70 % accuracy, and Charles achieved 96 % accuracy. Dogs also completed a 100-trial refresher walk session with 1-bromooctane 10^{-2} v/v prior to moving onto session five. At a walk, Adele achieved 99 % accuracy, Boomer achieved 92 % accuracy, and Charles achieved 96 % accuracy. We calculated proportion correct as the mean proportion of correct trials (correct alerts and correct rejections). Figure 4 shows Experiment 2 results for proportion of correct responses, core body temperature and heart rate across exercise time.

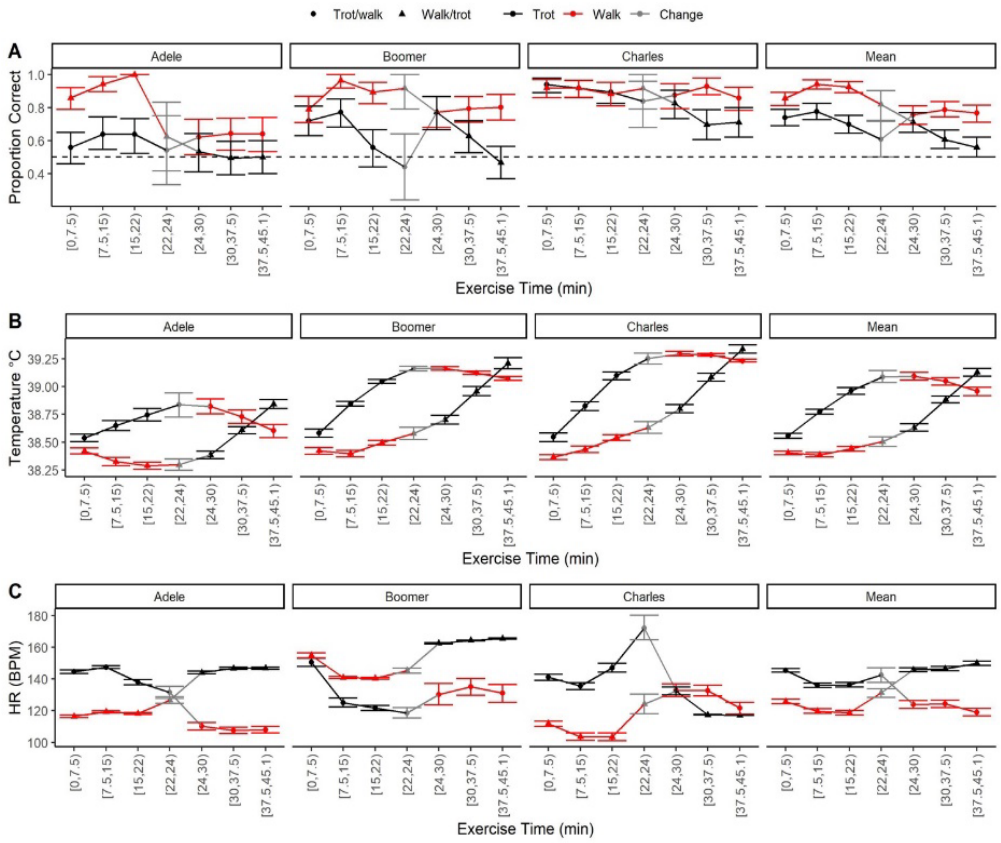

Figure 4. (A) Shows the mean proportion of correct responses across exercise time for both the walk/trot and trot/walk conditions. (B) Shows mean core body temperature across exercise time for both conditions. (C) Shows mean heart rate across exercise time for both conditions. Error bars show 95 % boot strap confidence intervals. The grey points show the mean when the pace changes.

3.2.1 Proportion correct

When starting at a trot, mean proportion correct declined slightly as exercise duration increased while trotting. The mean proportion correct at a trot in the trot/walk condition was 74 % accuracy from minutes 0–7.5 and decreased to 66.7 % accuracy during minutes 22–24. When pace was switched to a walk, olfactory performance recovered to similar accuracy as during minutes 0–7.5 of the trot (mean accuracy at a walk ranged between 75.7 % at minutes 24–30 to 76.7 % at minutes 37.5–45.1). During the walk/trot condition, mean dog olfactory performance ranged between 85.7% during minutes 0–7.5 to 90.9 % accuracy during minutes 22–24 at a walk. When switching pace to a trot, performance decreased rapidly from 71.3% mean accuracy during minutes 24–30 to 55.9 % mean accuracy (chance performance) during minutes 37.5–45.

3.2.2 Core body temperature

During the trot/walk condition, mean core body temperature rose at a trot from 38.6 °C during minutes 0–7.5 to 39.1 °C during minutes 22–24. When switching to a walk, mean core body temperature stabilized from 39.1 °C during minutes 24–30 to 39.0 °C during minutes 37.5–45.1. During the walk/trot condition, at a walk, mean core body temperature began at 38.4 °C during minutes 0–7.5, and only rose 0.1 °C at minutes 22–24 (38.5 °C). When switching to a trot, mean core body temperature rose substantially from 38.6 °C at minutes 24–30 to 39.1 °C at minutes 37.5–45.1.

3.2.3 Heart rate

During the trot/walk condition, at a trot, mean heart rate began elevating at minutes 0–7.5 (145 bpm) and remained steady to minutes 22–24 (148 bpm). When switching to a walk, mean heart rate began decreasing from 124 bpm at

minutes 24–30 to 119 bpm at minutes 37.5–45.1. During the walk/trot condition, mean heart rate at a walk did not fluctuate greatly from minute 0 (126 bpm) to minute 24 (126 bpm). When switching to a trot, mean heart rate increased from 146 bpm at minutes 24–30 to 150 bpm at minutes 37.5–45.1.

3.3 Machine learning results

The setup includes (1) Predicting Performance, which uses a Random Forest classifier with physiological metrics (heart rate, acceleration) to estimate task performance under different conditions, accompanied by a screenshot showing the prediction interface displaying metrics such as heart rate and acceleration; (2) Gait Classification, which uses TinyML models to classify the dog's gait and identify anomalies based on accelerometer data, with a screenshot showing real-time gait classification results; (3) Pose Estimation, which employs classical neural networks to evaluate body posture during tasks, providing insights into the dog's movement dynamics, shown alongside a screenshot illustrating the key points of the dog's posture during treadmill activity; (4) Facial Expression Analysis, which uses large multimodal models to assess emotional states during exercise, interpreting features such as stress or exhaustion levels, with a screenshot depicting the analysis of facial expression and stress level indicators.

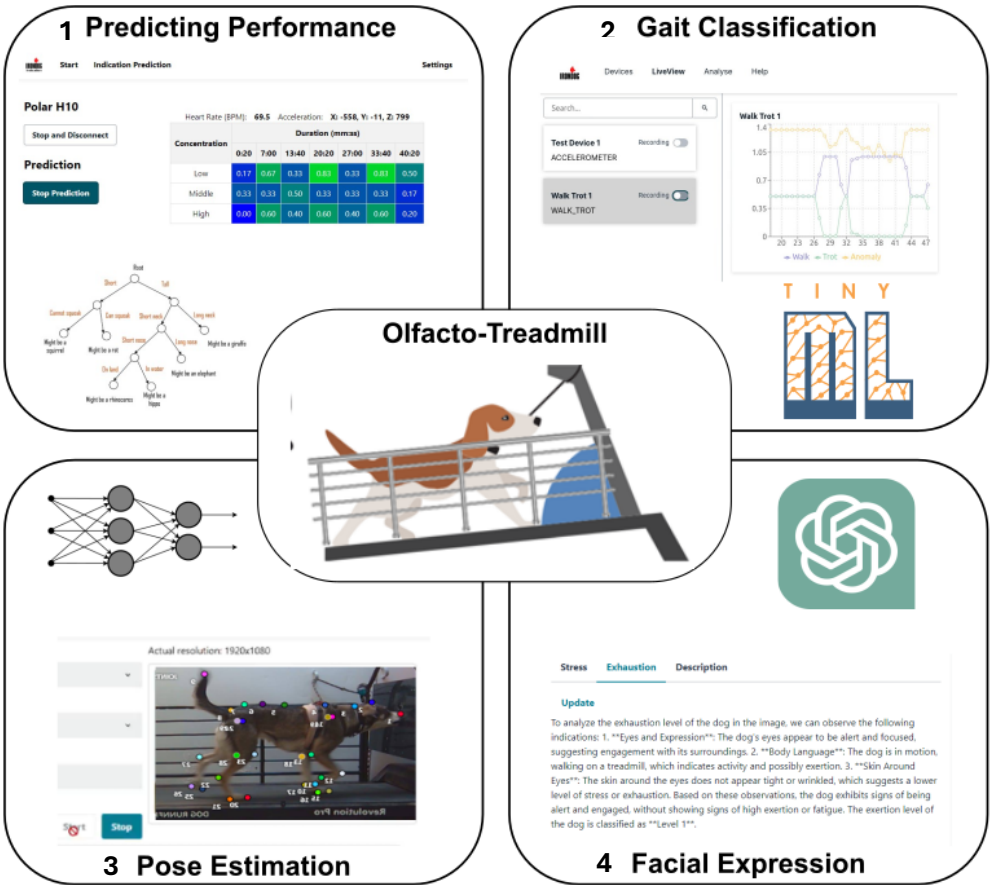

Figure 5. Overview of machine learning approaches used to analyze data from olfaction tasks performed by detection dogs.

4. DISCUSSION

In Experiment 1, we replicated our prior work,[17] while adding core body temperature as an additional measure. These results showed that dogs under the trot condition experienced a 1 °C increase in core temperature, compared to a <0.25 °C in the walk condition. Detection performance in the walk condition remained stable, with some dogs even improving over the 30-minute session. In contrast, in the trot condition, performance began to decline after 12 minutes,

with dogs reaching chance levels (~50 % detection rates) by the end of the session. Interestingly, this decline correlated with a 0.5 °C increase in body temperature, double the increase observed in the walk condition.

While these results suggest that increased exercise intensity leads to a performance decrement, the degree of core temperature elevation was modest compared to previous studies.[25,26] More importantly, the decline in detection performance began when core body temperature had increased by just 0.5 °C, raising questions about whether the temperature increase directly impairs olfaction or is merely a byproduct of increased exercise intensity. Future studies will need to manipulate environmental temperature while holding exercise intensity constant to test whether core temperature exerts a direct effect on detection, supporting the cooling interference hypothesis.

In Experiment 2, we observed that dogs experiencing a decline in performance during trot sessions were able to recover quickly during walk phases, even though their core temperature remained elevated by more than 0.5 °C. This suggests that the rate of temperature gain, rather than the absolute temperature, may be a more critical factor in influencing olfactory performance. Furthermore, temperature might serve as a proxy for exercise intensity and duration, rather than directly causing the decline in performance.

Of practical relevance, we found that starting the session with a high-intensity exercise phase (trot) followed by a lower-intensity phase (walk) resulted in better overall detection accuracy compared to the reverse sequence. This implies that, for more complex detection tasks, it may be beneficial to complete the most physically demanding tasks first to maximize performance.

To further understand the impact of exercise intensity and physiological changes on detection performance, we initiated an exploration into predictive modeling using physiological data. We utilized a wearable device, the Polar® H10, to collect real-time physiological metrics and developed a machine learning model to predict detection dog performance. Our results demonstrated that, using only five parameters extracted from wearable data, we could predict with 80 % accuracy whether a dog would indicate the presence of an odor during trot exercises. These findings highlight the potential for using physiological monitoring to anticipate declines in detection performance in real-time field conditions. Moving forward, integrating additional physiological measures like core temperature has the potential to increase prediction accuracy substantially.

Our work in gait classification and markerless pose estimation further supports this predictive framework. We successfully used accelerometer data to train a neural network capable of classifying gaits—walk and trot—with 99 % accuracy. This classification has been integrated into our prediction pipeline, allowing for real-time monitoring and classification of gait as an independent input for performance predictions. Additionally, our efforts to integrate facial expression classification using large multimodal models represent a novel approach that has only become feasible with the recent advancements in vision models within the past year. This cutting-edge methodology provides another layer of insight into how stress, fatigue, and emotional states might influence detection outcomes, placing our work at the forefront of technical development. While these findings provide significant insights, they also raise several questions for further investigation. Manipulating core temperature through environmental conditions, while maintaining consistent exercise intensity, will help clarify whether core body temperature directly affects olfaction or simply reflects exercise load. Additionally, incorporating non-olfactory tasks will allow us to determine whether performance decrements are specific to olfaction or linked to broader factors such as motivation and fatigue. Finally, integrating machine learning-based prediction models with other physiological and behavioral measures, including rest breaks, conditioning, and training, could provide valuable guidelines for optimizing the performance of working dogs in the field.

ACKNOWLEDGMENTS

The authors would like to acknowledge Dr. Patricia McDaniel and her team for their mentorship, guidance, and indirect technical assistance. We would also like to acknowledge Adele, Boomer, and Charles for their hard work and effort. Funding was provided by the U.S. Army via the Chemical Biological Advanced Materials and Manufacturing Science (CBAMMS) Program (PE 0601102A Project VR9) at the Combat Capabilities Development Command Chemical Biological Center (DEVCOM CBC).

REFERENCES

[1] Furton, K.G.; Myers, L.J. The scientific foundation and efficacy of the use of canines as chemical detectors for explosives. *Talanta.* **2001**, *54* (3), pp 487–500.

[2] Jones, K.E.; Dashfield, K.; Downend, A.B.; Otto, C.M. Search-and-rescue dogs: an overview for veterinarians. *J. Am. Vet. Med. Assoc.* **2004**, *225* (6), pp 854–860.
[3] Angle, T.; Gillette, R. Telemetric measurement of body core temperature in exercising unconditioned Labrador retrievers. *Can. J. Vet. Res.*. **2011**, *75*, pp 157–159.
[4] Baker, J.; DeChant, M.; Jenkins, E.; Moore, G.; Kelsey, K.; Perry, E. Body Temperature Responses During Phases of Work in Human Remains Detection Dogs Undergoing a Simulated Deployment. *Animals.* **2020**, *10* (4), p 673.
[5] Baker, J.; Davis, M. Effect of conditioning on exercise-induced hyperthermia and post-exercise cooling in dogs. *Compar. Ex. Phys.* **2018**, *14*, pp 91–97.
[6] Carter, A.J.; Hall, E.J. Investigating factors affecting the body temperature of dogs competing in cross country (canicross) races in the UK. *J. Therm. Biol.* **2018**, *72*, pp 33–38.
[7] Diverio, S.; Barbato, O.; Cavallina, R.; Guelfi, G.; Iaboni, M.; Zasso, R.; Di Mari, W.; Santoro, M.M.; Knowles, T.G.A. A simulated Avalanche search and rescue mission induces temporary physiological and behavioural changes in military dogs. *Physiol. Behav.* **2016**, *163*, pp 193–202.
[8] O'Brien, C.; Karis, A.; Tharion, W.; Sullivan, H.; Hoyt, R. Core temperature responses of military working dogs during training activities and exercise walks. *US Army Med. Dep. J.* **2017**, pp 71–78.
[9] Robbins, P.J.; Ramos, M.T.; Zanghi, B.M.; Otto, C.M. Environmental and Physiological Factors Associated With Stamina in Dogs Exercising in High Ambient Temperatures. *Front. Vet. Sci.* **2017**, *4*, p 144.
[10] Rovira, S.; Muñoz, A.; Benito, M. Effect of exercise on physiological, blood and endocrine parameters in search and rescue-trained dogs. *Vet. Med.* **2008**, *53* (6), pp 343–346.
[11] Steiss, J.; Ahmad, H.A.; Cooper, P.; Ledford, C. Physiologic responses in healthy Labrador Retrievers during field trial training and competition. *J. of Vet. Intern. Med.* **2004**, *18* (2), pp 147–151.
[12] Altom, E.K.; Davenport, G.M.; Myers, L.J.; Cummins, K.A. Effect of dietary fat source and exercise on odorant-detecting ability of canine athletes. *Res. Vet. Sci.* **2003**, *75* (2), pp 149–155.
[13] Angle, C.T.; Wakshlag, J.J.; Gillette, R.L.; Steury, T.; Haney, P.; Barrett, J.; Fisher, T. The effects of exercise and diet on olfactory capability in detection dogs. *J. Nutr. Sci.* **2014**, *3*, e44.
[14] Gazit, I.; Terkel, J. Explosives detection by sniffer dogs following strenuous physical activity. *Appl. Anim. Behav. Sci.* **2003**, *81* (2), pp 149–161.
[15] Schmidt-Nielsen, K.; Bretz, W.L.; Taylor, C.R. Panting in dogs: unidirectional air flow over evaporative surfaces. *Science.* **1970**, *169* (3950), pp 1102–1104.
[16] McKeague, B.; Finlay, C.; Rooney, N. Conservation detection dogs: A critical review of efficacy and methodology. *Ecology and Evolution.* **2024**, *14* (2), p e10866.
[17] Aviles-Rosa, E.; Schultz, J.; Maughan, M.N.; Gadberry, J.D.; DiPasquale, D.M.; Farr, B.; Henderson, A.; Best, E.; Discepolo, D.R.; Buckley, P.; Perry, E.B.; Zoran, D.L.; Hall, N.J. A canine model to evaluate the effect of exercise intensity and duration on olfactory detection limits: the running nose. *Front. Allergy.* **2024**, *5*, p 1367669
[18] Concha, A.; Mills, D.S.; Feugier, A.; Zulch, H.; Guest, C.; Harris, R.; Pike, T.W. Using sniffing behavior to differentiate true negative from false negative responses in trained scent-detection dogs. *Chem. Senses.* **2014**, *39* (9), pp 749–754
[19] Brugarolas, R.; Yuschak, S.; Adin, D.; Roberts, D.L.; Sherman, B.L.; Bozkurt, A. Simultaneous Monitoring of Canine Heart Rate and Respiratory Patterns during Scent Detection Tasks. *IEEE Sens. J.* **2019**, *19* (4), pp 1454–1462.
[20] Foster, M.; Brugarolas, R.; Walker, K.; Mealin, S.; Cleghern, Z.; Yuschak, S.; Clark, J.C.; Adin, D.; Russenberger, J.; Gruen, M.; Sherman, B.L.; Roberts, D.L.; Bozkurt, A. Preliminary Evaluation of a Wearable Sensor System for Heart Rate Assessment in Guide Dog Puppies. *IEEE Sens. J.* **2020**, *20* (16), pp 9449–9459.
[21] Chambers, R.D.; Yoder, N.C.; Carson, A.B.; Junge, C.; Allen, D.E.; Prescott, L.M.; Bradley, S.; Wymore, G.; Lloyd, K.; Lyle, S. Deep Learning Classification of Canine Behavior Using a Single Collar-Mounted Accelerometer: Real-World Validation. *Animals.* **2021**, *11* (6), pp 1–19.
[22] Farr, B.D.; Ramos, M.T.; Otto, C.M. The Penn Vet Working Dog Center Fit to Work Program: A Formalized Method for Assessing and Developing Foundational Canine Physical Fitness. *Front. Vet. Sci*. **2020**, *7*, p 470.
[23] Aviles-Rosa, E.O.; Gallegos, S.F.; Prada-Tiedemann, P.A.; Hall, N.J. An Automated Canine Line-Up for Detection Dog Research. *Front. Vet. Sci.* **2021**, *8*, pp 775381–775381.
[24] Stigall, A.R.; Farr, B.D.; Ramos, M.T.; Otto, C.M. A Formalized Method to Acclimate Dogs to Voluntary Treadmill Locomotion at Various Speeds and Inclines. *Animals (Basel).* **2022**, *12* (5), p 567.
[25] O'Brien, C.; Tharion, W.J.; Karis, A.J.; Sullivan, H.M. Predicting military working dog core temperature during exertional heat strain: Validation of a Canine Thermal Model. *J. Therm. Biol.* **2020**, *90*, p 102603.
[26] O'Brien, C.; Berglund, L.G. Predicting recovery from exertional heat strain in military working dogs. *J. Therm. Biol.* **2018**, *76*, pp 45–51.

Build a better melanin: computationally guided approaches to produce melanins with noncanonical amino acids

David C. Garcia[a,b], Ivan Iordanov[a]*
[a]U.S. Army Combat Capabilities Development Command Chemical Biological Center, Research & Operations Directorate, 8198 Blackhawk Rd, Aberdeen Proving Ground, MD 21010
[b]Precise Systems, 22290 Exploration Dr, Lexington Park, MD 20653

ABSTRACT

Compared to petroleum-based synthetic plastics and materials, biological polymers are biodegradable, biocompatible, and can be produced in mass using domestic supply lines. Melanin is one of these biological macromolecules and outside of its role in the human body, could potentially serve as an important and modular building block for packaging, biomedicines, electronic devices, and coatings. Its versatility is further improved as its fundamental substrate, tyrosine, is substitutable by noncanonical amino acids that can impart more complex chemistries like click reactions and protein tagging, as well as desired properties like enhanced durability, antibiotic properties, and modified optical properties. Biologically produced melanin, however, has been hampered by its natural propensity to polymerize as biological production strains are not naturally able to produce it in high concentrations; this limits the amount of melanin that can be synthesized as well as the kinds of melanins that can be produced as testing potential building blocks can be both time intensive and likely to fail due to cellular viability. To this end, we propose taking advantage of high-throughput computational and cell-free synthetic biology techniques to rapidly test the noncanonical amino acids as potential building blocks for novel melanins with emergent properties.

Keywords: Biomanufacturing, bioproduction, machine learning, noncanonical amino acids

1. INTRODUCTION

The canonical melanin production pathway makes use of a single enzyme to carry out an irreversible hydroxylation on a monophenol and a secondary oxidation on a o-diphenol to produce the corresponding o-quinone which polymerizes into melanin.[1] Whereas previous work has shown that melanin can be produced using chemical and biological synthesis, both the production and subsequent purification steps are expensive and time consuming.[2,3] Cell-free systems can bypass these limitations as the lack of a cell membrane both removes the limitations of melanin's insolubility and the need for cell lysis when purifying.[4] Producing melanin-like polymers from noncanonical amino acids (ncAA) could serve an effective method of producing protective coatings, obscurants with enhanced capabilities such as photoactivity, radiological protection, and enhanced durability.[5–8] However, simple methodologies such as substrate screening create massive search spaces with infinite potential reactions to be tested. Cell-free systems inherently lend themselves to rapid prototyping of both novel substrates and enzymes as the chemical environment can easily be modified to include ncAAs as well as dozens of enzymatic homologs made from synthesized DNA.[9]

Organisms make use of tyrosinase-based melaninization due to the ease of acquiring the substrate, tyrosine, but regulatory mechanisms prevent internal pools of the amino acid from being completely, or too quickly, drained.[10,11] As a result, melanin production is tightly regulated and not inherently purposed for high production; cell-free systems beyond not being limited by the need to maintain cellular viability, are capable of making use of ncAAs as a substrate due to the inherently modifiable nature of the cell-free reaction. The large nature of the search space, however, incentivizes downselections of the potentially massive search space inherent to ncAA chemistry. Powerful tools like AlphaFold and Rosetta have greatly improved the ability for accurate predictions of protein activity on specific molecules, allowing for high-performance computing clusters to check potentially thousands of molecules before undertaking the expense of synthesizing specific molecules.[12,13] Further adding density functional theory calculations provides levels of redundancy to the selection, improving the odds of empirical verification.[14] We hypothesize that the polymerization of ncAAs into melanins can be predicted based on the reaction enthalpy of polymerization and binding energies to the enzyme docking site. Furthermore, the degree and type of polymerization can be controlled through manipulating the relative energies of different binding orientations through functionalizing the monomer. In the context of developing new materials, the ability to rapidly screen potential new material both computationally and

empirically will be a substantial capability for the Department of Defense and help define future efforts for developing novel materials.

In this work, a computational set of tools are used to downselect ncAAs that can be oxidized and polymerized into melanin using similarly downselected tyrosinase enzymes. Our aim will ultimately be to demonstrate that ncAAs can serve as effective substrates to produce melanin biopolymers with novel properties. Using cell-free protein synthesis (CFPS) reactions we expressed a set of enzymes and test them against a list of potential substrates for polymerization and found both enzymes and substrates capable of producing melanin-like polymers. We anticipate this work will be foundational in the field of materials science and advance both our understanding of the fundamental principles dictating biopolymerization as well as the enzymatic mechanisms used in nature to produce melanin particles.

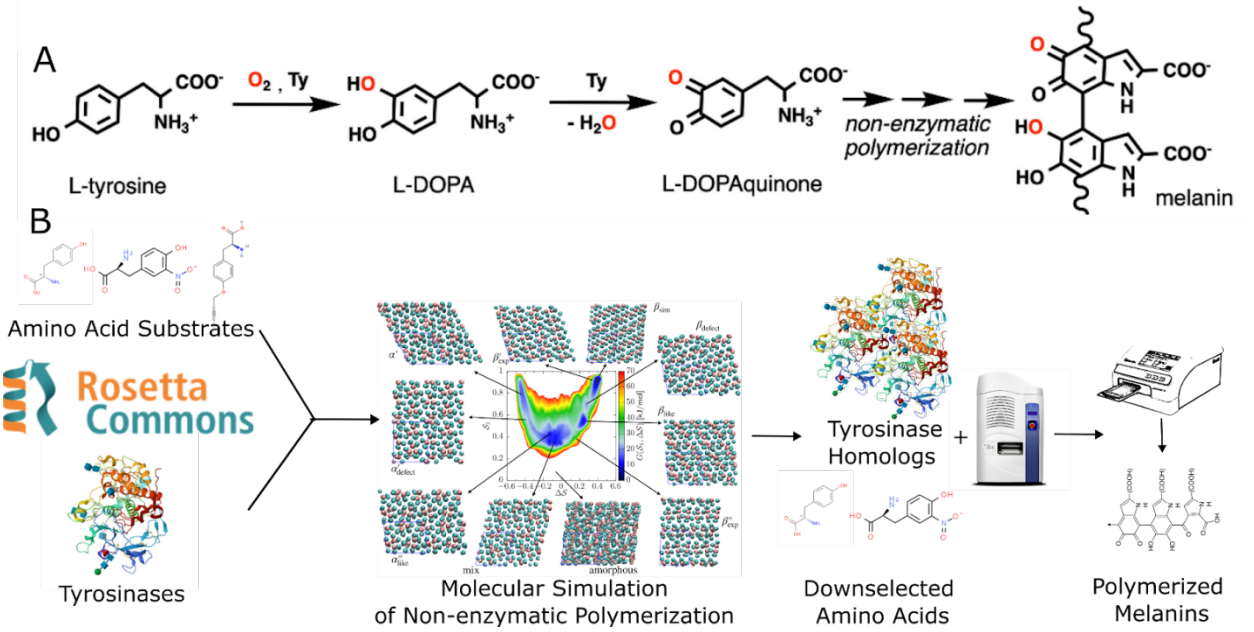

Figure 1. Overview of proposed strategy for developing high-throughput materials characterization platform. A: The monooxygenation step of L-tyrosine to L-DOPA further oxidation to L-DOPAquinone occurs via the addition of tyrosinase. B: Melanin is then produced from a non-enzyme driven polymerization between L-DOPAquinone molecules into an insoluble melanin.

2. METHODOLOGIES

2.1 Cell-free protein synthesis

2.1.1 Cell-free extract production

Cell-free extracts were prepared as previously described.[15] Briefly, BL21 (DE3) *Eschericia coli* were grown in 1 L of 2 × YTPG media (pH 7.2) in a 2.5 L Tunair shake flask and incubated at 34 °C and 220 rpm to an OD_{600} of 3.0. Cells were pelleted by centrifuging for 15 minutes at 5,000 × g and 4 °C, washed three times with cold S30 buffer (10 mM tris-acetate pH 8.2, 14 mM magnesium acetate, 60 mM potassium acetate, 2 mM dithiothreitol), and stored at -80 °C. The thawed cells were suspended in 0.8 mL of S30 buffer per 1 g of wet cell mass. The cells were then lysed by sonication, thawed, and suspended cells were transferred into 1.5 mL microcentrifuge tubes and placed in an ice-water bath to minimize heat damage during sonication. The cells were lysed using a Q125 Sonicator (Qsonica, Newtown, CT) with 3.175 mm diameter probe at frequency of 20 kHz and 50% amplitude. For each 1.4 mL sample, the input energy during sonication was monitored and ceased at ~944 Joules. The lysate was then centrifuged once at 12,000 RCF at 4 °C for 10 minutes. A run-off reaction was performed by incubating at 37 °C and 250 rpm, followed by a second centrifugation (10,000 RCF at 4 °C for 10 minutes). The extract was then aliquoted and flash frozen.

2.1.2 Cell-free protein synthesis reactions

All CFPS reactions were performed using a pTWIST (amp) plasmid containing a T7-expressed enzyme. All DNA was prepared using PCR to produce linear constructs. CFPS reactions contained 30 % v/v lysate and PANOx-SP buffer, as described in detail previously.[13] Briefly, each 1,000 nL reaction was assembled using an Echo 525 Acoustic Liquid Handler (Beckman Coulter, Indianapolis, IN). Each reaction consisted of 300 nL of cell-free extract, 400 nL of PANOx-SP buffer, 50 nL DNA, and varying concentrations of copper sulfate and a melanin-producing substrate, or water based on experimental needs. The final reagent concentrations used in the PANOx-SP buffer are listed in Table 1.

Table 1. Energy mixture components for PANOx-SP base reactions used for enzyme production.

Component	PANOx-SP Final Concentration
Magnesium	12 mM
Potassium glutamate	130 mM
Ammonium glutamate	10 mM
Magnesium acetate	3.7 mM
Potassium acetate	6.2 mM
Tris acetate	5.67 mM (pH 8.2)
HEPES	7.5 mM (pH 7.4)
ATP	1.2 mM
GTP	0.85 mM
CTP	0.85 mM
UTP	0.85 mM
Folic acid	0.072 mM
tRNA	170.6 µg/mL
20 Amino acids	2 mM
PEP	33 mM
NAD	0.33 mM
CoA	0.27 mM
Spermidine	1.5 mM
Putrescine	2 mM
Oxalic acid	4 mM
T7 RNA polymerase	100 µg/mL
RNase inhibitor	1.2 U/µL
DTT	0.5 mM

2.1.3 Cell-free melanin biosynthesis

Following the production of the cell-free melanins, each cell-free reaction was combined with various concentrations of the substrate to be tested as well as CuCl4. Unless otherwise noted, each reaction was 1 µL volume and assembled using an Echo 525 Acoustic Liquid Handler (Beckman Coulter, Indianapolis, IN). Each reaction consisted of 600 nL of a cell-free reaction with the expressed enzyme and with the rest of the volume made up of the relevant substrate, $CuCl_4$ and water. Each reaction was incubated at 37 °C and read for absorbance using a BioTek Synergy Neo2 Hybrid Multimode Reader (Agilent, Santa Clara, CA) at 450 nM using a 536 well plate (Corning Incorporated, Corning, New York).

2.2 Computational enzymatic search – sequence similarity network analysis

To find sensitive enzymes that could be used for cell-free proteins synthesis we first created a sequence similarity network using 1000 tyrosinases from the uniprot database. These enzymes were split up into clusters using the Enzyme Function Initiative - Enzyme Similarity Tool to split them into genetically dissimilar clusters and they were then visualized using cytoscape. Out of 20 clusters the first enzyme from each cluster was selected for synthesis using twist into the pTWIST (amp) backbone vector.

3. RESULTS

3.1 Cell-free expression of tyrosinases – development of sequence similarity network for tyrosinase testing

As a means of both testing the cell-free expression platform as well as our ability to successfully synthesize enzymes a sequence similarity network was created based on enzymes from the uniprot database (Table 1 and Figure 2). These were then split into 20 different clusters and ordered using the twist DNA synthesis service. A variety of enzymes from both prokaryotic and eukaryotic organisms were selected to maximize the likelihood that an enzyme would function on a selected substrate.

Table 2. Initial set of sequences ordered for cell-free tyrosinase expression.

Twist_name	Node Count Cluster Number	Sequence Length	Species	Superkingdom	Taxonomy ID
DG_Tyr_1	1	529	*Aptenodytes forsteri*	Eukaryota	9233
DG_Tyr_2	2	274	*Streptomyces glaucescens*	Bacteria	1907
DG_Tyr_3	3	324	*Streptomyces toyocaensis*	Bacteria	55952
DG_Tyr_4	4	439	*Scytonema sp. HK-05*	Bacteria	1137095
DG_Tyr_5	5	297	*Aliterella atlantica CENA595*	Bacteria	1618023
DG_Tyr_6	6	853	*Mytilus coruscus*	Eukaryota	42192
DG_Tyr_7	7	376	*Mizuhopecten yessoensis*	Eukaryota	6573
DG_Tyr_8	8	268	*Actinoplanes utahensis*	Bacteria	1869
DG_Tyr_9	9	319	*Ruegeria sp. ANG-S4*	Bacteria	1577904
DG_Tyr_10	10	299	*Nitrosospira sp. Nsp1*	Bacteria	136547
DG_Tyr_11	11	294	*Modestobacter caceresii*	Bacteria	1522368
DG_Tyr_12	12	860	*Nitrosomonas sp. Nm51*	Bacteria	133720
DG_Tyr_13	13	550	*Ancylostoma ceylanicum*	Eukaryota	53326

Twist_name	Node Count Cluster Number	Sequence Length	Species	Superkingdom	Taxonomy ID
DG_Tyr_14	14	324	*Nitrosomonas cryotolerans ATCC 49181*	Bacteria	1131553
DG_Tyr_15	15	393	*Basidiobolus meristosporus CBS 931.73*	Eukaryota	1314790
DG_Tyr_16	16	511	*Calocera cornea HHB12733*	Eukaryota	1353952
DG_Tyr_17	17	394	*Basidiobolus meristosporus CBS 931.73*	Eukaryota	1314790
DG_Tyr_18	18	349	*Archangium sp. Cb G35*	Bacteria	1920190
DG_Tyr_19	19	770	*Mytilus galloprovincialis*	Eukaryota	29158
DG_Tyr_20	20	391	*Peterkaempfera bronchialis*	Bacteria	2126346
DG_Tyr_21	21	427	*Sinosporangium album*	Bacteria	504805

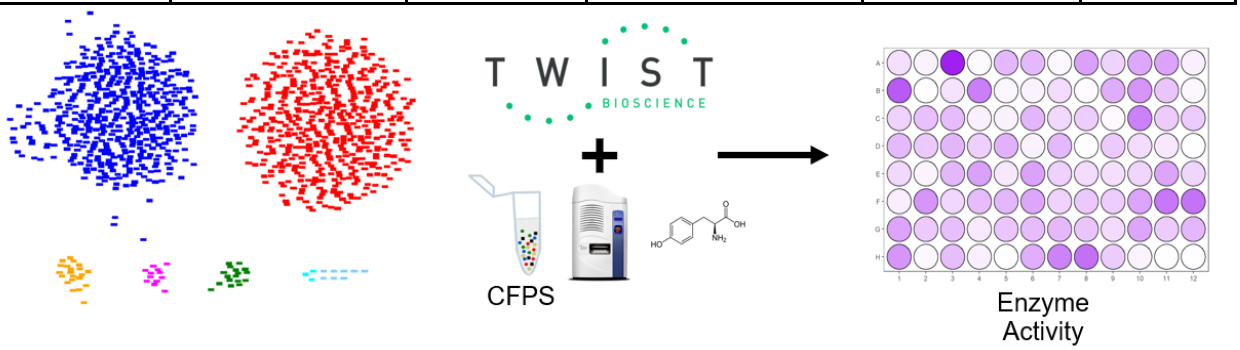

Figure 2. Representative sequence similarity network used to produce enzymes for enzyme activity testing.

3.2 Production of melanin or melanin-like polymers

Following the expression of the cell-free enzymes, we tested if the reactions could successfully produce melanin or a melanin like polymer. We tested three potential substrates for the cell-free reaction 1-naphthol, Anthracene, and 2-aminophenol (2-Aphenol). We found that several and varied enzymes could successfully polymerize the reagents used during the cell-free reaction (Figure 3). Notably, enzyme three was able to produce a more optically unclear material using both 2-Aphenol and anthracene but did not function on 1-naphthol. It is unclear why the enzyme did not function well on 1-naphthol, but it hints to the likelihood that some of our enzymes are more specific than others. Similarly, to finding enzymes that are promiscuous and can be used on any substrate, we are also interested in enzymes that are more specific to certain substrates. Specific enzymes not only ensure a purer product, but also limit the amount of peptide hydrolysis that is likely occurring in our reactions. Some of the enzymes are active enough that even without the presence of the substrate we saw significant amounts of polymerization indicating that the enzyme could not just polymerize the substrate but could also polymerize the protein in the cell-free extract. This is a useful finding for peptide chemistry and further shows that simply finding the most active enzyme could lead to an impure final product. In all cases we successfully produced a positive reaction using at least one enzyme.

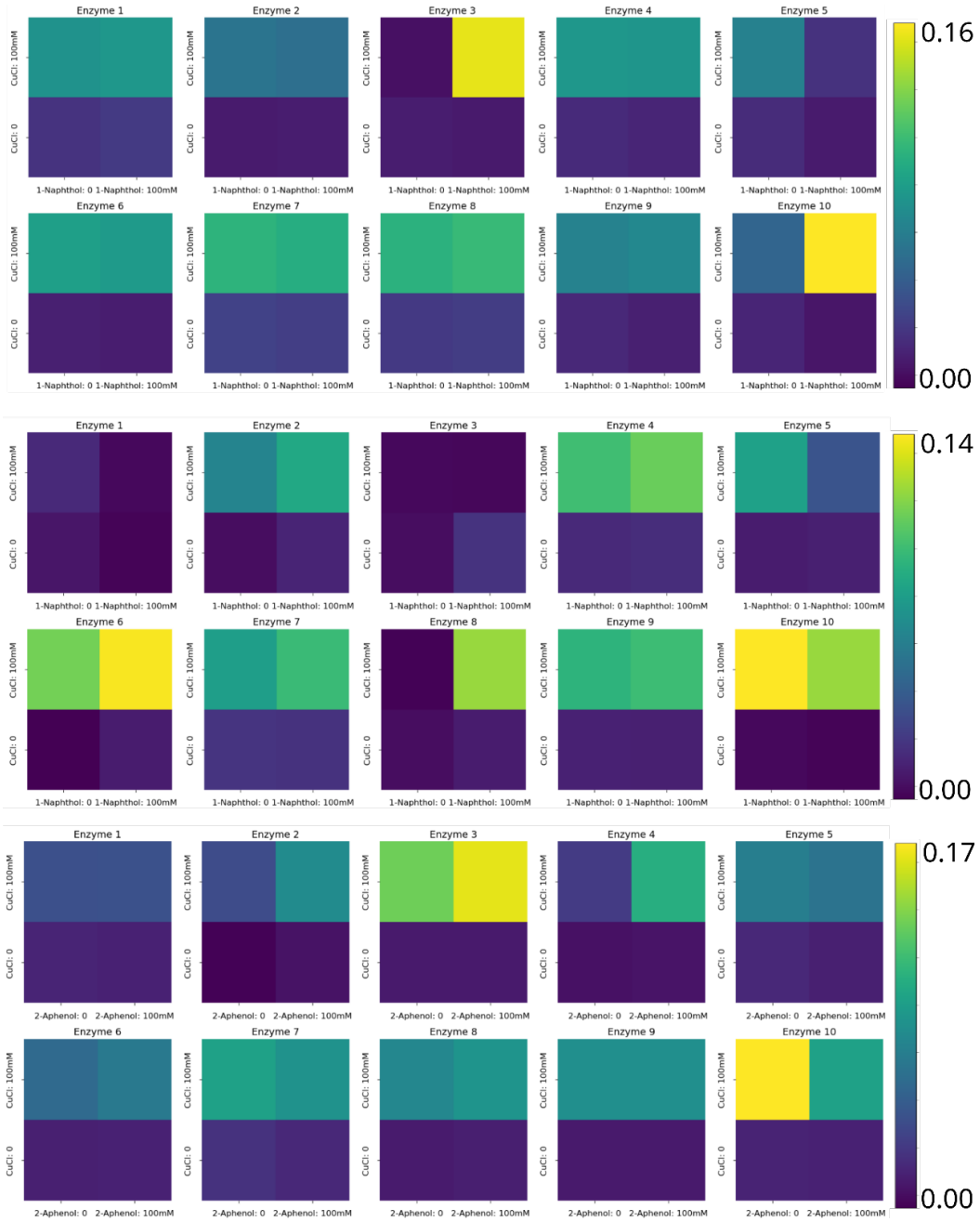

Figure 3. Representative data for the polymerization of substrates combined with cell-free produced tyrosinases. Top: Cell-free reactions for the polymerization of 1-naphthol. Middle: Cell-free reactions for the polymerization of anthracene. Bottom: Cell-free reactions for the polymerization of 2-aminophenol (2-Aphenol). Each reaction is an average of N=3 biological replicates read for absorbance at 450 nM.

CONCLUSIONS

This report describes our progress towards using cell-free systems to test tyrosinases for using ncAAs and nontraditional substrates as building blocks for melanin biopolymers. In this work, we described methods to select an initial set of enzymes for cell-free polymerization of monomer substrates. We found that several enzymes could successfully be used to convert anthracene and 2-aphenol, and 1-naphthol into a melanin-like polymer that could be read using a plate reader assay. Additionally, we described methods to computationally find enzymes that could be

used to find additional enzymes. Our progress so far has created an effective test bed for us to measure the polymerization of connected but disparate substrates using cell-free enzymes. Importantly, each of these reactions is performed in a single microliter well; thus, shifting the focus of this work from an experimental to an analytical bottleneck.

ACKNOWLEDGMENTS

We thank Dr. Gaurav Vora from the U.S. Naval Research Laboratory for providing valuable technical discussions, and Dr. Matthew Lux from the U.S. Army Combat Capabilities Development Command Chemical Biological Center for helpful discussions in support of this work. Funding was provided by the U.S. Army via the Chemical Biological Advanced Materials Manufacturing Program (PE 0601102A Project VR9) at the Combat Capabilities Development Command Chemical Biological Center.

REFERENCES

[1] Cao, W.; Zhou, X.; McCallum, N.C.; Hu, Z.; Ni, Q.Z.; Kapoor, U.; Heil, C.M.; Cay, K.S.; Zand, T.; Mantanona, A.J.; Jayaraman, A.; Dhinojwala, A.; Deheyn, D.D.; Shawkey, M.D.; Burkart, M.D.; Rinehart, J.D.; Gianneschi, N.C. Unraveling the structure and function of melanin through synthesis. *J. Am. Chem. Soc.* **2021**, *143* (7), pp 2622–2637.

[2] Lagunas-Muñoz, V.H.; Cabrera-Valladares, N.; Bolívar, F.; Gosset, G.; Martínez, A. Optimum melanin production using recombinant *Escherichia coli*. *J. Appl. Microbiol.* **2006**, *101* (5), pp 1002–1008.

[3] Zou, Y.; Tian, M. Fermentative production of melanin by *Auricularia auricula*. *J. Food Process. Preserv.* **2017**, *41* (3), p e12909.

[4] Garenne, D.; Haines, M.C.; Romantseva, E.F.; Freemont, P.; Strychalski, E.A.; Noireaux, V. Cell-free gene expression. *Nat. Rev. Methods Primers.* **2021**, *1* (49), pp 1–18.

[5] Sono, K.; Lye, D.; Moore, C.A.; Boyd, W.C.; Gorlin, T.A.; Belitsky, J.M. Melanin-based coatings as lead-binding agents. *Bioinorg. Chem. Appl.* **2012**, *2012*, p 361803.

[6] Leisle, L.; Valiyaveetil, F.; Mehl, R.A.; Ahern, C.A. Incorporation of non-canonical amino acids. In *Novel Chemical Tools to Study Ion Channel Biology*, Ahern, C., Pless, S., Eds.; *Advances in Experimental Medicine and Biology*; Springer New York: New York, NY, **2015**; Vol. 869, pp 119–151.

[7] Pakdel, E.; Xie, W.; Wang, J.; Kashi, S.; Sharp, J.; Zhang, Q.; Varley, R.J.; Sun, L.; Wang, X. Superhydrophobic natural melanin-coated cotton with excellent UV protection and personal thermal management functionality. *Chem. Eng. J.* **2022**, *433*, p 133688.

[8] Casadevall, A.; Cordero, R.J.B.; Bryan, R.; Nosanchuk, J.; Dadachova, E. Melanin, Radiation, and Energy Transduction in Fungi. *Microbiol. Spectr.* **2017**, *5* (2), pp 1–6.

[9] Karim, A.S.; Jewett, M.C. Cell-free synthetic biology for pathway prototyping. In *Methods in Enzymology*; Elsevier: Cambridge, MA, **2018**; Vol. 608, pp 31–57.

[10] D'Mello, S.; Finlay, G.; Baguley, B.; Askarian-Amiri, M. Signaling pathways in melanogenesis. *Int. J. Mol. Sci.* **2016**, *17* (7), p 1144.

[11] Slominski, A.; Tobin, D.J.; Shibahara, S.; Wortsman, J. Melanin pigmentation in mammalian skin and its hormonal regulation. *Physiol. Rev.* **2004**, *84* (4), pp 1155–1228.

[12] Schenkelberg, C.D.; Bystroff, C. InteractiveROSETTA: A graphical user interface for the PyRosetta protein modeling suite. *Bioinformatics.* **2015**, *31* (24), pp 4023–4025.

[13] Varadi, M.; Anyango, S.; Deshpande, M.; Nair, S.; Natassia, C.; Yordanova, G.; Yuan, D.; Stroe, O.; Wood, G.; Laydon, A.; Žídek, A.; Green, T.; Tunyasuvunakool, K.; Petersen, S.; Jumper, J.; Clancy, E.; Green, R.; Vora, A.; Lutfi, M.; Figurnov, M.; Cowie, A.; Hobbs, N.; Kohli, P.; Kleywegt, G.; Birney, E.; Hassabis, D.; Velankar, S. AlphaFold protein structure database: Massively expanding the structural coverage of protein-sequence space with high-accuracy models. *Nucleic Acids Res.* **2022**, *50* (D1), pp D439–D444.

[14] Madkhali, N.; Algessair, S. Exploring the optical properties of metal-modified melanin following ultraviolet irradiation: An experimental and theoretical study using density functional theory. *Heliyon.* **2024**, *10* (7), p e29287.

[15] Kwon, Y.-C.; Jewett, M.C. High-throughput preparation methods of crude extract for robust cell-free protein synthesis. *Sci. Rep.* **2015**, *5* (1), p 8663.